UNIVERSIDAD DE ZARAGOZA

DEPARTAMENTO DE INGENIERÍA QUÍMICA Y
TECNOLOGÍA DEL MEDIO AMBIENTE

INSTITUTO DE CARBOQUÍMICA (CSIC)

CATALIZADORES PARA PILAS DE COMBUSTIBLE DE ALCOHOL DIRECTO

TESIS DOCTORAL

Verónica Celorrio Remartinez

2012

UNIVERSIDAD DE ZARAGOZA

DEPARTAMENTO DE INGENIERÍA QUÍMICA Y TECNOLOGÍA DEL MEDIO AMBIENTE

INSTITUTO DE CARBOQUÍMICA (CSIC)

CATALIZADORES PARA PILAS DE COMBUSTIBLE DE ALCOHOL DIRECTO

MEMORIA

Presentada en el Departamento de Ingeniería Química y Tecnología del Medio Ambiente de la Universidad De Zaragoza, para optar al grado de Doctor en Ingeniería Química, por Verónica Celorrio Remartinez.

Zaragoza, a 27 de Febrero de 2012.

GOBIERNO DE ESPAÑA
MINISTERIO DE ECONOMÍA Y COMPETITIVIDAD

CSIC
Instituto de Carboquímica

El doctor D. Antonio Monzón Bescós, Catedrático del Departamento de Ingeniería Química y Tecnologías del Medio Ambiente de la Universidad de Zaragoza y tutor de doctorado de la Ingeniera Verónica Celorrio Remartinez.

AUTORIZA:

La presentación de la Tesis Doctoral titulada "CATALIZADORES PARA PILAS DE COMBUSTIBLE DE ALCOHOL DIRECTO'', dirigida por los doctores Dña. Mª Jesús Lázaro Elorri y D. Rafael Moliner Álvarez.

Zaragoza, a 27 de Febrero de 2012

Fdo.: Dr. D. Antonio Monzón Bescós.

C/ Miguel Luesma Castán, 4
50018 ZARAGOZA
Tfno.: 97 673 39 77
Fax: 97 673 33 18

GOBIERNO DE ESPAÑA
MINISTERIO DE ECONOMÍA Y COMPETITIVIDAD

CSIC
Instituto de Carboquímica

La doctora Dña. María Jesús Lázaro Elorri, directora del Instituto de Carboquímica del Consejo Superior de Investigaciones Científicas.

CERTIFICA:

Que el trabajo correspondiente a la presente Memoria titulada ‘’CATALIZADORES PARA PILAS DE COMBUSTIBLE DE ALCOHOL DIRECTO’’, ha sido realizada en dicho Instituto por Dña. Verónica Celorrio Remartinez, bajo la dirección de los doctores Dña. Mª Jesús Lázaro Elorri y D. Rafael Moliner Álvarez, para optar al grado de Doctor.

Zaragoza, a 27 de Febrero de 2012.

Fdo.: Dr. Dña. Mª Jesús Lázaro Elorri.

C/ Miguel Luesma Castán, 4
50018 ZARAGOZA
Tfno.: 97 673 39 77
Fax: 97 673 33 18

GOBIERNO DE ESPAÑA
MINISTERIO DE ECONOMÍA Y COMPETITIVIDAD

CSIC
Instituto de Carboquímica

Los doctores Dña. Mª Jesús Lázaro Elorri y D. Rafael Moliner Álvarez, Investigador Científico y Profesor de Investigación, respectivamente, del Instituto de Carboquímica del Consejo Superior de Investigaciones Científicas.

CERTIFICAN:

Que la presente Memoria titulada "CATALIZADORES PARA PILAS DE COMBUSTIBLE DE ALCOHOL DIRECTO", corresponde al trabajo realizado por la Ingeniera Dña. Verónica Celorrio Remartinez, en el citado centro, y autorizan su presentación para optar al grado de Doctor.

Para que así conste, expedimos el presente certificado en Zaragoza, a 27 de Febrero de 2012.

Fdo: Dra. Dña. Mª Jesús Lázaro Elorri Fdo.: Dr. D. Rafael Moliner Álvarez.

C/ Miguel Luesma Castán, 4
50018 ZARAGOZA
Tfno.: 97 673 39 77
Fax: 97 673 33 18

De acuerdo con la normativa vigente, esta Tesis Doctoral se presenta como un compendio de publicaciones. Los trabajos incluidos en esta Memoria son:
Artículos presentados a la Comisión de Doctorado de la Universidad de Zaragoza:

- V. Celorrio, L. Calvillo, M.V. Martínez-Huerta, R. Moliner, M.J. Lázaro. *Study of the Synthesis Conditions of Carbon Nanocoils for Energetic Applications*. Energy & Fuels 24 (2010) 3361-3365.
- V. Celorrio, L. Calvillo, S. Pérez-Rodríguez, M.J. Lázaro, R. Moliner. *Modification of the properties of carbon nanocoils by different treatments in liquid phase*. Microporous and Mesoporous Materials 142 (2011) 55-61.
- M.J. Lázaro V. Celorrio, L. Calvillo, E. Pastor, R. Moliner. *Influence of the synthesis method on the properties of Pt catalysts supported on carbon nanocoils for ethanol oxidation*. Journal of Power Sources 196 (2011) 4236-4241.
- V. Celorrio, L. Calvillo, R. Moliner, E. Pastor, M.J. Lázaro. *On the enhancement of activity of Pt and Pt-Ru catalysts in methanol electrooxidation by using carbon nanocoils as catalyst support*, en preparación.
- M.G. Montes de Oca, D. Plana, V. Celorrio, M.J. Lázaro, D.J. Fermín. *Electrocatalytic properties of strained Pd nanoshells at Au nanostructures: CO and HCOOH oxidation*. Journal of Physical Chemistry C 116 (2012) 692-699.
- V. Celorrio, M.G. Montes de Oca, D. Plana, R. Moliner, M.J. Lázaro, D.J. Fermín. *The Effect of Carbon Supports on the Electrocatalytic Reactivity of Au-Pd Core-Shell Nanoparticles*. Journal of Physical Chemistry C 116 (2012) 6275-6282.

C/ Miguel Luesma Castán, 4
50018 ZARAGOZA
Tfno.: 97 673 39 77
Fax: 97 673 33 18

According to the current regulations, this thesis is presented as a compendium of publications. The papers included in this work are:

Papers presented to the Doctoral Committee of the University of Zaragoza:

- V. Celorrio, L. Calvillo, M.V. Martínez-Huerta, R. Moliner, M.J. Lázaro. *Study of the Synthesis Conditions of Carbon Nanocoils for Energetic Applications*. Energy & Fuels 24 (2010) 3361-3365.

- V. Celorrio, L. Calvillo, S. Pérez-Rodríguez, M.J. Lázaro, R. Moliner. *Modification of the properties of carbon nanocoils by different treatments in liquid phase*. Microporous and Mesoporous Materials 142 (2011) 55-61.

- M.J. Lázaro V. Celorrio, L. Calvillo, E. Pastor, R. Moliner. *Influence of the synthesis method on the properties of Pt catalysts supported on carbon nanocoils for ethanol oxidation*. Journal of Power Sources 196 (2011) 4236-4241.

- V. Celorrio, L. Calvillo, R. Moliner, E. Pastor, M.J. Lázaro. *On the enhancement of activity of Pt and Pt-Ru catalysts in methanol electrooxidation by using carbon nanocoils as catalyst support*, under preparation.

- M.G. Montes de Oca, D. Plana, V. Celorrio, M.J. Lázaro, D.J. Fermín. *Electrocatalytic properties of strained Pd nanoshells at Au nanostructures: CO and HCOOH oxidation*. Journal of Physical Chemistry C 116 (2012) 692-699.

- V. Celorrio, M.G. Montes de Oca, D. Plana, R. Moliner, M.J. Lázaro, D.J. Fermín. *The Effect of Carbon Supports on the Electrocatalytic Reactivity of Au-Pd Core-Shell Nanoparticles*. Journal of Physical Chemistry C 116 (2012) 6275-6282.

C/ Miguel Luesma Castán, 4
50018 ZARAGOZA
Tfno.: 97 673 39 77
Fax: 97 673 33 18

A mi familia

AGRADECIMIENTOS

Una vez finalizada mi tesis doctoral, tengo que enfrentarme al capítulo más complicado, que no es otro que el de los agradecimientos. He de sintetizar en unas líneas mi gratitud hacia las personas que me han ayudado. Sin ellas, hubiese sido imposible afrontar este proyecto.

En primer lugar, un sincero agradecimiento a mis Directores, Mª Jesús Lázaro Elorri y Rafael Moliner Álvarez, por todo el tiempo que me han dado y por sus sugerencias e ideas de las que tanto provecho he sacado.

Al Consejo Superior de Investigaciones Científicas, por darme la oportunidad de realizar este trabajo en forma de una beca predoctoral. A los directores del Instituto de Carboquímica durante este periodo, el Dr. Juan Adánez y la Dra. Mª Jesús Lázaro, por permitir la realización de este trabajo en sus instalaciones. A la gente del grupo Conversión de Combustibles Fósiles y Valorización de Residuos, tanto a los de ahora, como a los que ya no están. En especial a Laura, por su ayuda en todo momento y a cualquier hora. A las chicas del turno de comida de las dos, por las conversaciones no científicas y las risas, que ayudan a continuar el resto de la jornada con una sonrisa.

I want to acknowledge Dr. David J. Fermín and all the people of the *Electrochemistry Group* of the Bristol University for their patient and friendship. Mi más sincero agradecimiento a David, por abrirme los ojos al mundo de la electroquímica, por su atención, por confiar en mí, y además por dejarme compartir con él momentos más distendidos. A Dani y Lupita, por su amistad y su ayuda en todo momento, porque fuimos y seguimos siendo un gran equipo de trabajo, y por ser mi familia cuando ellos estaban lejos. A Virginie por su amistad, por largas conversaciones delante de un ordenador, y por darme ánimos siempre. To the 18 Sunningdale's people, I will always remember our activities and international dinners.

A la Dra. Elena Pastor y a todo el grupo de *Ciencia Superficial y Electroquímica* de la Universidad de La Laguna, por hacerme sentir tan a gusto durante mi estancia con ellos. A Jonathan y Olmedo por su paciencia, los jueves laguneros (y los viernes y los sábados…), su ayuda siempre que la necesité (tanto profesional como personal) y básicamente por su amistad. A Dalila por los chocolates con churros y acompañarme en

largas tardes de compras. Y por supuesto a Lales, Nico y Yaiza, por dejarme formar parte de su familia durante ese tiempo.

A mis amigos. Mención especial para *Los Galácticos*, por saber sacarme siempre una sonrisa y estar ahí cuando más los he necesitado. A Esther-láctica, por saber estar para lo bueno y para lo malo en una atención 24 horas.

Y por último y no menos importante a mi familia, que me ha visto crecer durante todos estos años. Muchas gracias por su apoyo constante en todo momento, y por confiar en mí. Empezando por los más cercanos y hasta los más lejanos todos han ayudado. Desde los imprudentes que insistían en enterarse del tema de la tesis, hasta los que preguntaban que cuando estaría terminada, pasando por los que se reían de ella y de la investigación. Cada uno ya sabe la parte que le corresponde. A mi yaya Rosa y mi yayo Manolo, porque sé que les habría encantado compartir este momento conmigo. A Lola, por aguantar largas conversaciones de desahogo, y por ser la "culpable" de que yo entrara en este mundillo. A mis padres y mi hermano, por aguantar los altos y bajos durante estos cuatro años y darme siempre todo su apoyo para seguir adelante.

En general quisiera agradecer a todas y cada una de las personas que han vivido conmigo la realización de esta tesis doctoral, con sus altos y bajos y que no necesito nombrar porque tanto ellas como yo sabemos que les agradezco el haberme brindado todo el apoyo, colaboración, ánimo y sobre todo cariño y amistad.

INDICE

INDICE DE FIGURAS

INDICE DE TABLAS

Capítulo 1

Introducción

Los sistemas energéticos del futuro implicarán el uso directo de energía solar, la producción y el almacenamiento de vectores energéticos como el hidrógeno, y la utilización de sistemas avanzados de conversión de energía de una forma mucho más respetuosa con el medio ambiente, en comparación con el uso extendido de los combustibles fósiles en la actualidad. El hidrógeno es considerado como un nuevo vector energético, es decir, un transportador de energía primaria hasta los lugares de consumo, que ofrece importantes ventajas [MOLINER 2005].

Desde un punto de vista medioambiental, el hidrógeno es el vector energético ideal, ya que puede ser transformado en calor y energía mecánica, o en energía eléctrica. El balance de CO_2 para el proceso completo depende del combustible o el tipo de energía primaria utilizada para producir el hidrógeno. El hidrógeno se puede obtener por

diferentes métodos, pero básicamente todos se apoyan en el reformado de combustibles fósiles y en la electrólisis del agua.

Una de las tecnologías que ha centrado un gran interés en las últimas décadas son las pilas de combustible, ya que utilizan combustibles como el hidrógeno para la generación de energía limpia, eficiente, fiable y de alta calidad. Se espera que esta tecnología proporcione un apoyo importante en el suministro energético, necesario para impulsar a la industria, el transporte, las comunicaciones, la educación, la tecnología y la agricultura en los próximos años. Sin embargo, aunque actualmente se encuentran disponibles algunas aplicaciones con pilas de combustible, éstas se hallan aún en una etapa demostrativa. Por lo tanto, la tecnología de las pilas de combustible se encuentra todavía en una fase de investigación, y es a éste nivel en el que se trabaja en la industria y en diversas instituciones de investigación.

Algunos aspectos importantes que buscan perfeccionarse en la etapa de investigación son: búsqueda de nuevos materiales para fabricación y construcción de componentes; modelado; obtención de topologías eficientes de sistemas de control y potencia; desarrollo e implementación de simuladores y emuladores; desarrollo de sistemas de cogeneración de energía eléctrica; empleo en prototipos, sistemas demostrativos y sistemas reales en la industria automotriz; aplicaciones estacionarias y móviles [SOPIAN 2006].

1.1. PILAS DE COMBUSTIBLE

Las pilas de combustible son dispositivos electroquímicos que, en presencia de un catalizador, convierten directamente y de manera continua la energía química de un combustible en energía eléctrica con un rendimiento elevado. Esta obtención de electricidad, en forma de corriente continua, se lleva a cabo sin la necesidad de ningún proceso de combustión, ya que la oxidación del combustible y la reducción del comburente se producen en lugares físicos diferentes. La conversión electroquímica asegura un elevado rendimiento en el proceso de transformación energética, mayor del que se obtendría en las maquinas térmicas, ya que éstas últimas presentan la limitación impuesta por el ciclo de Carnot.

El concepto de funcionamiento de una pila resulta bastante simple. El elemento básico es una celda electroquímica formada por dos electrodos (ánodo y cátodo), y un electrolito que los pone en contacto. En el ánodo se produce la reacción de oxidación del combustible, en la que se liberan electrones incapaces de atravesar el electrolito, por lo que se ven forzados a atravesar un circuito externo. Los iones resultantes de la oxidación se mueven a través del electrolito para llegar al cátodo, lugar en el que se produce la reacción de reducción. La sustancia oxidante se reduce, ganando los electrones obtenidos en el ánodo y se recombina con los cationes correspondientes, formando así una especie neutra. Dicha especie depende del tipo de pila y del combustible que utilice.

Las pilas de combustible se clasifican normalmente de acuerdo al electrolito que utilizan, el cual determina el tipo de combustible y comburente, así como la temperatura de operación de las mismas. Por ello, resulta también habitual clasificar a las pilas de combustible según su temperatura de funcionamiento, considerándolas como de alta (> 200 ºC) o baja (< 200 ºC) temperatura. Las pilas de combustible de alta temperatura admiten combustibles de menor calidad o con cierto contenido en carbono, mientras que las de baja temperatura requieren ser alimentadas con hidrógeno de mayor pureza.

1.1.1. Pilas de combustible de electrolito polimérico (PEFC)

Entre los diferentes tipos de pilas de combustible, las de membrana de intercambio de protones (PEMFC) y las de metanol directo (DMFC) son las candidatas más prometedoras para aplicaciones portátiles y estacionarias, especialmente en el sector transporte, debido a las ventajas que presentan. Entre estas ventajas destacan su bajo peso, rápido arranque, y su operación a baja temperatura [WEE 2007].

Las pilas de combustible tipo PEM, operan a bajas temperaturas (80 ºC), lo que permite que arranquen rápidamente al necesitar menos tiempo de calentamiento. Esta baja temperatura de trabajo produce un menor desgaste en los componentes del sistema, lo que supone una mayor duración del mismo. Este tipo de pilas presentan algunas desventajas, entre las más destacadas se encuentran, el elevado costo, producido por el empleo metales preciosos como el platino como catalizador, y la gran sensibilidad que presentan a la contaminación por CO.

Los retos actuales están en disminuir el coste y aumentar la eficiencia, lo que se traduce en disminuir la carga de platino, reducir el espesor de la capa catalítica, optimizar la dispersión del catalizador y mejorar las prestaciones de la membrana polimérica [SASIKUMAR 2004].

1.2. PILAS DE COMBUSTIBLE DE MEMBRANA DE INTERCAMBIO DE PROTONES (PEMFC)

1.2.1. Descripción

La pila tipo PEM es una de las más sencillas conceptualmente, y en ella se alimenta el ánodo con hidrógeno gaseoso y el cátodo con oxígeno puro o presente en el aire ambiental. Las reacciones que se llevan a cabo son las siguientes:

Ánodo:	$H_2 \rightarrow 2\ H^+ + 2e^-$	[Ec. 1.1]
Cátodo:	$½\ O_2 + 2\ H^+ + 2e^- \rightarrow\ H_2O$	[Ec. 1.2]
Reacción global:	$H_2 + ½\ O_2 \rightarrow\ H_2O$	[Ec. 1.3]

En la Figura 1.1. pueden observarse los diferentes elementos en que se divide una pila de combustible PEM. Básicamente una unidad elemental (celda), se compone de una lámina de electrolito, dos electrodos (ánodo y cátodo), catalizador, placas bipolares y capas de difusión de gas.

Su funcionamiento comienza cuando se suministra hidrógeno al ánodo y oxígeno al cátodo. Ambos gases penetran por los canales de las placas bipolares de sus respectivos electrodos, y se distribuyen a lo largo de toda su superficie a través de las capas de difusión de gas. Una vez que los gases reactivos han atravesado la capa de difusión, se encuentran con el catalizador, que en el caso de las pilas PEM está formado por aleaciones metálicas basadas en platino. Esta capa de catalizador está situada entre la capa de difusión de gas y el electrolito, y en el caso del ánodo tiene como misión disociar la molécula de hidrógeno en protones y electrones. El catalizador catódico se encarga de combinar los iones H^+ provenientes del electrolito con el oxígeno del aire y los electrones del circuito exterior para dar agua como resultado.

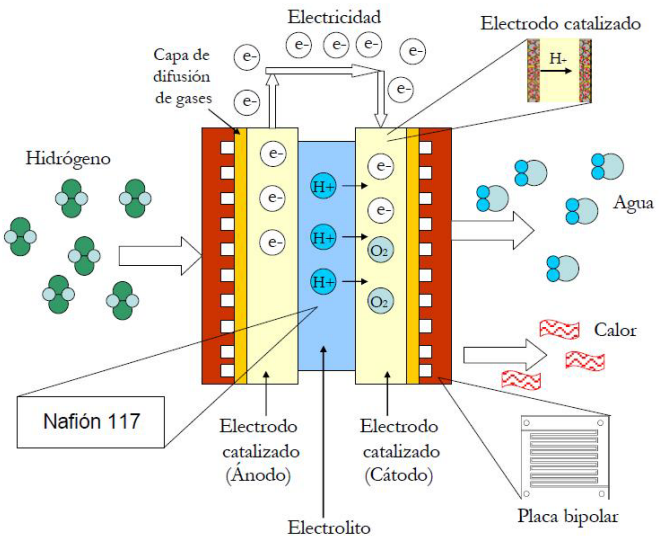

Figura 1.1. *Esquema general de funcionamiento de una pila PEM. Se pueden observar los diferentes elementos que intervienen en la reacción electroquímica, así como los componentes básicos de la estructura (electrodos, electrolito, placas bipolares y membrana difusora).*

En las PEMFC, la membrana es sólida y el único líquido existente en ella es el agua, producida por recombinación entre el oxígeno del cátodo y los protones y electrones procedentes del ánodo. Como las pilas tipo PEM operan a unos 80 ºC, el agua se produce de forma líquida y se expulsa por el excedente de flujo de alimentación del cátodo. Sin embargo, la deshidratación de la membrana disminuye en gran medida su conductividad protónica, por lo que la gestión de esta agua es fundamental para minimizar las pérdidas óhmicas y en definitiva asegurar el buen funcionamiento de la pila.

Uno de los costes más significativos en las PEMFC son los electrodos, donde se sitúan los catalizadores de platino. En los últimos años se ha tratado de reducir la cantidad de platino necesaria para la reacción. Se espera que en los próximos años se sigan reduciendo estas cantidades para poder reducir el coste global de las PEMFC y hacer viable su comercialización a gran escala.

Sin embargo, las PEMFC no sólo aceptan como combustible el hidrógeno puro, sino que toleran además hidrocarburos ligeros reformados, desde los que extraer el hidrógeno (metanol, gas natural o productos derivados del petróleo). Cuando una PEMFC opera con hidrocarburos reformados, el monóxido de carbono (CO) producido en el proceso debe ser eliminado ya que, al interaccionar con los catalizadores de platino los envenena, disminuyendo drásticamente su vida útil.

1.2.2. Electrodos de una PEMFC

En el corazón de una pila de combustible se encuentra el ensamblaje Ánodo/Electrolito/Cátodo, más conocido como MEA (*Membrane Electrode Assembly*). La MEA está compuesta por la membrana de intercambio de protones, y dos electrodos (ánodo y cátodo) de difusión de gas (*Gas Diffussion Electrode, GDE*). Normalmente, estos componentes se fabrican por separado y posteriormente se ensamblan sometiéndolos a altas presiones y temperaturas [LISTER 2004].

Los electrodos de difusión de gas, están a su vez compuestos por una capa de difusión de gas (*Gas Diffussion Layer, GDL*) y una capa catalítica (capa activa). En estos electrodos tienen lugar los tres fenómenos de transporte necesarios para el buen funcionamiento de la pila (Figura 1.2.), que son [LITSTER 2004]: i) transporte de los protones desde la membrana al catalizador; ii) transporte de los electrones desde el colector de corriente hasta el catalizador a través de la capa de difusión de gas; y iii) transporte de los reactivos y productos hasta y desde el catalizador.

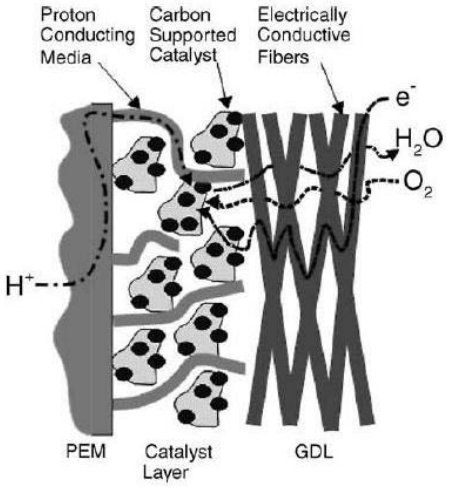

Figura 1.2. *Esquema de la estructura de un electrodo de difusión de gas (cátodo) de una pila de combustible PEM [LITSTER 2004].*

Uno de los mayores desafíos en la investigación de pilas de combustible hoy en día es el diseño y la obtención de la llamada interfase triple (*Triple Phase Boundary*, TPB) entre los gases reactantes, el electrolito (conductor iónico) y el catalizador que actúa como conductor electrónico (Figura 1.3.). El concepto de esta triple interfase consiste en que la oxidación del hidrógeno y la reducción del oxígeno sólo pueden ocurrir en los centros, llamados *triple phase boundaries*, donde se produce este contacto

triple [O'HAYRE 2005, SASIKUMAR 2004, SCHERER 1997]. Ésta superficie se logra haciendo uso de un electrodo poroso de difusión de gas que cumpla dos requisitos esenciales: i) gran superficie electroquímicamente activa y, ii) posible flujo de masa perpendicular al plano del electrodo/electrolito.

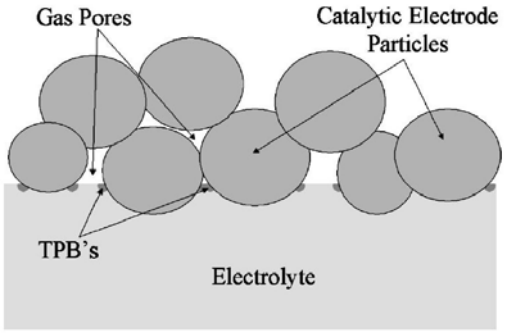

Figura 1.3. *Esquema simplificado de la interfase electrodo/electrolito en una pila de combustible, mostrando las zonas de reacción electroquímicamente activas (TPB) donde se produce el contacto catalizador-electrolito-gas [O'HAYRE 2005].*

1.2.3. Pilas de combustible de alcohol directo (DAFCs)

Los problemas de almacenamiento y distribución de hidrógeno como combustible han originado una búsqueda de combustibles alternativos que faciliten su uso, principalmente, cuando se considera la aplicación de las pilas de combustible en vehículos. De los diferentes combustibles susceptibles de ser oxidados en un ánodo, los alcoholes son los que han despertado mayor interés, entre ellos destacan el metanol, el etanol y el ácido fórmico. Las celdas que operan directamente con alcoholes (DAFC, *Direct Alcohol Fuel Cell*) tienen como principio la oxidación del alcohol en el ánodo que puede ser introducido en la celda como líquido o como gas. Si bien el electrolito puede ser una disolución ácida, la mayoría de los desarrollos actuales se basan en la tecnología de la celda de electrolito polimérico sólido [VIELSTICH 2003]. Las reacciones producidas en este tipo de pilas se presentan a continuación:

- Pilas de combustible de metanol directo (DMFC):

Ánodo:	$CH_3OH + H_2O \rightarrow CO_2 + 6\ H^+ + 6e^-$	[Ec. 1.4]
Cátodo:	$3/2\ O_2 + 6\ H^+ + 6e^- \rightarrow 3\ H_2O$	[Ec. 1.5]
Reacción global:	$CH_3OH + 3/2\ O_2 \rightarrow CO_2 + 2\ H_2O$	[Ec. 1.6]

- Pilas de combustible de etanol directo (DEFC):

Ánodo:	$CH_3CH_2OH + 3\ H_2O \rightarrow 2\ CO_2 + 12\ H^+ + 12e^-$	[Ec. 1.7]
Cátodo:	$3\ O_2 + 12\ H^+ + 12e^- \rightarrow 6\ H_2O$	[Ec. 1.8]
Reacción global:	$CH_3CH_2OH + 3\ O_2 \rightarrow 2\ CO_2 + 3\ H_2O$	[Ec. 1.9]

- Pilas de combustible de ácido fórmico directo (DFAFC):

Ánodo:	$HCOOH \rightarrow CO_2 + 2\ H^+ + 2e^-$	[Ec. 1.10]
Cátodo:	$½\ O_2 + 2\ H^+ + 2e^- \rightarrow H_2O$	[Ec. 1.11]
Reacción global:	$HCOOH + ½\ O_2 \rightarrow CO_2 + H_2O$	[Ec. 1.12]

El mayor problema de éste tipo de pilas es la formación de intermediarios de reacción durante los procesos de oxidación. Algunos de ellos resultan perjudiciales, como el CO, ya que se pueden adsorber en la superficie de los catalizadores, bloqueando los sitios catalíticos activos [VIELSTICH 2003, ARICÓ 2001].

Además, las celdas que usan alcoholes como combustible, tienen una serie de problemas asociados, como: i) el traspaso (*crossover*) del alcohol a través de la membrana, el cual produce un potencial mixto en el cátodo, además del envenenamiento del catalizador por la adsorción de los intermediarios [HEINZEL 1999]; ii) la cinética lenta de reducción de oxígeno; y iii) la lenta oxidación del alcohol por la formación de intermediarios adsorbidos, entre ellos el monóxido de carbono.

El efecto conocido como *crossover* es producido ya que, a pesar de que la membrana de electrolito debería ser "impermeable" a los reactivos, algunos de ellos consiguen atravesarlo. Asimismo, el combustible utilizado tiene una enorme tendencia a filtrarse, por lo que éste también tiende a atravesar la membrana polimérica. De este modo, tanto los electrones como las moléculas de combustible pueden atravesar la membrana de Nafion y llegar al cátodo, con lo que reaccionarían con el oxígeno allí presente sin producir ningún tipo de corriente eléctrica. La consecuencia más inmediata de todo esto es que la tensión de pila a circuito abierto es inferior a la esperada, y ésta consumirá combustible sin estar produciendo electricidad.

1.3. MATERIALES DE CARBONO COMO SOPORTE DE ELECTROCATALIZADORES

Los materiales de carbono han sido utilizados como soportes de catalizadores de metales preciosos durante muchos años. En comparación con otros materiales ampliamente utilizados como la alúmina o los óxidos de magnesio, los materiales carbonosos tienen la ventaja de ser estables tanto en medio ácido como básico. Además, los materiales carbonosos poseen otras características como una buena conductividad eléctrica, alta resistencia a la corrosión, propiedades superficiales adecuadas y alta área superficial específica; que los hacen interesantes para su uso como soportes.

Los materiales de carbono tienen una gran influencia en las propiedades de los metales nobles soportados, como en el tamaño de partícula, la morfología, la estabilidad y la dispersión [KIM 2006, YU 2007]. Por otra parte, los materiales carbonosos también pueden afectar el rendimiento del electrocatalizador en la pila de combustible, alterando los mecanismos de transporte de masa, la conductividad eléctrica de la capa catalítica, el área electroquímica activa, y la estabilidad de las nanopartículas metálicas durante el funcionamiento de la pila [HALL 2004, INOUE 2009]. Por lo tanto, la optimización de los soportes carbonosos es muy importante para el desarrollo de las pilas de combustible de baja temperatura.

Estos materiales tienen que cumplir una serie de requisitos [LIU 2006, CHAI 2004]: i) alta área superficial para conseguir una buena dispersión del catalizador; ii) estructura porosa adecuada para tener una buena difusión de los reactivos y productos hasta y desde las partículas de catalizador; iii) buena conductividad eléctrica para facilitar la transferencia de electrones entre los electrodos de la pila de combustible durante las reacciones electroquímicas; iv) química superficial adecuada para facilitar la interacción entre el precursor del metal y el soporte durante el proceso de síntesis y obtener una elevada dispersión y pequeño tamaño de las partículas de metal; v) resistencia a la corrosión para garantizar la durabilidad del catalizador; vi) permitir la recuperación del metal; vii) ser reproducible y; viii) barato. Sin embargo, es difícil encontrar un material carbonoso que cumpla todos los requisitos. Por ello, a la hora de seleccionar un soporte es necesario elegir entre unas propiedades u otras.

Con respecto a la estructura porosa adecuada del soporte carbonoso, es preferible una estructura mesoporosa (poro de anchura interna comprendido entre 2 y 50 nm). Por lo general, un ánodo de alto rendimiento requiere una interfase triple de reacción (gas-electrodo-electrolito) a escala nanométrica, donde ocurren las reacciones electroquímicas, cuya formación se ve favorecida por una estructura mesoporosa del soporte [JOO 2006]. La utilización del catalizador disminuye con la presencia de microporos en la estructura del soporte carbonoso, debido a que el transporte de masa de reactivos y productos es pobre en estos microporos. Sin embargo, cuando el tamaño de los poros es mayor de 50 nm (macroporos), el área superficial se hace pequeña y la resistencia eléctrica aumenta. Por lo tanto, los carbones mesoporosos son atractivos para su utilización como soportes de catalizadores, mejorando tanto la dispersión como la utilización de los catalizadores metálicos.

Entre todos los tipos de materiales de carbono, los negros de carbono son los más utilizados como soporte de electrocatalizadores para pilas de combustible de electrolito polimérico, debido a su alta conductividad eléctrica y resistencia a la corrosión, su estructura porosa y área superficial específica [BEZERRA 2007]. Hay muchos tipos de negros de humo, como el negro de acetileno, el Negro Ketjen, el Negro Perla, o el Vulcan XC-72. Estos materiales presentan propiedades diferentes dependiendo de su proceso de fabricación, tales como la porosidad, conductividad eléctrica, la química superficial y la superficie específica.

Hoy en día, el Vulcan XC-72, que tiene una superficie específica alrededor de 250 $m^2\ g^{-1}$ y está formado por una agregación de partículas de tamaño entre 30-60 nm, se utiliza ampliamente como soporte de electrocatalizadores, especialmente en las pilas de combustible de electrolito polimérico [SHAO 2006, WIKANDER 2006]. Este material se utiliza como soporte en electrocatalizadores comerciales, como por ejemplo los producidos por E-TEK y Johnson Matthey. Sin embargo, a pesar de que es necesaria una elevada y accesible área superficial, estas propiedades no son suficientes para la obtención de un catalizador eficaz. Otros factores, tales como el tamaño y la distribución de tamaño de poros, o la química superficial, también afectan a las propiedades y la actividad los electrocatalizadores soportados en negros de humo [ZHOU 2008, GROLLEAU 2008, CARMO 2007].

Por estos motivos, se están estudiando nuevos materiales de carbono como las nanofibras de carbono, los nanotubos de carbono, los carbones mesoporosos ordenados, los xerogeles de carbono o las nanoespirales de carbono, con el fin de mejorar el rendimiento electroquímico de los catalizadores en la pila de combustible [SALGADO 2008, ALCAIDE 2009, SEVILLA 2007].

1.3.1. Nanoespirales de carbono (CNC)

Desde el descubrimiento de los nanotubos de carbono por Iijima [IIJIMA 1991], se ha desarrollado un gran interés por el diseño de nuevos materiales de carbono grafítico nanoestructurado. Hoy en día, el grafito es el material de carbono más importante para aplicaciones electroquímicas, debido a sus propiedades únicas. Su alta conductividad eléctrica y su estabilidad térmica y química hacen posible su uso como soporte catalítico, nanocomposite, o material para electrodos [MOLINER 2008].

Muchas formas de carbono grafítico nanoestructurado, incluyendo los nanotubos de carbono, las nanofibras de carbono y las nanoespirales de carbono, se pueden producir usando diferentes reacciones en fase gas. Entre estos materiales, las nanoespirales de carbono (CNC) están atrayendo gran atención debido a la combinación de su buena conductividad eléctrica, derivada de su estructura grafítica y a una porosidad amplia que permite reducir al mínimo las resistencias difusionales de reactivos y productos. Sin embargo, los métodos convencionales de obtención de este tipo de materiales como la descarga en arco eléctrico [UGARTE 1995], la vaporización por láser [GUO 1995] y la deposición química en fase vapor (CVD) [YANG 2007], presentan limitaciones en términos económicos y de producción a gran escala, debido a las altas temperaturas que requieren. Por tanto, hay un creciente interés por el desarrollo de nuevos métodos de síntesis de nanoestructuras de carbono grafítico que resulten más económicos y sencillos.

En los últimos años, los fenómenos de grafitización catalítica se han desarrollado considerablemente. La grafitización catalítica origina un aumento de la cristalinidad del carbono mediante la formación del material grafítico que tiene lugar por medio de la interacción entre el carbono amorfo y las partículas de un metal o compuesto inorgánico que constituyen el catalizador del proceso de grafitización. Entre

los metales que actúan como catalizadores se encuentran ciertos metales de transición, tales como níquel, hierro, cobalto, manganeso y aluminio [OYA 1979].

En el primer trabajo presentado en este compendio de publicaciones, titulado "*Study of the Synthesis Conditions of Carbon Nanocoils for Energetic Applications*", se propuso la grafitización catalítica como método de síntesis de nanoespirales de carbono (CNC), para de obtener materiales de carácter grafítico a relativamente bajas temperaturas. Se estudió la síntesis de CNC mediante la grafitización catalítica de geles de resorcinol-formaldehído, utilizando una mezcla de sales de níquel y cobalto como catalizadores de la grafitización. El objetivo de este trabajo es determinar las condiciones más adecuadas para obtener un material grafítico, llegando a un compromiso entre su grado de grafitización y su área superficial, mediante la variación de la relación molar de los distintos reactivos utilizados. Además, el método de síntesis utilizado tiene la ventaja de introducir las partículas metálicas en la síntesis de los compuestos, evitando el paso de impregnación de los materiales de carbono con partículas metálicas después de su síntesis.

1.3.2. Efecto de la química superficial del soporte

En la última década, se ha prestado gran atención a la interacción metal-soporte [YU 2007, PRADO-BURGUETE 1989]. Se considera que esta interacción tiene gran influencia sobre el crecimiento, estructura y dispersión del metal sobre el soporte carbonoso, mejorando las propiedades catalíticas y la estabilidad del electrocatalizador. Además, esta interacción también puede afectar la transferencia de electrones entre las partículas de metal y el soporte de carbono durante las reacciones electroquímicas, lo que afecta el funcionamiento del catalizador en la pila de combustible. Este efecto se atribuye al cambio de la estructura electrónica del metal por la interacción metal-carbono.

La interacción electrónica en la interfase metal-soporte puede ser modificada por la presencia de grupos funcionales en la superficie del carbón. Los grupos funcionales superficiales pueden afectar significativamente a la síntesis y al rendimiento de los electrocatalizadores, siendo los responsables tanto del equilibrio ácido-base como de las propiedades redox de los soportes de carbono. La química superficial de los materiales

de carbono puede ser modificada por tratamientos de oxidación, tanto en fase gas como fase líquida y/o térmicamente [MORENO-CASTILLA 1995, FIGUEIREDO 1999, NOH 1990].

Sin embargo, el efecto de la química superficial del soporte sobre las propiedades del electrocatalizador no se ha estudiado en profundidad. Los soportes de carbono no son materiales inertes. Durante las reacciones electroquímicas, la interacción metal-soporte se atribuye a la presencia de un efecto electrónico metal-soporte. Esta interacción se considera beneficiosa para la mejora de las propiedades catalíticas y la estabilidad del electrocatalizador. Sin embargo, la funcionalización del soporte resulta en una disminución de su conductividad eléctrica [SEBASTIÁN 2010]. Por otro lado, se ha observado que tanto la electrooxidación de metanol como de CO pueden estar influenciadas por la química superficial del soporte [CALVILLO 2007, SALGADO 2008]. Por lo tanto son necesarios estudios en profundidad.

En el caso de los materiales de carbono que nos ocupan, como son las nanoespirales de carbono, después del tratamiento térmico, la mayor parte de los trabajos recogidos en la literatura, reportan el uso de un tratamiento con HNO_3 con el fin de eliminar las partículas metálicas usadas durante la síntesis, mientras que otros someten la muestra a un tratamiento con ácido clorhídrico [SEVILLA 2007]. Con éstos tratamientos en medio ácido, además de conseguir la eliminación de las partículas metálicas utilizadas como catalizadores de la grafitización, se consigue la modificación de la química superficial del material. Sin embargo, no se han encontrado estudios sobre la influencia de diferentes tratamientos en las propiedades de éstos materiales en la literatura.

Por ello, en el segundo trabajo presentado en este compendio de publicaciones, titulado "*Modification of the properties of carbon nanocoils by different treatments in liquid phase*", se propone la modificación del método de síntesis de las nanoespirales de carbono con el objetivo de obtener materiales con alto grado de estructura grafítica. Para ello, se realizaron distintos tratamientos con HNO_3, mezclas HNO_3-H_2SO_4, mezclas H_2SO_4-H_2O_2 y H_2O_2; a distintas temperaturas y durante distintos tiempos. Los distintos tratamientos llevan a la obtención de materiales de carbono con distintas características fisicoquímicas.

1.4. ELECTROCATÁLISIS

Toda reacción electroquímica consta de dos reacciones separadas, una semirreacción de oxidación que se produce en el ánodo, y otra de reducción producida en el cátodo.

En el caso concreto de las pilas PEM, la reacción que se produce entre el hidrógeno y el oxígeno ocurre muy lentamente, por lo que es necesario acelerar el proceso para que el dispositivo funcione y produzca potencia eléctrica. De hecho, que una molécula de hidrógeno llegue al ánodo y sufra una disociación en iones y electrones no es inmediato ni trivial, pues para conseguirlo se tiene que superar una energía de activación que ha de ser considerablemente inferior a la energía liberada en la reacción para que esta se dé a un ritmo suficientemente rápido. También es importante reseñar que el funcionamiento de las PEM está limitado en gran medida por la baja velocidad de reacción que presenta la reducción del O_2, la cual es approximadamente 100 veces más lenta que la reacción de oxidación del H_2.

La química nos dice que usar catalizadores o aumentar la temperatura son posibles soluciones a un ritmo de reacción demasiado lento, pero las pilas PEM operan a una temperatura de unos 80 ºC, por lo que debido fundamentalmente a los problemas de gestión del agua, aumentar la temperatura resultaría inviable.

Dado que a esta temperatura las reacciones son aún muy lentas, la única solución posible es utilizar catalizadores que aumenten la velocidad de las semirreacciones de oxidación y de reducción. Este último punto es un factor de vital importancia en la fabricación y diseño de las pilas de combustible, ya que se hace necesario reducir al máximo la cantidad de catalizador, debido a su elevado precio, sin perjudicar el buen funcionamiento del dispositivo.

Un catalizador para pilas de combustible debe cumplir una serie de requisitos, como son poseer una alta actividad intrínseca tanto para la oxidación electroquímica del combustible en el lado del ánodo como para la reducción de O_2 en el cátodo, una buena durabilidad, una buena conductividad eléctrica, ser barato de fabricar y ser reproducible.

1.4.1. Métodos de preparación de electrocatalizadores

La preparación de catalizadores metálicos soportados es uno de los aspectos más importantes en la tecnología de los procesos químicos. Estos metales están dispersos sobre soportes de alta área superficial para maximizar la superficie accesible del componente activo, dado que la velocidad de la reacción química es generalmente proporcional a la cantidad de sitios activos superficiales. Actualmente, los catalizadores metálicos soportados se están utilizando en numerosos procesos industriales, pero la etapa de preparación está gobernada por procesos complejos de difícil entendimiento y la reproducibilidad de los diferentes métodos de preparación sigue siendo un problema. En los últimos años se ha publicado un número considerable de trabajos relacionados con los procesos que tienen lugar durante esta etapa y el efecto de variables tales como el soporte, la sal metálica utilizada como precursor y la técnica de deposición [SALGADO 2008].

1.4.1.1. Catalizadores monometálicos y aleaciones

Un objetivo importante en la síntesis de electrocatalizadores es lograr altos grados de dispersión del metal noble sobre la superficie del soporte carbonoso. Para conseguir este objetivo es vital desarrollar metodologías que permitan un control preciso del tamaño de las partículas de catalizador, logrando depositar partículas de tamaño nanométrico y con una distribución de tamaños muy estrecha. A continuación se describen una serie de métodos que se diferencian en la estrategia empleada para alcanzar el objetivo anterior [CHAN 2004]:

- *Método de impregnación.* Es el método más comúnmente empleado para la preparación de catalizadores. Básicamente, consiste en la impregnación de los poros del soporte con el precursor del catalizador (p. ej. $PtCl_6^{-2}$). Posteriormente, el precursor es reducido química (con hidracina, borohidruro, ácido fórmico, etilenglicol, metanol o hidrógeno) o electroquímicamente a nanopartículas metálicas. La morfología del soporte carbonoso y su distribución de tamaños de poro juegan un papel muy importante en la introducción del precursor y en proporcionar un espacio confinado en el que tenga lugar el crecimiento de las nanopartículas metálicas.

Una variación de este método es la impregnación incipiente. Aquí, el volumen de la solución de metal que impregna es equivalente al volumen de poro del carbón. Este método tiene la ventaja de que el metal está sólo depositado en el interior de la estructura porosa del material carbonoso [YU 2007].

- *Método coloidal.* El control del tamaño de las nanopartículas metálicas se logra mediante impedimento electrostático (la agregación de las nanopartículas se evita por repulsión electrostática debido a iones adsorbidos o coloides cargados) o impedimento estérico (se añade un agente protector, tal como NR_4^+, PPh_3, PVP o PVA, que se adhiere a la superficie de las nanopartículas y evita así su agregación). Este método permite, además, obtener distribuciones de tamaños de nanopartícula estrechas. Una alternativa al uso de un agente protector que posteriormente hay que eliminar, es la preparación de coloides metálicos mediante la combinación apropiada del precursor, disolvente, agente reductor y electrolito [WANG 2000[b]].
- *Método de microemulsión.* La microemulsión se forma gracias al empleo de surfactantes, que forman micelas en cuyo interior queda confinada la fase líquida que contiene al precursor. Esta microemulsión se encuentra uniformemente dispersada en una fase líquida continua inmiscible con la fase líquida que contiene al precursor. Actúa, por tanto, como un micro o nanoreactor, de modo que el control del tamaño de las partículas metálicas se logra fácilmente controlando el tamaño de la microemulsión [SOLLA-GULLÓN 2004].

Desde el punto de vista práctico, tan importante como las propias nanopartículas catalíticas, es el soporte sobre el que se encuentran depositadas, pues éste va a permitir una optimización del catalizador, así como su estabilización.

1.4.1.2. Catalizadores con estructura *core-shell*

La síntesis de las nanopartículas con estructura *core-shell* se realiza mediante la reducción sucesiva de un metal (A), sobre un núcleo compuesto por otro metal (B). Normalmente, la capa del metal (A) se encuentra sometida a presión (*strain*) y, por tanto, puede presentar importantes propiedades catalíticas [RUVINSKY 2008]. Con la estructura *core-shell* se consigue aumentar la actividad del metal utilizado en la

superficie, en comparación con las partículas monometálicas del mismo [BALDAUF 1996, EL-AZIZ 2002, KIBLER 2003, RUVINSKY 2008]. De esta forma, sustituyendo el núcleo de las nanopartículas con metales más baratos o no preciosos, se consigue una elevada eficiencia de utilización del catalizador y reducir su coste. Esta mejora de la actividad se puede atribuir a los cambios electrónicos, estructurales y morfológicos inducidos en las nanopartículas *core-shell*. Esto implica que las propiedades catalíticas de un metal se pueden modificar seleccionando un metal apropiado como núcleo [LU 2002]. Un esquema representativo de la estructura *core-shell* se presenta en la Figura 1.4.

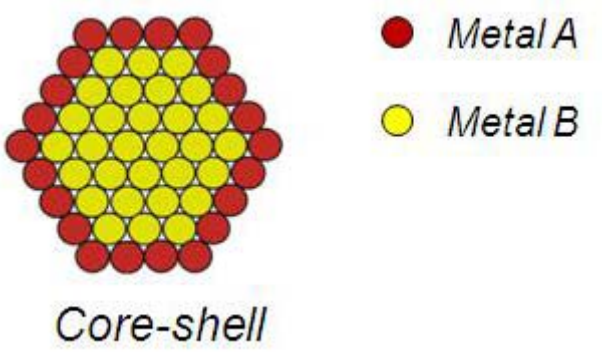

Figura 1.4. *Representación esquemática de la estructura core-shell.*

Los métodos de crecimiento en semilla (*seeding growth methods*), son los más utilizados para sintetizar nanopartículas con estructura *core-shell*. En éstos métodos se utilizan pequeñas nanopartículas como "semillas", que impulsan el crecimiento de nanopartículas más grandes con el tamaño deseado en presencia de una sal metálica y un agente reductor. Además, este tipo de métodos presentan la ventaja de eliminar la nucleación, facilitando el crecimiento de las partículas [LU 2002, JANA 2001, BROWN 1998, HU 2005, LI 2006].

La relación entre el diámetro total de las partículas *core-shell* (D_{CS}) y el volumen necesario a agregar de la sal metálica que se quiere usar como *shell*, viene dado por:

$$D_{\mathrm{CS}} = D_{\mathrm{core}} \left(1 + \frac{\overline{V}_{\mathrm{shell}} \left[shell \right] V_{shell}}{\overline{V}_{\mathrm{core}} \left[core \right] V_{\mathrm{core}}} \right)^{1/3} \qquad \text{[Ec. 1.13]}$$

Donde D_{core} y $\bar{V}$ corresponden al diámetro de las nanopartículas utilizadas como semilla y al volumen molar del metal correspondiente. Los términos de concentración, se refieren a las disoluciones de los precursores correspondientes. Así, el porcentaje en peso de ambos metales en las nanoestructuras *core-shell* puede ser controlado mediante la variación de la relación de los volúmenes de los mismos, obteniéndose nanopartículas bimetálicas de distinta composición.

1.4.2. Catalizadores para DAFC

Para conseguir que el ánodo sea más tolerable a la presencia de CO, hasta el momento, se ha demostrado que los catalizadores basados en platino soportado en materiales carbonosos son los mejores para las pilas de combustible de alcohol directo (DAFC). Sin embargo, el platino es un metal precioso, y su limitada disponibilidad y su elevado precio representan grandes obstáculos para el uso extendido de este tipo de pilas. Por tanto, uno de los grandes retos para reducir el coste de estos sistemas es el desarrollo de catalizadores que no contengan platino o con un bajo contenido del mismo. Por ello, se han estudiado catalizadores binarios y ternarios basados en platino y catalizadores que no contienen platino para este tipo de pilas [ZHOU 2004]. Sin embargo, aunque se han realizado grandes progresos en el desarrollo de catalizadores no basados en platino, éstos todavía presentan baja actividad y estabilidad, lo que hace que su uso en pilas de combustible de baja temperatura no sea viable, al menos en un futuro cercano. Por tanto, la comercialización de la tecnología DAFC depende del desarrollo de catalizadores con un bajo contenido en platino que mejore la utilización del metal y reduzca así la cantidad necesaria de éste y, como consecuencia, los costes de esta tecnología.

1.4.2.1. Catalizadores para la oxidación de metanol

La oxidación total de metanol consiste en un mecanismo de reacciones que ocurren de forma paralela. Un modelo simplificado para la electrooxidación de metanol sobre Pt se recoge en la Figura 1.5 [PLANES 2007, GARCÍA 2011]. La producción de CO_2 (y por consiguiente la eficiencia a CO_2) está relacionada con la formación de CO_{ads} u otras especies adsorbidas (no detalladas en el esquema). En consecuencia, un

incremento en la eficiencia a CO_2 tiene que estar acompañado por un aumento en la cantidad de CO_{ads} y/o la formación de otras especies adsorbidas.

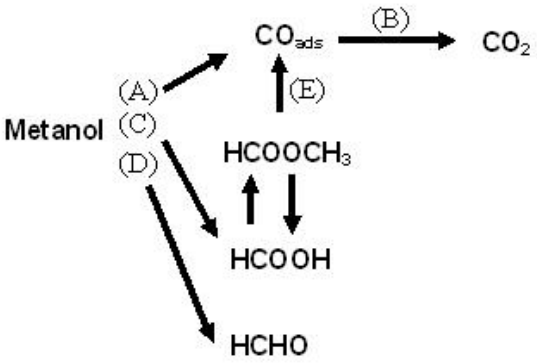

Figura 1.5. *Modelo para la electrooxidación de metanol sobre electrodos basados en Pt.*

Los mecanismos mencionados necesitan de un catalizador capaz de disociar el enlace C-H así como de facilitar la reacción de los intermediarios formados con especies oxigenadas para dar lugar a CO_2. El platino es conocido por ser el mejor catalizador para romper el enlace C-H. Sin embargo, algunos de éstos intermediarios de reacción, como el CO, se adsorben fuertemente en los centros de Pt, inhibiendo la electrooxidación, lo que resulta en una pérdida de actividad de la pila. Se ha observado que al utilizar un catalizador de Pt/C combinado con Ru, Rh o Ir se obtiene una mayor tolerancia hacia el CO; siendo el rol del segundo metal incrementar la adsorción de especies OH sobre la superficie del catalizador a potenciales más bajos, así como disminuir la adsorción de las especies que envenenen el catalizador [AVGOUROPOULOS 2005].

Los catalizadores más estudiados y utilizados en el ánodo de una DMFC son los catalizadores bimetálicos Pt-Ru [PAULUS 2000, SOLLÁ-GULLÓN 2004, DICKINSON 2002]. El aumento en la actividad de los catalizadores de Pt-Ru en comparación con los catalizadores de Pt puro para la oxidación de metanol, ha sido atribuido a un mecanismo bifuncional, así como a efectos electrónicos. El mecanismo bifuncional implica la adsorción de especies oxigenadas en los átomos de Ru a potenciales bajos, facilitando la oxidación de CO a CO_2, que puede resumirse de la siguiente manera [LIU 2006]:

$$Pt + CH_3OH \rightarrow PtCO_{ads} + 4\,H^+ + 4\,e^- \quad \text{[Ec. 1.14]}$$

$$Ru + H_2O \rightarrow Ru(OH)_{ads} + H^+ + e^- \quad \text{[Ec. 1.15]}$$

$$PtCO_{ads} + Ru(OH)_{ads} \rightarrow CO_2 + Pt + Ru + H^+ + e^- \quad \text{[Ec. 1.16]}$$

Numerosos factores como la composición de la aleación, la uniformidad, la morfología, el tamaño de partícula, el estado electrónico y las impurezas, afectan las características de los catalizadores PtRu/C. Las propiedades del soporte carbonoso son también importantes respecto a las características de las partículas catalíticas bimetálicas Pt-Ru.

Actualmente, el consenso alcanzado en la literatura es que la relación atómica óptima Pt-Ru es 1:1, y que un menor tamaño de partícula mejorara la utilización del catalizador. Antolini *et al*. estudiaron el efecto de la composición del catalizador preparando catalizadores de PtRu/C en distinta proporción. Los resultados indicaron que existe una gran interacción metal-carbón, siendo el tamaño de partícula del catalizador PtRu/C más pequeño que los catalizadores Pt/C y Ru/C. Además se observó cómo en el catalizador bimetálico, la distancia intercristalina disminuía con respecto a los metales Pt y Ru puros. En este trabajo, los autores concluyeron que (i) las interacciones metal-soporte afectan a las características morfológicas del catalizador PtRu/C; (ii) las interacciones Pt-C son más fuertes en presencia de Ru; (iii) las interacciones Pt-C y Ru-C entorpecen la formación de la aleación Pt-Ru; (iv) la distancia intercristalina disminuye con el contenido de Ru; (v) las variaciones morfológicas no afectan la actividad en el electrodo de la PEMFC; (vi) al trabajar en presencia de CO se recomienda el uso de una relación Pt:Ru de 1:1-1:3 [ANTOLINI 2001], lo que concuerda con otros autores [TAKASU 2003; CRABB 2004].

Por otra parte, se ha demostrado, que el método de síntesis utilizado para preparar catalizadores metálicos soportados en materiales carbonosos, puede afectar a la composición, morfología y dispersión de los catalizadores; así como a su comportamiento electroquímico [SALGADO 2010]. Por estos motivos, en el tercer trabajo presentado en este compendio de publicaciones, titulado "*On the enhancement of activity of Pt and Pt-Ru catalysts in methanol electrooxidation by using carbon nanocoils as catalyst support*", se prepararon catalizadores de Pt y Pt-Ru soportados en nanoespirales de carbon mediante distintos métodos, comparando su actividad en la oxidación de CO y metanol con catalizadores comerciales de Pt/C y PtRu/C

suministrados por E-TEK. El objetivo de este trabajo fue el estudio de los distintos métodos de síntesis en las propiedades tanto fisicoquímicas como electroquímicas de los catalizadores preparados.

1.4.2.2. Catalizadores para la oxidación de etanol

La alta toxicidad del metanol es un importante inconveniente para su uso. Además, la baja eficiencia de los electrocatalizadores, especialmente de los catalizadores del ánodo a bajas temperaturas y la permeación de metanol a través de la membrana (*crossover*), limita el desarrollo de esta tecnología. En este contexto, el uso de etanol como combustible parece ser una posible solución, debido a que no es tóxico y se puede producir en grandes cantidades a partir de productos agrícolas (bioetanol) [ANTOLINI 2009[b], ANDREADIS 2006, SONG 2005[a]]. Además, el etanol proporciona una densidad de energía volumétrica (21 MJ L^{-1}) similar a la de la gasolina (31 MJ L^{-1}).

Comparado con el metanol, el etanol presenta una menor permeación a través de la membrana debido a su mayor tamaño molecular [SONG 2005[b]]. Además, el etanol permeado al cátodo presenta un efecto menor sobre el funcionamiento de la pila en comparación con el metanol, debido a su menor permeabilidad a través de la membrana de Nafion® y a su lenta cinética de oxidación electroquímica sobre el catalizador Pt/C del cátodo.

La capacidad de oxidar etanol directamente a CO_2 y agua es un buen factor para juzgar la buena efectividad de un electrocatalizador en este tipo de pilas. Por lo tanto, serán de interés los materiales electródicos que desplacen el potencial de inicio de la oxidación de etanol a potenciales más bajos [SONG 2006[c]].

El platino resulta ser el material más activo para la oxidación de etanol, sin embargo, hay que tener en cuenta que para el caso de los catalizadores monometálicos de platino, se produce una inhibición de su actividad, sobre todo cuando se trabaja en estado estacionario. Además, para aumentar tanto la utilización como la eficiencia del combustible, es necesario romper el enlace C-C y provocar su completa oxidación a CO_2. Por lo tanto, se hace necesaria la presencia de un segundo o incluso un tercer metal para modificar la superficie del platino.

Como se observa en la Figura 1.5, muchos son los metales que pueden incrementar la actividad del platino en la oxidación de etanol [LAMY 2002, ANTOLINI 2007, SONG 2006c]. Sin embargo, las mayores potencias se observan para los catalizadores de Pt/Sn. Los catalizadores PtSn/C son capaces de desplazar el potencial al que se inicia la oxidación de etanol, con respecto a los catalizadores de PtRu/C y Pt/C. A pesar de que se ha demostrado que los catalizadores de PtRu presentan un efecto sinergético que aumenta su eficiencia en la oxidación de metanol, este efecto no es deseable para la oxidación de etanol. Sin embargo, la adición de un tercer elemento como W, Mo o Sn, puede mejorar la actividad de los catalizadores de Pt-Ru, como se puede observar en la Figura 1.5.

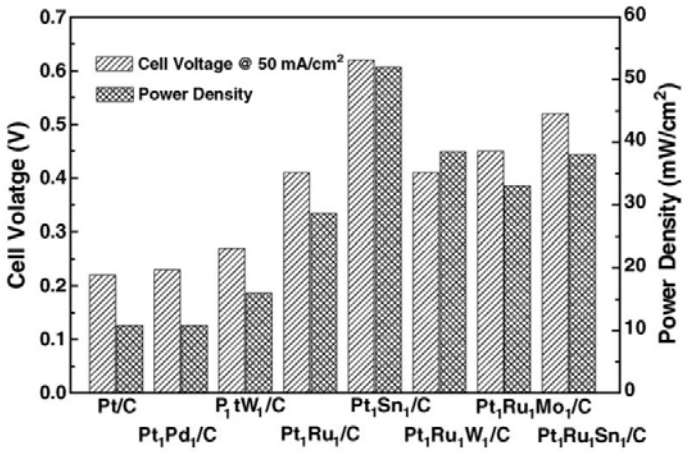

Figura 1.6. *Efecto de la adición de distintos metales a la actividad del platino en la oxidación de etanol medidas en una monocelda PEMFC alimentada con etanol en las mismas condiciones de operación [SONG 2006].*

Los catalizadores ternarios Pt-Ru-M probados para la reacción de oxidación de etanol, presentan siempre mejor comportamiento que los bimetálicos de Pt-Ru, sin embargo, los trabajos publicados son escasos [TANAKA 2005, ZHOU 2004]. Por el contrario, se pueden encontrar una gran variedad de trabajos dedicados a catalizadores ternarios Pt-Sn-M, que al parecer presentan mejores comportamientos que los Pt-Sn y siempre mejores que los Pt-Ru-M [SPINACÉ 2005, ROUSSEAU 2006].

Sin embargo, a pesar de que el etanol se muestra como un buen candidato como combustible en pilas de alcohol directo, no se encuentran el la literatura estudios relativos al comportamiento de las nanoespirales de carbono como soporte de electrocatalizadores para la oxidación de etanol. Por esto, en el cuarto trabajo presentado en este compendio de publicaciones, titulado "*Influence of the synthesis*

method on the properties of Pt catalysts supported on carbon nanocoils for ethanol oxidation", se prepararon catalizadores de Pt soportados sobre nanoespirales de carbono mediante distintas rutas sintéticas (reducción con ácido fórmico, borohidruro de sodio o etilenglicol), estudiando su comportamiento en la electrooxidación de CO y etanol, con el fin de poder establecer el efecto de los distintos métodos en su actividad. Además, para estudiar el efecto del soporte sobre las propiedades de los catalizadores, se prepararon también catalizadores de platino soportados sobre Vulcan XC-72R (soporte comercial). Para completar el estudio, los resultados obtenidos se compararon con los de un catalizador comercial Pt/C suministrado por E-TEK.

1.4.2.3. Catalizadores para la oxidación de ácido fórmico

Las pilas de combustible de ácido fórmico directo (DFAFCs) parecen ser una alternativa prometedora tanto a las DMFCs como a las DEFCs. Ya que aunque el ácido fórmico tiene una densidad de energía volumétrica más baja que el metanol (2086 Wh L^{-1} vs. 4690 Wh L^{-1}), la menor permeación a través de la membrana, *crossover*, permite el uso de concentraciones más altas de combustible [JEONG 2007, ZHOU 2007, YU 2008]. Wang *et al*. comprobaron que el *crossover* a través de la membrana polimérica podía ser reducido en un factor de 5 al sustituir el metanol por ácido fórmico, obteniendo así un mejor rendimiento bajo las mismas condiciones de operación [WANG 2004]. La penetración de ácido fórmico a través de la membrana de Nafion es mucho menor que la del metanol debido a la repulsión entre los iones $HCOO^-$ y SO_3^- en la membrana. Por otra parte, la concentración óptima de operación usando ácido fórmico como combustible puede llegar a ser de valores de 20 M [ANTOLINI 2009[a]], mientras que en el caso del metanol en una DMFC ésta concentración es sólo de 2 M. La oxidación de ácido fórmico se ha descrito en términos de un "mecanismo de doble vía" (*dual pathway mechanism*), que incluye [CAPON 1973]:

$$\text{Vía 1:}\quad HCOOH \rightarrow CO_2 + 2H^+ + 2e^- \qquad \text{[Ec. 1.17]}$$

$$\text{Vía 2:}\quad HCOOH \rightarrow CO_{ads} + H_2O \rightarrow CO_2 + 2H^+ + 2e^- \qquad \text{[Ec. 1.18]}$$

La principal diferencia entre las vías (1) y (2) es el grado de adsorción de CO que puede envenenar a los electrocatalizadores. Se ha demostrado que la oxidación de ácido fórmico sobre catalizadores de paladio ocurre principalmente a través de la vía

(1); mientras que la vía (2) predomina en los electrocatalizadores basados en platino, lo que conlleva el envenenamiento de los mismos. Por otro lado, el coste del paladio es inferior al del platino, por lo que se espera que sea un buen sustituto del Pt como catalizador en las pilas de combustible. El uso del Pd tiene también interés ya que es 50 veces más abundante que el Pt en la Tierra. Además, el Pd por sí mismo es un excelente catalizador para la electrooxidación de combustibles orgánicos [ANTOLINI 2009[a]]. Sin embargo, los catalizadores basados en Pd pueden someterse a una desactivación sustancial en las condiciones operativas. Recientemente, Yu y Pickup han demostrado que ésta desactivación es debida a un envenenamiento del catalizador por adsorción de CO, que se produce a escalas de tiempo más largas que para el caso de los catalizadores que usan Pt [YU 2009[a]].

La electrooxidación de ácido fórmico sobre Pd ha sido ampliamente estudiada [HA 2005, LARSEN 2006, ZHANG 2006, HUANG 2008, HU 2010, WANG 2008, HUANG 2009]. Kolb *et al*. demostraron que las intensidades obtenidas para la oxidación de ácido fórmico sobre paladio son fuertemente dependientes de las distintas orientaciones de los planos cristalográficos; así, las densidades de corriente varían de la forma: Pd(111) < Pd(110) < Pd(100) [BALDAUF 1996, HOSHI 2006]. Sin embargo, hay una discusión existente en la literatura acerca de la estabilidad con el tiempo de los catalizadores de paladio en las pilas de combustible de ácido fórmico directo [YU 2009[a], YU 2009[b], JUNG 2011, ZHOU 2010].

Una forma de modificar las propiedades de las nanoestructuras metálicas es a través de la formación de sistemas bimetálicos; ya bien en forma de aleación [STRASSER 2010] o con estructura *core-shell* [ZHOU 2007, PARK 2010]. Entre las diversas nanopartículas bimetálicas, el sistema Pd-Au se considera como un catalizador altamente reactivo para una gran variedad de reacciones tales como la oxidación de pequeñas moléculas orgánicas y las reacciones de evolución de hidrógeno. Estudios muy recientes han demostrado que la reactividad de las nanopartículas de Pd puede variar considerablemente si se encuentran aleadas con Au [LIU 2010]. La relación atómica de ambos metales afecta significativamente la posición de la banda *d*, que desempeña un papel crucial en la interacción con adsorbatos orgánicos.

Por otro lado, las investigaciones sobre el papel del soporte sobre la actividad de nanoestructuras previamente sintetizadas, por ejemplo, a través de la síntesis coloidal,

son relativamente escasos. Este enfoque permite disociar los efectos del soporte en el crecimiento de partículas, de las interacciones químicas específicas vinculadas a la reactividad de los centros metálicos, es decir, cualquier efecto observado en la actividad catalítica podría estar directamente relacionado con el soporte y no con el tamaño de partícula, distribución, etc.

Por los motivos presentados anteriormente, la estrategia a seguir en los trabajos 5 y 6 presentados en el presente compendio de publicaciones titulados "*Electrocatalytic properties of strained Pd nanoshells at Au nanostructures: CO and HCOOH oxidation*" y "*The Effect of Carbon Supports on the Electrocatalytic Reactivity of Au-Pd Core-Shell Nanoparticles*", se basa en el crecimiento de capas epitaxiales de paladio sobre núcleos de oro, con el fin de generar nanopartículas con estructura *core-shell* de composición conocida. En dichos trabajos, se presenta un estudio sistemático de la actividad para la oxidación de ácido fórmico de nanoestructuras *core-shell* de Au-Pd en función del espesor de Pd; tanto para las puras partículas metálicas soportadas en electrodos de SnO_2 dopados con In (Trabajo 5), como para las mismas partículas soportadas en Vulcan XC-72 (Trabajo 6).

Capítulo 2

Dispositivos experimentales y técnicas de caracterización

2.1. DISPOSITIVOS EXPERIMENTALES

2.1.1. Carbonización

El proceso de carbonización del soporte carbonoso se llevó a cabo en la instalación a escala banco mostrada en la Figura 2.1. El sistema consta de un reactor de Kanthal de 68 cm de longitud y 2.5 cm de diámetro. El reactor cuenta en su parte inferior con una placa distribuidora que permite tener una distribución homogénea del gas de reacción a través de la muestra. Esta parte inferior del reactor actúa como precalentador del gas de reacción antes de su contacto con la muestra. El reactor se introduce en un horno tubular cerámico Watlow. La temperatura del sistema se controla

a través de un termopar insertado en el reactor y conectado a un controlador de temperatura que permite programar rampas de calentamiento y tiempos de reacción.

El flujo de gas alimentado al sistema (N_2) se controla a través de un rotámetro. El conducto de los gases de salida del reactor se encuentra calorifugado mediante una resistencia para evitar la posible condensación de los productos de reacción y así, evitar la posible obstrucción del conducto. Los gases de salida se hacen pasar por un borboteador y un enfriador para lavar los gases antes de conducirlos hasta el sistema de extracción.

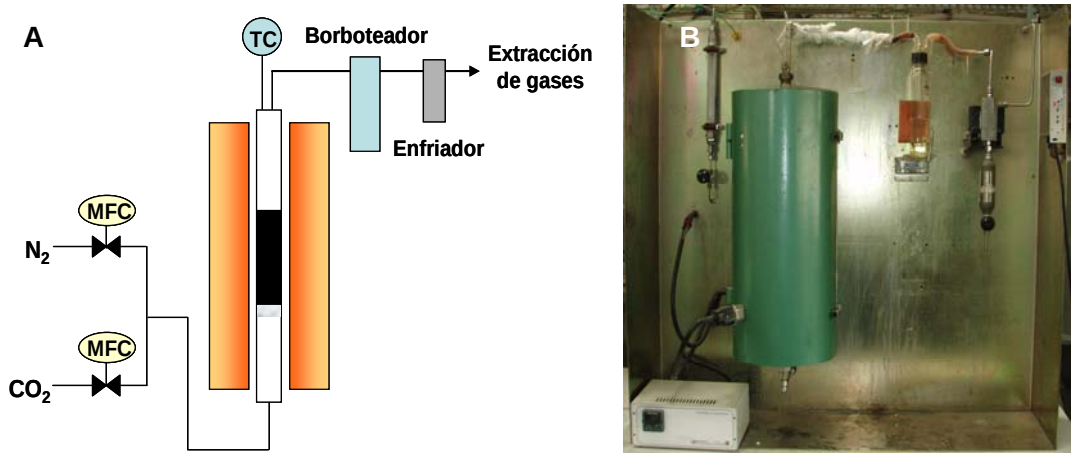

Figura 2.1. *Instalación de carbonización. A) Esquema; B) Fotografía.*

2.1.2. Celda electroquímica convencional

La celda electroquímica utilizada se muestra en la Figura 2.2, se trata de una celda de vidrio que posee cinco bocas cónicas, tres de las cuales están destinadas al electrodo de trabajo (electrocatalizador a estudiar depositado como capa fina sobre carbón vítreo), el electrodo de referencia (electrodo de hidrógeno) y el contraelectrodo (barra de carbón vítreo). En la cuarta entrada se colocó el borboteador de gas inerte, para desoxigenar el electrolito donde se llevan a cabo las reacciones, mientras que la quinta sirve para la salida de gases.

El dispositivo que controla los parámetros voltamétricos es un potenciostato que se conecta a la celda con un arreglo de tres electrodos inmersos en una solución que se encuentra en reposo. El potenciostato dirige y monitorea el potencial en el electrodo de trabajo (WE) con respecto al electrodo de referencia (RE) no polarizable. Con este

dispositivo se hace pasar una corriente entre el WE y el contraelectrodo (CE), mientras que casi no hay flujo de corriente a través del RE debido a su alta impedancia.

Figura 2.2. *Celda electroquímica convencional utilizada.*

2.1.3. Espectrometría de masas diferencial electroquímica

El dispositivo empleado para la realización de los estudios de espectrometría de masas diferencial electroquímica (DEMS) consiste en una celda electroquímica acoplada a un espectrómetro de masas Pfeiffer-Vacuum (Figura 2.3), el cual contiene el detector Prisma QMS 200 permitiendo la adquisición simultánea de hasta 72 señales masa/carga (m/z).

La celda electroquímica está acoplada a una cámara del espectrómetro donde existe una presión del orden de 10^{-3} mbar, que se consigue con una bomba de vacío rotativa, separada por una válvula micrométrica de una segunda cámara donde la presión es del orden de 10^{-8} mbar, obtenida con una bomba de vacío turbomolecular. En esta segunda cámara, se encuentra otra bomba de vacío rotativa, que en el instante en que se enciende el equipo proporciona la presión necesaria (10^{-2} mbar) para que la bomba turbomolecular pueda comenzar a girar. La apertura de la válvula micrométrica ajustando la presión a $5 \cdot 10^{-6}$ mbar, origina una diferencia de presión entre las dos cámaras que permite que los productos gaseosos y/o volátiles procedentes de la celda electroquímica sean dirigidos hacia la segunda cámara, donde se produce su ionización

y su detección (en una copa de Faraday) gracias a un cuadrupolo que deja pasar aquellos iones de la relación masa/carga deseada.

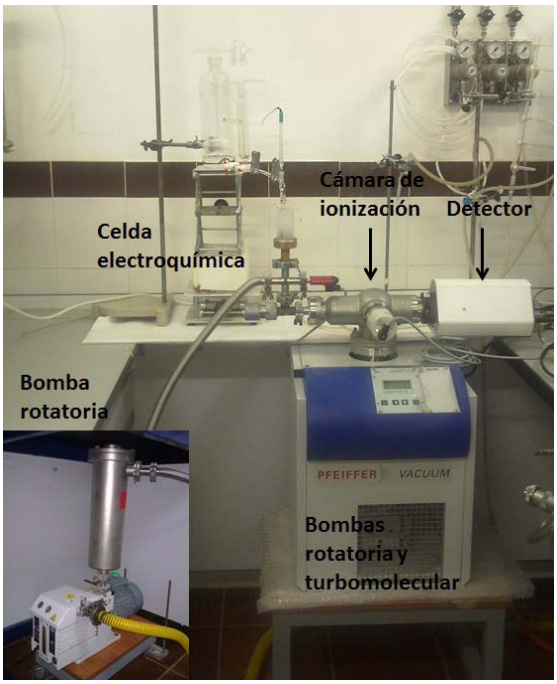

Figura 2.3. *Fotografía de la instalación donde se realizaron los experimentos de espectroscopía de masas diferencial.*

Figura 2.4. *Fotografía de la celda electroquímica utilizada para los experimentos DEMS.*

Se utilizó una celda de plexiglas de 50 mL de capacidad, mostrándose su esquema en la Figura 2.4. En la parte inferior se encuentra una membrana hidrófoba de teflón (Scimat Ltd., 200/40/60), que es la interfase entre la celda electroquímica y el espectrómetro de masas, permeable a los productos gaseosos y/o volátiles generados durante la reacción electroquímica. La membrana se coloca sobre una pieza de acero poroso, cuya misión es dar la estabilidad mecánica necesaria para el sistema de vacío. El sellado entre la celda y la entrada del espectrómetro se consigue con un anillo de vitón.

Como electrodo de trabajo se utilizaron los electrocatalizadores a estudiar depositados sobre una tela de carbón (ver sección 2.3.2.2.), un electrodo de hidrógeno como electrodo de referencia y una barra de carbón vítreo como contraelectrodo.

2.2. CARACTERIZACIÓN FISICOQUÍMICA

2.2.1. Microscopía electrónica

Las técnicas de microscopía electrónica se utilizaron para realizar un estudio tanto de la estructura del material carbonoso preparado, como de la dispersión y el tamaño de partícula de los electrocatalizadores preparados.

2.2.1.1. Microscopía electrónica de transmisión (TEM)

La utilización de un fino haz de electrones acelerados a una gran velocidad como fuente de iluminación, confieren al microscopio electrónico una alta resolución. En esta técnica, un haz de electrones acelerados a una gran velocidad al aplicarles una elevada diferencia de potencial, atraviesa la muestra produciéndose la dispersión de los mismos en diferentes trayectorias características de la estructura del material observado. Colocando una barrera física de pequeña apertura angular por debajo del plano de la muestra, los electrones dispersados según ciertos ángulos, serán eliminados del haz, siendo la imagen formada menos intensa en aquellas zonas correspondientes a una mayor masa de la misma. La imagen formada es aumentada y proyectada sobre una pantalla fluorescente para su visualización en tiempo real, pudiendo registrarse tanto digitalmente como en negativos para su estudio posterior.

Los microscopios utilizados en este trabajo fueron un TEM 200kV JEM-2100F y un TEM 200kV JEOL JEM-2010F situados en el Instituto de Catálisis y Petroleoquímica (CSIC) de Madrid y en la Universidad de Zaragoza, respectivamente.

2.2.1.2. Dispersión de energía de rayos X (SEM-EDX)

El microscopio electrónico tiene la facultad de poder controlar un haz de electrones de alta energía sobre una zona determinada de una muestra. Estos electrones pueden ceder parte de su energía a la muestra dando lugar a toda una serie de fenómenos de transiciones energéticas en el material estudiado que han dado lugar a un gran número de técnicas espectroscópicas, entre las que destaca el análisis por dispersión de energía de rayos X (EDX).

Cuando el haz de electrones se enfoca sobre la muestra provoca una serie de tránsitos electrónicos entre diferentes niveles de energía. El átomo excitado se relaja a su estado inicial por la transferencia de un electrón de un orbital exterior a una capa interior, lo que da lugar a la emisión de rayos X. Cada elemento tiene un espectro de emisión característico que consiste en una serie de máximos nítidos, cada uno de los cuales corresponde a una transición electrónica desde un orbital de alta energía a un orbital de baja energía. Este espectro es característico de cada elemento por lo que proporciona un método de análisis elemental que es de los más usados en ciencia de materiales. Por ello, se ha utilizado esta técnica para determinar la carga metálica de los catalizadores y la relación atómica entre los metales.

Los microscopios utilizados en este trabajo fueron un SEM EDX Hitachi S-3400 N de presión variable hasta 270 Pa con analizador EDX Röntec XFlash de Si(Li) del que se dispone en el Instituto de Carboquímica, y un JEOL JSM 5600LV acoplado a un detector ISIS 300 presente en el Departamento de Química de la Universidad de Bristol.

2.2.2. Difracción de rayos X (XRD)

La difracción de rayos X (*X-Ray Diffraction*, XRD) es fundamentalmente una técnica de caracterización estructural de sólidos. Por ello, esta técnica se utilizó tanto para estudiar la estructura grafítica de los materiales carbonosos sintetizados, como para determinar el tamaño de cristal de los metales en los catalizadores preparados.

Esta técnica se fundamenta en la incidencia, con un determinado ángulo, de un haz de rayos X sobre una muestra plana. El haz se escinde en varias direcciones debido a la simetría de la agrupación de átomos y, por difracción, da lugar a un patrón de intensidades que es función de la distancia entre los planos cristalinos que configuran la estructura y del ángulo de difracción, y puede interpretarse aplicando la ley de Bragg. Dependiendo de la estructura cristalina, en el espectro se registran los picos correspondientes al ordenamiento de la muestra.

Los tamaños de los diferentes cristales de los metales utilizados, se calcularon a partir del ensanchamiento de los picos derivados del metal, aplicando la ecuación de Scherrer. Siendo la ecuación de Scherrer la siguiente:

$$B_{cristal} = \frac{k.\lambda}{L\cos\theta} \qquad \text{[Ec. 2.1]}$$

donde λ es la longitud de onda utilizada, L el tamaño medio de cristal medido en la dirección perpendicular a la superficie, θ es el ángulo de Bragg, y k una constante que para cristales cúbicos pequeños toma el valor de 0.94 [SURYANARAYANA 1998].

Los análisis se realizaron en un equipo Bruker AXS D8 Advance con una configuración θ-θ utilizando radiación Cu K_α y grafito como segundo monocromador existente en el Instituto de Carboquímica.

2.2.3. Espectroscopia Raman

La Espectroscopía Raman es una técnica fotónica de alta resolución que proporciona en pocos segundos información química y estructural de casi cualquier compuesto orgánico o inorgánico, permitiendo así su identificación. El análisis mediante espectroscopia Raman se basa en el examen de la luz dispersada por un material al incidir sobre él un haz de luz monocromático. Una pequeña porción de la luz es dispersada inelásticamente experimentando ligeros cambios de frecuencia, característicos del material analizado e independientes de la frecuencia de la luz incidente. Se trata de una técnica de análisis no destructiva, que se realiza directamente sobre el material a analizar sin ningún tipo de preparación especial.

Los análisis Raman se realizaron en un equipo de espectroscopia Micro-Raman confocal modelo Horiba Jobin Yvon HR800 UV, dotado con dos tipos de láser diferente

(rojo y verde), óptica preparada para láser UV y detector CCD, del que dispone el Instituto de Carboquímica.

2.2.4. Oxidación a temperatura programada (TPO)

Una característica muy importante de los materiales carbonosos para su aplicación como soporte de electrocatalizadores es su estabilidad térmica, ya que tiene gran importancia sobre la durabilidad y estabilidad de los catalizadores.

La oxidación a temperatura programada (*Temperature Programed Oxidation*, TPO) además es una técnica utilizada para caracterizar la naturaleza y la cantidad de carbono presente en cualquier material. Consiste en exponer la muestra a un flujo de oxígeno puro o aire en un horno mientras se incrementa la temperatura del mismo. El carbono presente en la muestra se oxida al reaccionar con el oxígeno y se mide la pérdida de peso que experimenta en una termobalanza.

La curva TPO obtenida proporciona información sobre la reactividad a la oxidación y la cantidad de carbono de la muestra, así como de la presencia de distintos tipos de materiales carbonosos si los hubiera.

Los análisis se realizaron en atmósfera de aire utilizando una termobalanza SETARAM Setsys Evolution a presión atmosférica presente en el Instituto de Carboquímica. El rango de temperaturas estudiado fue de 30 a 1000 ºC con una velocidad de calentamiento de 5 ºC min^{-1}.

2.2.5. Desorción a temperatura programada (TPD)

La química superficial es un parámetro importante en la preparación de un catalizador altamente disperso. Mediante la técnica de desorción a temperatura programada (*Temperature Programed Desorption*, TPD) se obtiene información acerca de la cantidad de grupos oxigenados de la superficie de los materiales carbonosos, su estabilidad térmica y su naturaleza.

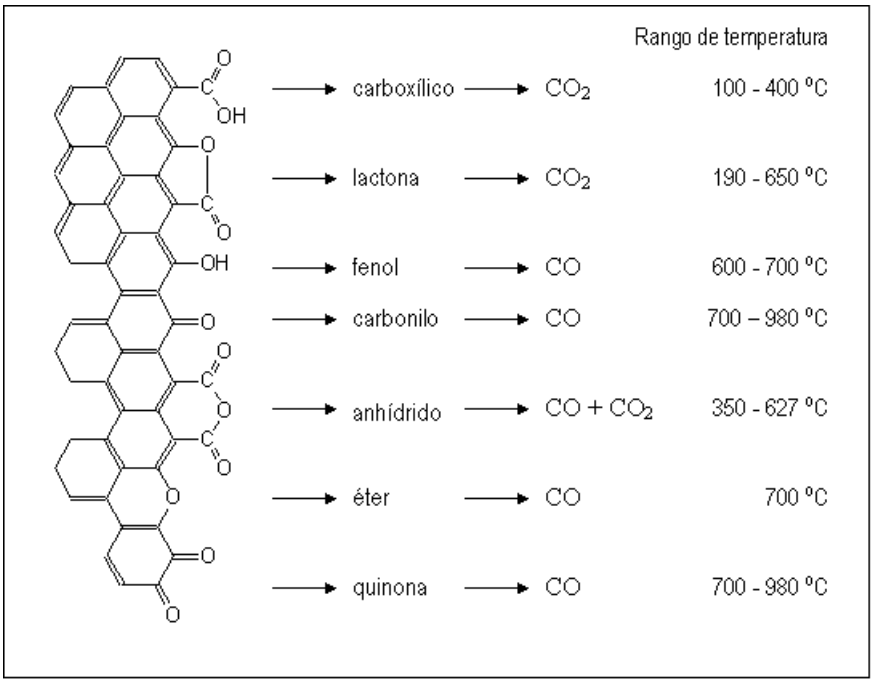

Figura 2.5. *Grupos de la superficie del carbón y su descomposición por TPD [FIGUEIREDO 1999].*

La desorción a temperatura programada es una de las técnicas más utilizadas para evaluar la química superficial de los distintos tipos de materiales carbonosos, aunque existe controversia en la asignación de los picos de las curvas de desorción a determinadas especies de grupos superficiales [SZMANSKI 2002]. Está generalmente admitido que los grupos ácidos fuertes se descomponen a bajas temperaturas en forma de CO_2, y que los ácidos débiles, los grupos neutros y los básicos se descomponen a altas temperaturas en forma de CO (Figura 2.5) [FIGUEIREDO 1999]. Los grupos carboxílicos, anhídrido y lactona se consideran ácidos fuertes, mientras que los grupos fenol, carbonilo, quinona y otros son básicos o ácidos débiles. De esta forma, las curvas de desorción de CO y CO_2 se obtienen como resultado de una serie de emisiones debidas a la descomposición de diversos componentes de cada tipo de grupo superficial oxigenado. Por lo tanto, fue necesario realizar la deconvolución de las curvas de desorción, mediante el programa Origin, con el fin de estimar una composición superficial del material carbonoso estudiado.

Los experimentos TPD se realizaron desde temperatura ambiente hasta 1050 ºC utilizando una velocidad de calentamiento de 10 ºC min^{-1}. Las cantidades de CO y CO_2 desorbidas fueron analizadas por espectrometría de masas en línea. La determinación de las deconvoluciones se calculó utilizando el software de origen.

2.2.6. Fisisorción de nitrógeno

Los precursores de carbono utilizados, así como los métodos y condiciones de preparación, determinan la estructura porosa de los soportes preparados. El área superficial y la distribución de tamaños de poro de los materiales carbonosos, entre otras propiedades, condicionarán su comportamiento como soporte y, por lo tanto, la actividad de los diferentes catalizadores.

El método más común utilizado en la bibliografía para la determinación del área superficial, pese a sus conocidas limitaciones debidas a la excesiva simplificación del modelo, es el método BET (Brunauer, Emmet y Teller), por lo que es el que se ha utilizado también en este trabajo. El volumen total de poros, se calculó a partir de la cantidad de nitrógeno adsorbida a una presión relativa de 0.99. El volumen de microporos, así como el volumen de poros estructurales, de espacios interparticulares y el área superficial externa; se estimaron usando el método α_S. Los datos de adsorción de referencia usados para este análisis corresponden a una muestra de negro de carbono [KRUK 1997].

El método α desarrollado por Sing [SING 1968] compara la forma de la isoterma patrón con la isoterma problema. Para ello, toma valores de volúmenes adsorbidos a cada presión relativa, representándolos en función de los correspondientes valores de α. Siendo α el cociente entre el volumen adsorbido a una presión relativa dada y el adsorbido a presión relativa de 0.40 ($Vs/V_{0.4}$). La razón de esta elección se justifica por el hecho de que, en el caso de las isotermas de nitrógeno a 77K, a una presión relativa de 0.4, se puede suponer que los microporos ya están llenos y aun no ha comenzado la condensación capilar [MARTÍN 1990]. Si no existen fenómenos de condensación capilar ni hay microporos, la representación de ($Vs/V_{0.4}$) frente a α debe conducir a una línea recta. Mientras que las desviaciones positivas (por encima de la línea recta) de la representación de ($Vs/V_{0.4}$) frente a α evidencian la existencia de condensación capilar, las desviaciones negativas (por debajo de la línea recta), muestran la existencia de microporos. Así, mientras que el volumen de microporos viene dado por la intersección con el eje de ordenadas de la extrapolación del tramo lineal inicial de la curva, el volumen de poros estructurales viene dado por la intersección con el eje de ordenadas de la extrapolación de la meseta a presiones relativas elevadas (restando el volumen de

microporos). El volumen de espacios interparticulares se calcula como la diferencia entre el volumen total de poros y el volumen de microporos y poros estructurales. Por otra parte, la pendiente de la meseta a presiones relativas elevadas esta relacionada con la superficie externa del material.

Se utilizó el método de Barrett, Joyner y Halenda (método BJH) [BARRETT 1951], para calcular una distribución de tamaños de poro. En este trabajo se tomó como diámetro medio de poro el máximo de la curva obtenida por este método.

El análisis de las isotermas de adsorción también aporta gran información acerca de la estructura porosa de la muestra. El primer paso en su interpretación es la identificación de su forma y, a partir de ella, del posible mecanismo de adsorción. La mayor parte de las isotermas pertenecen a uno de los seis grupos reconocidos por la IUPAC en 1985 [SING 1985]. Estas pueden presentar ciclos de histéresis que en ocasiones se pueden relacionar con determinadas estructuras.

El aparato utilizado para realizar estos análisis fue un Micromeritics ASAP 2020, presente en el Instituto de Carboquímica. Antes de llevar a cabo el análisis, las muestras fueron desgasificadas a 150 ºC, hasta alcanzarse un vacío estable de 10^{-5} mmHg.

2.3. CARACTERIZACIÓN ELECTROQUÍMICA

Las técnicas electroquímicas experimentales para el estudio de la cinética electródica, como la mayoría de los métodos físico-químicos, consisten en medir la respuesta a una señal impuesta. La señal perturba el estado de equilibrio del sistema y el comportamiento resultante constituye la respuesta, cuya detección permite obtener la información acerca de las propiedades del sistema. La perturbación del equilibrio de un sistema electroquímico se consigue mediante la variación del potencial del electrodo, paso de corriente, variación de concentración de especie electroactiva, cambios de presión o temperatura, o por medio de otros procedimientos de excitación. En general, a una variación de potencial o a la aplicación de una corriente, el sistema responde a estas perturbaciones con cambios en su comportamiento, que pueden seguirse por las variaciones del potencial del electrodo, de la corriente o de la carga.

En general, las técnicas electroquímicas experimentales proporcionan información acerca de la relación entre la densidad de corriente y el potencial, tiempo transcurrido desde el comienzo del proceso y en algunas ocasiones, de la carga transferida. La selección de la técnica a emplear para un estudio determinado requiere la elección de la variable eléctrica a controlar y considerar la posibilidad de obtención de la variable a medir.

Normalmente, las técnicas electroquímicas utilizan un sistema compuesto por tres electrodos. Un electrodo de referencia, un electrodo de trabajo y un electrodo auxiliar o contraelectrodo [WANG 2000ª].

- Electrodo de referencia (RE*, Reference Electrode*): este electrodo se caracteriza por poseer un valor de potencial constante y conocido, luego, por tanto, permite conocer a qué potencial ocurre el proceso de reducción u oxidación estudiado.
- Electrodo de trabajo (WE*, Working Electrode*): es el electrodo donde ocurre la reacción de interés, por tanto, la reacción que va a ser objeto de estudio. El electrodo de trabajo es un electrodo plano que posee un disco de naturaleza inerte y de diámetro perfectamente conocido.
- Electrodo auxiliar o contraelectrodo (CE*, Counter Electrode*): es un electrodo no polarizable el cual está acoplado al electrodo de trabajo. Juega el papel de colector.

2.3.1. Caracterización en una celda electroquímica convencional

2.3.1.1. Aspectos teóricos

2.3.1.1.1. Voltamperometría cíclica

El término voltametría se usa para clasificar el grupo de técnicas electroanalíticas en las que la corriente que fluye a través de la celda electroquímica es medida mientras se varía el potencial aplicado a los electrodos.

La voltametría cíclica es una de las técnicas de caracterización electroquímica que puede aportar más información con un dispositivo experimental relativamente sencillo. Consiste en variar el potencial del electrodo de trabajo (WE) con el tiempo,

entre dos límites, superior e inferior, a la vez que se registra la corriente que circula a través de este electrodo.

El barrido de potencial se puede realizar a distintas velocidades, cubriendo diferentes intervalos de potencial. La elección de estas variables depende de la respuesta cinética del sistema electroquímico. En ciertas condiciones de perturbación, con determinados procesos electroquímicos, se puede lograr un verdadero estado estacionario. A medida que aumenta la velocidad de barrido, disminuye la influencia de los procesos de transporte de materia que condicionan la respuesta estacionaria del sistema, y se ponen de manifiesto los procesos de transferencia de carga. En consecuencia, este método es útil para estudiar los procesos de oxidación, reducción, electroadsorción y electrodesorción que ocurren en la interfaz.

El perfil corriente-potencial que se obtiene se denomina voltamperograma cíclico (VC) y depende de la naturaleza de la interfaz electroquímica. Aplicando diferentes programas de potencial es posible obtener información acerca de los procesos que tienen lugar sobre la superficie del electrodo de trabajo en diferentes regiones de potencial.

2.3.1.1.2. Cronoamperometría

Mediante esta técnica se determina la variación de la corriente en función del tiempo debido a la aplicación de un salto de potencial sobre el sistema. Normalmente el experimento comienza con la aplicación de un potencial inicial, en el cual no circula corriente eléctrica en el sistema, para pasar posteriormente a otro potencial donde la corriente eléctrica depende del comportamiento difusional del sistema.

Al aplicar el salto de potencial, la concentración en la superficie de la especie activa se hace cero, pero después, con la renovación de dicha especie procedente del seno de la solución, se obtiene un comportamiento característico de variación de la corriente en función del tiempo y de la distancia al electrodo (Figura 2.6).

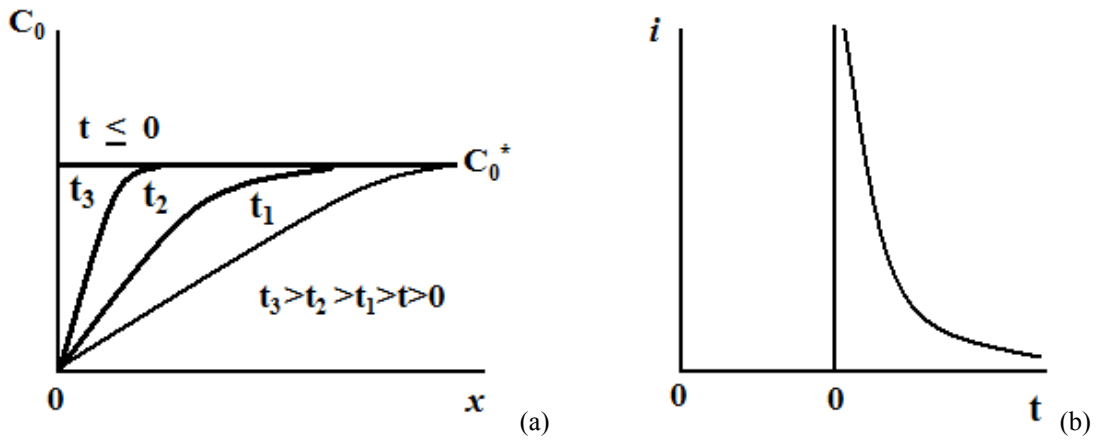

Figura 2.6. *(a) Perfiles de concentración de la especie oxidada para diferentes tiempos durante un mismo experimento; (b) variación de la corriente en función del tiempo.*

2.3.1.2. Aspectros experimentales

Inicialmente, se procede a la preparación del electrodo de trabajo a partir de los diferentes materiales electrocatalíticos soportados sobre carbono preparados, mediante la técnica de electrodo de capa ultrafina. Una alícuota (40 µL) de una mezcla homogénea de 2 mg del electrocatalizador en polvo, 15 µL de Nafion (Aldrich, 5%) y 500 µL de agua Milli-Q, se deposita sobre una superficie de carbón vítreo pulida (un disco de 0.071 cm^2 de área geométrica), y se seca en atmosfera de argón antes de su utilización.

Una vez montado el sistema de celda electroquímica (Figura 2.2), con los correspondientes electrodos de referencia y contraelectrodo; se procede a hacer pasar un gas inerte por la disolución de electrolito de fondo (H_2SO_4 0.5 M) para desairear todo el sistema. El electrodo de trabajo recién preparado como se indica se introduce en la boca central de la celda.

Antes de cada experimento, el electrodo de trabajo se activa en la disolución del electrolito soporte mediante la voltamperometría cíclica. Para ello se aplican barridos cíclicos de potencial a una velocidad de 0.5 V s^{-1}, entre los límites de potencial. El límite inferior se establece en el potencial al que se inicia la evolución del hidrógeno, mientras que el límite superior se fija en el potencial a partir del cual se solubilizan los óxidos metálicos (evitando de esta manera una pérdida de material electrocatalítico).

Después de la activación de la superficie del electrodo de trabajo, se fija el potencial al que se va a realizar el experimento de adsorción de monóxido de carbono (E_{ad}). A continuación, se hace borbotear el CO en la disolución del electrolito de fondo presente en la celda durante un tiempo mínimo de 10 min, asegurando de esta manera que los adsorbatos formados alcancen el máximo recubrimiento posible de la superficie del electrodo de trabajo. Pasado este tiempo, se elimina el CO de la disolución mediante el borboteo de gas inerte en la disolución de la celda. Finalmente, se aplica la voltamperometría cíclica a una velocidad de barrido de 0.02 V s^{-1}.

Una vez activado el electrodo, comprobado el estado de la superficie y haber realizado la caracterización por adsorbatos de CO, se introduce en la celda una disolución de alcohol preparada en el electrolito soporte previamente desaireado ($CH_3OH/CH_3CH_2OH/HCOOH$ 2 M + H_2SO_4 0.5 M). Seguidamente, se inicia un barrido hacia potenciales positivos, a una velocidad determinada hasta el límite superior de potencial establecido, registrándose la VC correspondiente. A partir del perfil de corriente obtenido se pueden obtener los valores de potencial al que comienza la oxidación de alcoholes, así como los potenciales de pico de las diferentes contribuciones presentes en el VC. Finalmente, partiendo del potencial inicial impuesto al electrodo, se aplica un salto a un potencial final de 0.60 V, registrándose la respuesta de la corriente con el tiempo.

2.3.2. Espectrometría de masas diferencial electroquímica (DEMS)

2.3.2.1. Aspectos teóricos

La técnica de espectrometría de masas diferencial electroquímica (DEMS) permite detectar los productos e intermediarios gaseosos o volátiles generados en los procesos electroquímicos, con una gran sensibilidad en un corto tiempo de respuesta. La detección de los átomos, moléculas o fragmentos de moléculas se obtiene a partir del cociente entre su masa (m) y su carga (z), producida por el espectrómetro de masas. El análisis instantáneo del espectro de masas de estas sustancias durante su producción en la celda electroquímica constituye el vínculo directo entre la corriente que circula y la reacción que tiene lugar en el electrodo [WOLTER 1982].

El hecho de disponer de una celda electroquímica conectada a un espectrómetro de masas permite registrar simultáneamente los voltamperogramas cíclicos de intensidad de la señal de masa (VCEMs): (m/z)-potencial; y los VCs: corriente faradaica-potencial. La intensidad de la señal de masa ofrece en muchas investigaciones una respuesta más sensible a las condiciones superficiales que un simple VC, por lo que el uso combinado de ambas técnicas es de gran importancia para elucidar mecanismos de reacción, donde participan productos e intermediarios volátiles o gaseosos.

El análisis cuantitativo de las señales de masa implica proceder a la calibración del DEMS para cada sustancia. Esta calibración se basa en que la señal de intensidad de masa está relacionada con la correspondiente corriente electrónica por una constante que es distinta para cada sustancia producida o consumida en el electrodo. Como la mayor parte de las sustancias que se investigan por DEMS producen CO_2 en su oxidación, esta calibración es la que se ha aplicado más extensamente. El procedimiento consiste en oxidar una monocapa adsorbida de CO para determinar la constante que relacione ambas corrientes, iónica (m/z = 44) y electrónica.

$$k^{CO_2} = \left[2 \frac{Q_i^{CO_2}}{Q_f^{CO_2}} \right] \qquad \text{[Ec. 2.1]}$$

donde k^{CO_2} es la constante de calibración a determinar, $Q_i^{CO_2}$ es la carga iónica obtenida de la integración de la señal m/z = 44 para el intervalo de potencial de interés, y $Q_f^{CO_2}$ es la carga faradaica involucrada en el proceso electroquímico de oxidación de CO a CO_2. En la Ec. 2.1, el 2 proviene del número de electrones intercambiados por cada molécula de CO_2 detectada. Al tratarse de un cociente, es posible trabajar con magnitudes de corriente o de densidad de corriente.

En un proceso electroquímico más complejo, como la oxidación del metanol, la corriente electrónica deriva de la contribución de distintos procesos y existe una k^j para cada uno de los *j* productos detectados en el espectrómetro. Esto es así aún cuando todas las constantes no se puedan determinar por la complejidad de las reacciones involucradas. A pesar de ello, conociendo una de ellas se puede establecer de

forma cualitativa la importancia de cada vía de reacción según trascurre el tiempo, el potencial, etc., ya que siempre se cumplirá que para cualquier especie *j*:

$$Q_f^j = \frac{nQ_i^j}{k^j} \qquad \text{[Ec. 2.2]}$$

donde *n* es el número de electrones intercambiados para producir la molécula detectada. El rendimiento de la vía que produce la especie *j*, R^j, para todo el proceso de medida vendría dado por:

$$R^j = \frac{Q_f^j}{Q_f^T} = \frac{nQ_i^j}{k^j \times Q_f^T} \qquad \text{[Ec. 2.3]}$$

En esta ecuación Q_f^j es la carga faradaica empleada en generar una cantidad de carga de iones de la especie *j* Q_i^j, mientras Q_f^T es la cantidad de carga faradaica total para todos los procesos que tienen lugar sobre la superficie electródica.

2.3.2.2. Aspectos experimentales

Los electrodos de trabajo utilizados en este tipo de experimentos, se obtuvieron mediante la deposición de una suspensión de una disolución de Nafion 10% wt. y los catalizadores preparados sobre un electrodo de difusión de gas previamente preparado. La capa de difusión de gas consiste en una lámina de tela de carbono sobre la cual se deposita un estrato de carbón y teflón en un solo lado.

En las experiencias de DEMS, se siguió una metodología similar a la de los experimentos en la celda electroquímica convencional. Sin embargo, y con el fin de no saturar el detector del espectrómetro de masas, las velocidades de barrido, así como las concentraciones de las disoluciones de alcoholes utilizadas, fueron más bajas.

Para los estudios de adsorción de CO, se utilizó una velocidad de barrido de 0.005 V s^{-1}. En el caso del estudio de oxidación alcoholes la velocidad utilizada fue de 0.001 v s^{-1}, mientras que la concentración de alcohol utilizada fue de 0.5 M.

Capítulo 3

Resumen

3.1. INTRODUCCIÓN

Entre los diferentes tipos de celdas de combustible, las más apropiadas para suministrar energía a dispositivos portátiles, vehículos eléctricos y medios de transporte, son las de electrolito polimérico (PEMFCs) y alcohol directo (DAFCs) debido a sus bajas temperaturas de operación (60-100 ºC) y a su rápida puesta en funcionamiento. Los catalizadores más utilizados en el ánodo de estas celdas son el platino y sus aleaciones. Teniendo en cuenta que la catálisis es un fenómeno de superficies, un aspecto a considerar en el diseño de los catalizadores es que presenten un área superficial elevada. Con este propósito, la fase activa del catalizador se dispersa en un soporte conductor, normalmente materiales carbonosos. Sin embargo, el desarrollo de las PEMFCs, desde el punto de vista de los electrocatalizadores, está limitado por el envenenamiento del catalizador del ánodo con CO, el cual está presente como impureza en el gas de reformado que se utiliza como fuente de H_2 para este tipo de celdas. Por

ello, en la actualidad gran parte de las investigaciones están dirigidas a la preparación de ánodos más tolerantes al CO. En presencia de 50-100 ppm de CO en el combustible, las aleaciones de Pt-Ru soportadas en materiales carbonosos han mostrado una actividad electrocatalítica mayor que el Pt puro. En relación a los materiales utilizados en el cátodo, el Pt es el metal que muestra la mayor actividad catalítica hacia la reacción de oxidación de oxígeno.

Entre todos los tipos de materiales de carbono, los negros de carbono son los más utilizados como soporte de electrocatalizadores para pilas de combustible de electrolito polimérico, debido a su alta conductividad eléctrica y resistencia a la corrosión, su estructura porosa adecuada y elevada superficie específica [BEZERRA 2007]. Sin embargo, estos materiales presentan una alta resistencia óhmica y problemas de transferencia de masa cuando son utilizados en aplicaciones de pila de combustible.

Al haberse demostrado que los soportes de carbono tienen una gran influencia sobre la accesibilidad de los sitios catalíticos activos, se están dedicando grandes esfuerzos a la búsqueda de una arquitectura óptima del soporte carbonoso. En los últimos años, la estrategia a seguir es el uso de nuevos materiales con una estructura mesoporosa. Se proponen como soporte de electrocatalizadores materiales carbonosos no convencionales, con una estructura porosa y química superficial controlables, tales como las nanoespirales de carbono [HYEON 2003], xerogeles y aerogeles de carbono [MARIE 2004], y los carbones mesoporosos ordenados [CALVILLO 2007].

3.2. OBJETIVOS

Los objetivos globales de esta tesis doctoral se enumeran a continuación:

- Estudiar las propiedades físico-químicas de las nanoespirales de carbono, prestando especial atención a la variación de dichas características en función de las condiciones de síntesis.
- Estudiar distintos métodos de funcionalización de las nanoespirales de carbono con objeto de modificar su química superficial, aumentar el área superficial específica y desarrollar una mayor porosidad.

- Preparación de catalizadores metálicos y bimetálicos soportados sobre las nanoespirales de carbono sintetizadas. Estudio de la influencia del soporte y del método de síntesis en las propiedades de los electrocatalizadores para la electrooxidación de CO y alcoholes.
- Exploración de nuevas y novedosas configuraciones para el desarrollo de catalizadores activos y estables con nanoestructura *core-shell* para la electrooxidación de alcoholes en pilas de combustible DAFC.

3.3. SOPORTES CARBONOSOS

Los materiales de carbono han sido utilizados industrialmente durante décadas como soporte de catalizadores [AUER 1998]. Los carbones activados, los negros de carbono, así como el grafito y los materiales grafíticos han sido aplicados en diversos procesos catalíticos. Los materiales de carbono tienen una gran influencia sobre las propiedades de los metales nobles soportados en ellos, como el tamaño de partícula, la morfología, la distribución de tamaños de partícula, la estabilidad y la dispersión [KIM 2006, YU 2007]. Por otro lado, los soportes de carbono también pueden afectar al rendimiento de los catalizadores en la pila de combustible mediante la alteración de los procesos de transporte de masa, de la conductividad eléctrica de la capa catalítica, del área electroquímica activa, y de la estabilidad de las nanopartículas metálicas durante el funcionamiento de la misma [HALL 2004, INOUE 2009]. Por lo tanto, la optimización de los soportes de carbono es muy importante en el desarrollo de la tecnología PEMFC.

Las propiedades ideales de un soporte de carbono para su uso en pilas de combustible son [LIU 2006, DICKS 2006]: i) alta área superficial para conseguir una buena dispersión del catalizador; ii) estructura porosa adecuada para tener una buena difusión de los reactivos y productos hasta y desde las partículas de catalizador; iii) buena conductividad eléctrica para facilitar la transferencia de electrones entre los electrodos de la pila de combustible durante las reacciones electroquímicas; iv) química superficial adecuada para facilitar la interacción entre el precursor del metal y el soporte durante el proceso de síntesis y obtener una elevada dispersión y pequeño tamaño de las partículas de metal; y v) resistencia a la corrosión para garantizar la durabilidad del

catalizador. Además de estos requisitos, deben ser materiales de bajo costo y permitir el reciclaje del metal al final de la vida del catalizador.

3.3.1. Vulcan XC-72R

El Vulcan XC-72 se utiliza ampliamente como soporte de electrocatalizadores, especialmente en las pilas de combustible de electrolito polimérico [SHAO 2006, WIKANDER 2006]. En este momento, este material se utiliza como soporte en electrocatalizadores comerciales (E-TEK y Johnson Matthey). Por restos motivos, fue utilizado en este trabajo como comparación. A continuación, se presenta una revisión de las propiedades del material de carbono Vulcan XC-72R.

La morfología del Vulcan XC-72R se estudió mediante microscopía electrónica de barrido (SEM) y difracción de rayos X (XRD). En la Figura 3.1 se muestran dos de las imágenes obtenidas mediante SEM. Se observa como el Vulcan consiste en una agregación de partículas esféricas, llamadas partículas primarias, con un tamaño en el rango de 30 a 60 nm. El grado de agregación de las partículas se conoce como "estructura" del negro de carbono.

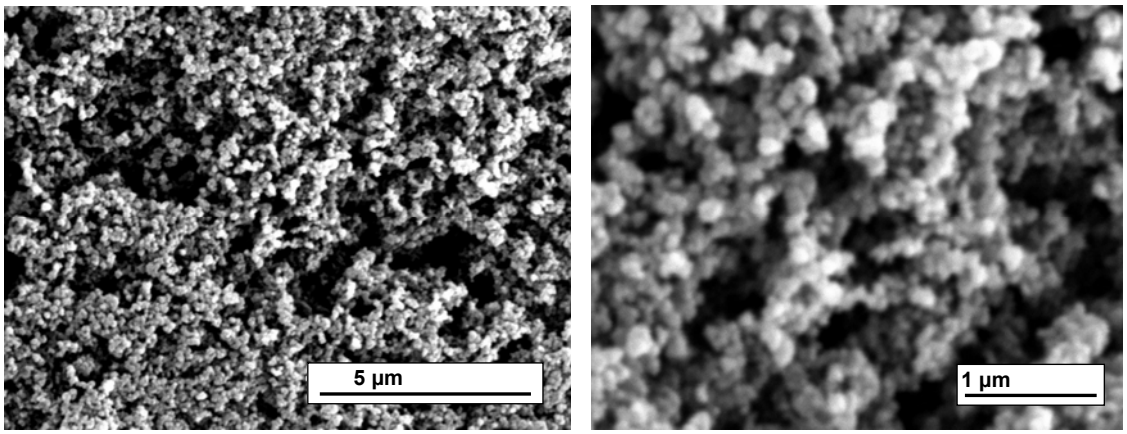

Figura 3.1. Imágenes SEM del Vulcan XC-72R.

En la Figura 3.2, donde se muestra el difractograma XRD del Vulcan XC-72R, se observa un pico a $2\theta = 24.85º$ que confirma que su morfología presenta cierto grado de cristalinidad, similar a la del grafito, que se denomina estructura turbostrática.

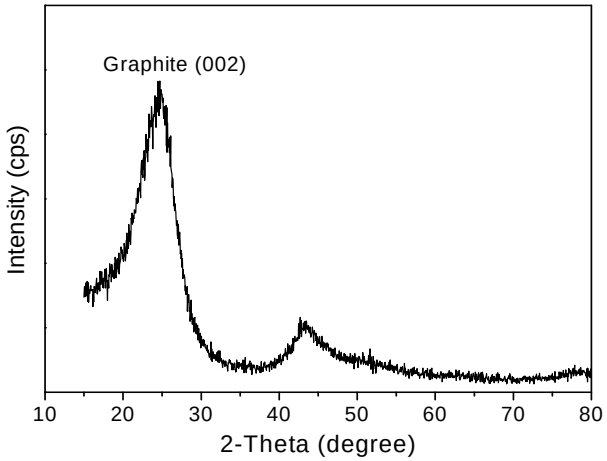

Figura 3.2. Difractograma del Vulcan XC-72R.

La estabilidad térmica del Vulcan XC-72R, así como el efecto de los tratamientos de oxidación sobre la misma, se estudió mediante experimentos de oxidación a temperatura programada (TPO). La estabilidad térmica (o resistencia a la corrosión) de los materiales utilizados como soporte de catalizadores en las pilas de combustible PEM es una característica importante a tener en cuenta, ya que afecta la durabilidad del catalizador. Debido a su estructura, el Vulcan XC-72R presentaba una resistencia muy elevada a la oxidación en aire, ya que su gasificación tenía lugar alrededor de 660 ºC [LÁZARO 2011[b]].

Tabla 3.1. *Parámetros texturales del Vulcan obtenidos mediante fisisorción de nitrógeno a 77 k*

Material	S_{BET} [a] ($m^2\ g^{-1}$)	V_{Total} [b] ($cm^3\ g^{-1}$)	$V_{Micropore}$ [c] ($cm^3\ g^{-1}$)	$V_{Mesopore}$ [d] ($cm^3\ g^{-1}$)	$S_{Micropore}$ [c] ($m^2\ g^{-1}$)	$S_{Mesopore}$ [d] ($m^2\ g^{-1}$)
Vulcan XC-72R	218	0.41	0.03	0.38	65	153

[a] Determinado mediante la ecuación BET (Brunauer, Emmett y Teller).
[b] Determinado mediante el método de punto único a $P/P_0 = 0.99$.
[c] Determinado mediante el método t-plot.
[d] Calculado a partir de la diferencia entre el valor total y el valor de microporos.

Las propiedades texturales del Vulcan se analizaron mediante fisisorción de N_2. En la Tabla 3.1 se recogen los parámetros texturales obtenidos mediante esta técnica. El Vulcan presentaba una superficie específica relativamente grande (S_{BET}) de 218 $m^2\ g^{-1}$ y un volumen total de poros (V_{Total}) de 0.41 $cm^3\ g^{-1}$. Se observó una estructura mesoporosa, pero con una gran cantidad de microporos (30% de la superficie total). Los microporos no son adecuados para la aplicación de los materiales como soporte de electrocatalizadores, ya que, es posible, que una parte de las nanopartículas metálicas

queden dentro de estos microporos, lo que resulta una disminución de la actividad electroquímica debido a la dificultad de acceso de los reactivos [LIU 2006, ANTOLINI 2009].

La química superficial del Vulcan XC-72R se estudió mediante experimentos de desorción a temperatura programada (TPD). Durante los experimentos TPD, los grupos oxigenados superficiales ácidos se descomponen en forma de CO_2 a bajas temperaturas, mientras que los grupos básicos y neutros se descomponen en forma de CO a altas temperaturas [FIGUEIREDO 1999]. Los perfiles de CO y CO_2 pueden ser analizados y los picos obtenidos se pueden relacionar con los distintos tipos de grupos funcionales dependiendo de la temperatura de descomposición de los mismos [AKSOYLU 2001, SAMANT 2004, FIGUIREDO 1999]. El Vulcan presentó una pequeña cantidad de grupos oxigenados superficiales, ya que no había sufrido ningún tratamiento de oxidación. Se observaron grupos desorbidos a altas temperaturas en forma de CO (grupos fenol y quinona), sin embargo, no se obtuvieron grupos desorbidos en forma de CO_2.

3.3.2. Nanoespirales de carbono (CNC)

Las nanoespirales de carbono (CNC) constituyen una nueva clase de nanomateriales de carbono con propiedades que difieren significativamente de otras formas de carbono. Existen distintos métodos para sintetizar CNC, como la descarga con arco, la vaporización láser, la deposición térmica de vapor químico y la grafitización catalítica de precursores de carbono. El proceso de grafitización catalítica reduce los costes de fabricación de una manera significativa, debido a la disminución de las temperaturas de síntesis. Diferentes precursores de carbono como los geles de resorcinol-formaldehído [HYEON 2003] o los compuestos sacáridos [SEVILLA 2007] pueden ser utilizados como precursores de carbono, mientras que como catalizadores del proceso de grafitización se utiliza una mezcla de sales de metales de transición.

En esta tesis, se propuso la grafitización catalítica como procedimiento de síntesis de CNC, de esta forma, los materiales de carbono pueden obtenerse a baja temperatura (< 1000 ºC). Así, se llevó a cabo un estudio de síntesis de CNC por grafitización catalítica de geles de resorcinol-formaldehído utilizando una mezcla de sales de níquel y cobalto como catalizadores de grafitización. El objetivo, era

determinar las condiciones más adecuadas para obtener este tipo de materiales variando la relación molar de los reactivos utilizados, alcanzando un acuerdo entre el grado de grafitización y el área superficial.

3.3.2.1. Estudio de las condiciones de síntesis

La síntesis de las nanoespirales de carbono (CNC) se llevó a cabo siguiendo el método descrito en [CELORRIO 2010]. Brevemente, la síntesis consistió en disolver una mezcla de sales de níquel (Panreac) y cobalto (Sigma-Aldrich) en 100 mL de una disolución acuosa de formaldehído (Sigma-Aldrich) y sílice (Supelco). A continuación, se añadió resorcinol a la disolución (Sigma-Aldrich), manteniéndose bajo condiciones de agitación durante 0.5 h. Después de un tratamiento térmico de la mezcla de reacción a 85 ºC durante 3 horas en un sistema cerrado, el sistema se abrió y se secó a 108 ºC. Finalmente, fue carbonizada en una atmósfera de nitrógeno a 900 ºC durante 3 horas. Se utilizó una disolución 5 M de NaOH (Panreac) para eliminar las partículas de sílice, seguido por un tratamiento con HNO_3 (65%, Fluka) concentrado a temperatura ambiente durante 2 horas para eliminar las sales metálicas.

Mediante este proceso, se prepararon nanoespirales de carbono (CNC-1, CNC-2 y CNC-3) con distintas características. Para ello, se variaron las relaciones molares de los reactivos a utilizar. Las relaciones molares de reactivos utilizadas y la nomenclatura de los distintos materiales preparados se presentan en la Tabla 3.2.

Tabla 3.2. *Condiciones de preparación y nomenclatura de las nanoespirales de carbono.*

Sample	H_2O/Co salt/Ni salt/Resolcinol/Formaldehído/Silica
CNC-1	100:0.2:0.2:1:2:0
CNC-2	100:0.4:0.4:1:2:0.6
CNC-3	100:0.2:0.2:1:2:0.6

La Figura 3.3.a. muestra los patrones de difracción de rayos X de los CNC sintetizados. La muestra CNC-1 presenta un patrón de difracción típico de un carbono ligeramente grafítico. Se observa un pico ancho a ~24º y uno de menor intensidad alrededor de ~44º, característicos de los planos (002) y (100) de la estructura del grafito. Un aumento en la cantidad de sílice utilizada en la síntesis produjo una reducción del ancho del pico de difracción principal (002) e hizo el (100) más visible.

Además, el pico principal de difracción de rayos X para las muestras CNC-2 y CNC-3 parece ser una superposición de un pico amplio y uno más estrecho centrado en ~ 26º. Esto sugiere que en su mayor parte, las muestras están bien grafitizadas, sin embargo, siguen existiendo otras grafitizadas en menor medida.

La naturaleza y el grado de grafitización de las muestras también se estudiaron mediante espectroscopía Raman. Los espectros Raman de primer (1200-1700 cm^{-1}) y de segundo orden (2500-2900 cm^{-1}) de las nanoespirales de carbono se muestran en la Figura 3.3.b. En el espectro Raman de primer orden aparecen dos bandas: la banda G o grafítica, y la banda D asociada a la presencia de distintos tipos de defectos estructurales [CUESTA 1994]. Además de estas dos grandes bandas, algunos autores postulan la existencia de otras más pequeñas; como la banda D' y la D'' [ROUZAUD 1983, VIDANO 1978]. En este caso, puede asociarse a la presencia de carbono amorfo asociado al carbono grafítico, así como a la ligera funcionalización del material sufrida en el tratamiento con ácido nítrico. Por otra parte, en el espectro Raman de segundo orden aparece la banda G' característica de materiales ordenados.

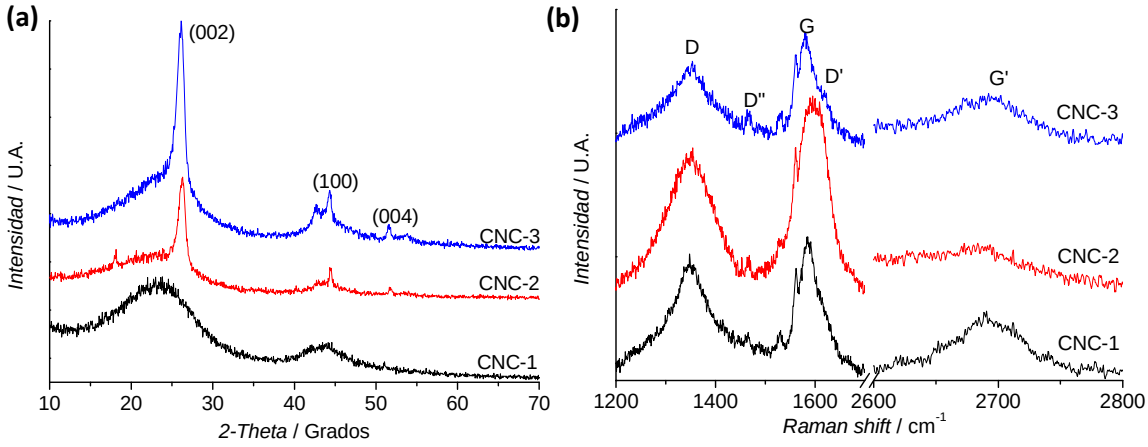

Figura 3.32. Difractogramas XRD (a) y espectros Raman de primer y segundo orden (b) de las CNC.

La morfología de las nanoespirales de carbono sintetizadas se estudió mediante microscopía electrónica de transmisión (TEM). Estos materiales poseían una morfología en espiral, como se puede observar en las imágenes TEM. Cada una de ellas presentaba planos grafíticos bien alineados como puede verse en las imágenes HRTEM en la Figura 3.4.A y 3.4.B; lo que confirma los resultados obtenidos por XRD y

espectroscopía Raman. Las imágenes TEM (C y D de la Figura 3.4.) muestran que los CNC tienen un diámetro de alrededor de 30-40 nm y consisten en largas cintas curvas de carbono. Además, se forman partículas de alrededor de 100-150 nm se que contienen varios CNC, como puede verse en la Figura 3.4.D.

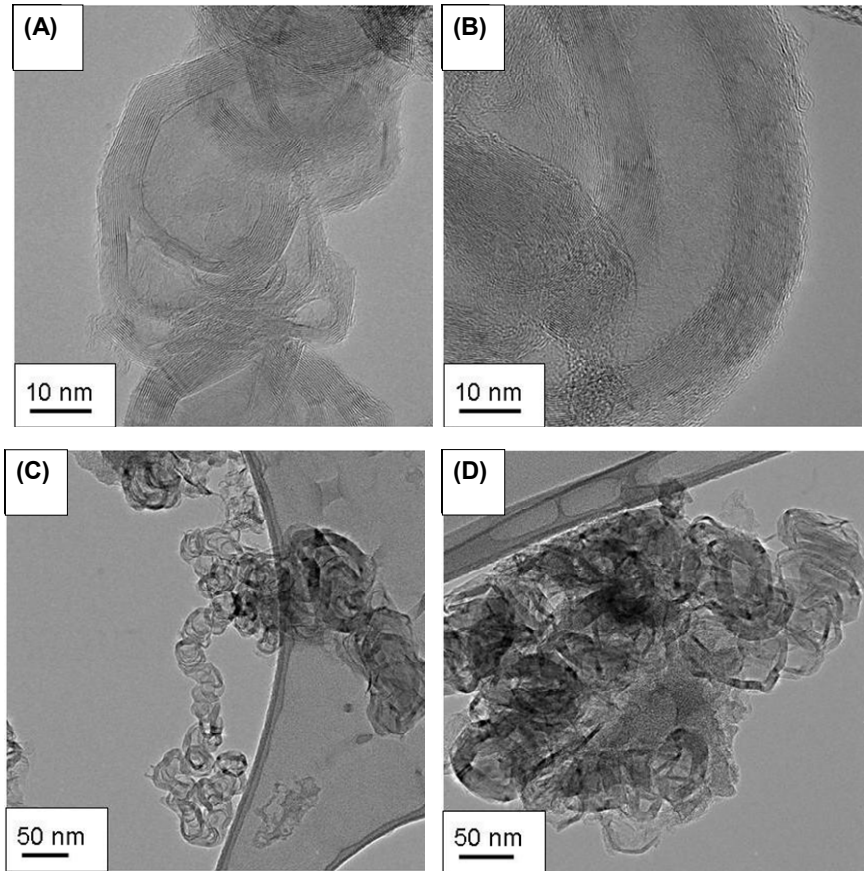

Figura 3.4. Imágenes HRTEM (A, B) y TEM (C, D) de las nanoespirales de carbono.

La estabilidad térmica se estudió mediante experimentos TPO bajo una atmósfera de aire. Todas las muestras mostraron una alta resistencia a la oxidación en aire, con patrones similares de cambio de peso. Las oxidaciones se produjeron alrededor de 600 ºC, siendo la muestra de CNC-3 la más resistente a la oxidación, aunque no hubo diferencias significativas con el resto de materiales [CELORRIO 2011]. Este hecho puede estar relacionado con su carácter ligeramente más grafítico. También se observó que la oxidación de los materiales de carbono era completa, es decir, no había residuos después de los experimentos TPO. Esto indica que la eliminación de la sílice y de las

partículas metálicas con NaOH y los tratamientos con HNO_3, respectivamente, había sido completa.

En la Tabla 3.3 se presentan los parámetros texturales obtenidos mediante fisisorción de N_2. Los materiales presentaban una superficie específica entre 120-220 m^2 g^{-1} y un volumen de poro de 0.10-0.19 cm^3 g^{-1}. Tanto la superficie específica como el volumen de poros disminuyó a medida que aumentaba el grado de la grafitización de muestra. Así, la muestra CNC-3 mostró la menor área superficial y volumen de poros, y la muestra de CNC-1 mostró los valores más altos. La forma de estas isotermas obtenidas (no mostradas) era típica de materiales nanoparticulados que carecen de poros estructurales. En este caso, la adsorción tiene lugar sobre la superficie externa de las nanoestructuras. Los resultados derivados del análisis α_S demuestran que las nanoespirales de carbono carecen de poros estructurales, por lo que la adsorción tiene lugar en la superficie externa de las nanoestructuras. Por lo tanto, el área BET (S_{BET}) coincide con la superficie externa (S_{ext}).

Tabla 3.3. *Parámetros texturales de las nanoespirales de carbono.*

Material	S_{BET}[a] (m^2 g^{-1})	V_{Total}[b] (cm^3 g^{-1})	Método Alfa-Sing		
			S_{ext} (m^2 g^{-1})	V_{micro} (cm^3 g^{-1})	V_i (cm^3 g^{-1})
CNC-1	120	0.10	122	0.0	0.10
CNC-2	220	0.19	223	0.0	0.19
CNC-3	124	0.16	126	0.0	0.16

[a] Determined by the BET (Brunauer, Emmett and Teller) equation.
[b] Determined by the single point method at P/P_0=0.99.

Las nanoespirales de carbono se trataron con ácido nítrico concentrado a temperatura ambiente durante 2 horas para eliminar las partículas metálicas utilizadas como catalizadores en el proceso de grafitización. Este tratamiento se suele utilizar para modificar la química superficial de materiales de carbono, creando grupos oxigenados superficiales. Por lo tanto, este efecto también fue estudiado. Las muestras contenían principalmente grupos carboxílicos y fenol. Se espera que los grupos carboxílicos produzcan una disminución de la hidrofobicidad de los materiales de carbono y que los grupos fenólicos hagan la superficie más accesible.

3.3.2.2. Modificación de las propiedades de las nanoespirales de carbono

El último paso del proceso de síntesis de CNC implica la eliminación de las sales metálicas con un tratamiento oxidativo, comúnmente HNO_3. Sin embargo, durante este tratamiento no sólo se eliminan las sales metálicas, sino también parte del carbono amorfo y grafítico. Por otro lado, este tratamiento puede crear grupos oxigenados superficiales, modificando la química superficial de las CNC. La mayor parte de los trabajos recogidos en la literatura, reportan el uso de un tratamiento con HNO_3 con el fin de eliminar las partículas metálicas usadas durante la síntesis, mientras que otros someten la muestra a un tratamiento con ácido clorhídrico [SEVILLA 2007]. Con éstos tratamientos en medio ácido, además de conseguir la eliminación de las partículas metálicas utilizadas como catalizadores de la grafitización, se consigue la modificación de la química superficial del material. Sin embargo, no se han encontrado estudios sobre la influencia de diferentes tratamientos en las propiedades de éstos materiales en la literatura. Debido a sus buenas propiedades, el material CNC-3 fue elegido para realizar este estudio.

Los tratamientos de oxidación son capaces de introducir grupos oxigenados superficiales, mejorando así la mojabilidad de los materiales de carbono en solventes polares como el agua. Esta característica es muy importante para lograr una buena interacción entre el precursor de metal y el soporte carbonoso y por lo tanto, permitir el anclaje de la fase activa [CALVILLO 2007, CALVILLO 2009]. Con este objetivo, el tratamiento HNO_3 a temperatura ambiente durante 2 h fue sustituido por diferentes tratamientos con ácido nítrico (Nc), mezclas nítrico-sulfúrico (NS), peróxido de hidrógeno (Ox) y mezclas ácido sulfúrico-peróxido de hidrógeno (SOx). Estos tratamientos se llevaron a cabo a 25 (Ta) y 80 ºC (Tb) durante 0.5 y 2 h.

Los materiales de carbono obtenidos se caracterizaron mediante las mismas técnicas que el material original (sección 3.3.2.1.) con el fin de estudiar el efecto de estos tratamientos en las propiedades finales de las CNC.

Los experimentos TPO mostraron que el uso de distintos tratamientos de oxidación no afectaba a la resistencia a la oxidación de una manera significativa. En todos los casos, la oxidación se llevó a cabo alrededor de 600 ºC [CELORRIO 2011]. Además, se pudo observar que no todos los tratamientos de oxidación fueron efectivos

para la total eliminación de las sales metálicas utilizadas como catalizadores de la grafitización. Se obtuvo un residuo después de los tratamientos con H_2O_2 y H_2SO_4-H_2O_2, lo que indica que estos tratamientos no eliminaron por completo los metales utilizados.

Los distintos tratamientos en fase líquida tuvieron una gran influencia en las propiedades texturales de los materiales de carbono. Se obtuvieron materiales con superficies específicas (S_{BET}) en el rango de 30-250 $m^2\ g^{-1}$ y un volumen total de poro (V_{TOTAL}) de 0.08-0.30 $cm^3\ g^{-1}$. Como se puede observar en la Tabla 3.4., los materiales de carbono tratados con mezclas H_2SO_4-H_2O_2 (SOx) mostraron las superficies específicas y el volumen total de poros más bajos. Este resultado podría atribuirse a la destrucción parcial de la estructura del material durante el tratamiento de oxidación. Para el resto de agentes oxidantes, se obtuvieron parámetros texturales similares para todas las condiciones de oxidación (temperatura y tiempo), a excepción de las condiciones más severas (80 ºC durante 2 h). En este último caso, se observó una disminución tanto de la superficie específica como del volumen de poro.

Tabla 3.4. *Propiedades texturales de los materiales obtenidos después de los tratamientos de oxidación.*

Muestra	S_{BET}[a] ($m^2\ g^{-1}$)	V_{Total}[b] ($cm^3\ g^{-1}$)	Método Alfa-Sing		
			S_{ext} ($m^2\ g^{-1}$)	V_{micro} ($cm^3\ g^{-1}$)	V_i ($cm^3\ g^{-1}$)
CNC NcTa0.5	243	0.31	249	0.0	0.31
CNC NcTa2	124	0.16	126	0.0	0.16
CNC NcTb0.5	235	0.22	241	0.0	0.22
CNC NcTb2	246	0.24	252	0.0	0.24
CNC NSTa0.5	117	0.13	120	0.0	0.13
CNC NSTa2	213	0.19	218	0.0	0.19
CNC NSTb0.5	202	0.18	207	0.0	0.18
CNC NSTb2	120	0.13	123	0.0	0.13
CNC SOxTa0.5	84	0.12	86	0.0	0.12
CNC SOxTa2	75	0.10	77	0.0	0.10
CNC SOxTb0.5	74	0.11	76	0.0	0.11
CNC SOxTb2	46	0.09	47	0.0	0.09
CNC OxTa0.5	168	0.17	172	0.0	0.17
CNC OxTa2	183	0.19	187	0.0	0.19
CNC OxTb0.5	192	0.22	196	0.0	0.22
CNC OxTb2	187	0.20	196	0.0	0.20

[a] Determinado mediante la ecuación BET (Brunauer, Emmett y Teller).

[b] Determinado mediante el método de punto único a $P/P_0 = 0.99$.

La Tabla 3.5 resume las cantidades de los diferentes tipos de grupos oxigenados a partir de la deconvolución de los perfiles de CO y CO_2 obtenidos en los experimentos TPD. Para cada agente oxidante, se observó un aumento en el número de grupos oxigenados con la severidad del tratamiento, es decir, a una temperatura o tiempo mayores. Los tratamientos con H_2O_2 fueron los menos efectivos en la creación de grupos funcionales, ya que el H_2O_2 es el agente oxidante más débil de entre todos los tratamientos utilizados. El tratamiento de oxidación más eficaz en la creación de grupos superficiales oxigenados, especialmente grupos anhídrido/lactona, fue el tratamiento con mezclas HNO_3-H_2SO_4 a temperatura de ebullición durante 2 h. En los picos de evolución de CO_2, se observó que principalmente se crearon grupos anhídrido/lactona que son estables a bajas temperaturas; mientras que de los picos de evolución de CO se dedujo la formación de los grupos fenólicos, que son estables a altas temperaturas (Tabla 4.5).

Tabla 3.5. *Estimación del tipo y número de grupos oxigenados creados durante los tratamientos de oxidación mediante la deconvolución de los perfiles TPD. Los experimentos TPD se llevaron a cabo en atmósfera inerte, con una velocidad de calentamiento de 10 ºC min^{-1} hasta 1050 ºC. Las cantidades de CO y CO_2 desorbidas fueron analizados por espectrometría de masas.*

Muestra	**Área de pico CO_2 (µmol g^{-1})**		**Área de pico CO (µmol g^{-1})**		
	Carboxílico	**Anhídrido Lactona**	**Anhídrido**	**Fenol**	**Quinona**
CNC NcTa0.5	498	254	106	797	64
CNC NcTa2	440	410	450	1690	200
CNC NcTb0.5	595	1100	12	1862	173
CNC NcTb2	506	1077	36	1214	1131
CNC NSTa0.5	210	1060	890	960	240
CNC NSTa2	270	1420	1250	840	140
CNC NSTb0.5	570	2220	410	1460	210
CNC NSTb2	590	3220	0	3000	0
CNC SOxTa0.5	332	958	43	1111	448
CNC SOxTa2	237	1152	59	1341	111
CNC SOxTb0.5	287	953	24	1116	395
CNC SOxTb2	510	1165	43	862	32
CNC OxTa0.5	260	160	20	500	30
CNC OxTa2	240	110	20	420	90
CNC OxTb0.5	430	110	30	410	30
CNC OxTb2	280	340	0	310	200

3.4. CATALIZADORES MONOMETÁLICOS Y ALEACIONES

Las nanoespirales de carbono han recibido recientemente mucha atención como soporte catalítico para electrodos de pilas de combustible, debido a la combinación de su buena conductividad eléctrica (derivada de su estructura grafítica), y una amplia porosidad que permite que las resistencias difusionales de reactivos y productos se reduzcan al mínimo. En la literatura, son escasos los trabajos sobre catalizadores soportados sobre nanoespirales de carbono tanto para su uso tanto en el ánodo como en el cátodo de pilas de combustible. Hyeon *y cols*. sintetizaron aleaciones Pt/Ru (1:1) al 60% en peso, soportadas en CNC. Su comportamiento fue estudiado para la oxidación de metanol, demostrando su buena actividad electrocatalítica [HYEON 2003]. Sevilla *y cols*. también demostraron la alta actividad catalítica de los electrocatalizadores PtRu/CNC para la oxidación de metanol [SEVILLA 2007]. Comparado su actividad con la de un catalizador Pt/Vulcan preparado por el mismo método, demostraron que los catalizadores soportados en CNC mostraban una mayor utilización de la fase activa [SEVILLA 2008, SEVILLA 2009]. Park *y cols*. emplearon nanoespirales de carbono de distintas superficies específicas y cristalinidad como soporte de catalizadores de Pt/Ru [PARK 2004, HAN 2003]. Se encontró que los catalizadores soportados en nanoespirales de carbono mostraron un mejor comportamiento electrocatalítico hacia la electrooxidación de metanol que aquellos soportados en Vulcan XC-72. Por otro lado, Imran Jafri *y cols*. estudiaron la actividad de nanopartículas de Pt soportadas en CNC para la reacción de reducción de oxígeno en pilas de combustible de intercambio protónico [IMRAN JAFRI 2010], los resultados obtenidos apoyan el uso de este nuevo tipo de material como soporte catalítico para PEMFCs.

3.4.1. Síntesis

En la literatura, diferentes métodos de síntesis son utilizados para preparar electrocatalizadores de platino como impregnación, intercambio iónico, precipitación, coloidal, y los métodos en fase vapor. Sin embargo, los trabajos en la literatura sobre la comparación de catalizadores sintetizados por distintos métodos son escasos [SALGADO 2008, LÁZARO 2011[a]], no encontrándose estudios sobre el efecto del

método de síntesis en las propiedades de electrocatalizadores que utilicen nanoespirales de carbono como soporte.

El método de impregnación-reducción es uno de los métodos más utilizados para la fabricación de catalizadores. Es posible impregnar materiales carbonosos de alta área superficial, como los negros de humo, con precursores metálicos mediante la mezcla de ambos en una solución acuosa. Después de la etapa de impregnación, es necesaria una etapa de reducción para reducir el precursor a su estado metálico. Los agentes reductores más comunes en fase líquida son $Na_2S_2O_3$, $NaBH_4$, $Na_4S_2O_5$, N_2H_4, y HCOOH. Siendo el H_2 el agente reductor más común en fase gas.

Por los motivos expuestos, y con el objetivo de estudiar el efecto del método de síntesis tanto en las propiedades fisicoquímicas como electroquímicas, se sintetizaron catalizadores soportados sobre nanoespirales de carbono mediante diferentes métodos. Los catalizadores fueron preparados por impregnación y posterior reducción con borohidruro de sodio (BM) [CALVILLO 2007] o ácido fórmico (FAM) [ÁLVAREZ 2010], y mediante el método de reducción con alcohol utilizando metanol (MM) [GANGERI 2006] o mediante el método polyol utilizando etilenglicol como solvente y agente reductor (EGM) [LÁZARO 2011[a]].

Se seleccionó el material CNC-3 NcTa2 (de ahora en adelante denominado CNC) para preparar los catalalizadores, por presentar a priori las mejores propiedades como soporte de entre los materiales carbonosos sintetizados. Además, se utilizó Vulcan XC-72R para poder estudiar el efecto del soporte carbonoso en las propiedades de los catalizadores.

3.4.1.1. Electrocatalizadores de Pt y Pt-Ru

Se sintetizaron catalizadores de Pt y Pt-Ru soportados sobre Vulcan y CNC mediante los métodos BM, FAM, MM y EGM; con el fin de estudiar la influencia del método de síntesis sobre las propiedades físicoquímicas y electroquímicas de los catalizadores. Sus propiedades fueron comparadas con los de los catalizadores comerciales de E-TEK.

Se utilizó ácido hexacloroplatínico, H_2PtCl_6 (disolución al 8 % p/p, Aldrich), y cloruro de rutenio (III), $RuCl_3$ (99.999 %, Aldrich), como precursores metálicos. Se

prepararon catalizadores con un 20 % wt. de carga metálica, siendo para los catalizadores de Pt-Ru la relación atómica objetivo Pt:Ru de 1:1.

3.4.1.2. Electrocatalizadores de Pd

Se escogió el método de impregnación y posterior reducción con borohidruro de sodio (BM) para estudiar la influencia del soporte carbonoso en las propiedades de electrocatalizadores de paladio. Además, se estableció una comparación con el catalizador comercial Pd/C de E-TEK.

Como precursor metálico se utilizó Na_2PdCl_6 (98 wt. % $Na_2PdCl_6 \cdot 6\ H_2O$, Sigma-Aldrich). Se utilizaron cantidades adecuadas de soporte y precursor metálico para obtener una carga total de metal del 20 wt.%.

3.4.2. Caracterización fisicoquímica

La caracterización física de los electrocatalizadores es muy importante en distintas áreas de investigación tales como la preparación de nuevos tipos de electrocatalizadores con alta actividad y selectividad, el reconocimiento de sus estructuras, y la investigación de los mecanismos de catalizadores y aditivos.

En esta sección, se estudió el tamaño y la morfología de las partículas metálicas en función del soporte y del método de síntesis utilizado.

3.4.2.1. Electrocatalizadores de Pt y Pt-Ru

En las Tablas 3.6 y 3.7 se muestra la nomenclatura y la carga metálica, obtenida mediante EDX, de los catalizadores preparados así como de los catalizadores comerciales. Además, se presenta la relación atómica Pt:Ru, para el caso de los catalizadores Pt-Ru/C. Como se observa en la tabla, en todos los casos se consiguió una carga metálica de alrededor del 20%. Sin embargo, la relación atómica Pt:Ru obtenida depende del método de síntesis utilizado. Se ha demostrado que muchos factores pueden afectar la composición, morfología y dispersión de los catalizadores PtRu/C cuando se utilizan métodos de reducción en solución [LIU 2006].

Las propiedades morfológicas y cristalográficas de los catalizadores fueron estudiadas por difracción de rayos X. Los patrones de difracción de rayos X se presentan en la Figura 3.5.

Tabla 3.6. *Contenido metálico total y características físicas de los electrocatalizadores soportados en Vulcan XC-72.*

Electrocatalizador	Contenido metálico (wt.%)	Pt:Ru	D (nm)	SA ($m^2 g^{-1}$)	Parámetro de red (Å)
Pt/Vulcan-BM	17.3	---	3.7	76	3.9029
PtRu/Vulcan-BM	20.3	68:32	3.7	88	3.9006
Pt/Vulcan-FAM	19.2	---	3.2	88	3.9158
PtRu/Vulcan-FAM	14.6	66:34	4.5	73	3.9057
Pt/Vulcan-MM	15.3	---	5.8	48	3.9598
PtRu/Vulcan-MM	14.2	57:43	4.0	86	3.8930
Pt/Vulcan-EGM	20.0	---	5.4	52	3.9174
PtRu/Vulcan-EGM	17.4	50:50	4.4	81	3.9006
Pt/C E-TEK	16.3	---	3.0	93	3.9231
PtRu/C E-TEK	20.0	50:50	3.4	105	3.9031

Tabla 3.7. *Contenido metálico total y características físicas de los electrocatalizadores soportados en CNC.*

Catalizador	Contenido metálico (wt.%)	Pt:Ru	D (nm)	SA ($m^2 g^{-1}$)	Parámetro de red (Å)
Pt/CNC-BM	20.0	---	4.7	60	3.9198
PtRu/CNC-BM	17.3	66:34	3.9	91	3.9062
Pt/CNC-FAM	19.3	---	3.8	74	3.9233
PtRu/CNC-FAM	20.4	71:29	4.3	74	3.9031
Pt/CNC-MM	20.1	---	4.8	58	3.9184
PtRu/CNC-MM	20.0	74:26	2.7	117	3.8830
Pt/CNC-EGM	16.2	---	5.6	50	3.9158
PtRu/CNC-EGM	20.0	50:50	3.8	94	3.8981

Todos los catalizadores Pt/C presentaban difractogramas de XRD típicos de la estructura cúbica centrada en las caras (fcc) del Pt, indicando la efectiva reducción del precursor metálico. Se observaron picos a 2θ = 40, 47, 67, 81 y 85º, asociados a los planos cristalinos Pt(111), Pt(200), Pt(220), Pt(311) y Pt(222), respectivamente. En el caso de los catalizadores de Pt-Ru/C no se observaron picos característicos del Ru metálico con estructura hexagonal empaquetada (hcp) ni del óxido de Ru, indicando que

el Ru se había incorporado a la estructura fcc del Pt. Además, en los difractogramas se observó un pico a 2θ = 26.2º, característico del plano (002) del grafito, que se atribuye a las nanoespirales de carbono utilizadas como soporte. En el caso de los catalizadores soportados en Vulcan XC-72R, este pico era menos intenso debido al menor grado de cristalinidad del mismo.

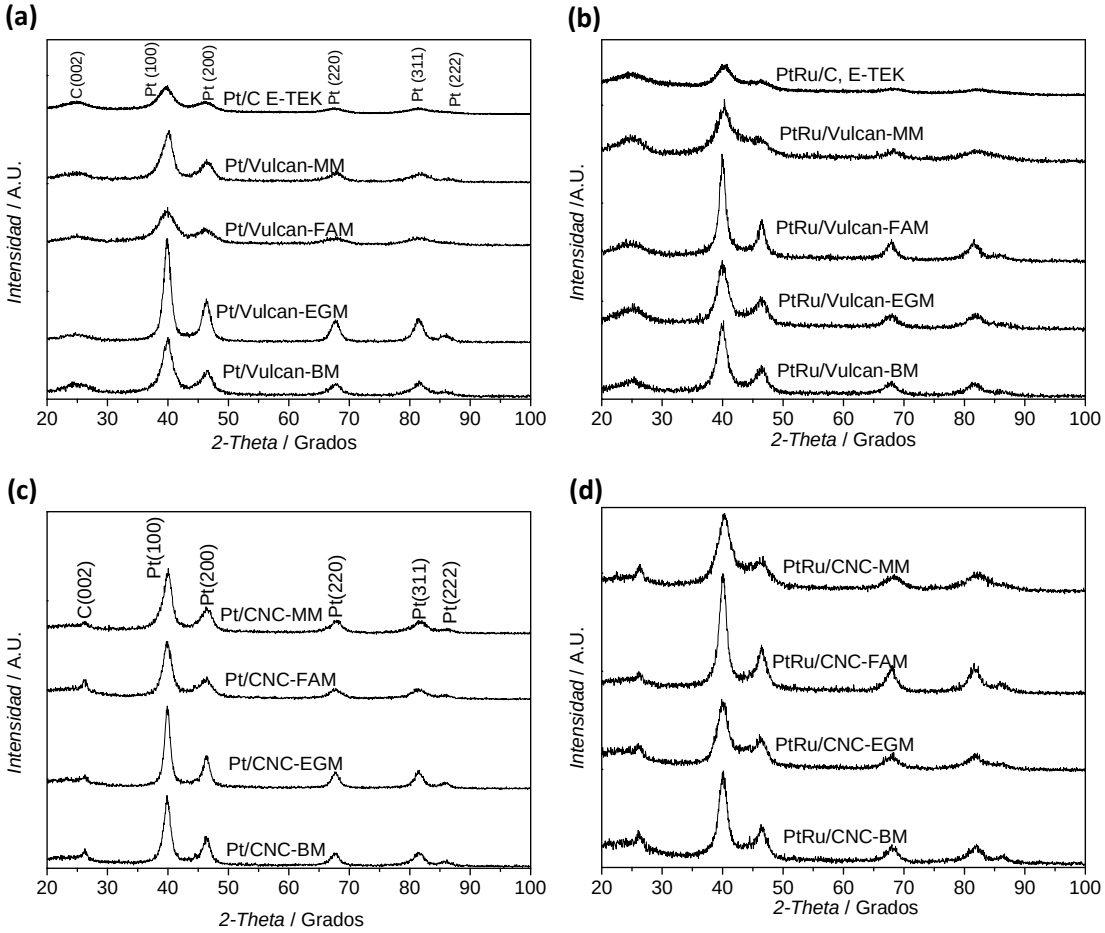

Figura 3.5. *Difractogramas XRD de los electrocatalizadores Pt/Vulcan (a), Pt-Ru/Vulcan (b), Pt/CNC (c) y Pt-Ru/CNC (d).*

De acuerdo con la literatura, el tamaño y la morfología de las partículas metálicas soportadas en materiales de carbono dependen de la interacción metal-soporte [BESSEL 2001, ISMAGILOV 2005]. A partir de los difractogramas de rayos X, se calculó el tamaño medio de cristalito (D) mediante la ecuación Debye-Scherrer, utilizando el pico (220) de la estructura fcc del Pt (Tablas 3.6 y 3.7). A partir de estos resultados se deduce que tanto el método de síntesis como el soporte utilizado tienen una gran influencia en el tamaño de los cristales metálicos. En general, se obtuvieron tamaños mayores usando CNC como soporte que para el caso de los catalizadores soportados en

Vulcan. Sin embargo, estas diferencias no fueron significativas. Esto podría atribuirse a que el Vulcan tiene un gran número de sitios de nucleación, lo que lleva a la formación de partículas más pequeñas. Por el contrario, los carbones de carácter grafitico, como las CNC, tienen un menor número de sitios de nucleación, ya que sólo los defectos en su superficie pueden funcionar como tal, y por lo tanto, se obtienen partículas de Pt de mayor tamaño.

Para el caso de los electrocatalizadores de Pt, los tamaños de partícula más pequeños se obtuvieron mediante FAM y los más grandes mediante EGM. Para los catalizadores de Pt-Ru se obtuvo un tamaño de partícula menor para los catalizadores soportados en Vulcan usando el método BM, mientras que para los soportados en CNC el tamaño de partícula más pequeño se obtuvo con MM.

A partir del cálculo de los tamaños promedio de cristalito de los electrocatalizadores utilizando la ecuación de Scherrer para el pico (220), se concluyó que las nanopartículas de platino presentan tamaños mayores de cristalito que las bimetálicas de Pt-Ru, lo que sugiere que la adición de Ru podría inhibir la aglomeración de las partículas de Pt [ANTOLINI 2001]. Además, el tamaño de los cristales dependía del método de síntesis utilizado así como del soporte.

El área superficial metálica (SA), calculada mediante la ecuación SA ($m^2\ g^{-1}$) = $6\times10^3/\rho d$, donde d es el tamaño medio de partícula metálica en nm, y ρ es la densidad del Pt o de la aleación en su caso considerando, $\rho_{Pt\text{-}Ru}$ ($g\ cm^{-3}$) = $\rho_{Pt}X_{Pt} + \rho_{Ru}X_{Ru}$, donde ρ_{Pt} es la densidad del Pt que tiene un valor de 21.4 $g\ cm^{-3}$ y ρ_{Ru} es 12.3 $g\ cm^{-3}$; y X_{Pt} and X_{Ru} son los porcentajes en masa de Pt y Ru respectivamente. Estos valores se recogen en las Tablas 3.6 y 3.7.

A partir de patrones de difracción de rayos X, se calcularon los parámetros de red cuyos resultados se resumen en las Tablas 4.6 y 4.7. El valor del parámetro de red de los electrocatalizadores Pt/C disminuye con el aumento del tamaño de los cristales. La dependencia de los parámetro de red en el tamaño de los cristales se ha descrito anteriormente en la literatura [SALGADO 2008, ANTOLINI 2006]. Para los electrocatalizadores basados en Pt, estos valores fueron de alrededor de 3.92 Å, que es el correspondiente al valor del platino puro. Los parámetros de red para los electrocatalizadores PtRu/C fueron menores que los correspondientes Pt/C. Este

resultado está de acuerdo con trabajos anteriores, indicando una fuerte interacción Pt-Ru [JIANG 2005].

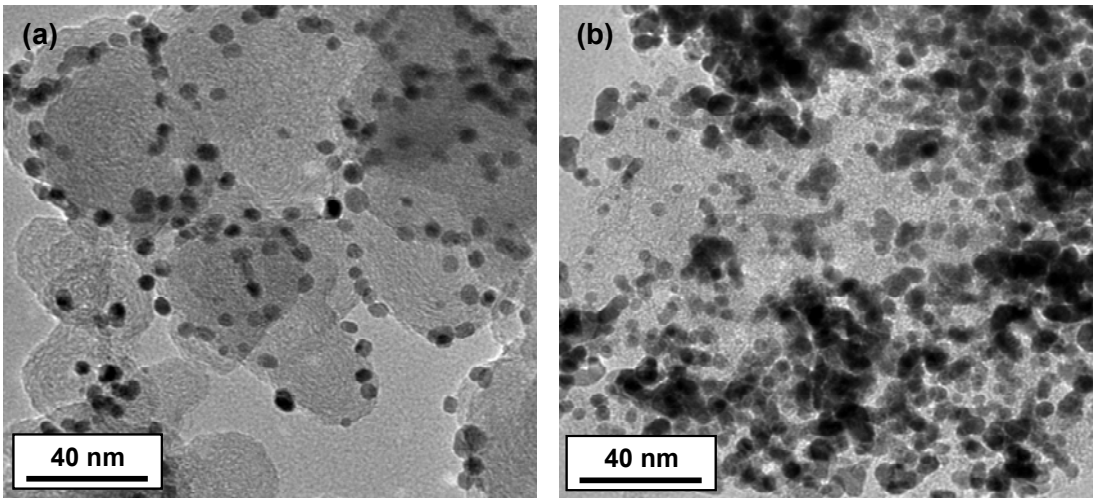

Figura 3.6. Imágenes *TEM de los catalizadores de Pt soportados en: (a) Pt/Vulcan; y (b) Pt/CNC.*

Se eligieron los catalizadores de Pt sintetizados por EGM para estudiar el tamaño de partícula y la dispersión metálica mediante TEM. La Figura 3.6 muestra imágenes TEM obtenidos para los catalizadores de Pt soportados en los distintos materiales de carbono. Al utilizar Vulcan como soporte, se obtuvo una buena distribución de las partículas de platino (a). Sin embargo, se observó la formación de aglomerados de Pt se observó en el caso de aquellos soportados en CNC (b), lo que concuerda con los resultados obtenidos por difracción de rayos X y puede atribuirse a la gran cantidad de grupos oxigenados de este material.

3.4.2.2. Electrocatalizadores de Pd

Se sintetizaron catalizadores de Pd soportados en CNC y Vulcan mediante reducción del correspondiente precursor metálico con borohidruro de sodio. Los difractogramas de rayos X obtenidos para estos catalizadores y el catalizador comercial (Pd/C, E-TEK) se presentan en la Figura 3.7.

Las señales más importantes se observan a 39.4º y 45.6º, correspondientes a los planos (111) y (200) del Pd, mientras que los picos a 67.41º y 81.31º están asociados con los planos (220) y (311), respectivamente. En todos los casos, el pico observado a ~26º se asocia con el soporte de carbono (plano 002 característico del grafito).

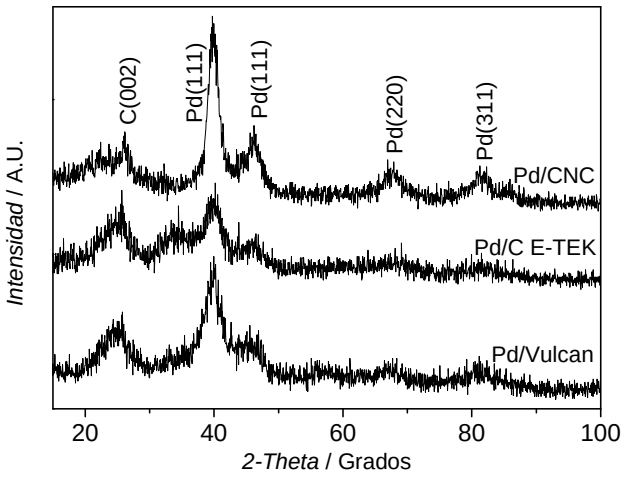

Figura 3.7. *Difractogramas de rayos X para las nanopartículas de Pd soportadas sobre los distintos materiales de carbono.*

El tamaño de cristalito promedio (D) de las partículas de Pd se calculó aplicando la ecuación de Scherrer al pico (220). Las dimensiones de nanopartículas de Pd, así como la carga metálica estimada mediante EDX para todas las muestras, se resumen en la Tabla 3.8. Como se puede observar, se obtuvieron tamaños de partícula menores cuando se usaban CNC como soporte. Esta tendencia sugiere que los grupos oxigenados en la superficie del carbono podrían estar actuando como sitios para la nucleación de las nanopartículas de paladio, aumentando la dispersión total de los catalizadores.

Tabla 3.8. *Contenido metálico y propiedades físicas de los catalizadores.*

Catalizador	**Contenido metálico (wt.%)**	**D (nm)**	**SA*** **($m^2\ g^{-1}$)**
Pd/CNC-BM	20.0	4.6	109
Pd/Vulcan-BM	19.9	5.0	100
Pd/C, E-TEK	20.0	2.0	250

* $\rho_{Pd} = 12.0\ g\ cm^{-3}$

La Figura 3.8 muestra imágenes TEM de los catalizadores Pd/CNC y Pd/Vulcan. Se observó una buena distribución de las partículas de paladio cuando se utilizaron CNC como soporte. Sin embargo, se observó la formación de aglomerados de Pd en el caso de las nanopartículas soportadas sobre Vulcan XC-72. Para ambos soportes, el tamaño de partícula observado correspondía con el calculado mediante la ecuación de Scherrer.

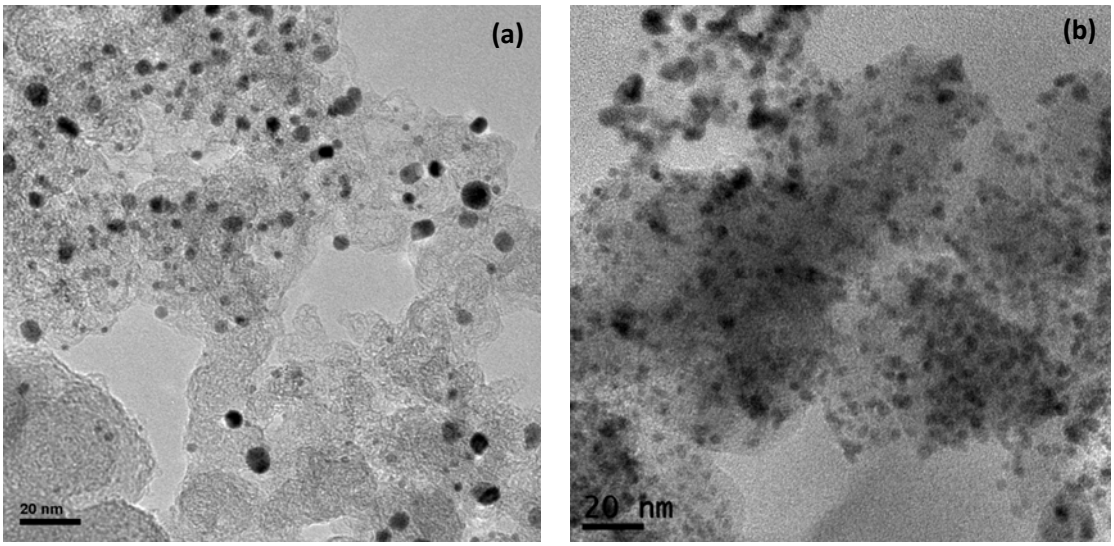

Figura 3.8. *Imágenes TEM de las muestras Pd/CNC (a) y Pd/Vulcan (b). En la escala, la barra corresponde a 20 nm.*

3.4.3. Oxidación de monóxido de carbono

La presencia de CO en el ánodo de las pilas de combustible de electrolito polimérico es un problema en el desarrollo y posterior operación de este tipo de dispositivos. El CO es absorbido en la superficie del metal, desactivando los sitios activos para la reducción del combustible, causando la rápida pérdida de actividad (envenenamiento) del catalizador. Con el fin de establecer la tolerancia al CO de los catalizadores preparados, se llevó a cabo la adsorción y oxidación electroquímica de CO sobre los catalizadores sintetizados. Se adsorbió CO (99.99%) en la superficie del metal por burbujeo de este gas a 1 atm a través del electrolito, para lograr una cobertura de una monocapa de CO. El proceso de adsorción de CO se llevó a cabo a un potencial constante, dependiendo del tipo de nanopartículas metálicas a estudiar. A continuación, para eliminar el CO de la disolución, se realizó una purga con N_2/Ar. Por otra parte, a partir de estos resultados, se determinó el área electroactiva de los catalizadores mediante la integración del pico de oxidación CO_{ad}. En el caso de los catalizadores de Pt y Pt-Ru, se asumió una carga de 420 μC cm^{-2} en la oxidación de una monocapa de CO adsorbido, mientras que este valor fue de 490 μC cm^{-2} para los catalizadores Pd. Estas áreas electroactivos se utilizaron para normalizar las densidades de corriente que se muestran en el texto.

3.4.3.1. Electrocatalizadores de Pt

Las Figuras 3.9 y 3.10 muestran los voltamogramas obtenidos para todos los catalizadores, así como el segundo ciclo después de la oxidación, lo que corresponde al voltamograma en el electrolito de fondo para la superficie limpia. En el segundo ciclo, ocurren en la superficie del electrodo de Pt reacciones interesantes. A potenciales superiores a ~0.8 V, la superficie de Pt se oxida a PtOH y PtOx en el barrido en dirección anódica, mientras que los óxidos de Pt se reducen a la forma de Pt metálico en el barrido catódico. A potenciales menores de ~0.3 V, una vez que la capa de CO se elimina, se observan dos pares de picos debido a la adsorción y desorción de hidrógeno.

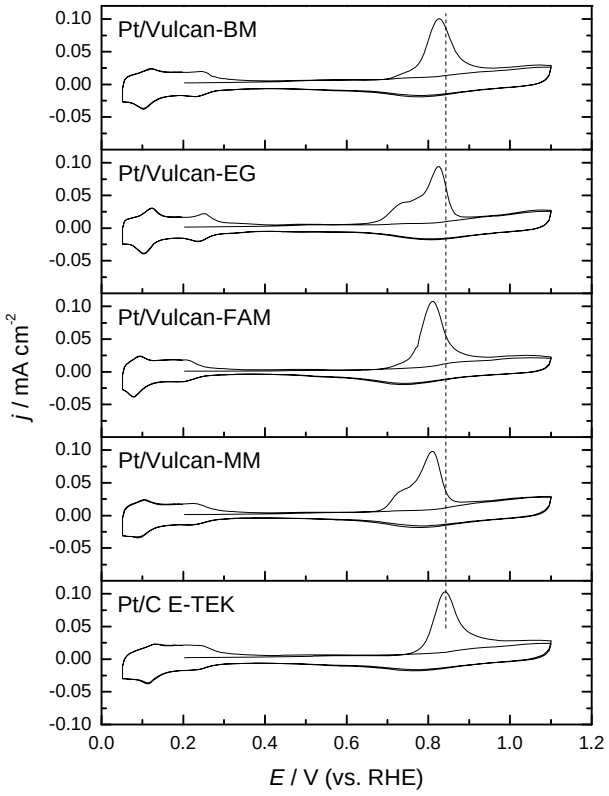

Figura 3.9. *Oxidación de una monocapa de CO para los catalizadores Pt/Vulcan preparados y del catalizador comercial Pt/C de E-TEK en 0.5 M H_2SO_4. E_{ad} = 0.20 V; υ = 0.020 V s^{-1}; T = 25 ºC.*

En el caso de los catalizadores de platino soportados sobre Vulcan (Figura 3.9), no se observaron diferencias significativas entre los catalizadores sintetizados por diferentes métodos. El potencial al que aparece el pico de oxidación de CO_{ad} era el mismo para todos los catalizadores (~0.82 V). Sin embargo, para los catalizadores Pt/Vulcan-BM y Pt/Vulcan-FAM la electrooxidación de CO comenzaba en torno a 0.70

V, mientras que para Pt/Vulcan-EGM y Pt/Vulcan-MM, ésta tuvo lugar a potenciales más negativos. Para éstos dos últimos dos catalizadores, se observó un hombro centrado en 0.72 V, lo que implica que para estos catalizadores parte del CO adsorbido se oxida a potenciales más negativos. A partir de estos resultados, se deduce que el CO se oxida más fácilmente en los catalizadores Pt/Vulcan-EGM y Pt/Vulcan-MM.

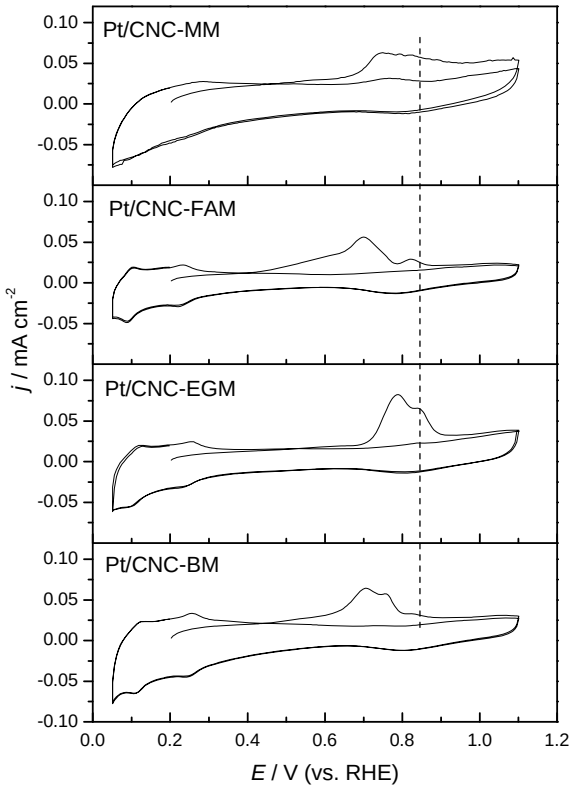

Figura 3.10. *Oxidación de una monocapa de CO para los catalizadores Pt/CNC preparados en 0.5 M H_2SO_4. E_{ad} = 0.20 V; υ = 0.020 V s^{-1}; T = 25 ºC.*

Para los catalizadores Pt/CNC (Figura 3.10), la oxidación de CO se desplaza negativamente en comparación con los catalizadores Pt/Vulcan y el Pt/C de E-TEK. Para estos catalizadores, se observaron en los CVs dos picos de oxidación de CO. Un pico alrededor de 0.84 V, que corresponde al observado para los catalizadores soportados sobre Vulcan XC-72R. Y, además, un segundo pico de oxidación de CO alrededor de 0.70 V para Pt/CNC-BM y Pt/CNC-FAM y alrededor de 0.79 V para Pt/CNC-EG. Esto implica que el CO se oxida más fácilmente en estos materiales. La presencia de este pico adicional a un potencial menor podría ser atribuida a la naturaleza y la química superficial del soporte de carbono, especialmente a los grupos oxigenados superficiales de las CNC [ANTOLINI 2009[b], YU 2009], lo que podría alterar la estructura

electrónica del metal, ayudando al proceso de oxidación de CO y obteniendo catalizadores más tolerantes al CO que los soportados sobre Vulcan.

3.4.3.2. Electrocatalizadores de Pt-Ru

Con la adición de Ru, el área de hidruro del voltamograma disminuye y se produce un desplazamiento del pico de oxidación hacia potenciales más negativos. Además, el potencial al que comienza la oxidación de CO se desplaza negativamente con respecto a los catalizadores correspondientes de Pt. Este hecho podría explicarse por la presencia de Ru, que es más fácilmente electrooxidable y forma especies Ru-OH_{ads} a potenciales más negativos que el Pt, lo que ayuda a oxidar el CO_{ads}, a través de un mecanismo bifuncional [GASTEIGER 1994]. La oxidación de CO en el catalizador comercial PtRu/C de E-TEK comenzaba a 0.52 V vs. RHE y se obtuvo el pico de oxidación a 0.58 V.

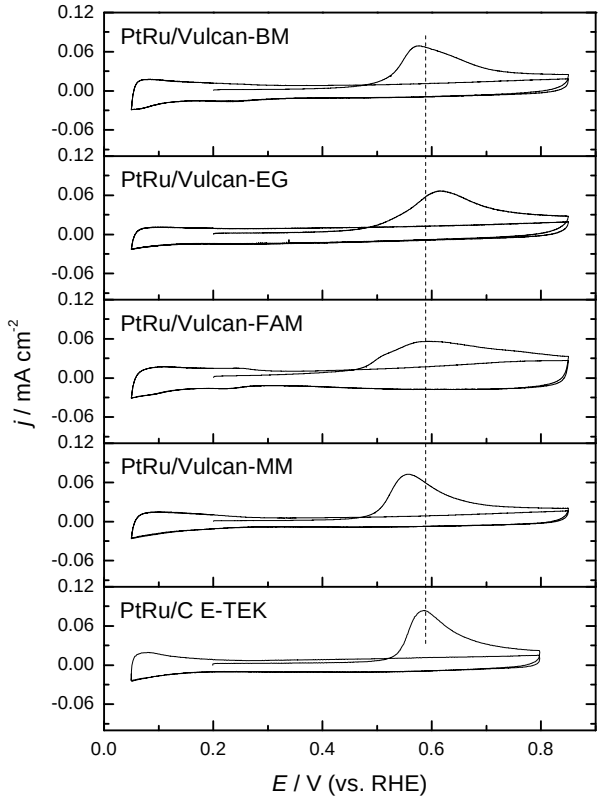

Figura 3.11. *Oxidación de una monocapa de CO adsorbida sobre los catalizadores PtRu/Vulcan en 0.5 M H_2SO_4. E_{ad} = 0.20 V; υ = 0.020 V s^{-1}; T = 25 ºC.*

En los catalizadores soportados sobre nanoespirales de carbono (Figura 3.12), tanto en el potencial de inicio como el potencial de pico se desplaza hacia valores más

negativos, respecto al catalizador comercial. La comparación entre los diferentes catalizadores Pt-Ru es complicada, ya que se obtuvieron distintas relaciones atómicas Pt:Ru. En la literatura, se ha reportado el desplazamiento del potencial de pico de oxidación a potenciales más negativos a medida que aumenta el contenido Ru [CRABB 2004]. Para los catalizadores estudiados en este trabajo, se observó que el CO_{ads} era más fácilmente oxidado en el catalizador sintetizado por el método BM (PtRu/CNC-BM), como ocurrió para los catalizadores de Pt, a pesar de que tenía un contenido de Ru más bajo de lo esperado (relación Pt:Ru = 66:34).

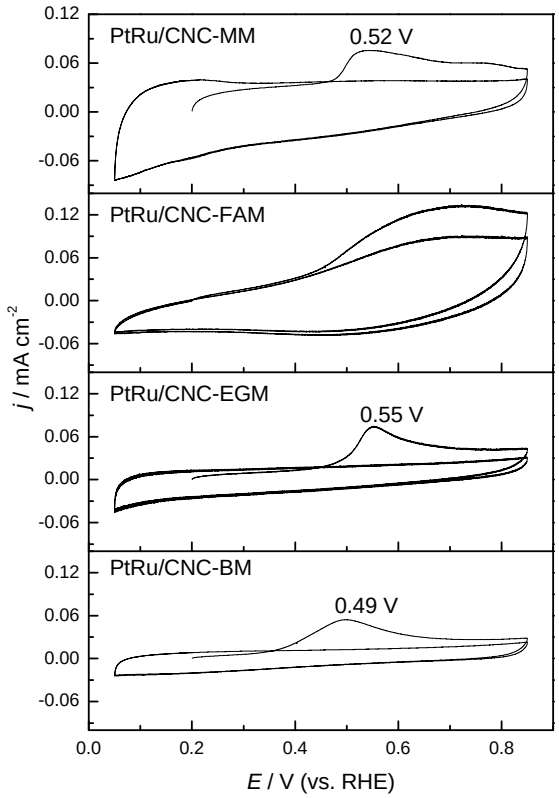

Figura 3.12. *Oxidación de una monocapa de CO adsorbido sobre los catalizadores PtRu/CNC en 0.5 M H_2SO_4. E_{ad} = 0.20 V; υ = 0.020 V s^{-1}; T = 25 ºC.*

3.4.3.3. Electrocatalizadores de Pd

Las características voltamétricas asociadas con la oxidación de CO en los electrocatalizadores Pd/CNC, Pd/Vulcan y Pd/C E-TEK se contrastan en la Figura 3.13. La región de adsorción de hidrógeno aparece bloqueada en el primer ciclo debido al CO adsorbido en la superficie de Pd. La característica principal es el pico de oxidación de CO situado a 0.92 V para el catalizador comercial. La desaparición del pico de CO en el

segundo ciclo, y la reaparición de los picos correspondientes al hidrógeno a potenciales más negativos, indica la eliminación completa del CO en el primer ciclo. La principal característica de la Figura 3.13 se asocia con el potencial de oxidación de CO, que es comparable para los tres catalizadores.

Aunque el Pd posee una tolerancia al CO muy baja, inferior a la de platino puro (el pico de oxidación de CO_{ads} se obtiene a potenciales más positivos), diversas pruebas en PEMFC alimentadas con H_2/CO descritas en la bibliografía, han revelado que la presencia de Pd aumenta la tolerancia al CO de catalizadores de Pt y Pt-Ru [ANTOLINI 2009[a]].

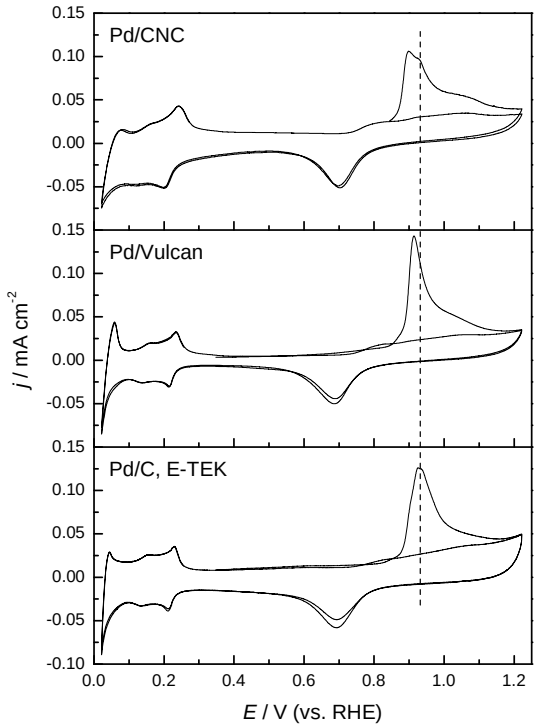

Figura 3.13. *Voltagramas de oxidación de CO obtenidos para los electrocatalizadores Pd/CNC, Pd/Vulcan y Pd/C de E-TEK en 0.5 M H_2SO_4. E_{ad} = 0.056 V; υ = 0.020 V s^{-1}; T = 25 ºC.*

3.4.4. Oxidación de metanol

Aunque se han investigado un gran número de electrodos monometálicos, de estos, el platino parece ser el mejor electrocatalizador para la reacción de oxidación de metanol (MOR) en medio ácido. Sin embargo, la electrooxidación utilizando catalizadores de platino se ve complicada por la adsorción de intermediarios sobre los sitios activos y, por lo tanto, la actividad catalítica disminuye con el tiempo.

La actividad del platino en la reacción MOR es baja y por lo tanto, no es adecuado para su uso en pilas de combustible de metanol directo (DMFC). Se ha demostrado que la aleación de Pt con Ru, Sn o Mo proporciona electrocatalizadores anódicos más tolerantes al CO, con un mejor rendimiento. Entre ellos, las aleaciones Pt-Ru han demostrado ser las más eficaces. La presencia de Ru facilita la oxidación de las especies de CO y, en consecuencia, aumenta la actividad electrocatalítica de oxidación del metanol. Por otro lado, Pd es completamente inactivo durante la electrooxidación de metanol en soluciones ácidas.

La actividad de los catalizadores para la oxidación electroquímica de metanol fue estudiada con el fin de determinar su viabilidad como electrocatalizadores para pilas de combustible de metanol directo (DMFC). Las Figuras 3.14 y 3.15 ilustran los voltamogramas cíclicos registrados a temperatura ambiente para los catalizadores estudiados en una solución de CH_3OH 2 M + H_2SO_4 0.5 M.

Los catalizadores de Pt presentaron el típico comportamiento irreversible de la electrooxidación de metanol, el potencial de comienzo de la oxidación era en torno a 0.60 V vs RHE para todos ellos. Watanabe *y cols*. [WATANABE 1989] examinaron la influencia de la dispersión de los cristales de platino en la oxidación electrocatalítica de metanol, afirmando que no se producían efectos por el tamaño de los cristales (incluso para cristales tan pequeños de 1.4 nm de diámetro). Por esta razón, los resultados son totalmente comparables. La mayor densidad de corriente se logró con el catalizador Pt/CNC-BM durante el barrido positivo a un potencial de alrededor de 0.98 V, correspondiente a la oxidación del metanol. Este resultado podría estar asociado a la mayor tolerancia al CO de este catalizador, como se ha mostrado anteriormente (sección 3.4.3.1). Además, se observó otro pico alrededor de 0.85 V durante el barrido catódico, que se atribuye a la oxidación de los compuestos intermedios formados durante la oxidación del metanol.

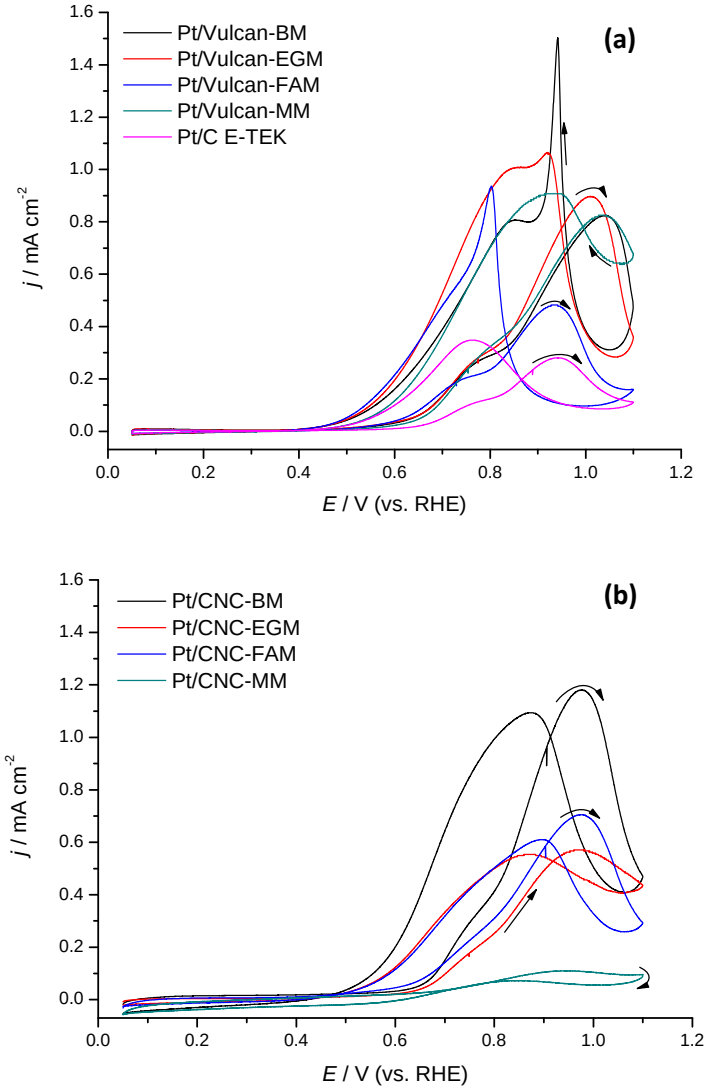

Figura 3.14. *Voltagramas cíclicos de los electrocatalizadores de Pt/Vulcan (a) y Pt/CNC (b) en una solución 2 M CH_3OH+ 0.5 M H_2SO_4. υ = 0.02 V s^{-1}; T = 25 ºC.*

Para los catalizadores de Pt-Ru, el potencial al que tenía comienzo la oxidación de metanol variaba entre 0.3 y 0.5 V, pero siempre a potenciales más negativos que para los correspondientes catalizadores de Pt. En este caso, el catalizador PtRu/CNC-MM mostró la mayor actividad para la oxidación de metanol. Para este catalizador, la densidad de corriente creció más rápido que para el comercial PtRu/C E-TEK. Se observó que este catalizador (PtRu/CNC-MM) mostraba una densidad de corriente aproximadamente 5 veces mayor que el catalizador comercial a un potencial de 0.6 V. Este resultado está de acuerdo con los resultados publicados por Jusys *y cols*. [JUSYS 2003] que confirman que a potenciales positivos (0.6-0.5 V) los catalizadores ricos en Pt son más activos en la reacción MOR.

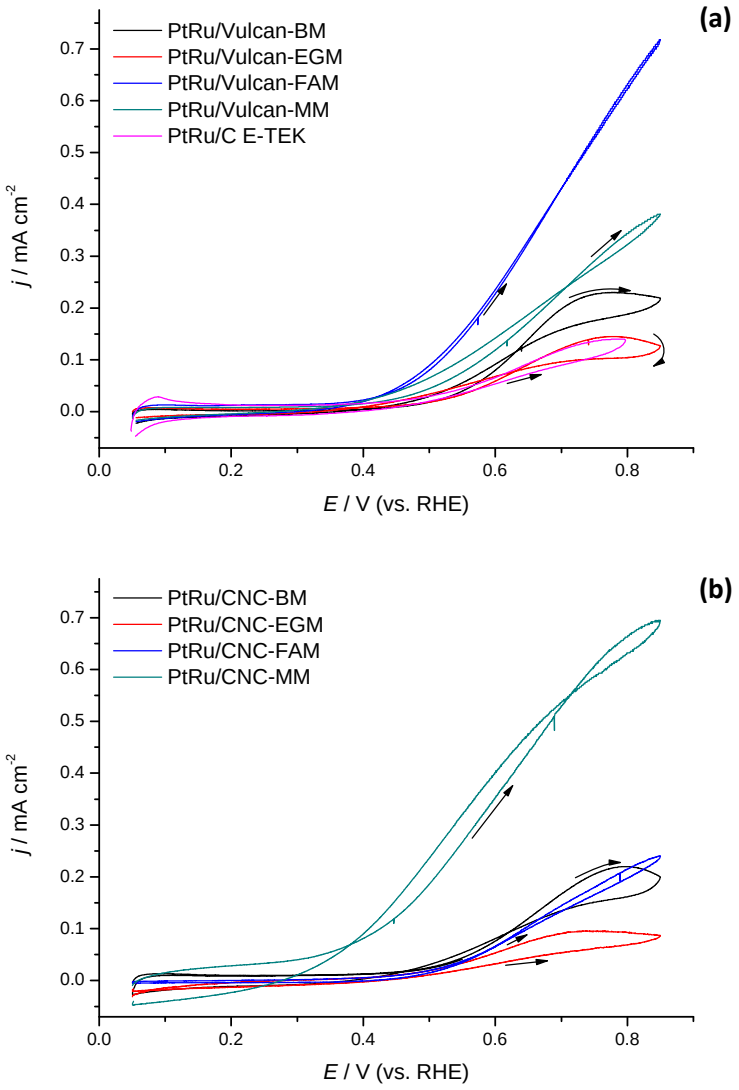

Figura 3.15. *Voltagramas cíclicos de los electrocatalizadores de Pt-Ru/Vulcan (a) y PtRu/CNC (b) en una solución 2 M CH_3OH+ 0.5 M H_2SO_4. υ = 0.02 V s^{-1}; T = 25 ºC.*

Las Figuras 3.16 y 3.17 muestran las densidades de corriente potenciostáticas, normalizadas por la superficie electroactiva, en función del tiempo a 0.60 V vs RHE. En todos los casos, se consiguió una estabilización de la actividad en un corto período de tiempo. Se puede observar que para los catalizadores de Pt-Ru, los valores alcanzados fueron superiores a los de los correspondientes catalizadores Pt. El aumento de la respuesta se produjo en el orden: Pt/CNC-MM < Pt/CNC-FAM < PtRu/CNC-EGM < Pt/CNC-EGM ~ Pt/C E-TEK < PtRu/CNC-FAM < Pt/CNC-BM ~ Pt/Vulcan-MM < PtRu/Vulcan-BM < PtRu/CNC-BM < Pt/Vulcan-BM < Pt/Vulcan-EGM < PtRu/Vulcan-EGM < Pt/Vulcan-FAM < PtRu/Vulcan-MM ~ PtRu/C E-TEK <

PtRu/Vulcan-FAM < PtRu/CNC-MM. Estos valores siguieron la misma tendencia que la observada mediante voltamperometría cíclica.

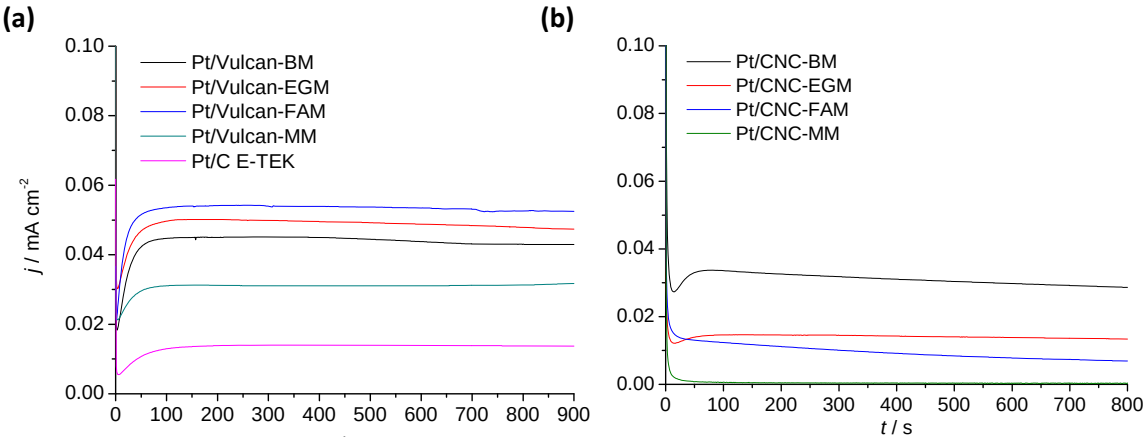

Figura 3.16. *Curvas cronoamperométricas para los catalizadores Pt/Vulcan (a) y Pt/CNC (b) registrada en 2 M CH_3OH + 0.5 M H_2SO_4 a E = 0.60 V y temperatura ambiente.*

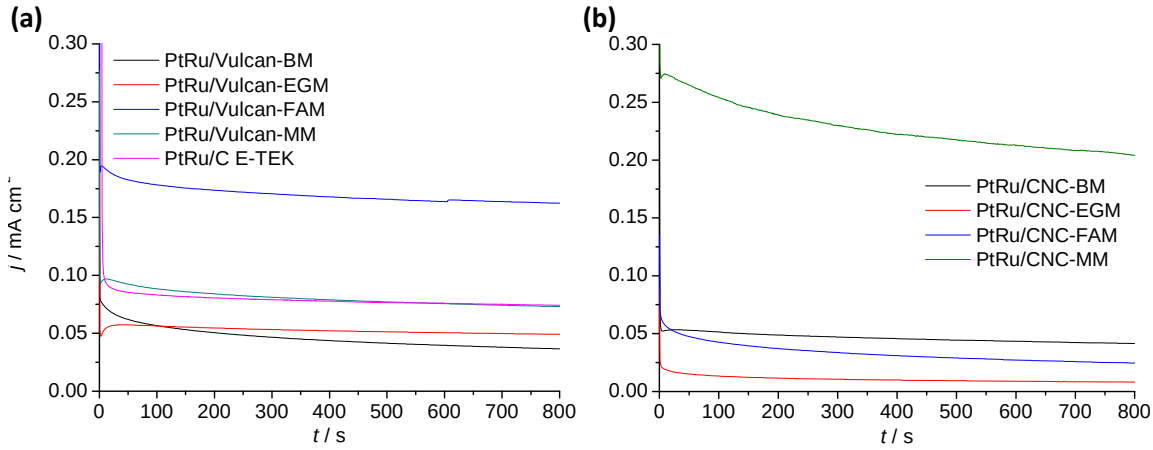

Figura 3.17. *Curvas cronoamperométricas para los catalizadores PtRu/Vulcan (a) y PtRu/CNC (b) registrada en 2 M CH_3OH + 0.5 M H_2SO_4 a E = 0.60 V y temperatura ambiente.*

A pesar de que el uso de las nanoespirales de carbono facilita la oxidación de CO (sección 3.4.3.1), por regla general, se puede observar que el comportamiento de los catalizadores para la oxidación de metanol no mejora notoriamente. Esto podría explicarse, desde el punto de vista del mecanismo de reacción de la oxidación de metanol (ver Figura 1.5), afirmando que la etapa limitante en esta reacción no es la oxidación del CO_{ads} a CO_2, sino la oxidación de los intermediarios de reacción formados.

Para efectuar un estudio más preciso, se procedió a efectuar un análisis comparativo entre los catalizadores Pt/CNC-BM, Pt/Vulcan-FAM, Pt/C E-TEK,

PtRu/CNC-MM, PtRu/Vulcan-FAM y PtRu/C E-TEK del mecanismo de oxidación del metanol mediante la técnica de espectrometría de masas diferencial electroquímica (DEMS). Los análisis DEMS permiten la detección de productos volátiles y gaseosos así como los intermediarios generados en las reacciones electroquímicas con buena sensibilidad.

La formación de ácido fórmico (m/z = 46) durante la oxidación de metanol no puede ser directamente controlada mediante DEMS, debido a la superposición del espectro de masas con el del CO_2^- (m/z = 45). Sin embargo, el ácido fórmico reacciona con el metanol formando metilformiato, por lo tanto, la formación de ácido fórmico en la MOR se puede seguir mediante el control de la corriente iónica m/z = 60.

La formación de formaldehído en la MOR no puede ser controlada por DEMS ni directa ni indirectamente. La imposibilidad del control directo es debida a la superposición del espectro de masas del formaldehído con el del metanol a m/z = 28-30. Esto indirectamente es debido a que la reacción entre el formaldehído y metanol para formar dimetoximetano sólo se produce a temperaturas elevadas y/o altas concentraciones de metanol y, por lo tanto, no puede ser utilizado como un indicador de formaldehído a temperatura ambiente y bajas concentraciones de metanol.

Las Figuras 3.18 y 3.19 muestran los VCs (línea negra) y las correspondientes señales VCEMs (Voltamograma Cíclico de Espectrometría de Masas) para seguir la producción de CO_2 (m/z = 44) y de ácido fórmico (medido a través de la señal de formación de metilformiato m/z = 60), durante la electrooxidación de metanol. Además, en esta figura se incluye la corriente faradaica esperada para el 100 % de conversión de metanol a CO_2 (línea roja), calculada a partir de la señal m/z = 44 una vez efectuada la calibración del DEMS. La diferencia en el área entre las corrientes experimentales (líneas negras) y teóricas (líneas rojas) corresponde a la carga extra asociada con la formación de productos distintos a CO_2 (hay que señalar que mediante DEMS es posible establecer, aunque indirectamente, la producción de ácido fórmico, pero no de formaldehído).

La baja concentración de alcohol utilizada en estos experimentos se debe al hecho de que, a concentraciones más altas, se observó un aumento continuo de la señal de CO_2 (m/z = 44), lo que hacía complicado el análisis cuantitativo de los resultados.

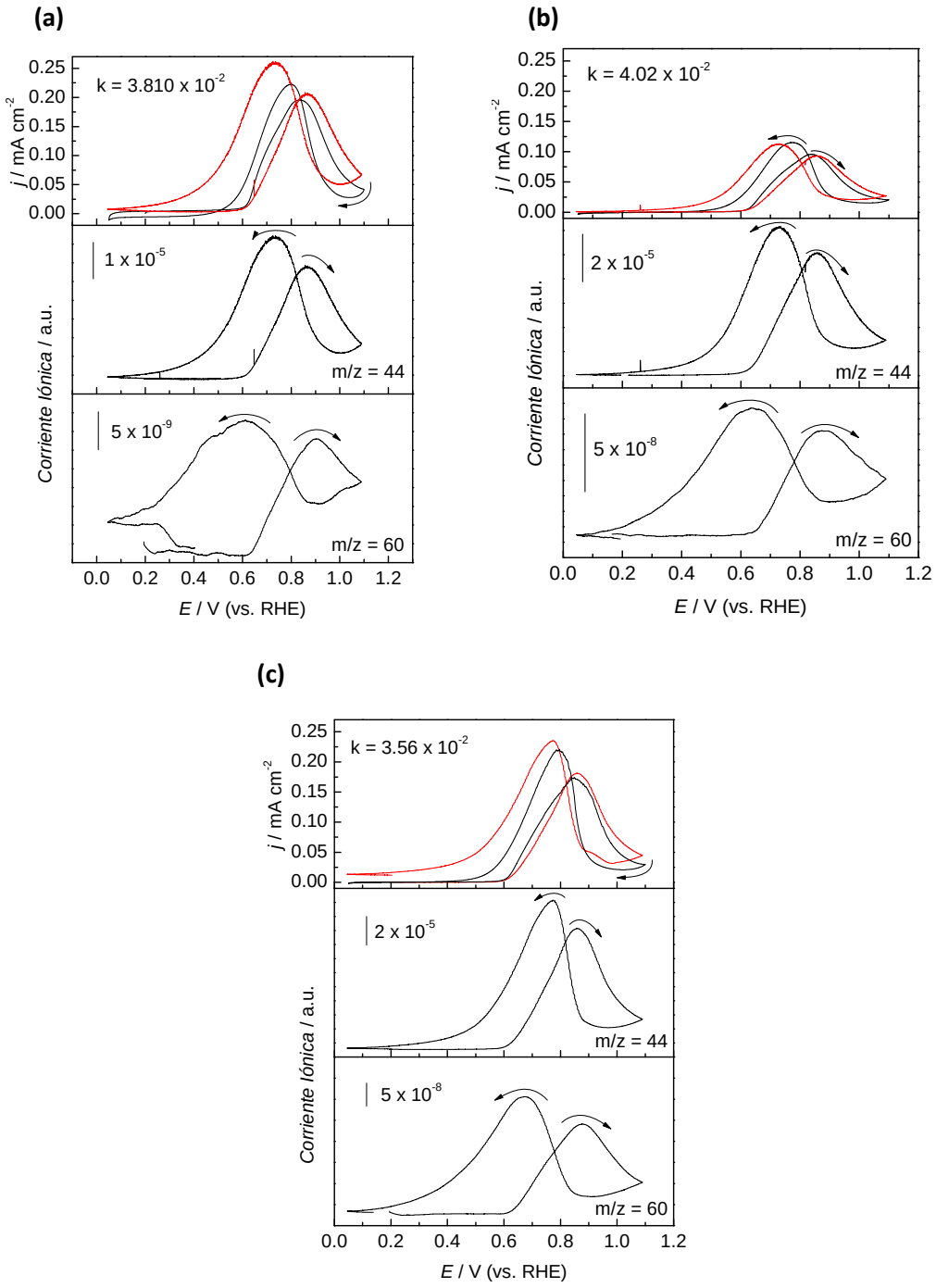

Figura 3.18. *VCs y VCEMs para la oxidación de metanol 0.5 M en H_2SO_4 0.5 M para los electrodos Pt/CNC-BM (a), Pt/Vulcan-FAM (b) y Pt/C E-TEK (c). υ = 0.001 V s^{-1}; T = 25 ºC.*

En el caso de los electrocatalizadores de platino, la corriente iónica m/z = 44 (paneles centrales) por lo general sigue la reacción faradaica de oxidación de metanol

(MOR) en curso, teniendo en cuenta la constante de tiempo de la celda DEMS. Una comparación de la corriente faradaica (línea de negra, paneles superiores) y de la corriente iónica m/z = 44, muestra que la corriente depende de la dirección del barrido de potencial, con corrientes másicas relativamente mayores en el barrido catódico. Los VCEMs para la formación de metilformiato (m/z = 60) también siguen la señal faradaica. Sin embargo, la separación entre el barrido de potencial en dirección positiva y negativa es mayor en comparación con la señal m/z = 44, a pesar de que la constante de tiempo es la misma. Esta desviación se explica por la relativa reacción lenta de formación de éster entre el ácido fórmico y el metanol en comparación con la formación instantánea de CO_2 [JUSYS 2003].

En cuanto a los electrocatalizadores de PtRu, la formación de CO_2 comienza alrededor de 0.4 V, es decir, unos 200 mV más negativos que en el caso de los catalizadores de Pt. Mientras que la formación de metilformiato comienza en 0.5 V, que es el mismo potencial que en el caso del Pt.

Una comparación más precisa entre los resultados para los diferentes electrodos y condiciones se puede hacer a partir de la integración de las corrientes faradaicas e iónicas durante el barrido en sentido anódico, a partir de los VCs y los VCEMs del CO_2, respectivamente. El promedio de la eficiencia para cada catalizador se calcula sobre la base de los valores de estas integrales y se resumen en la Tabla 3.9. Se observa que los electrodos presentan eficiencias de conversión a CO_2 similares (~ 100%). Los altos valores de eficiencia de conversión a CO_2 están relacionados con la adsorción y la re-oxidación de subproductos. Sin embargo, los electrodos sintetizados mediante el uso de CNC como soporte muestran una menor eficiencia de conversión a CO_2, que se asocia a una mayor formación de subproductos (por ejemplo, ácido fórmico y formaldehído).

Por tanto, se puede deducir que la oxidación de metanol sobre los catalizadores de Pt/CNC ocurre mediante la vía de producción de intermedios de reacción. Las interacciones Pt-CNC favorecen la oxidación de CO_{ads}, mientras que no ayudan en la reacción de oxidación de los intermediarios, por lo que las densidades de corriente obtenidas son menores (Figura 3.16).

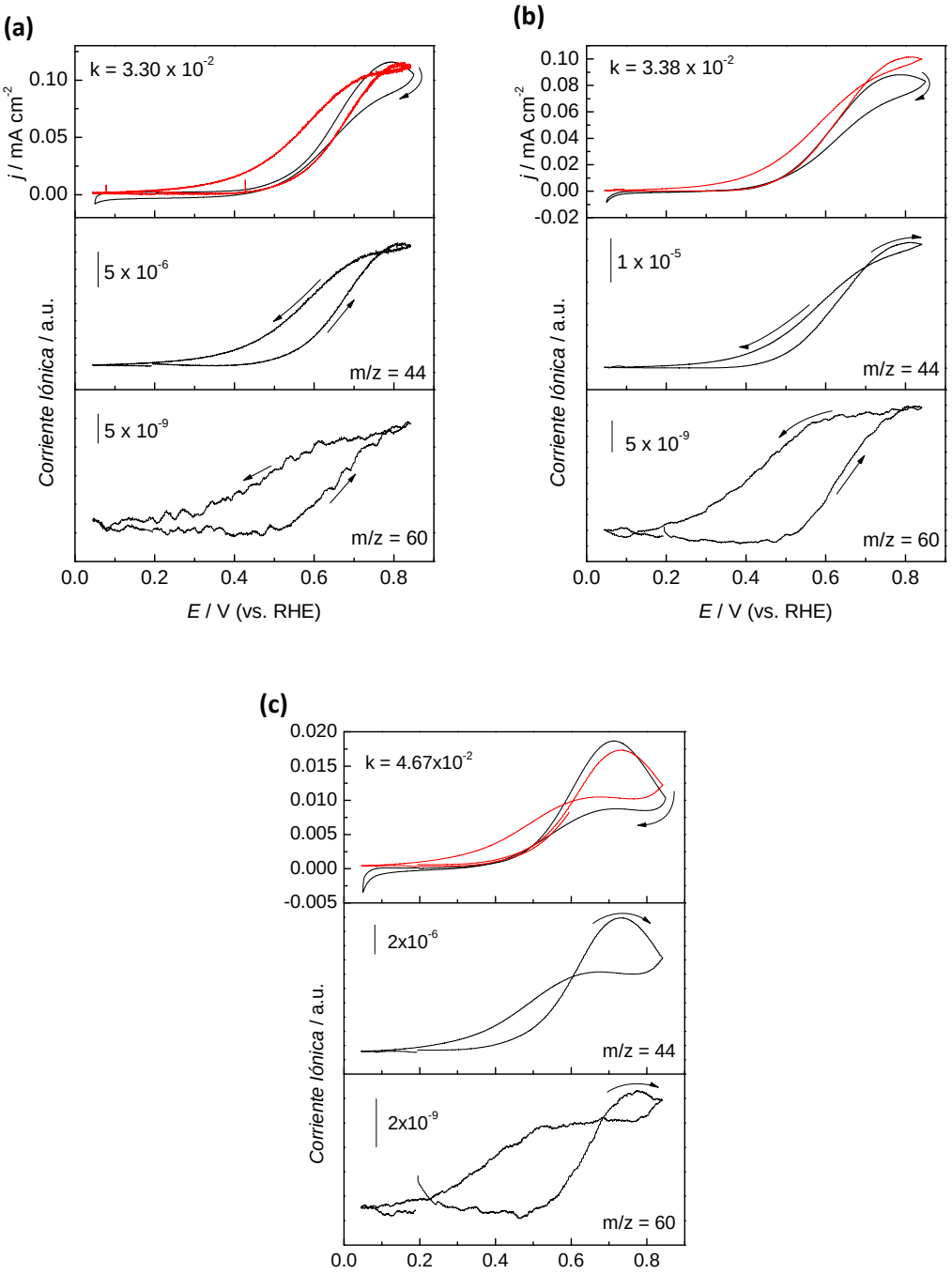

Figure 3.19. *CVs y VCEMs para la oxidación de metanol 0.5 M en H_2SO_4 0.5 M en los electrodos PtRu/CNC-MM (a), PtRu/Vulcan-FAM (b) y PtRu/C E-TEK (c). υ = 0.001 V s^{-1}; T = 25 ºC.*

Para el caso de los catalizadores de PtRu/CNC, sin embargo, la densidad de corriente alcanzada después de 800 s en los experimentos en condiciones potenciostáticas (deducida de la Figura 3.17) es mayor. Por lo que se puede deducir que

el uso de los CNC como soporte de nanopartículas de Pt-Ru, facilita la oxidación de los intermedios de reacción.

Tabla 3.9. *Eficiencia media a CO_2 calculada.*

Muestra	Eficiencia de conversión a CO_2 (%)
Pt/CNC-BM	97
PtRu/CNC-MM	85
Pt/Vulcan-FAM	100
PtRu/Vulcan-FAM	100
Pt/C E-TEK	100
PtRu/C E-TEK	94

3.4.5. Oxidación de etanol

Hoy en día, es difícil establecer el catalizador adecuado para la oxidación electroquímica de etanol. Además del platino, se han estudiado otros metales como el oro, el rodio o el paladio, mostrando algún tipo de actividad. Sin embargo, sólo los materiales a base de platino muestran apropiadas corrientes de oxidación, especialmente en medio ácido [TSIAKARAS 2007], pero la eficiencia de operación de las DEFCs con estos catalizadores es todavía insuficiente para aplicaciones prácticas.

Por estos motivos, los catalizadores de Pt soportados en Vulcan y en CNC se evaluaron en la oxidación del etanol. En la Figura 3.20 se muestran los voltagramas cíclicos registrados en una solución CH_3CH_2OH 2 M + H_2SO_4 0.5 M a temperatura ambiente.

Las curvas de todos los catalizadores muestran un aumento en la corriente alrededor de 0.50 V durante el barrido positivo de potencial, la aparición de un pico anódico depende de los distintos catalizadores. En el barrido catódico, de observó de nuevo una contribución anódica, dependiendo el potencial del catalizador.

Como se puede observar, el inicio de la electrooxidación de etanol se produjo entre 0.50 y 0.64 V en función del catalizador. Para el mismo material, se encontraron diferencias significativas en las densidades de corriente alcanzadas por los catalizadores preparados siguiendo distintos métodos de síntesis.

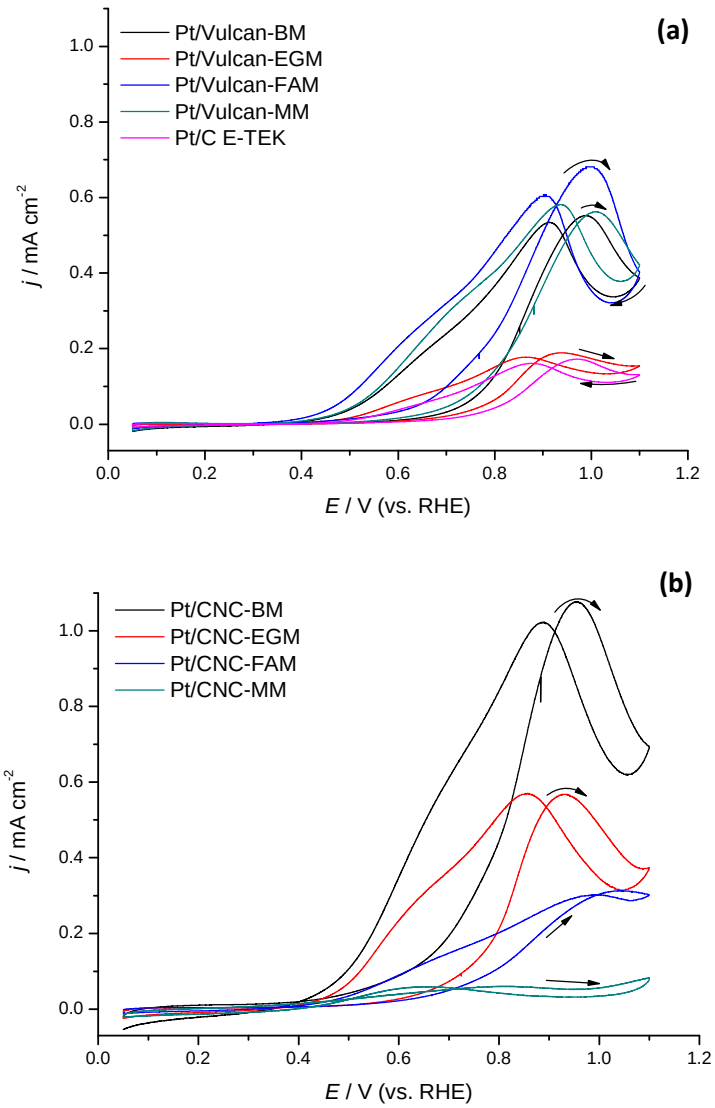

Figura 3.20. *Voltagramas cíclicos de los electrocatalizadores de Pt/Vulcan (a) y Pt/CNC (b) en una solución 2 M CH_3CH_2OH + 0.5 M H_2SO_4. υ = 0.02 V s^{-1}; T = 25 ºC.*

Con el fin de determinar el rendimiento de los catalizadores hacia la electrooxidación de etanol bajo condiciones potenciostáticas, se registraron curvas corriente-tiempo a 0.60 V y 25 ºC durante 850 s en la misma solución (Figura 3.21). Los catalizadores de Pt soportados sobre CNC sintetizados por BM y EGM presentaban una mayor densidad de corriente. Estos valores incrementaban en el orden: Pt/CNC-MM < Pt/C E-TEK < Pt/Vulcan-EGM < Pt/Vulcan-BM < Pt/Vulcan-FAM = Pt/CNC-FAM < Pt/CNC-EGM < Pt/CNC-BM. Sin embargo, en todos los casos, se logró un rendimiento estable en un corto período de tiempo. Estos resultados confirman que los catalizadores de Pt/CNC son notablemente más activos en la electrooxidación de etanol

que los catalizadores soportados sobre Vulcan XC-72R, comúnmente empleados para los electrodos técnicos de DAFCs.

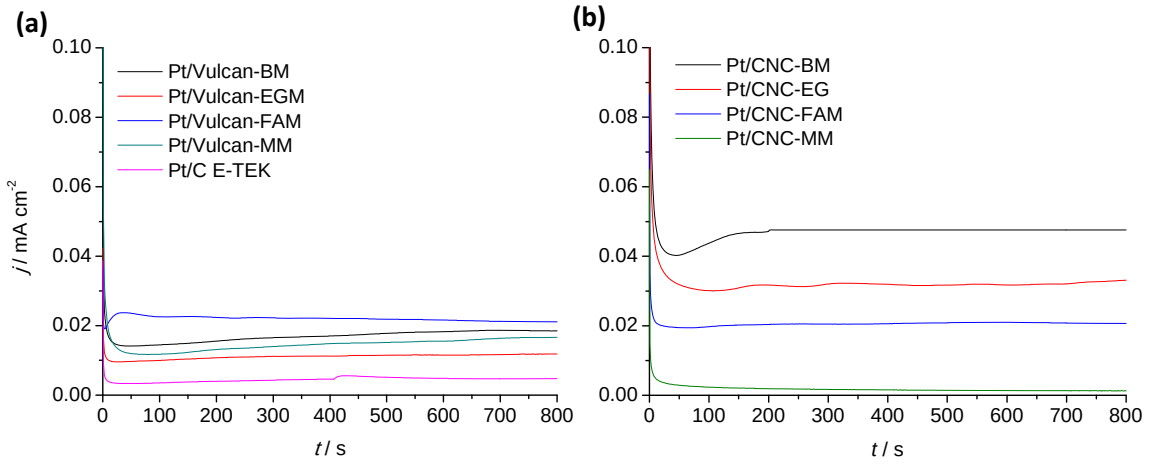

Figure 3.21. *Curvas cronoamperométricas para los electrocatalizadores Pt/Vulcan (a) y Pt/CNC (b) registradas en 2 M CH_3CH_2OH + 0.5 M H_2SO_4 a E = 0.60 V y temperatura ambiente.*

En general, los electrocatalizadores que utilizaban CNC como soporte presentaban un mejor comportamiento en la oxidación del etanol. Durante la oxidación del etanol, la etapa limitante es la rotura del enlace C-C y no la oxidación del CO absorbido. Por tanto, el aumento de las densidades de corriente mediante el uso de CNC se podría atribuir a que las interacciones Pt-CNC ayudan en este proceso.

A pesar de numerosos estudios, el mecanismo de reacción de la electrooxidación de etanol (EOR) sigue siendo poco claro e incluso contradictorio. La electrooxidación de etanol se desarrolla mediante un mecanismo complejo de múltiples pasos que implica una serie de productos intermedios adsorbidos y también da lugar a diferentes subproductos de la oxidación incompleta [HITMI 1994]. El CO adsorbido, y los residuos hidrocarbonados C1 y C2 han sido identificados como los principales intermediarios por medio de espectroscopia infrarroja in situ y DEMS [IWASITA 1994, SCHMIEMANN 1994], mientras que el acetaldehído y ácido acético se han detectado como los principales subproductos utilizando espectroscopia infrarroja, cromatografía iónica y líquida [HITMI 1994, LAMY 2001].

En este caso, los análisis DEMS se han utilizado para proporcionar información sobre la naturaleza de los intermediarios y los productos de oxidación de los electrocatalizadores. Debido a las interferencias producidas entre las corrientes iónicas

de los principales productos de oxidación del etanol, CO_2^+ y CH_3CHO^+, obtenidos ambos en m/z = 44, la formación de dióxido de carbono y acetaldehído es monitoreada a través de las señales m/z = 22 (CO_2^{++}) y m/z = 29 (COH^+), respectivamente. Sin embargo, la señal para la producción de CO_2 era muy baja, por lo que el análisis cuantitativo no fue posible.

Además, se siguió la relación m/z = 15 correspondiente al metano y/u otro tipo de fragmentos iónicos de la formación de acetaldehído (CH_3^+).

En la Figura 3.22 se pone de manifiesto que la respuesta electroquímica de las señales m/z = 15, 29 y 44 son similares y pueden estar relacionadas con la formación de acetaldehído. Todos ellas comienzan a un potencial de ~0.40 V, simultáneamente con el inicio de la oxidación del etanol. Por otro lado, la señal para la formación de CO_2 (m/z = 22) era muy baja y se producía a potenciales más positivos ~0.5 V en la dirección de barrido anódica. Este hecho podría explicarse de acuerdo con el mecanismo de la electrooxidación de etanol en los sitios de Pt [CAMARA 2004]. Según esto, el acetaldehído se readsorbe en el Pt como especies acetilo y se disocia en fragmentos CH_x y monóxido de carbono que pueden ser completamente oxidados a CO_2 a potenciales mayores.

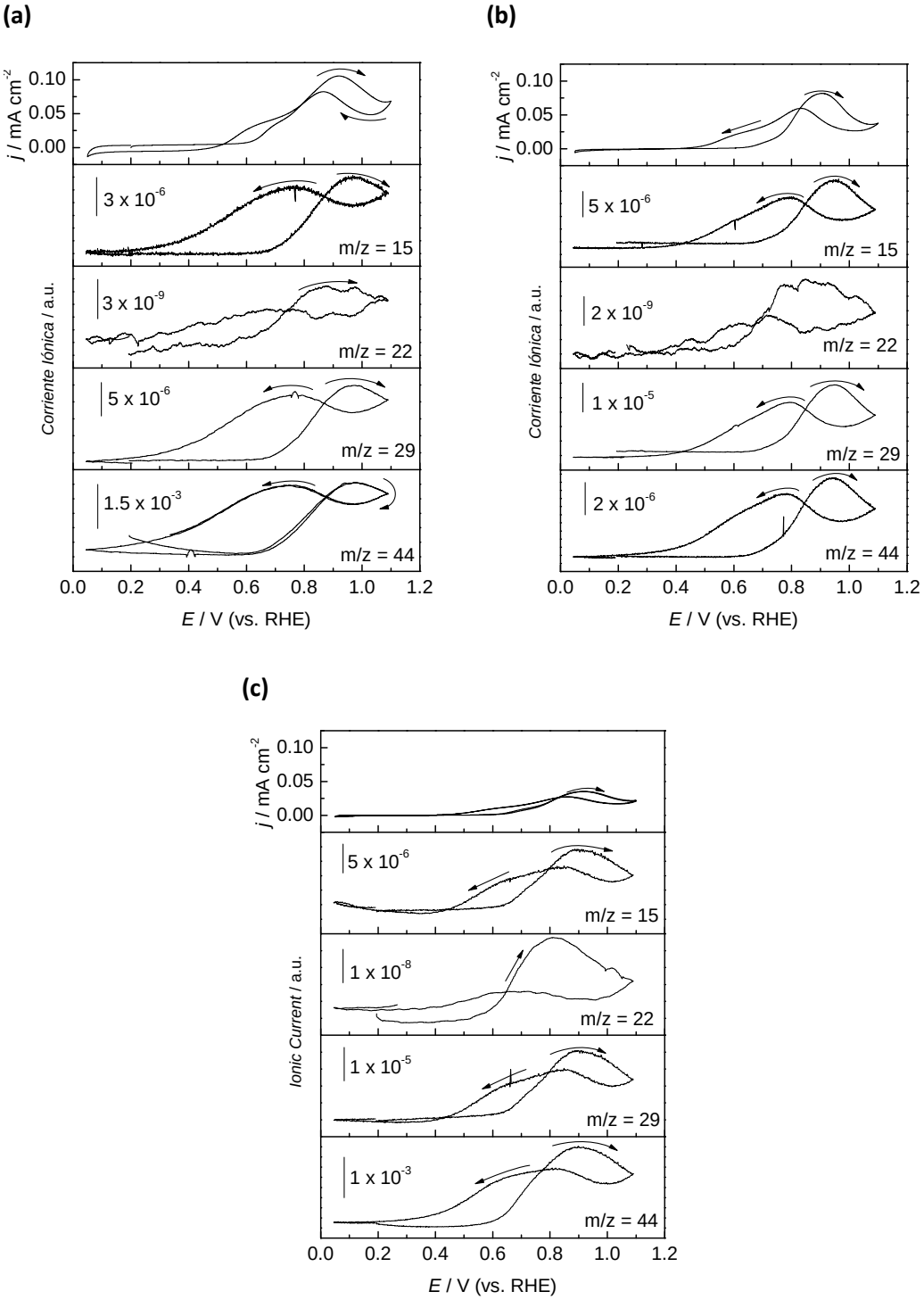

Figura 3.22. *VCs y VCEMs para la oxidación de etanol 0.5 M en H_2SO_4 0.5 M en los electrocatalizadores Pt/CNC-BM (a), Pt/Vulcan-FAM (b) y Pt/C E-TEK (c). υ = 0.001 V s^{-1}; T = 25 ºC.*

3.4.6. Oxidación de ácido fórmico

El ácido fórmico ha sido investigado como un combustible alternativo al hidrógeno y al metanol en PEMFCs. El ácido fórmico es un electrolito líquido fuerte, por lo tanto, se espera que facilite el transporte tanto electrónico como de protones en el compartimento del ánodo de la pila de combustible.

Los catalizadores nanoestructurados de Pt se envenenan debido a la adsorción del CO producido como intermediario en la reacción de electrooxidación de ácido fórmico. Esto sugiere, que es probable que la descomposición de HCOOH en nanopartículas de platino se produzca a través de un mecanismo de doble vía [CAPON 1973]. Sin embargo, esta descomposición sobre Pd se produce principalmente a través de una vía directa, evitando la formación de CO como intermediario. Por estas razones, sólo los electrocatalizadores de paladio sintetizados se probaron para la oxidación de ácido fórmico.

La oxidación de ácido fórmico se caracterizó por voltamperometría cíclica y cronoamperometría. Los voltamogramas cíclicos se registraron en HCOOH 2 M + H_2SO_4 0.5 M a una velocidad de barrido de 0.02 V s^{-1}. Las curvas potenciostáticas de densidad de corriente-tiempo (*j*-*t*) se registraron en la misma solución a 0.60 V durante 900 s.

Los voltamogramas cíclicos asociados a la oxidación de ácido fórmico en los catalizadores Pd/CNC, Pd/Vulcan y E-TEK se contrastan en la Figura 3.23. Los tres catalizadores presentan un pico ancho en el barrido anódico y una caída de corriente con la formación del óxido de paladio, que inhibe la oxidación de ácido fórmico. En el barrido catódico, una vez que la superficie de Pd se recupera, el ácido fórmico es de nuevo oxidado; obteniéndose densidades de corriente similares que en el barrido anódico, lo que indica un alto grado de tolerancia hacia el envenenamiento de los electrodos [MIYAKE 2008]. Para el catalizador Pd/Vulcan se obtuvieron densidades de corriente más bajas que en los otros dos electrocatalizadores.

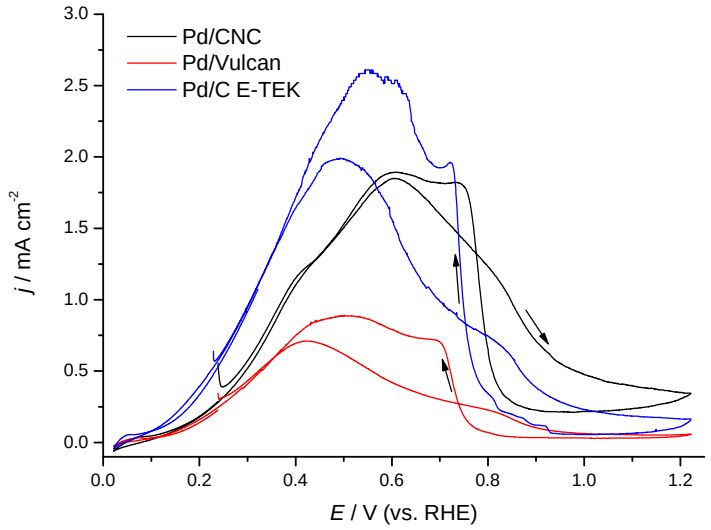

Figura 3.23. *Voltagramas cíclicos para los catalizadores Pd/CNC, Pd/Vulcan y Pd/C de E-TEK en 2 M HCOOH + 0.5 M H_2SO_4. υ = 0.020 V s^{-1}; T = 25 ºC.*

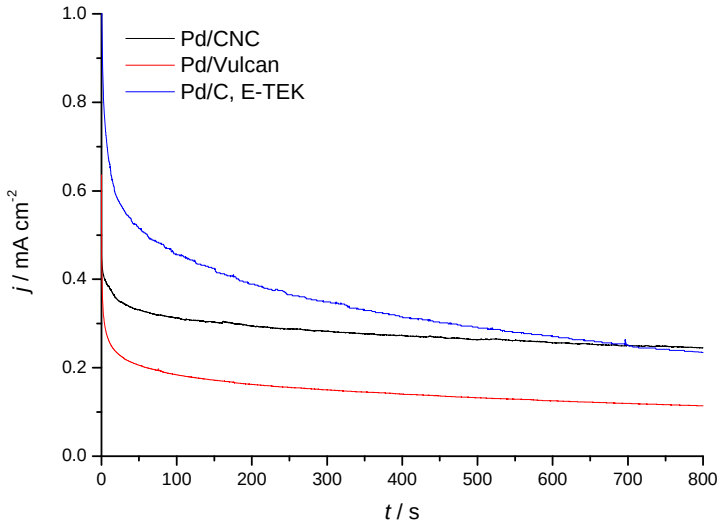

Figura 3.24. *Curvas cronoamperométricas para los catalizadores de Pd/C, registradas en 2 M HCOOH + 0.5 M H_2SO_4 a E = 0.60 V y temperatura ambiente.*

Los transitorios a 0.6 V en presencia de HCOOH se presentan en la Figura 3.24. Se caracterizan por una disminución en la corriente con el tiempo asociados a la desactivación de los electrocatalizadores. Sin embargo, el catalizador Pd/C de E-TEK necesitaba más tiempo para estabilizarse. A tiempos cortos (< 600 s), la densidad de corriente más alta se obtuvo para el Pd/C E-ETEK pero, después de 700 s, la muestra Pd/CNC fue la más estable y dio la mayor densidad de corriente. En general, la tendencia de desactivación parece ser similar en todas las muestras. Además, los

cambios relativos en las densidades de corriente obtenidas son consistentes con los de los voltamogramas cíclicos (Figura 3.23). A partir de este análisis, se observa que el catalizador más activo es Pd/CNC.

Sin embargo, como se ha mencionado anteriormente, los catalizadores sintetizados presentaban una mala estabilidad con el tiempo. Por lo que se dedicaron diversos estudios a mejorar la estabilidad de catalizadores de Pd para la oxidación de HCOOH.

3.5. CATALIZADORES CON ESTRUCTURA *CORE-SHELL*

En general, es aceptado, que la oxidación de HCOOH en Pd se produce principalmente a través de una vía directa, evitando la formación de CO como intermedio. Sin embargo, los catalizadores de Pd son sometidos a una desactivación sustancial en condiciones operativas, por lo que ha surgido una discusión en la literatura sobre la estabilidad a largo plazo de estos catalizadores en pilas de combustible de ácido fórmico directo [YU 2009[a]].

Teniendo en cuenta que el crecimiento epitaxial de películas delgadas sobre un sustrato metálico puede dar lugar a cambios sustanciales en la estructura de la banda *d*, que juega un papel crucial en la actividad catalítica del material [MONTES DE OCA 2011, EL-AZIZ 2002]. Se estudió la influencia del *strain* de capas de Pd crecidas sobre nanopartículas de Au.

Por otro lado, las investigaciones sobre el papel del soporte sobre la actividad de nanoestructuras previamente sintetizadas, por ejemplo, a través de la síntesis coloidal, son relativamente escasas. Este enfoque permite disociar los efectos del soporte en el crecimiento de partículas, de las interacciones químicas específicas vinculadas a la reactividad de los centros metálicos, es decir, cualquier efecto observado en la actividad catalítica podría estar directamente relacionado con el soporte y no con el tamaño de partícula, distribución, etc.

Por tanto, se intentó elucidar el efecto de un soporte carbonoso en particular, Vulcan XC-72R (Vulcan), sobre la actividad electrocatalítica de nanoestructuras *core-*

shell de Au-Pd (CS) en la oxidación de CO y HCOOH. El espesor de las capas de Pd se varió sistemáticamente con el fin de evaluar si los llamados efectos del soporte contrarrestan o mejoran los cambios en reactividad inducidos por el *strain* de las capas de Pd.

3.5.1. Síntesis

El método de preparación de las nanopartículas *core-shell* de Au-Pd (CS) fue similar al método presentado en [MONTES DE OCA 2011]. Las nanopartículas de Au-Pd fueron sintetizadas por la reducción selectiva de H_2PdCl_4 sobre "semillas" de oro de 19 nm en presencia de ácido ascórbico. Se obtuvieron diferentes espesores de recubrimiento de Pd variando la cantidad de H_2PdCl_4 0.1 M a añadir a soluciones de 50 mL de nanopartículas de Au colocadas en un baño de hielo y bajo agitación magnética. Después de esto, se añadió un exceso de ácido L-ascórbico (0.1 M) gota a gota con el fin de evitar la formación de nanopartículas aisladas de Pd.

La síntesis de las nanopartículas de Pd se realizó por reducción de ácido hexacloropaladato (IV) en presencia de citrato trisódico. Para ello, se llevó a ebullición una solución de Na_2PdCl_4 bajo agitación, y se añadió el citrato trisódico. La mezcla se mantuvo bajo agitación y reflujo durante por lo menos 4 horas y, posteriormente, se dejó enfriar la solución hasta temperatura ambiente.

El ensamblaje electrostático de las nanoestructuras se realizó siguiendo métodos previamente establecidos. Las nanopartículas se adsorbieron en electrodos de óxido de estaño dopado con indio (ITO), modificados con poli-L-lisina hidrobromuro [MONTES DE OCA 2011, MONTES DE OCA 2012].

Para preparar las muestras soportadas, se utilizó Vulcan como soporte (C). Se calcularon las cantidades necesarias de disolución de las nanopartículas para obtener una carga de metal de 20 wt.%. El material carbonoso se añadió a estas soluciones y se mantuvo en agitación durante 48 h. Finalmente, el material obtenido se filtró, lavó con agua milli-Q y secó a 60 ºC durante la noche.

3.5.2. Caracterización físicoquímica

En la Figura 3.25 se muestran imágenes TEM representativas de las NPs con estructura *core-shell* de Au-Pd obtenidas por reducción de los precursores de Pd sobre Au. Mientras que el tamaño del núcleo se mantiene constante en la síntesis, el aumento de los depósitos se manifiesta por un aumento del tamaño de las partículas en general. La secuencia de las imágenes TEM muestra un claro contraste entre núcleo de Au y las capas de Pd, lo que confirma un incremento sistemático del espesor de Pd.

El diámetro medio de las estructuras *core-shell* obtenido de la medida de al menos 200 partículas por muestra, y su composición básica estimada a partir de las mediciones EDX se resumen en la Tabla 3.10. La composición másica obtenida por EDX era muy consistente con la composición del baño de síntesis, lo que demuestra que la nucleación de Pd se produce exclusivamente en las superficies de oro.

Tabla 3.10. *Diámetro medio (D), espesor de Pd (δ) y composición en peso Au:Pd.*

Muestra	D / nm	δ / nm	Au:Pd mass ratio (%)
Au	19.3 ± 1.2	---	100:0
CS1	21.8 ± 1.1	1.3 ± 0.9	80:20
CS3	24.7 ± 1.3	2.7 ± 1.0	60:40
CS5	29.5 ± 1.2	5.1 ± 0.9	40:60
CS10	38.9 ± 1.5	9.9 ± 1.1	20:80
Pd	10 ± 1.8	---	0:100

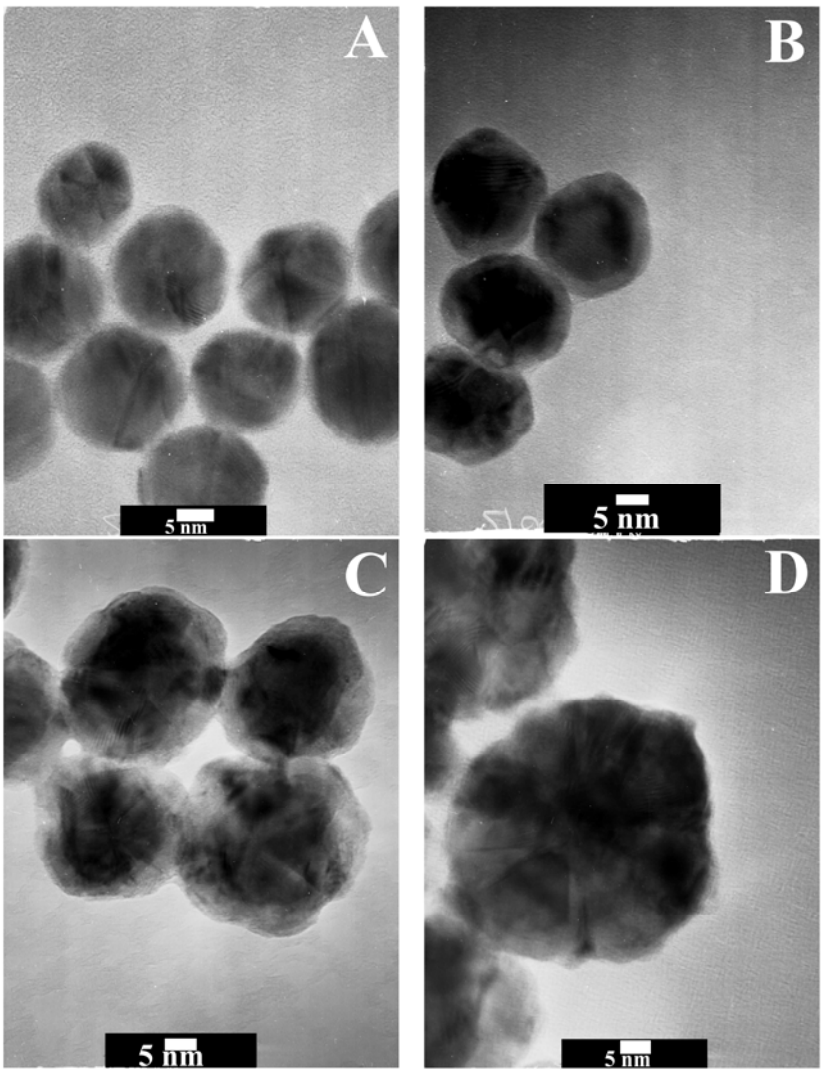

Figura 3.25. *Imágenes HRTEM de las nanopartículas core-shell con núceos de Au de diámetro 19.3±1.2 nm, recubiertos de capas de Pd de espesores 1.3±0.09 nm (A), 2.7±0.1 nm (B), 5.1±0.9 nm (C) y 9.9±1.0 nm (D), respectivamente [MONTES DE OCA 2012].*

Diversas imágenes TEM de las nanoestructuras CS soportadas en Vulcan (Figura 3.26) muestran que las nanopartículas se dispersan bien en el soporte de carbono, lo que garantiza una baja densidad de agregados.

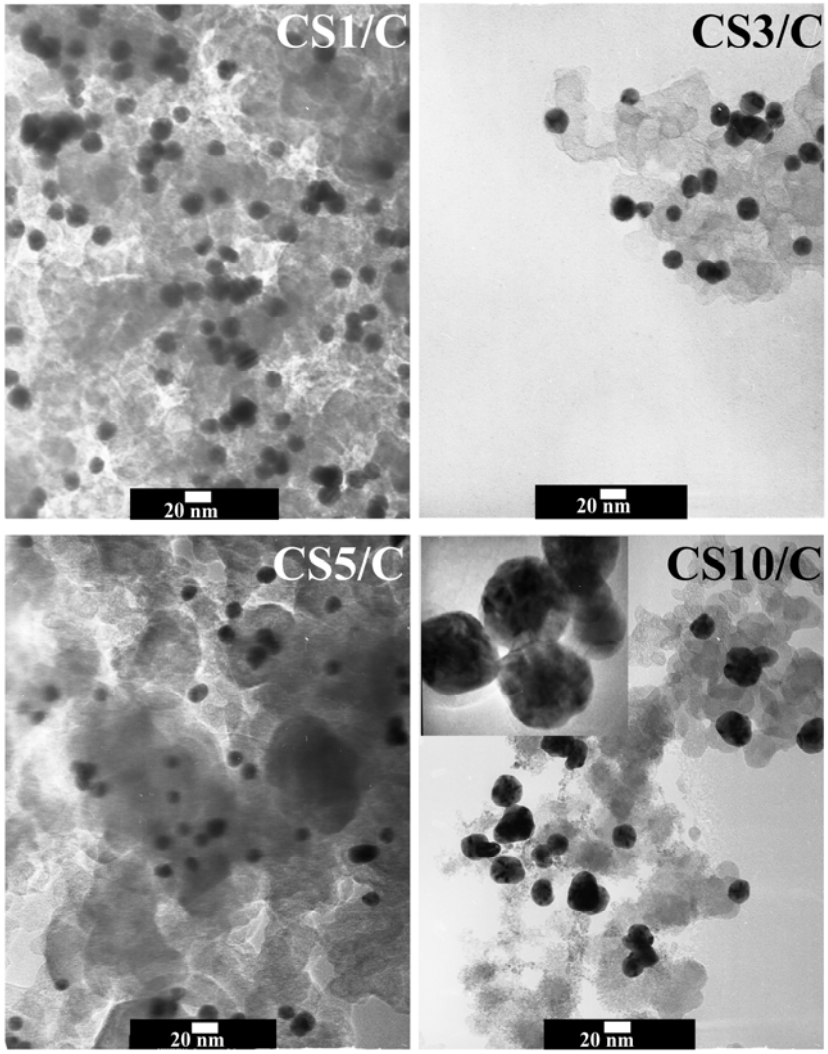

Figura 3.26. *Imágenes TEM de las distintas nanoestructuras CS soportadas en Vulcan. La inserción en la muestra CS10 es una imagen a mayor aumento que muestra el contraste entre el corazón de Au y las capas de Pd [CELORRIO 2012].*

La Tabla 3.11 resume la carga metálica promedio de cada catalizador según las estimaciones de EDX. La carga total de metal en los catalizadores estaba en el rango de 15 a 20%.

Tabla 3.11. *Carga metálica promedio de las nanopartículas soportadas en Vulcan.*

Muestra	Carga metálica (wt.%)
Au/C	19.5 ± 1.2
CS1/C	15.0 ± 1.9
CS3/C	19.2 ± 2.1
CS5/C	18.5 ± 2.9
CS10/C	17.5 ± 1.4
Pd/C	18.4 ± 2.5

La figura 3.27 muestra los difractogramas de rayos X de los distintos catalizadores. Las muestras de Au presentaban bien definidos los picos de difracción debidos a la estructura policristalina del Au. Las señales a 38.3°, 43.9°, 64.8°, 77.7° y 81.5º se deben a los planos (111), (200), (220), (311) y (222) de la estructura cúbica centrada en las caras (fcc) del oro, respectivamente. El pico de difracción de mayor intensidad se observó a 38.3°, lo que sugiere que las nanopartículas de Au tienen una fuerte orientación (111). Por el contrario, no se observaron picos de difracción claros en las muestras de Pd, lo que sugiere una baja estructura cristalina de las nanopartículas monometálicas. La presencia de NPs de Au sirve de molde para el crecimiento de las capas de Pd, lo que permite la progresiva aparición de picos de difracción de Pd en las muestras con estructura *core-shell*. El pico de difracción atribuido al Pd (111) aparecía a 2θ = 40.2° en las muestras CS3, CS5 y CS10; aumentando su intensidad con el aumento del espesor de Pd. Además de los picos asociados con las nanoestructuras metálicas, las muestras soportadas en Vulcan (Figura 4.22.b) muestran un pico a 2θ = 26º, característico del plano (002) del grafito.

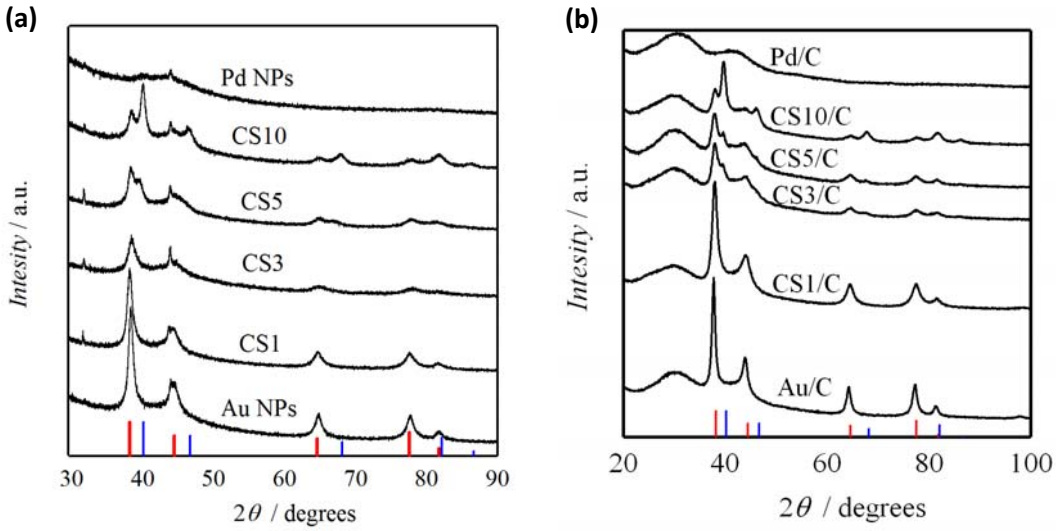

Figura 3.27. *Difractogramas de rayos X de las nanoestructuras metálicas ensambladas en ITO (a) o soportadas en Vulcan (b). Las líneas rojas en la parte inferior de la gráfica, a 38.1°, 44.4°, 64.6°, 77.5° y 81.7° indican el patrón estándar de difracción de Au (PDF 040 784), mientras que las líneas azules a 40.1°, 46.7°, 68.1°, 82.1° y 86.6° pertenecen al Pd (PDF 461 043) [MONTES DE OCA 2012, CELORRIO 2012].*

3.5.3. Oxidación de monóxido de carbono

La Figura 3.28 muestra una comparación de la oxidación de CO en las diferentes nanoestructuras CS ensambladas en ITO (a) o soportadas en Vulcan (b). Se puede observar como la oxidación de CO es claramente dependiente del espesor de Pd. La oxidación de CO sobre las nanopartículas CS1 y CS3 tenía lugar a potenciales más positivos que para el caso de las nanopartículas de Pd puro, las CS5 y las CS10; por lo que se deduce que el CO se adsorbe más fuertemente a medida que disminuye el espesor de Pd. También es interesante señalar que se observó un cambio similar en el potencial para la formación del óxido de Pd. La oxidación de CO, así como la formación del óxido, están influenciadas por la adsorción de especies oxigenadas en la superficie del Pd [EL-AZIZ 2002]. La adsorción de CO es una reacción controlada cinéticamente y depende de la disminución del espesor de Pd. En el caso de las nanoestructuras CS5 y CS10 se observó que el pico de oxidación de CO tenía su comienzo, así como su máximo, en el mismo potencial que en el caso de las nanopartículas de Pd.

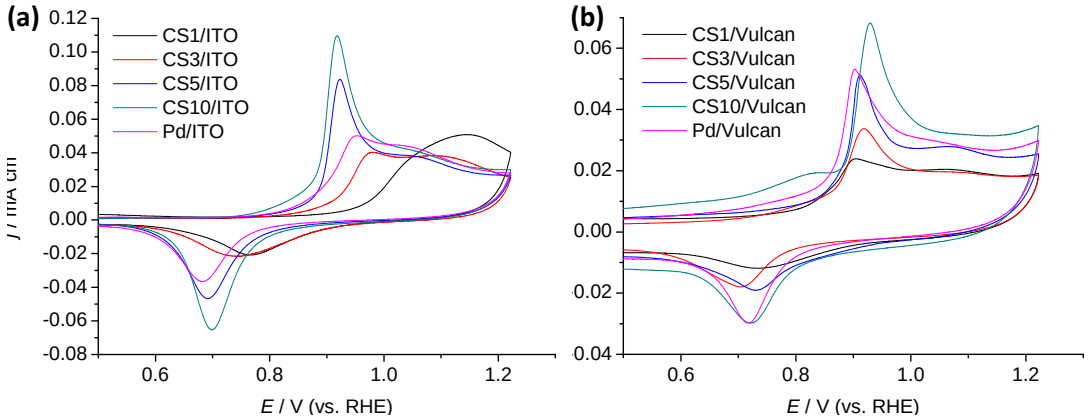

Figura 3.28. *Primer ciclo de la oxidación de CO sobre las nanopartículas ensambladas en ITO (a) o soportadas sobre Vulcan XC-72 (b).*

En el caso de las nanopartículas soportadas sobre Vulcan (Figura 3.28.b), se observó un desplazamiento del pico de oxidación de CO hacia potenciales más positivos a medida que aumentaba el espesor de paladio, indicando una cinética de transferencia más lenta para el proceso de oxidación de CO. Por otro lado, el pico de oxidación era más estrecho a medida que el espesor de Pd iba aumentado, lo que indica que la mayor

parte del CO_{ads} se oxida a potenciales menores. Además, se observa como las densidades de corriente aumentan a la vez que el espesor de paladio.

La Figura 3.29 muestra que la densidad de carga promedio para la oxidación de una monocapa de CO (Q_{CO}), lo cual es indicativo de la cobertura de CO en la superficie de Pd, aumenta de 160 a 310 μC cm^{-2} conforme aumenta el espesor de paladio. Las nanopartículas CS10 presentan un valor cercano al del Pd policristalino, como era de esperar debido al pequeño valor de su *strain* [MONTES DE OCA 2011]. Por otra parte, las nanopartículas CS1 presentaban una carga comparable a una capa pseudomórfica de Pd sobre Au(111), que ha sido reportada como 113 μC cm^{-2} [EL-AZIZ 2002]. La densidad de carga para las nanopartículas de Pd es 257 μC cm^{-2}, menor que la obtenida para las nanopartículas CS10. Esta diferencia de carga entre las NPs de Pd y las CS10 se puede relacionar con la baja estructura cristalina de las nanopartículas de Pd. La adsorción de CO en las nanopartículas CS es dependiente de la estructura cristalina y del *strain* de las capas de Pd.

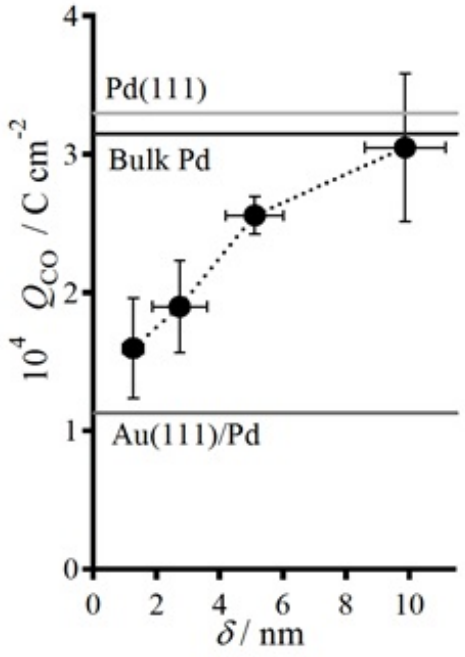

Figura 3.29. *Densidad de carga promedio para la oxidación de CO (Q_{CO}) en función del espesor de Pd para las nanoestructuras core-shell de Au-Pd.*

3.5.4. Oxidación de ácido fórmico

Las propiedades catalíticas de las nanopartículas de Pd y de Au-Pd soportadas en Vulcan o ensambladas en ITO, también se evaluaron para la oxidación de ácido fórmico. La Figura 3.30 muestra los voltamogramas cíclicos registrados a temperatura ambiente para las nanopartículas ensambladas en ITO (a) y soportadas en Vulcan (b) registradas en una solución HCOOH 2 M + H_2SO_4 0.5 M.

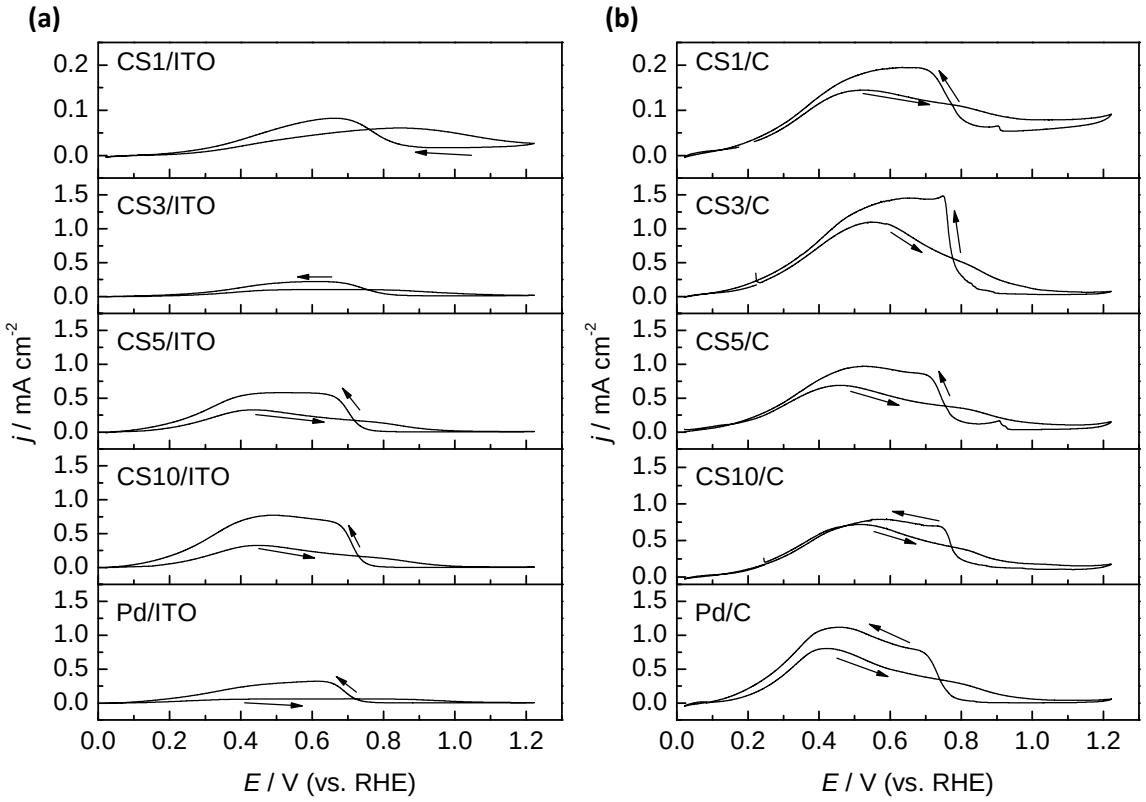

Figure 3.30. *Voltamogramas cíclicos de las nanopartículas de Pd y core-shell ensambladas en ITO (a) y suportadas en Vulcan (b), a 0.02 V s^{-1}, en una solución 2 M HCOOH + 0.5 M H_2SO_4.*

La oxidación del ácido fórmico comienza a 0.12 V y continúa hasta que alcanza un máximo en el barrido positivo a 0.42 V. Al aumentar el contenido de Pd, se observa un ligero desplazamiento del pico hacia potenciales más negativos. A potenciales positivos, se observa una caída de las densidades de corriente, asociada con la formación de óxido de Pd. En el barrido catódico, la superficie permanece inactiva hasta que tiene lugar la reducción del óxido de paladio. Las densidades de corriente para los barridos de ida y vuelta fueron casi idénticas, mientras que para barridos consecutivos fueron altamente reproducibles (resultados no mostrados), lo que indica una baja

tendencia al envenenamiento de la superficie de los electrodos a través de intermediarios adsorbidos.

Las corrientes eran similares para los CS con capas gruesas de Pd y para las NPs de Pd puro, mientras que eran más bajas para aquellas con capas delgadas de Pd (CS1). Se observó una tendencia similar para las muestras ensambladas en ITO, así como en las soportadas en Vulcan.

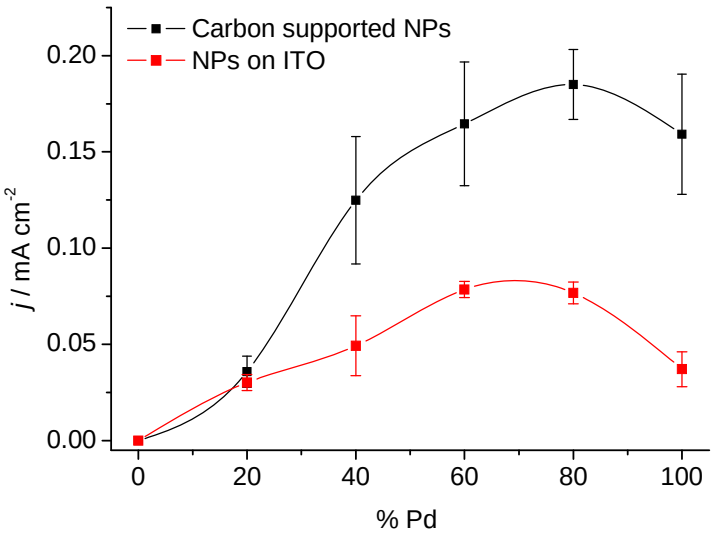

Figure 3.31. *Densidades de corriente después de 750 s asociadas con la oxidación de HCOOH a 0.60 V (vs. RHE) en las distintas nanoestructuras ensambladas en ITO (línea roja) y soportadas en Vulcan (línea negra) en 0.5 M H_2SO_4 + 2M HCOOH.*

La Figura 3.31 compara las densidades de corriente medias para la oxidación de ácido fórmico obtenidas después de 750 s a 0.60 V (vs. RHE) para las distintas nanoestructuras. Las aéreas electroquímicas de los catalizadores se determinaron a partir de los voltamogramas de oxidación de CO, utilizando las densidades de carga obtenidas previamente como parámetros de normalización. Las densidades de corriente asociadas a la oxidación de HCOOH incrementaban al aumentar el espesor de Pd, probablemente debido a la formación de facetas cristalinas altamente reactivas en las capas de Pd más gruesas. Aunque las muestras CS/ITO y CS/C presentaban la misma tendencia, las densidades de corriente para las nanopartículas soportadas en Vulcan eran mayores, especialmente en las NPs de Pd y aquellas CS con un espesor de Pd mayor. Este comportamiento está relacionado con una desactivación más lenta en presencia del soporte carbonoso. Por tanto, la actividad global de los catalizadores depende de la

composición/estructura de las nanoestructuras metálicas, mientras que el soporte juega un papel importante en la acumulación de intermediarios en los sitios activos.

Los electrocatalizadores suportados en Vulcan, se estudiaron mediante DEMS para la oxidación de ácido fórmico, para conocer más a fondo su mecanismo de reacción. La oxidación de ácido fórmico se produce a través de un mecanismo de doble vía. La vía de reacción más conveniente para la oxidación del ácido fórmico es a través de una reacción de deshidrogenación, que no forma CO como intermedio de reacción. La vía directa de oxidación de ácido fórmico produce CO_2 directamente. El segundo mecanismo de la reacción es a través de la deshidratación, formando CO adsorbido como intermedio de reacción. Son necesarios grupos OH adsorbido para oxidar el CO a CO_2 gaseoso. Por lo tanto, el único producto de reacción posible para ser monitoreado por DEMS es el CO_2 (m/z = 44).

La Figura 3.32 muestra los CVs (paneles superiores) y los VCEMs registrados simultáneamente para la relación masa/carga m/z = 44 (paneles inferiores) para las distintas nanoestructuras CS soportadas en Vulcan en HCOOH 0.5 M + H_2SO_4 0.5 M. Se puede observar que las señales de la masa de CO_2 siguen los perfiles voltamétricos correspondientes para la oxidación del ácido fórmico mostrados en los paneles superiores.

Como era de esperar, ya que el CO_2 es el único producto en la oxidación de ácido fórmico, la eficacia de la formación de CO_2 era del 100% en todos los casos. Las posibles diferencias entre la corriente en la VC y la corriente faradaica calculada a partir de los VCEMs podrían ser debidas a la contribución de la carga de la doble capa y al proceso de adsorción-desorción de OH a la corriente en la VC [CUESTA 2009].

Parece que los átomos de Pd proporcionan una superficie especial que permite al ácido fórmico adsorberse y deshidrogenarse de una manera fácil y muy reactiva. Por lo tanto, no se produce CO adsorbido y la reacción de oxidación de ácido fórmico es muy rápida.

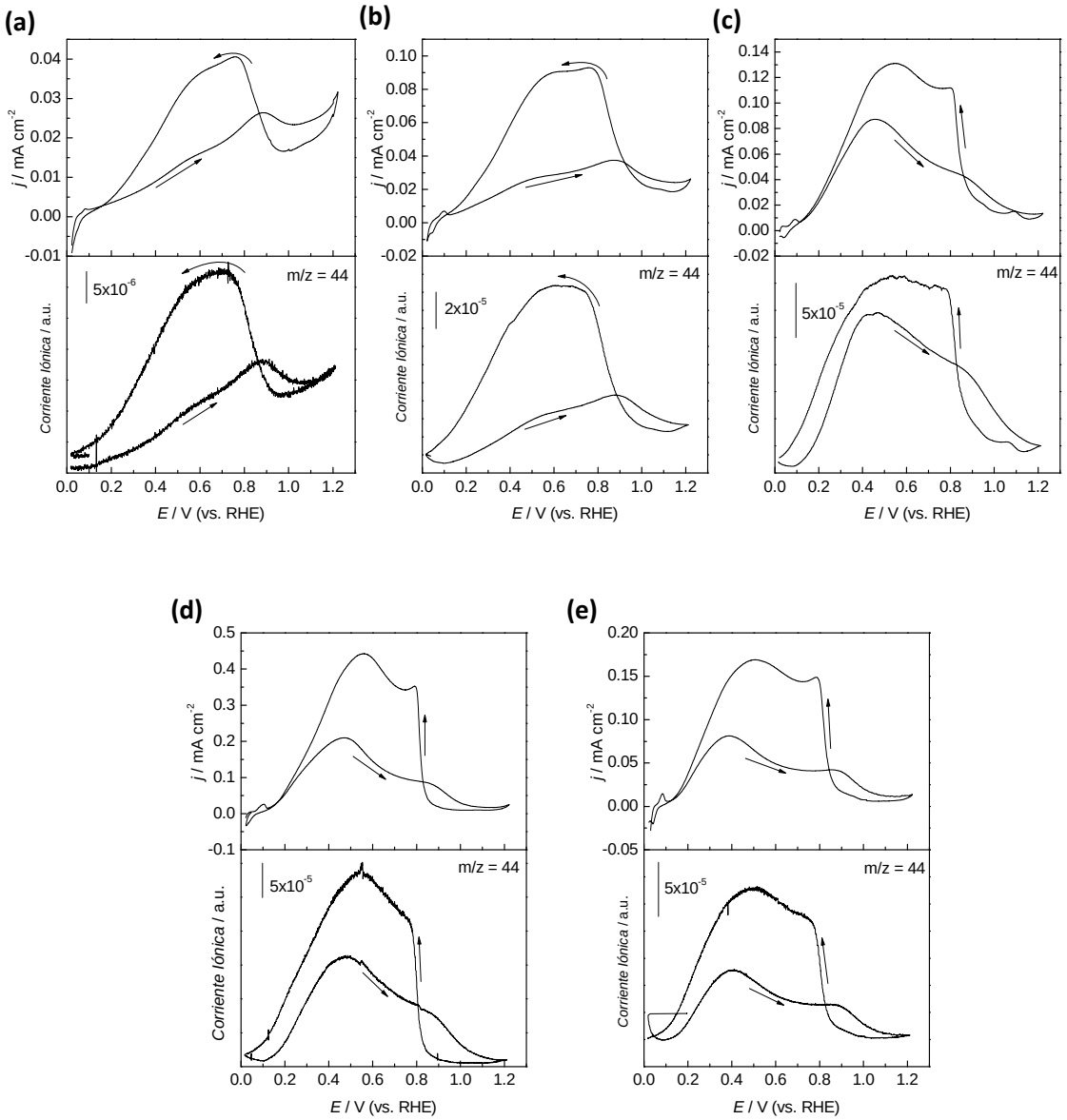

Figura 3.32. *Experimentos DEMS para los electrodos: CS1/C (a), CS3/C (b), CS5/C (c), CS10/C (d) y Pd/C (e).* $\upsilon = 0.001\ V\ s^{-1}$*; T = 25 ºC.*

3.6. CONCLUSIONES

En la presente tesis, se han estudiado las condiciones de síntesis de nanoespirales de carbono (CNC), variando la relación molar de los reactivos utilizados. Esta síntesis involucra el tratamiento térmico de compuestos formados por un precursor de carbono (gel de resorcinol-formaldehído), sílice, y una sal de metales de transición (una mezcla de sales de cobalto y níquel). La caracterización de estos materiales mediante distintas técnicas permitió conocer tanto sus propiedades texturales como estructurales y la

morfología de los materiales carbonosos sintetizados, confirmando su alta área superficial, su porosidad bien definida y su buena cristalinidad. El material que presentó las mejores características para ser utilizado como soporte carbonoso de catalizadores de metales nobles para ser utilizado en pilas de combustible fue el denominado CNC-3.

La superficie de las nanoespirales de carbono se puede modificar sustituyendo el tratamiento de HNO_3 por otros agentes oxidantes en fase líquida. Para realizar este estudio se eligió el material CNC-3. Así, se crearon grupos carboxílicos, lactonas, fenoles y quinonas, aumentando su cantidad con la severidad de los tratamientos. Los grupos carboxílicos son estables a bajas temperaturas y aumentan la capacidad de mojabilidad del carbón, lo que facilita la interacción entre el precursor metálico y el material de carbono durante la etapa de impregnación. Por otro lado, los grupos fenoles y quinonas son estables a altas temperaturas y actúan como sitios de anclaje del metal, impidiendo la redistribución y la aglomeración del metal durante la etapa de reducción.

El material denominado CNC-3 NcTa2 fue seleccionado para preparar nanopartículas de Pt y Pt-Ru soportadas sobre el mismo, mediante distintos métodos de síntesis. Los mismos procedimientos fueron utilizados para preparar nanopartículas soportadas en Vulcan. En términos generales, se obtuvieron tamaños medios de partícula mayores cuando se utilizó CNC como soporte, debido al menor número de sitios de nucleación (en carbones grafíticos, sólo los defectos de la superficie pueden funcionar como sitios de nucleación). Se encontró una gran influencia del método de síntesis y del soporte de carbono en el tamaño de las partículas.

La oxidación de CO en los electrocatalizadores de Pt y Pt-Ru se vio favorecida por el uso del CNC como soporte, ya que el pico de oxidación CO_{ads} se obtuvo a un potencial menor que utilizando Vulcan como soporte. Sin embargo, en el caso de los catalizadores de Pt, esta mejora no ayudó en la oxidación de metanol, alcanzando densidades de corriente más elevadas utilizando Vulcan como soporte. Esto podría atribuirse a una mayor formación de productos intermediarios (como se observa mediante el análisis DEMS) que podrían envenenar las partículas de metal. Por el contrario, se produjo una mejora en la reacción de oxidación de etanol cuando se utilizó CNC como soporte. Debido a que el paso clave en la EOR es la rotura del enlace C-C, se podría afirmar que las interacciones Pt-CNC favorecen esta reacción.

Se prepararon también electrocatalizadores de Pd soportado en CNC y Vulcan, utilizando borohidruro de sodio como agente reductor. El pico de oxidación de CO se obtuvo a potenciales ligeramente más negativos utilizando CNC, sin embargo, estos potenciales fueron siempre más positivo que en el caso de los catalizadores de Pt y Pt-Ru. Se estudió la oxidación de ácido fórmico, siendo las nanopartículas de Pd soportadas en CNC más activas y estables que las soportadas en Vulcan y que el catalizador comercial Pd/C de E-TEK.

Al crecer capas metálicas sobre un sustrato distinto, la estructura de la banda *d*, que desempeña un papel importante en la actividad catalítica del metal, puede ser modificada. Por esta razón, se prepararon nanopartículas con estructura *core-shell* de Au-Pd. Se estudió la influencia del espesor de las capas de Pd, así como la influencia del soporte. Como las nanoestructuras estaban previamente formadas, este enfoque permite disociar los efectos del soporte en el crecimiento de las partículas, se utilizó Vulcan y electrodos de SnO_2 dopado (ITO).

Se demostró que la reactividad de las nanoestructuras *core-shell* de Au-Pd a la oxidación de CO y HCOOH no sólo estaba determinada por la composición y estructura de las capas de Pd, sino también por la interacción con el soporte. Del análisis de los voltamogramas de CO se concluyó que la cobertura de CO estaba estrechamente vinculada con el *strain* promedio de las partículas *core-shell*, mientras que el soporte de carbono afecta al potencial de aparición de la oxidación de CO. La oxidación de HCOOH también muestra una fuerte dependencia del soporte. Las partículas soportadas en Vulcan presentaban velocidad de desactivación más lenta en los experimentos cronoamperométricos, en comparación con las ensambladas en ITO. Además, las nanopartículas *core-shell* con capas más gruesas de Pd, presentaron mayores densidades de corriente que las partículas de Pd puro para la oxidación de HCOOH.

4

Summary

4.1. INTRODUCTION

Among the different types of fuel cells, the most suitable for powering portable devices, electric vehicles and transportation, are the polymer electrolyte (PEMFCs) and direct alcohol (DAFCs) fuel cells, due to their low operating temperatures (60 - 100 °C) and fast start up. Common catalysts used at the anodic side of these cells are platinum and platinum alloys. Considering that catalysis is a surface phenomenon, an aspect to be take into account in the design of the catalysts is their high surface area. For this purpose, the active catalyst phase is dispersed in a conductive support, typically carbon materials. However, the development of PEMFCs, from the viewpoint of the electrocatalyst, is limited by the anode catalyst poisoning with CO, which is present as an impurity in the reformed gas used as a source of H_2 for this type of cells. Therefore, nowadays, much of the research is aimed at the preparation of more CO tolerant anodes. In the presence of 50-100 ppm of CO in the fuel, Pt-Ru alloys supported on carbon

materials have shown an electrocatalytic activity higher than pure Pt. Regarding to the materials used in the cathode side, Pt is showing higher catalytic activity towards the oxygen oxidation reaction.

Among all types of carbon materials, carbon blacks are the most used as electrocatalyst support for polymeric electrolyte fuel cells, due to their high electrical conductivity and corrosion resistance, their porous structure and specific surface area [BEZERRA 2007]. However, these materials show high ohmic resistance and problems of mass transfer in fuel cell applications.

As carbon supports have been found to strongly influence the accessibility of the catalytic active sites, great efforts are being made to find the optimum architecture of carbon supports. In recent years, an important strategy to reduce the performance degradation due to mass transport resistance has been the use of alternative carbon supports with a suitable mesoporous structure. Novel non-conventional carbon materials with controllable porous structures and surface chemistry, such as carbon nanocoils [HYEON 2003], carbon xerogels and aerogeles [MARIE 2004], and ordered mesoporous carbons [CALVILLO 2007], have been proposed as electrocatalyst supports.

4.2. OBJECTIVES

The general objectives of this thesis are listed below:

- Study the physicochemical properties of carbon nanocoils, giving particular attention to the variation of these characteristics depending on the synthesis conditions.
- Study different oxidation treatments on carbon nanocoils, in order to modify their surface chemistry, increase the specific surface area and develop a higher porosity.
- Synthesis of mono and bimetallic catalysts supported on the as-prepared carbon nanocoils. Study the influence of the support (compared with the commercial carbon black Vulcan XC-72R) and the synthesis method on the electrocatalysts' properties for CO and alcohol oxidation.

- Explore new and novel configurations for the development of active and stable catalysts with a core-shell nanostructure for the electrooxidation of alcohols in DAFC.

4.3. CARBON SUPPORTS

Carbon materials are generally used as catalysts supports because of their stability in both acidic and basic media, good electrical conductivity, high corrosion resistance, surface properties and high specific surface area. Carbon has been used for many years as a support for industrial precious metal catalysts [AUER 1998]. Activated carbons, carbon blacks, graphites and graphitized materials have been applied in various catalytic processes. Carbon materials have a strong influence on the properties of supported noble metal catalysts, such as metal particle size, morphology, size distribution, stability, and dispersion [KIM 2006, YU 2007]. On the other hand, carbon supports can also affect the performance of fuel cell catalysts by altering mass transport, catalyst layer electrical conductivity, electrochemically active area, and metal nanoparticle stability during operation [HALL 2004, INOUE 2009]. Consequently, a carbon support with suitable properties must be selected in order to obtain an active catalyst, since its properties have strong effects on the preparation and performance of supported catalysts. Hence, the optimization of carbon supports is very important in PEMFC technology development.

The ideal properties of a carbon support for its use in fuel cells are [LIU 2006, DICKS 2006]: i) high specific surface area, for a high level of catalyst dispersion; ii) suitable pore structure, for the adequate diffusion of reactant and by-products; iii) electrical conductivity, in order to facilitate electron transfer during the electrochemical reactions; iv) suitable surface chemistry for a good interaction between the catalyst nanoparticles and the carbon support; and v) high corrosion resistance. In addition to these requirements, supports must be low cost materials and permit metal recycling at the end of the catalyst life.

4.3.1. Vulcan XC-72R

Vulcan XC-72 is extensively used as electrocatalyst support, especially in polymeric electrolyte fuel cells [SHAO 2006, WIKANDER 2006]. At present, this material is used as support in commercial electrocatalysts (E-TEK and Johnson Matthey). A review of the properties of Vulcan XC-72R as electrocatalyst support for low temperature fuel cells is presented here.

Morphology was studied using scanning electron microscopy (SEM) and X-ray diffraction (XRD). Figure 4.1 shows two SEM images of Vulcan XC-72R. It can be seen that Vulcan consists of an aggregation of spherical particles, primary particles, with size in the range of 30 to 60 nm. The aggregation grade of particles is known as the structure of the carbon black.

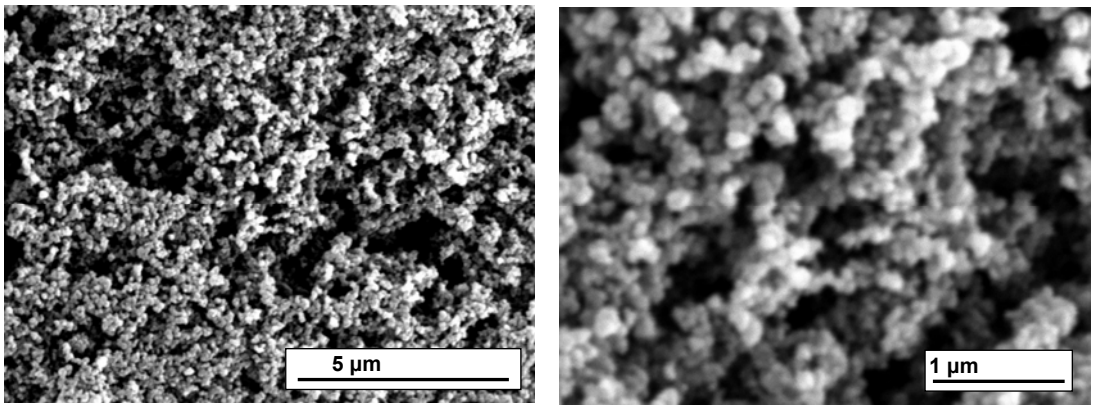

Figure 4.1. *SEM images of Vulcan XC-72R.*

Vulcan was also analyzed by XRD. The XRD pattern is presented in Figure 4.2. A peak around 2θ = 24.85º, characteristic of graphite, can be observed, confirming that Vulcan has an intermediate structure between amorphous and graphitic, called turbostratic structure.

The thermal stability of Vulcan XC-72R was determined by temperature programmed oxidation (TPO) experiments. The thermal stability (or resistance to corrosion) of the material used as support in PEM fuel cell catalysts is an important characteristic to be take into account, because it affects the catalyst durability. Due to its structure, Vulcan exhibits a high resistance to oxidation in air, which was found to take place at around 660 ºC [LAZARO 2011[b]].

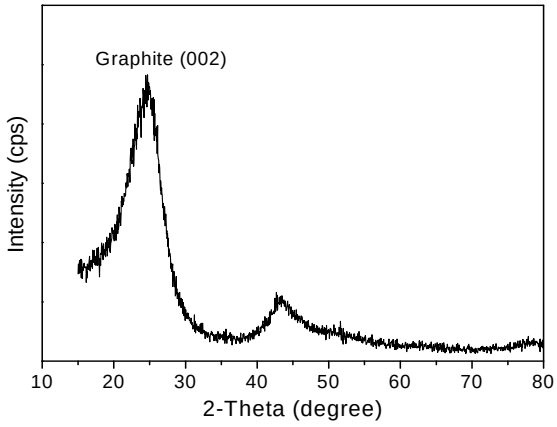

Figure 4.2. *XRD pattern of Vulcan XC-72R.*

The textural properties of Vulcan were analyzed by N_2-physisorption. Table 4.1 shows the textural parameters obtained from this technique. Vulcan was found to have a relatively large specific surface area (S_{BET}) of 218 $m^2\ g^{-1}$ and a total pore volume (V_{Total}) of 0.41 $cm^3\ g^{-1}$. It has a mesoporous structure, but containes a large number of micropores (30 % of total surface area). Micropores are not suitable for the application of this material as electrocatalyst support. It is possible that an important portion of nanoparticles may sink into these micropores, resulting in little or no electrochemical activity because of the difficulty of reactant accessibility [LIU 2006, ANTOLINI 2009].

Table 4.1. *Textural parameters of Vulcan obtained by nitrogen physisorption at 77 K.*

Material	S_{BET} [a] ($m^2\ g^{-1}$)	V_{Total} [b] ($cm^3\ g^{-1}$)	$V_{Micropore}$ [c] ($cm^3\ g^{-1}$)	$V_{Mesopore}$ [d] ($cm^3\ g^{-1}$)	$S_{Micropore}$ [c] ($m^2\ g^{-1}$)	$S_{Mesopore}$ [d] ($m^2\ g^{-1}$)
Vulcan XC-72R	218	0.41	0.03	0.38	65	153

[a] Determined by the BET (Brunauer, Emmett and Teller) equation.
[b] Determined by the single point method at P/P_0=0.99.
[c] Determined by the t-plot method.
[d] Calculated from the difference between the total and micropore values.

The surface chemistry of Vulcan was studied using temperature programmed desorption (TPD) experiments. Acidic groups are decomposed into CO_2 at lower temperatures, while basic and neutral groups are decomposed into CO at higher temperatures [FIGUEIREDO 1999]. CO and CO_2 profiles can be analyzed and the peaks obtained can be related to the different functional groups depending on their decomposition temperature [AKSOYLU 2001, SAMANT 2004, FIGUIREDO 1999]. Vulcan had a small amount of surface oxygen groups, since it was not subjected to any

oxidation treatment; it only presented groups that desorbed at high temperatures as CO (phenol and quinone groups).

4.3.2. Carbon nanocoils (CNC)

Carbon nanocoils (CNC) constitute a new class of carbon nanomaterials with properties that differ significantly from other forms of carbon. There are several methods to synthesize CNC, like arc discharge, laser vaporization, thermal chemical vapor deposition or catalytic graphitization of carbon precursors. The catalytic graphitization process reduces the costs of manufacturing significantly, because high temperatures are not needed. Different carbon precursors like resorcinol-formaldehyde gels [HYEON 2003] or saccharides [SEVILLA 2007] can be used as carbon precursors, and a mixture of transition metal salts as graphitization catalysts.

In this work, the catalytic graphitization is proposed as the synthesis procedure for CNCs; this way, carbon materials containing graphitic structures can be obtained at low temperature (< 1000 ºC). Thus, the synthesis of CNCs by the catalytic graphitization of resorcinol-formaldehyde gel, using a mixture of nickel and cobalt salts as the graphitization catalysts, has been studied. The aim of this work was to determine the most suitable conditions to obtain a graphitic material, making an arrangement between the graphitization degree and surface area, by varying the molar ratio of the reactants.

4.3.2.1. Study of the synthesis conditions

Carbon nanocoils were synthesized by catalytic graphitization of resorcinol-formaldehyde gel, as described in [CELORRIO 2010]. In a typical synthesis, formaldehyde (Sigma-Aldrich) and silica sol (Supelco) were disolved in 100 mL of deionized water, then a mixture of nickel (Panreac) and cobalt (Sigma-Aldrich) salts was added under stirring conditions. Subsequently, resorcinol (Sigma-Aldrich) was added, and the stirring conditions were maintained for 0.5 h. After a heat treatment, at 85 ºC for 3 h, in a closed system of this reaction mixture, the system was then opened, and the mixture dried at 108 ºC. Finally it was carbonized in a nitrogen atmosphere, at 900 ºC, for 3 h. A 5 M NaOH (Panreac) solution was used to remove silica particles,

followed by a treatment with concentrated HNO_3 (65%, Fluka), at room temperature, during 2 h to remove the metal salts.

Three carbon materials (CNC-1, CNC-2 and CNC-3) were synthesized following this method by varying the molar ratio of the reactants. Table 4.2 shows the molar ratios and the nomenclature used for the different materials.

Table 4.2. *Molar ratios of reactants used in the preparation of carbon materials.*

Sample	H_2O/Co salt/Ni salt/Resolcinol/Formaldehyde/Silica
CNC-1	100:0.2:0.2:1:2:0
CNC-2	100:0.4:0.4:1:2:0.6
CNC-3	100:0.2:0.2:1:2:0.6

Figure 4.3.a shows the XRD patterns of the synthesized CNCs. A typical diffraction pattern of slightly graphitized carbon is represented by the data obtained for the CNC-1 sample. A characteristic broad (002) peak at ~24º and a less intense one at ~44º, which corresponds to a (100) reflection of a graphitic structure, were observed for this material. Addition of silica in the preparation of samples CNC-2 and CNC-3 decreased the width of the main (002) diffraction peak and made the other more visible. In addition, the main XRD peak for these samples appeared to be a superposition of a broad ~24º peak and a narrow one centered at ~26º. This suggests that most of the samples are well-graphitized, while a low percentage of them are graphitic to a smaller extent.

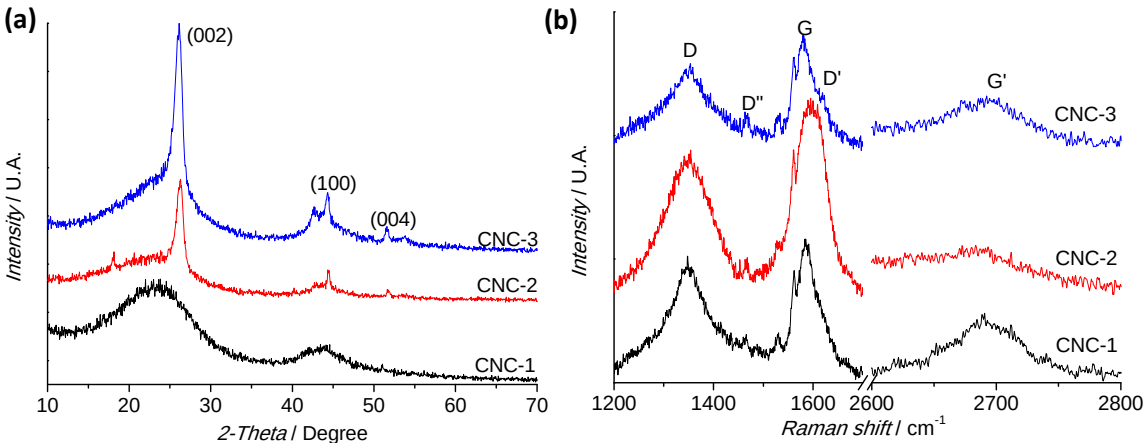

Figure 4.3. *XRD patterns (a) and first- and second-order Raman spectra (b) of CNC.*

The nature and graphitization degree of the carbon materials were further examined by Raman spectroscopy. The first-order (1200-1700 cm^{-1}) and second-order (2500-2900 cm^{-1}) Raman spectra of CNCs are shown in Figure 4.3.b. As can be seen, the first-order Raman spectra show two bands: the G band, or graphite, and the D band associated with the presence of different types of structural defects [CUESTA 1994]. In addition to these two great bands, some authors postulate smaller ones, such as D' and D'' bands [ROUZAUD 1983, VIDANO 1978]. These bands may be attributed to the presence of amorphous carbon associated with graphitic carbon, as well as the light functionalization suffered during the treatment with nitric acid. On the other hand, the second-order Raman spectra show the G' band characteristic of ordered materials.

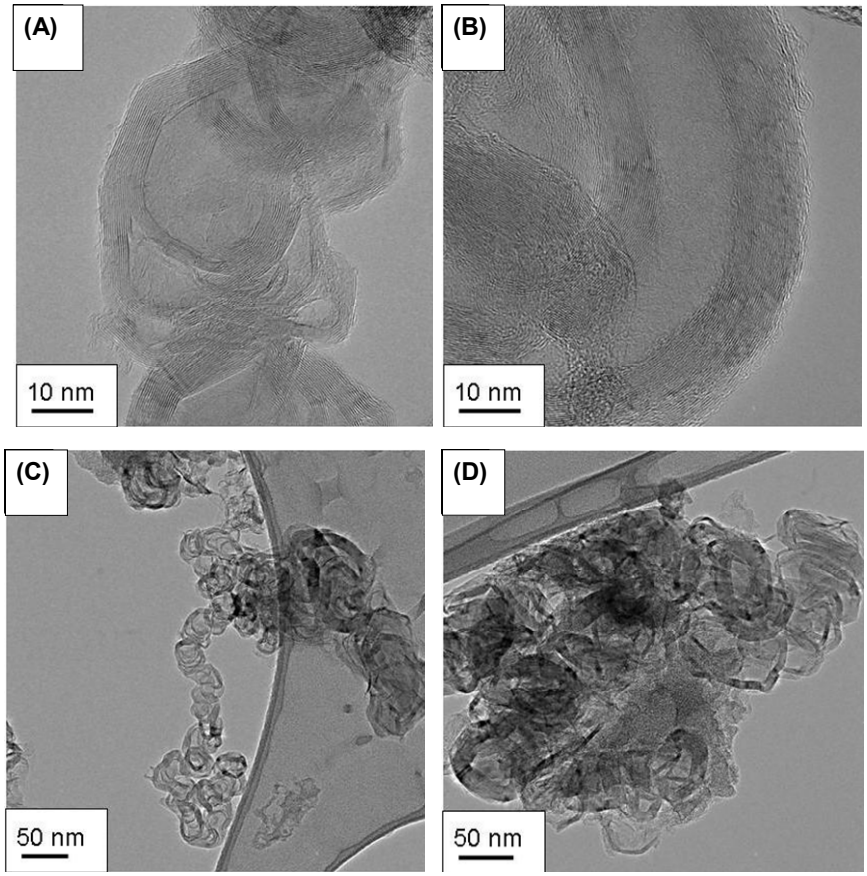

Figure 4.4. *HRTEM (A and B) and TEM (C and D) images of CNC-3.*

The morphology of the as-prepared CNCs was studied by TEM. A single nanocoil exhibited well-aligned graphitic layers, which can be observed in the high-resolution transmission electron microscopy (HRTEM) images in Figure 4.4 (panels A and B); this confirmed the XRD and Raman spectrometry results. TEM images (panels

C and D of Figure 4.4) showed that the nanocoils have a diameter of around 30-40 nm and consist of a long curved ribbon of carbon. Particles of around 100-150 nm were formed, containing several nanocoils, as can be seen in Figure 4.4.D

Thermal stability was studied by TPO experiments under an air atmosphere [CELORRIO 2011]. All samples exhibited a high resistance to oxidation in air, with similar weight change patterns. The oxidation occurred around 600 ºC, with the CNC-3 sample being the most resistant to oxidation. This fact can be related to its more graphitic nature. It must also be noted that the oxidation of the carbon materials was complete; that is, there was no residue after the TPO experiments. This indicated that the removal of the silica and metal particles with NaOH and HNO_3 treatments, respectively, was complete.

Textural properties of CNCs obtained by N_2-physisorption are summarized in Table 4.3. Carbon materials showed a specific surface area of 120-220 $m^2\ g^{-1}$ and a pore volume of 0.10-0.19 $cm^3 g^{-1}$. Both the specific surface area and the pore volume decreased as the graphitization degree of the sample increased. Thus, the CNC-3 sample showed the lowest surface area and pore volume, and the CNC-1 sample showed the highest. The shape of the isotherms was typical of nanoparticulate materials without structural pores. In this case, adsorption occurred on the external surface of the nanostructures. From the results derived from the α_S method it was confirmed that CNCs do not present structural pores, so adsorption occurred on the external surface of the nanostructures. Therefore, the BET surface area (S_{BET}) corresponds to the external surface area (S_{ext}).

Table 4.3. *Textural parameters of CNCs obtained by nitrogen physisorption at 77 K.*

Material	S_{BET}[a] ($m^2\ g^{-1}$)	V_{Total}[b] ($cm^3\ g^{-1}$)	α_S method		
			S_{ext} ($m^2\ g^{-1}$)	V_{micro} ($cm^3\ g^{-1}$)	V_i ($cm^3\ g^{-1}$)
CNC-1	120	0.10	122	0.0	0.10
CNC-2	220	0.19	223	0.0	0.19
CNC-3	124	0.16	126	0.0	0.16

[a] Determined by the BET (Brunauer, Emmett and Teller) equation.
[b] Determined by the single point method at P/P_0=0.99.

CNCs were treated with concentrated nitric acid for 2 h, at room temperature, to remove the metal particles used as catalysts in the graphitization process. This treatment

is commonly used to modify the surface chemistry of carbon materials, creating surface oxygen groups. Therefore, its effect on surface chemistry was also studied. Samples mainly contained carboxylic and phenol groups. It is expected that carboxylic groups will produce a decrease in the hydrophobicity of carbon materials and phenol groups will make the surface more accessible to the reactants.

4.3.2.2. Modification of the properties of carbon nanocoils

The last step of the CNCs synthesis process involves the elimination of the metals, using an oxidative treatment, commonly with HNO_3. However, during this treatment not only the metals are eliminated, but so are the amorphous and graphitic carbons. On the other hand, this treatment can create surface oxygen groups, modifying the surface chemistry of CNCs. After the heat treatment, most works report the use of a HNO_3 treatment in order to remove the metal particles used during the synthesis, although others report the use an HCl treatment [SEVILLA 2007]. However, studies on the influence of different treatments on the properties of the carbon materials are not found in the literature. Due to its good properties, CNC-3 material was chosen for this study.

Oxidation treatments introduce surface oxygen groups that improve the wettability of carbon materials with polar solvents, such as water. This characteristic is very important to achieve a good interaction between the metal precursor and the support and thus, enable the anchoring of an active phase [CALVILLO 2007, CALVILLO 2009]. With this aim, the HNO_3 treatment at room temperature for 2 h has been replaced by different treatments with nitric acid (Nc), nitric-sulphuric mixtures (NS), hydrogen peroxide (Ox) and sulphuric acid-hydrogen peroxide mixtures (SOx). These treatments were carried out at 25 (Ta) and 80 ºC (Tb), for either 0.5 or 2 h.

The carbon materials obtained have been characterized by means of the same techniques of the original material (section 4.3.2.1.), in order to study the effect of these treatments on the final properties of CNCs.

TPO experiments showed that the use of different oxidation treatments did not affect the resistance to oxidation in a significant way. In all cases, the oxidation took place around 600 ºC (see Ref. *Celorrio et al*. 2011). In addition, it can be observed that

not all oxidation treatments were effective in the total elimination of the metals used as graphitization catalysts. After the treatments with H_2O_2 and H_2SO_4-H_2O_2, a residue was obtained, indicating that the metals were not completely removed.

The liquid phase treatments had a great influence in the textural properties of the carbon materials. Thus, materials with specific surface areas (S_{BET}) in the range 30-250 $m^2\ g^{-1}$ and total pore volumes (V_{TOTAL}) of 0.08-0.30 $cm^3\ g^{-1}$ were obtained. As can be seen in Table 4.4, carbon materials treated with H_2SO_4-H_2O_2 mixtures (SOx) showed the lowest specific surfaces areas and total pore volumes. This result could be attributed to the destruction of the structure of the material during the oxidation treatments. For the other oxidizing agents, similar textural parameters were obtained for all the oxidation conditions (temperature and time), except for the most severe conditions (boiling temperature for 2 h). In the last case, a decrease of specific surface area and pore volume was observed.

Table 4.4. *Textural properties of CNCs obtained after the different oxidation treatments.*

Sample	S_{BET} ($m^2\ g^{-1}$)	V_{Total} ($cm^3\ g^{-1}$)	α_S method		
			S_{ext} ($m^2\ g^{-1}$)	V_{micro} ($cm^3\ g^{-1}$)	V_i ($cm^3\ g^{-1}$)
CNC NcTa0.5	243	0.31	249	0.0	0.31
CNC NcTa2	124	0.16	126	0.0	0.16
CNC NcTb0.5	235	0.22	241	0.0	0.22
CNC NcTb2	246	0.24	252	0.0	0.24
CNC NSTa0.5	117	0.13	120	0.0	0.13
CNC NSTa2	213	0.19	218	0.0	0.19
CNC NSTb0.5	202	0.18	207	0.0	0.18
CNC NSTb2	120	0.13	123	0.0	0.13
CNC SOxTa0.5	84	0.12	86	0.0	0.12
CNC SOxTa2	75	0.10	77	0.0	0.10
CNC SOxTb0.5	74	0.11	76	0.0	0.11
CNC SOxTb2	46	0.09	47	0.0	0.09
CNC OxTa0.5	168	0.17	172	0.0	0.17
CNC OxTa2	183	0.19	187	0.0	0.19
CNC OxTb0.5	192	0.22	196	0.0	0.22
CNC OxTb2	187	0.20	196	0.0	0.20

Table 4.5 summarizes the amounts of the different types of oxygenated groups calculated from the deconvoluted peak areas. For each oxidizing agent, an increase in the number of oxygenated groups was observed as the severity of the treatment increased, that is, as the temperature and time of the treatment were raised. Treatments with H_2O_2 were the least effective at creating functional groups, among all the

treatments used, due to H_2O_2 being the weakest oxidizing agent. The most effective oxidation treatment in creating surface oxygenated groups, especially anhydride/lactone groups, was the use of HNO_3-H_2SO_4, at boiling temperature, for 2 h. From the CO_2 peaks, it was observed that mainly anhydride/lactone groups, which are stable at low temperatures, were created, whereas the CO evolution peaks suggested the formation of phenol groups, which are stable at high temperatures (Table 4.5).

Table 4.5. *Estimation of the type and number of the oxygen groups created during the oxidation treatments from the deconvolution of TPD profiles. TPD experiments were carried out in an inert atmosphere, using a heating rate of 10 ºC min^{-1} up to 1050 ºC. The amounts of CO and CO_2 desorbed were analysed by mass spectrometry.*

Sample	CO_2 peak areas (µmol g^{-1})		CO peak areas (µmol g^{-1})		
	Carboxylic	Anhydride Lactone	Anhydride	Phenol	Quinone
CNC NcTa0.5	498	254	106	797	64
CNC NcTa2	440	410	450	1690	200
CNC NcTb0.5	595	1100	12	1862	173
CNC NcTb2	506	1077	36	1214	1131
CNC NSTa0.5	210	1060	890	960	240
CNC NSTa2	270	1420	1250	840	140
CNC NSTb0.5	570	2220	410	1460	210
CNC NSTb2	590	3220	0	3000	0
CNC SOxTa0.5	332	958	43	1111	448
CNC SOxTa2	237	1152	59	1341	111
CNC SOxTb0.5	287	953	24	1116	395
CNC SOxTb2	510	1165	43	862	32
CNC OxTa0.5	260	160	20	500	30
CNC OxTa2	240	110	20	420	90
CNC OxTb0.5	430	110	30	410	30
CNC OxTb2	280	340	0	310	200

4.4. MONOMETALLIC CATALYSTS AND ALLOYS

Carbon nanocoils have recently received great attention as catalytic support in fuel cell electrodes due to the combination of their good electrical conductivity, derived from their graphitic structure, and a wide porosity that allows the diffusional resistances of reactants/products to be minimized. Only few works have been performed on catalysts supported on carbon nanocoils for their use both at the anode and cathode of a direct methanol fuel cell. Hyeon *et al*. synthesized Pt/Ru (1:1) alloy catalyst (60% wt.), supported on CNC. They studied its behaviour towards methanol oxidation, showing its good electrocatalytic activity [HYEON 2003]. Sevilla *et al*. also demonstrated the high

catalytic activity of PtRu/CNC electrocatalyst for methanol oxidation [SEVILLA 2007]. In addition, they compared its activity to that of a Pt/Vulcan catalyst prepared by the same method, demonstrating that catalysts supported on CNC exhibited a higher utilization of metals [SEVILLA 2008, SEVILLA 2009]. Park *et al*. employed carbon nanocoils with variable surface areas and crystallinity as Pt/Ru catalyst supports [PARK 2004, HAN 2003]. They found that catalysts supported on carbon nanocoils exhibited better electrocatalytic performance towards methanol electrooxidation than the catalyst supported on Vulcan XC-72. On the other hand, Imran Jafri *et al*. studied the activity of Pt nanoparticles dispersed on multi-walled carbon nanocoils for the oxygen reduction reaction in proton-exchange membrane fuel cells [IMRAN JAFRI 2010], the results obtained support the use of this new type of catalyst support material for PEMFC.

4.4.1. Synthesis

In the literature, different synthesis methods have been used to prepare platinum electrocatalysts. Five general methods are usually employed: impregnation, ion exchange, precipitation, colloidal, and vapour phase methods. However, few works on the comparison of catalysts synthesized by different methods can be found in the literature [SALGADO 2008, LÁZARO 2011[a]], and none on carbon nanocoils.

The impregnation method is the most widely used due to its simplicity and good results. High surface area carbon blacks can be impregnated with catalyst precursors by mixing the two in an aqueous solution. Following the impregnation step, a reduction step is required to reduce the catalyst precursor to its metallic state. Common liquid phase reducing agents are $Na_2S_2O_3$, $NaBH_4$, $Na_4S_2O_5$, N_2H_4, and formic acid; whereas H_2 is the predominant gas phase reducing agent.

For the reasons presented above and in order to study the effect of the synthesis method on both the physicochemical and electrochemical properties, catalysts supported on carbon nanocoils were synthesized by different methods. Catalysts have been prepared by impregnation and subsequent reduction with sodium borohydride (BM) [CALVILLO 2007] and formic acid (FAM) [ÁLVAREZ 2010], as well as the alcohol-reduction method using methanol (MM) [GANGERI 2006] or the polyol method (EGM) using ethylene glycol as solvent and reducing agent [LÁZARO 2011[a]].

For these studies, the CNC-3 NcTa2 material (named CNC from here on) was selected. Vulcan XC-72R was used to compare the effect of the support on the properties of electrocatalysts.

4.4.1.1. Pt and Pt-Ru based electrocatalysts

Pt and Pt-Ru based catalysts supported on Vulcan and CNC have been synthesized by BM, FAM, MM and EGM methods (mentioned above), in order to study the influence of the synthesis method on the physicochemical and electrochemical properties of catalysts, as well as the influence of the carbon support. Their properties were compared with those of commercial catalysts from E-TEK.

H_2PtCl_6 (8 wt. % $H_2PtCl_6 \cdot 6\ H_2O$ solution, Sigma-Aldrich), and $RuCl_3$ (45-55% $RuCl_3$, Sigma-Aldrich) were used as metal precursors, and catalysts with a metal loading of 20 wt. % and a Pt:Ru atomic ratio of 50:50 were prepared.

4.4.1.2. Pd based electrocatalys

Impregnation followed by a reduction with sodium borohydride (BM) method was chosen to study the influence of the carbon support on the properties of palladium electrocatalysts. Furthermore, a comparison with a Pd/C commercial catalyst from E-TEK was established.

Na_2PdCl_6 (98 wt. % $Na_2PdCl_6 \cdot 6\ H_2O$, Sigma-Aldrich) was used as metal precursor. A set amount of the carbon materials and the precursor were used to obtain a total metal loading of 20 wt.%.

4.4.2. Physicochemical characterization

Electrocatalysts are some of the key materials used in low temperature fuel cells. Creating high performance catalysts is widely recognized as a key step for the further development and commercialization of low temperature fuel cells. In this section, the size and morphology of the metal particles will be studied as a function of the carbon support and the synthesis method used.

4.4.2.1. Pt and Pt-Ru based electrocatalysts

Tables 4.6 and 4.7 show the nomenclature used and the metal loading of the different electrocatalysts prepared and the commercial catalysts from E-TEK, obtained by EDX, as well as the Pt:Ru molar ratio. As can be seen, average metal loadings were close to the nominal value of 20 % wt. However, the Pt:Ru atomic ratio depended on the synthesis method. It has already been demonstrated that many factors can affect the composition, morphology and dispersion of PtRu/C catalysts, when solution-reduction methods are used [LIU 2006].

Table 4.6. *Total metal content and physical characteristics of catalysts supported on Vulcan.*

Electrocatalyst	wt.% Total metal content	Pt:Ru	D (nm)	SA ($m^2 g^{-1}$)	Lattice parameter (Å)
Pt/Vulcan-BM	17.3	---	3.7	76	3.9029
PtRu/Vulcan-BM	20.3	68:32	3.7	88	3.9006
Pt/Vulcan-FAM	19.2	---	3.2	88	3.9158
PtRu/Vulcan-FAM	14.6	66:34	4.5	73	3.9057
Pt/Vulcan-MM	15.3	---	5.8	48	3.9598
PtRu/Vulcan-MM	14.2	57:43	4.0	86	3.8930
Pt/Vulcan-EGM	20.0	---	5.4	52	3.9174
PtRu/Vulcan-EGM	17.4	50:50	4.4	81	3.9006
Pt/C E-TEK	16.3	---	3.0	93	3.9231
PtRu/C E-TEK	20.0	50:50	3.4	105	3.9031

Table 4.7. *Total metal content and physical characteristics of catalysts supported on CNC.*

Electrocatalyst	wt.% Total metal content	Pt:Ru	D (nm)	SA ($m^2 g^{-1}$)	Lattice parameter (Å)
Pt/CNC-BM	20.0	---	4.7	60	3.9198
PtRu/CNC-BM	17.3	66:34	3.9	91	3.9062
Pt/CNC-FAM	19.3	---	3.8	74	3.9233
PtRu/CNC-FAM	20.4	71:29	4.3	74	3.9031
Pt/CNC-MM	20.1	---	4.8	58	3.9184
PtRu/CNC-MM	20.0	74:26	2.7	117	3.8830
Pt/CNC-EGM	16.2	---	5.6	50	3.9158
PtRu/CNC-EGM	20.0	50:50	3.8	94	3.8981

The morphological and crystallographic properties of the catalysts were studied by X-ray diffraction. XRD patterns are reported in Figure 4.5.

All the Pt-supported electrocatalysts showed the typical form of the face-centered cubic (fcc) Pt structure, indicating the effective reduction of the metal precursor, producing crystalline nanoparticles. Peaks at 2θ = 40º, 47º, 67º, 81º and 85º, associated with the Pt crystal planes (111), Pt (200), Pt (220), Pt (311) and Pt (222), respectively, were observed. For the Pt-Ru/C catalysts, no peaks corresponding to metallic ruthenium with a hexagonal close packed (hcp) structure or ruthenium oxide phase were observed, indicating that Ru was incorporated into the Pt fcc structure. Furthermore, the XRD patterns displayed a peak at 2θ = 26.2º, characteristic of the graphite (002) plane, which is attributed to the CNCs used as support. In the case of Vulcan-supported and commercial catalysts, the peak attributed to the support was less intense, due to the lower crystalline grade of Vulcan XC-72R.

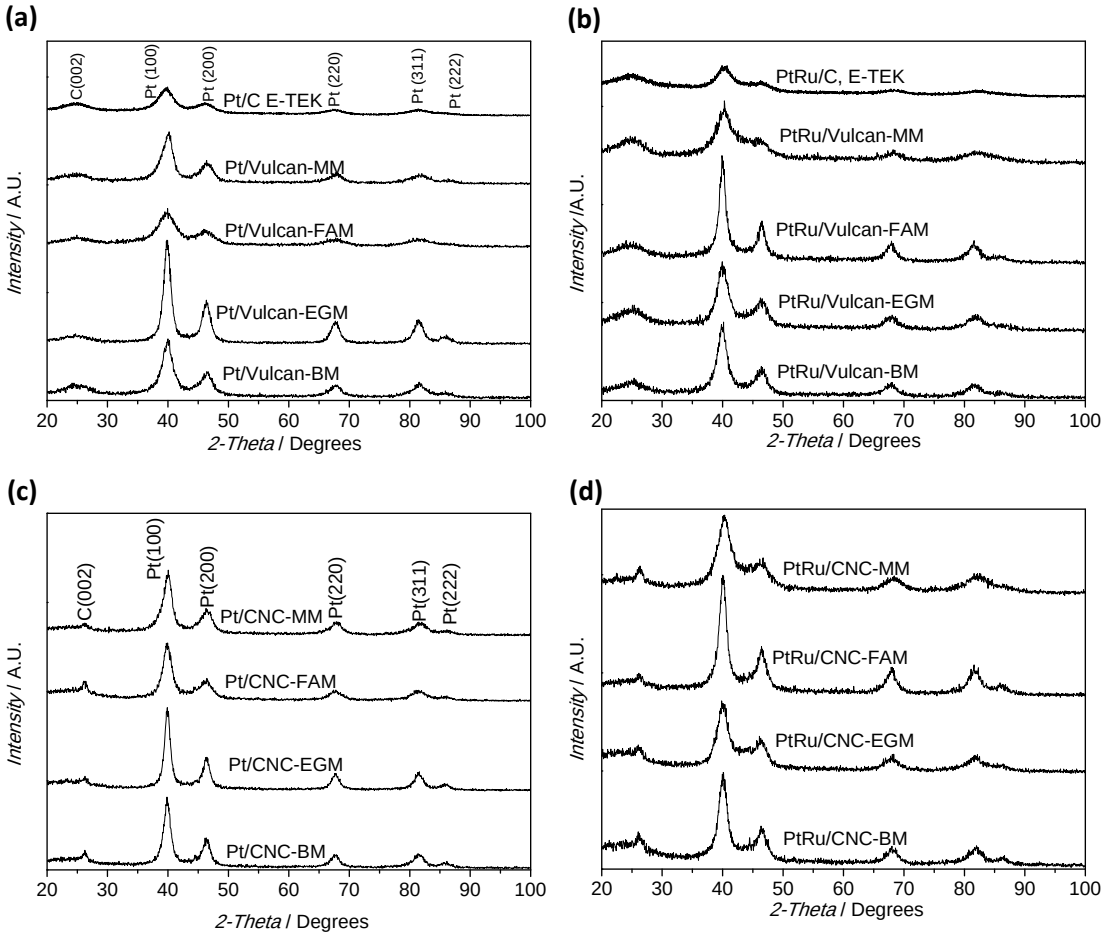

Figure 4.5. *XRD diffractograms for the Pt/Vulcan (a), Pt-Ru/Vulcan (b), Pt/CNC (c) and Pt-Ru/CNC (d) electrocatalysts.*

According to the literature, the size and morphology of metal particles supported on carbon materials depend on the metal-carbon interaction [BESSEL 2001, ISMAGILOV 2005]. The average metal crystallite sizes (D) were calculated through the Debye-Scherrer's equation, using the (220) XRD peak of the Pt fcc structure (Table 4.6 and 4.7). From these results it can be deduced that the synthesis method and the support have an important influence on the metal crystallite size. In general, higher average sizes were obtained when CNC were used as support, compared with those obtained using Vulcan. However, these differences were not significant. This could be attributed to the fact that Vulcan has a large number of nucleation sites, leading to the formation of smaller particles. In contrast, graphitized carbons, like CNC, have a lower number of nucleation sites because only the surface defects can function as nucleation sites, and thus larger Pt particles are obtained.

For Pt-supported catalysts in both carbon materials, the smallest particle sizes were obtained by FAM and the highest ones by EGM. In the case of Pt-Ru, BM results in a lower particles size for Vulcan-supported catalysts, whereas catalysts synthesized by MM presented the lowest crystallite sizes.

Through the calculation of the average metal crystallite sizes of the electrocatalysts using the Scherrer equation to the (220) XRD peak, it was concluded that platinum nanoparticles presented larger crystallite sizes than the bimetallic Pt-Ru ones, suggesting that the addition of the Ru species could inhibit the agglomeration of Pt particles [ANTOLINI 2001]. In addition, the crystallite size depended on the synthetic route.

The surface area (SA) was calculated applying the equation SA ($m^2\ g^{-1}$) = $6\times10^3/\rho d$, where d is the mean metal crystallite size in nm and ρ is the density of Pt or Pt-Ru, considering $\rho_{Pt\text{-}Ru}$ ($g\ cm^{-3}$) = $\rho_{Pt}X_{Pt} + \rho_{Ru}X_{Ru}$, where ρ_{Pt} of Pt metal is 21.4 $g\ cm^{-3}$ and ρ_{Ru} is 12.3 $g\ cm^{-3}$, and X_{Pt} and X_{Ru} are the weight percent of Pt and Ru, respectively, in the catalysts. These values are also reported in Tables 4.6 and 4.7.

The lattice parameters were calculated from XRD patterns and the results are summarized in Tables 4.6 and 4.7. The value of the lattice parameter of the Pt/C electrocatalysts decreases with increasing the crystallite size. The dependence of the lattice parameter on the crystallite size has been described previously in the literature [SALGADO 2008, ANTOLINI 2006]. For Pt-based electrocatalysts, these values were

close to 3.92 Å, which is the value of pure platinum. The lattice parameters for PtRu/C catalysts were smaller than those for the corresponding Pt/C catalysts. This result is in agreement with previous works and indicates the strong interaction between Pt and Ru [JIANG 2005].

Pt-based samples prepared by EGM were selected to study the metal particle size and the metal distribution by TEM. Figure 4.6 shows the TEM images obtained for the Pt catalysts supported on the different carbon materials. A good distribution of the platinum particles was obtained when Vulcan was used as support (a). However, the formation of Pt agglomerates was observed in the case of CNC (b), which is in good agreement with the results obtained by XRD and could be attributed to the high number of oxygenated groups of this carbon material.

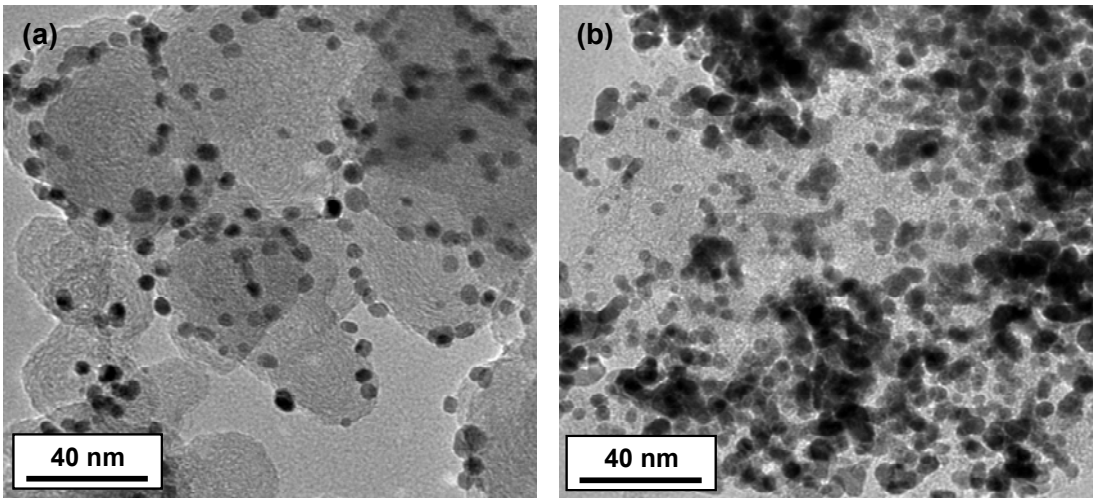

Figure 4.6. *TEM images of the Pt nanoparticles supported on: (a) Vulcan and (b) CNC.*

4.4.2.2. Pd based electrocatalysts

In addition, Pd catalysts supported on CNC and Vulcan were synthesized. Characteristic X-ray diffractograms obtained for these catalysts and the commercial one (Pd/C, E-TEK) are illustrated in Figure 4.7.

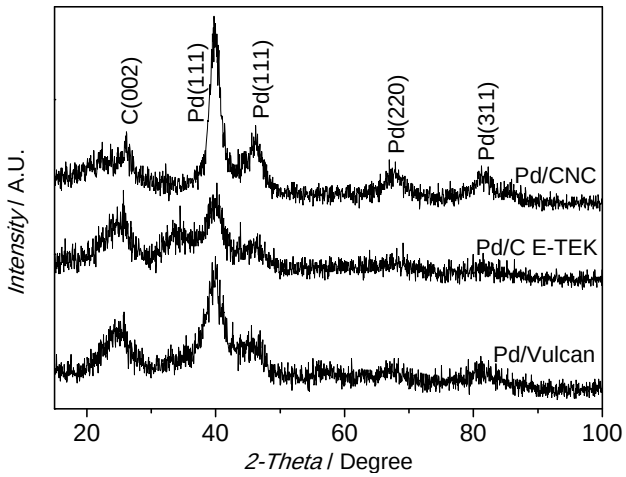

Figure 4.7. *X-ray diffratograms of the carbon supported Pd nanoparticles.*

The average Pd crystallite size (D) was calculated by the Scherrer equation using the (220) peak. These sizes and the metallic charge estimated by EDX for all samples are summarized in Table 4.8. As can be seen, small particle size was obtained when CNC were used as support. This trend suggests that oxygenated groups at the carbon surface could be acting as nucleation sites for the palladium nanoparticles, increasing the total dispersion of the catalysts.

Table 4.8. *Total metal content and physical characteristics of catalysts.*

Catalizador	**wt.% Total metal content**	**D (nm)**	**SA ($m^2 g^{-1}$)**
Pd/CNC-BM	20.0	4.6	109
Pd/Vulcan-BM	19.9	5.0	100
Pd/C, E-TEK	20.0	2.0	250

*ρ_{Pd} = 12.0 g cm^{-3}

In Figure 4.8, TEM images of the Pd/CNC and Pd/Vulcan catalysts are shown. A good distribution of the palladium particles was obtained when CNCs were used as support. However, the formation of Pd agglomerates was observed in the case of Vulcan. For both of them, a good correlation between the calculated and the observed particle size was found.

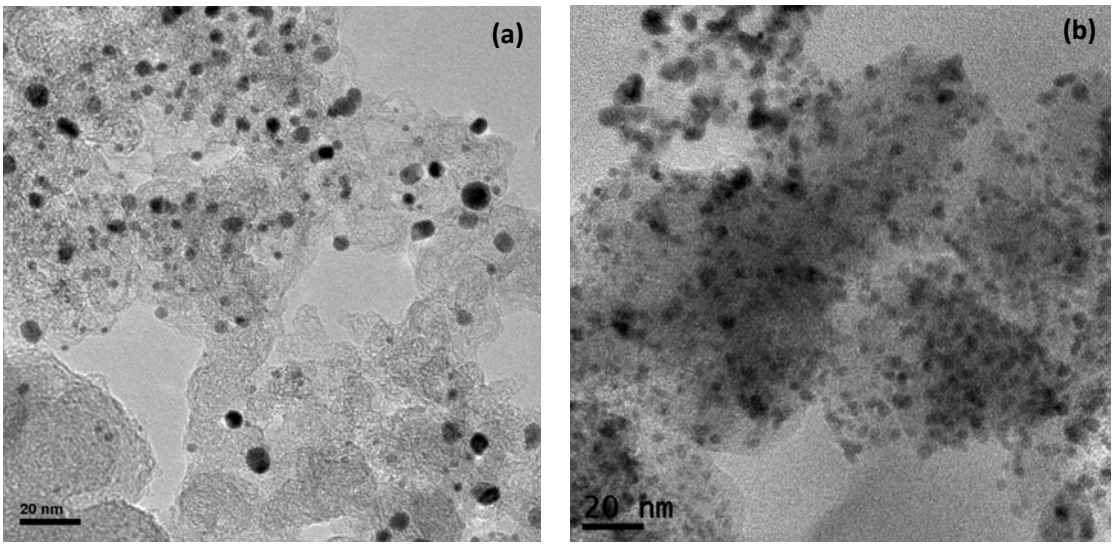

Figure 4.8. *TEM images of the Pd/CNC (a) and Pd/Vulcan (b) samples. The scale bar corresponds to 20 nm.*

4.4.3. Carbon monoxide oxidation

The presence of CO in the anode of polymeric electrolyte fuel cells is a problem in the development and subsequent operation of this type of devices. CO is strongly adsorbed on the metal surface, disabling the active sites for further reduction of the fuel, causing the rapid loss of activity (poisoning) of the catalyst. In order to establish the CO tolerance of catalysts, the electro-oxidation of a CO monolayer adsorbed on the catalyst surface was studied. CO (99.99 %) was adsorbed onto the metal surface by bubbling this gas at 1 atm through the electrolyte to achieve a full monolayer coverage of CO. The CO adsorption process was carried out at a constant potential, the magnitude depending on the nature of the metal nanoparticles. Subsequently, N_2 or Ar gases were used to purge out the CO from the solution, leaving only the CO adsorbed on the metal surface. Moreover, the electroactive area of catalysts was determined by the integration of the CO_{ad} peak. For Pt and Pt-Ru electrocatalysts, a charge density of 420 μC cm^{-2} was assumed, involving in the oxidation of a monolayer of linearly adsorbed CO, whereas this value was 490 μC cm^{-2} for the Pd catalysts. These electroactive areas were used to normalize the current densities given in the text.

4.4.3.1. Pt based electrocatalysts

Figures 4.9 and 4.10 show the CO-stripping voltammograms for all catalysts, as well as the second cycle after oxidation, which corresponds to the voltammogram in the base electrolyte for the clean surface. In the first scan, when the Pt surface is blocked by the adsorption of a CO monolayer, hydrogen adsorption becomes impossible. In the second scan, some interesting reactions occur at the surface of the Pt electrode. At potentials higher than approximately 0.8 V, the Pt surface is oxidized to PtOH and PtOx in the anodic potential scan direction, and these Pt oxides are reduced to metallic Pt in the cathodic potential scan direction. At potentials less positive than approximately 0.3 V, once the CO layer is removed, two pair of peaks are observed due to the hydrogen adsorption and desorption.

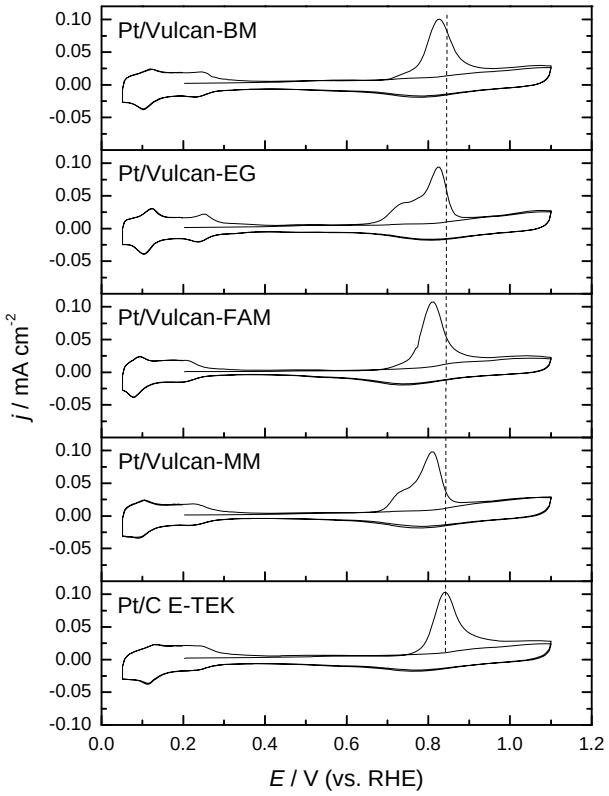

Figure 4.9. *CO-stripping voltammograms for the Pt/Vulcan electrocatalysts in 0.5 M H_2SO_4. E_{ad} = 0.20 V; υ = 0.020 V s^{-1}; T = 25 ºC.*

In the case of Vulcan-supported platinum catalysts (Figure 4.9), no significant differences were observed for the catalysts synthesised by different methods. The peak potential for the CO_{ad} oxidation occurred at the same potential for all catalysts (0.82 V). However, for Pt/Vulcan-BM, and Pt/Vulcan FAM, the electrooxidation of CO started at

around 0.70 V, whereas for Pt/Vulcan-EGM and Pt/Vulcan-MM, it started at more negative potentials. For the last two catalysts, a shoulder centred at 0.72 V was apparent, which implies that for these catalysts part of the adsorbed CO is oxidized at more negative potentials. From these results, it is deduced that CO is more easily oxidized on Pt/Vulcan-EGM and Pt/Vulcan-MM catalysts.

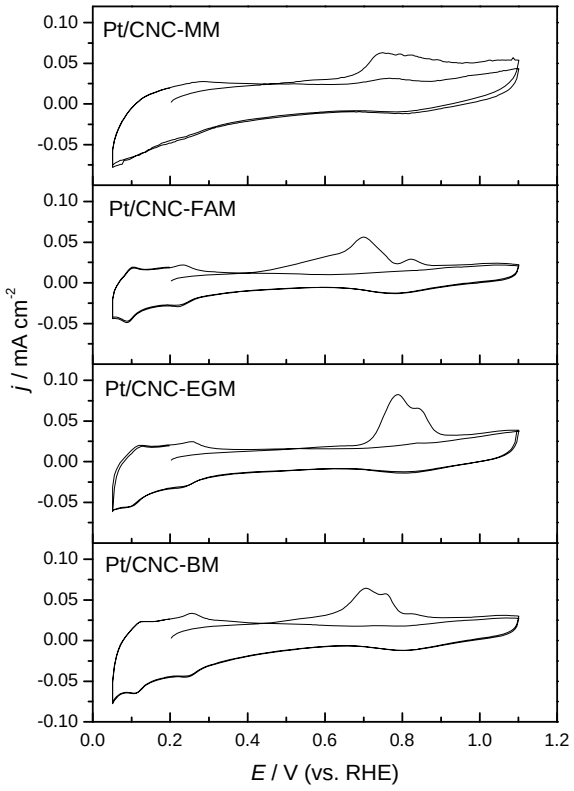

Figure 4.10. *CO-stripping voltammograms for the Pt/CNC electrocatalysts in 0.5 M H_2SO_4. E_{ad} = 0.20 V; υ = 0.020 V s^{-1}; T = 25 ºC.*

For Pt/CNC catalysts (Figure 4.10), the oxidation of CO_{ad} is shifted negatively compared with Pt/Vulcan and Pt/C E-TEK catalysts. For these catalysts, two CO oxidation peaks were observed in the cyclic voltammograms (CVs). One peak around 0.84 V was observed, which corresponds to that observed for catalysts supported on Vulcan XC-72R. In addition, a second CO oxidation peak was obtained around 0.70 V for Pt/CNC-BM and Pt/CNC-FAM and at 0.79 V for Pt/CNC-EG. This implies that CO can be easily oxidized on these materials. The presence of this additional peak at lower potentials could be attributed to the nature and surface chemistry of the carbon support, specifically to the surface oxygen groups of the CNCs [ANTOLINI 2009[b], YU 2009],

which could alter the electronic structure of the metal, helping the CO oxidation process and making catalysts more tolerant to CO than Vulcan-supported catalysts.

4.4.3.2. Pt-Ru based electrocatalysts

With the addition of Ru, the hydrogen region of the voltammogram decreased and a shift of the oxide stripping peak to more negative potential was produced. The onset potential of CO oxidation was shifted negatively for the Pt-Ru based catalysts, with respect to the corresponding Pt-based catalysts. This fact could be explained by the presence of Ru, which is more easily electro-oxidized than pure Pt, and forms Ru-OH_{ads} species at lower potentials, helping to oxidize the CO_{ads}, through a bifunctional mechanism [GASTEIGER 1994]. The oxidation of CO on the commercial PtRu/C catalyst from E-TEK was found to begin at 0.52 V vs. RHE and showed a current density peak at 0.58 V.

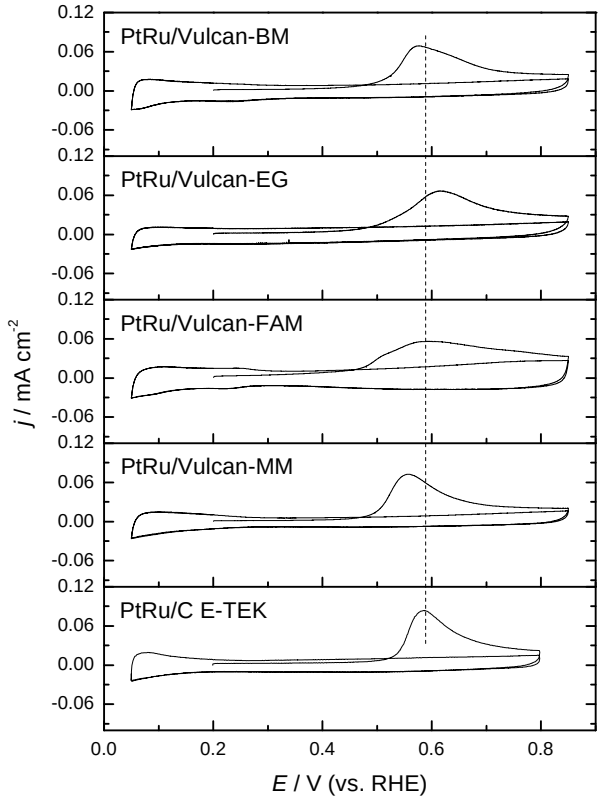

Figura 4.11. *CO-stripping voltammograms for the PtRu/Vulcan electrocatalysts in 0.5 M H_2SO_4. E_{ad} = 0.20 V; υ = 0.020 V s^{-1}; T = 25 ºC.*

For catalysts supported on carbon nanocoils, both the onset and the peak potential shifted towards more negative potentials, with respect to the commercial

catalyst. The comparison between the different PtRu catalysts is rather difficult, since different Pt:Ru ratios were obtained. In the literature, the shift of the oxidation peak potential to more negative potentials as the Ru content increases has been reported [CRABB 2004]. For the catalysts studied in this work, it was found that CO_{ads} was more easily oxidized on the catalyst synthesised by the BM method (PtRu/CNC-BM), as was observed for Pt catalysts, although it had a lower Ru content than expected (Pt:Ru ratio = 66:34).

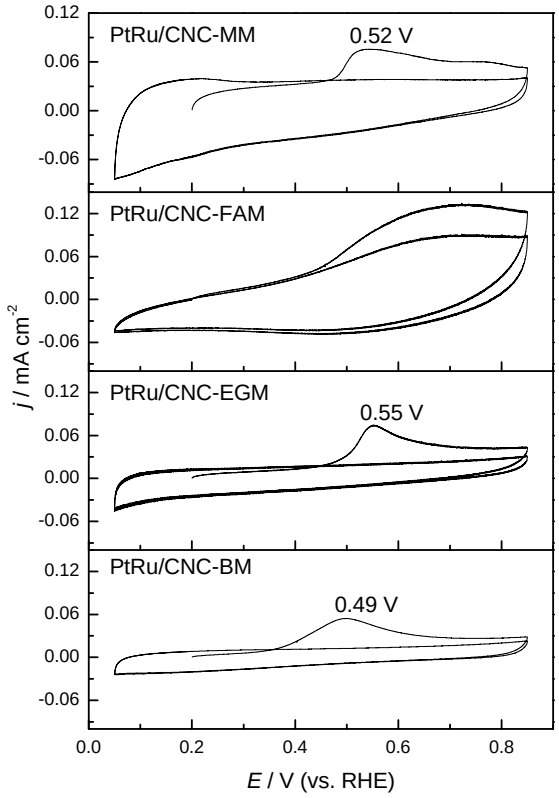

Figure 4.12. *CO-stripping voltammograms for the PtRu/CNC electrocatalysts in 0.5 M H_2SO_4. E_{ad} = 0.20 V; υ = 0.020 V s^{-1}; T = 25 ºC.*

4.4.3.3. Pd based electrocatalysts

The voltammetric features associated with CO stripping at Pd/CNC, Pd/Vulcan and Pd/C E-TEK electrocatalysts are contrasted in Figure 4.13. The hydrogen adsorption region appears blocked in the initial forward scan due to adsorbed CO at the Pd surface. The key feature in the first forward scan is the CO stripping peak located at 0.92 V in the commercial catalysts. The disappearance of the CO stripping peak on subsequent scans, and the reappearance of hydrogen peaks at more negative potentials,

indicate complete removal of CO in the first scan. The main feature of Figure 4.13 is associated with the potential of CO stripping, which is comparable for all three catalysts.

Although Pd possesses very low CO tolerance, inferior to that of pure Pt, tests in PEMFCs fuelled with H2/CO revealed that the presence of Pd increases the CO tolerance of Pt and Pt–Ru catalysts [ANTOLINI 2009[a]].

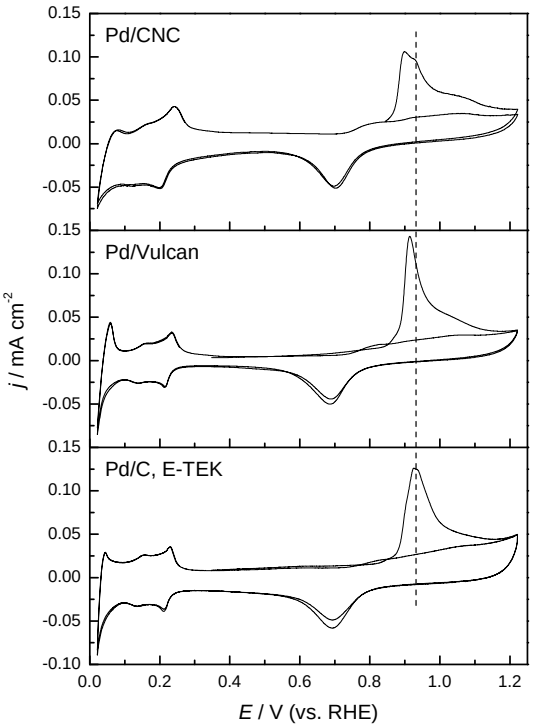

Figure 4.13. *CO stripping voltammograms for the Pd/CNC, Pd/Vulcan and Pd/C from E-TEK electrocatalysts in 0.5 M H_2SO_4. E_{ad} = 0.056 V; υ = 0.020 V s^{-1}; T = 25 ºC.*

4.4.4. Methanol oxidation

Although a large number of other mono-metallic electrodes have been investigated, platinum appears to be the best electrocatalyst for methanol oxidation reaction (MOR) in acid medium. However, the electrooxidation of methanol on platinum is complicated by poisoning intermediates, which causes the catalytic activity to diminish with time. Pd, on the other hand, is completely inactive for electrooxidation of methanol in acid solutions.

MOR activity of platinum is low and not suitable for use in direct methanol fuel cells (DMFCs). It has been shown that the alloying of Ru, Sn or Mo with Pt provides

more CO-tolerant anodes, with better performance. Among them, Pt-Ru alloys have shown to be the most effective. The presence of Ru facilitates the oxidation of CO species and, consequently, enhances the electrocatalytic activity for methanol oxidation.

The activity of the catalysts towards the electrochemical oxidation of methanol was studied in order to determine their viability as electrocatalysts for DMFCs. Figure 4.14 and 4.15 illustrate cyclic voltammograms recorded at room temperature for the catalysts studied in a 2 M CH_3OH + 0.5 M H_2SO_4 solution.

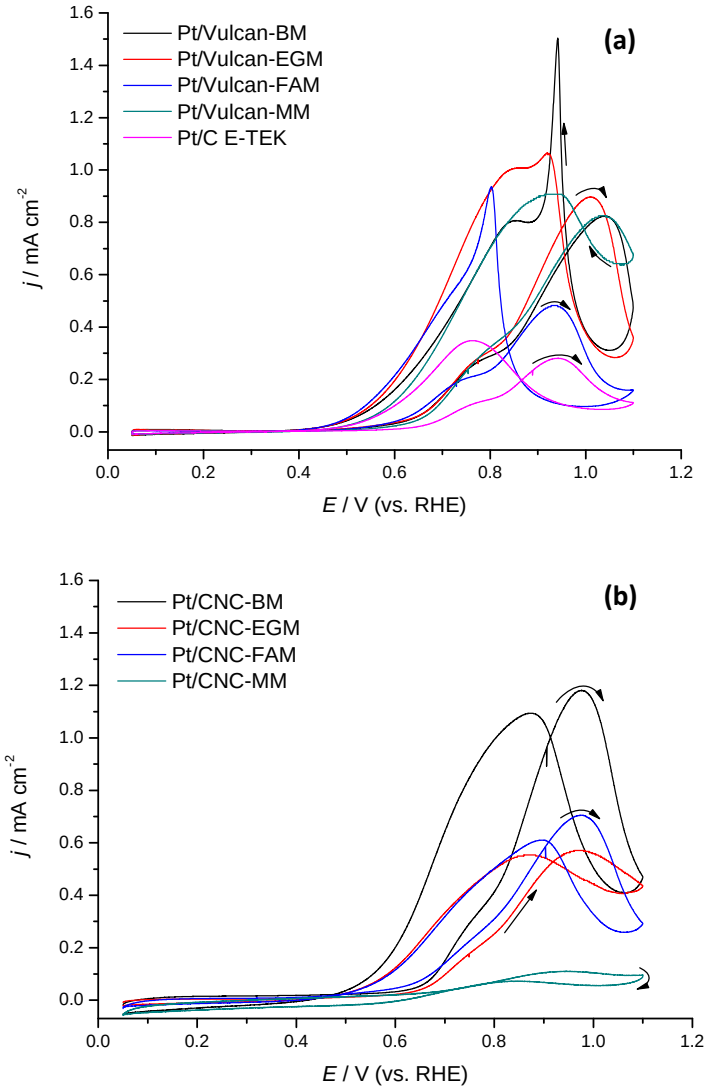

Figure 4.14. *Cyclic voltammograms for Pt/Vulcan (a) and Pt/CNC (b) electrocatalysts in 2 M CH_3OH+ 0.5 M H_2SO_4.υ = 0.02 V s^{-1}; T = 25 ºC.*

Pt based catalysts presented an irreversible behavior for methanol electrooxidation, the onset potential occurred at around 0.60 V vs. RHE for all them.

Watanabe et al. [WATANABE 1989] examined the influence of platinum crystallite dispersion on the electrocatalytic oxidation of methanol, affirming no crystallite size effects (even for crystallites as small as 1.4 nm diameter). For this reason, the results are entirely comparable. The highest current density was achieved by the Pt/CNC-BM catalyst during the positive scan at potentials around 0.98 V, corresponding to methanol oxidation. This result could be associated to the higher CO tolerance of this catalyst, as shown above. Another peak at around 0.85 V was observed during the backward scan, which is attributed to the oxidation of the intermediates formed during methanol oxidation.

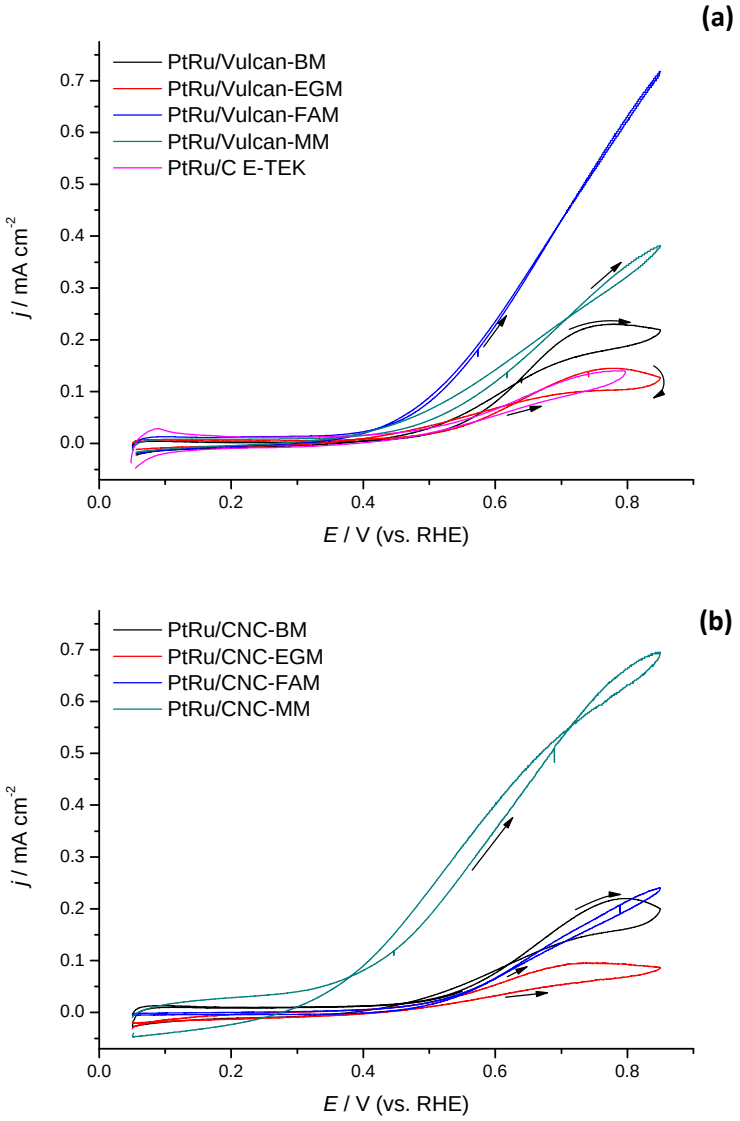

Figure 4.15. *Cyclic voltammograms for the PtRu/Vulcan (a) and PtRu/CNC (b) electrocatalysts in 2 M CH_3OH+ 0.5 M H_2SO_4. υ = 0.02 V s^{-1}; T = 25 ºC.*

For Pt-Ru catalysts, the onset potential shifted to more negative potentials respect to the corresponding Pt catalysts, varying between 0.3 and 0.5 V. The PtRu/CNC-MM catalyst showed the highest activity towards methanol oxidation. For this catalyst, the current density grew faster than for the commercial PtRu/C from E-TEK. It was found that PtRu/CNC-MM catalyst displayed a 5-fold higher specific current density than the commercial PtRu/C catalyst at 0.60 V vs. RHE. This result is in agreement with that published by Jusys et al. [JUSYS 2003], confirming that at positive potentials (0.6-0.65 V) the Pt-rich catalysts are more active in the MOR.

Potentiostatic current density-time (*j-t*) curves were recorded in a 2 M CH_3OH + 0.5 M H_2SO_4 solution, at 0.60 V for 900 s, in order to determine the performance of the catalysts towards methanol electrooxidation.

Figures 4.16 and 4.17 show the potentiostatic current densities, normalized by the electroactive surface area, as a function of time at 0.60 V vs. RHE. In all cases, a stable performance was achieved in a short time. It can be observed that for the Pt-Ru catalysts, the values reached were higher than those for the corresponding Pt catalysts. The response increased in the following order: Pt/CNC-MM < Pt/CNC-FAM < PtRu/CNC-EGM < Pt/CNC-EGM ~ Pt/C E-TEK < PtRu/CNC-FAM < Pt/CNC-BM ~ Pt/Vulcan-MM < PtRu/Vulcan BM < PtRu/CNC-BM < Pt/Vulcan-BM < Pt/Vulcan-EGM < PtRu/Vulcan-EGM < Pt/Vulcan-FAM < PtRu/Vulcan-MM ~ PtRu/C E-TEK < PtRu/Vulcan-FAM < PtRu/CNC-MM. These values followed the same trend observed by cyclic voltammperometry.

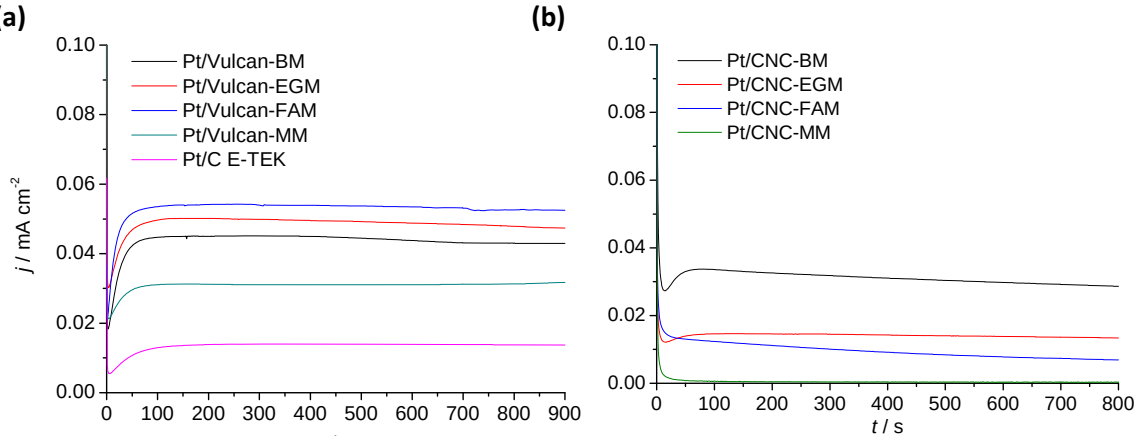

Figure 4.16. *Chronoamperometric curves for the Pt/Vulcan (a) and Pt/CNC (b) electrocatalysts, recorded in 2 M CH_3OH + 0.5 M H_2SO_4 solution, at E = 0.60 V and room temperature.*

Although a real comparison between the different catalysts is not easy, because different Pt-Ru ratios were obtained, these results are in agreement with that published by *Jusys et al.* [JUSYS 2003] confirming that at positive potentials (0.6-0.65 V) the Pt-rich catalysts are more active towards MOR.

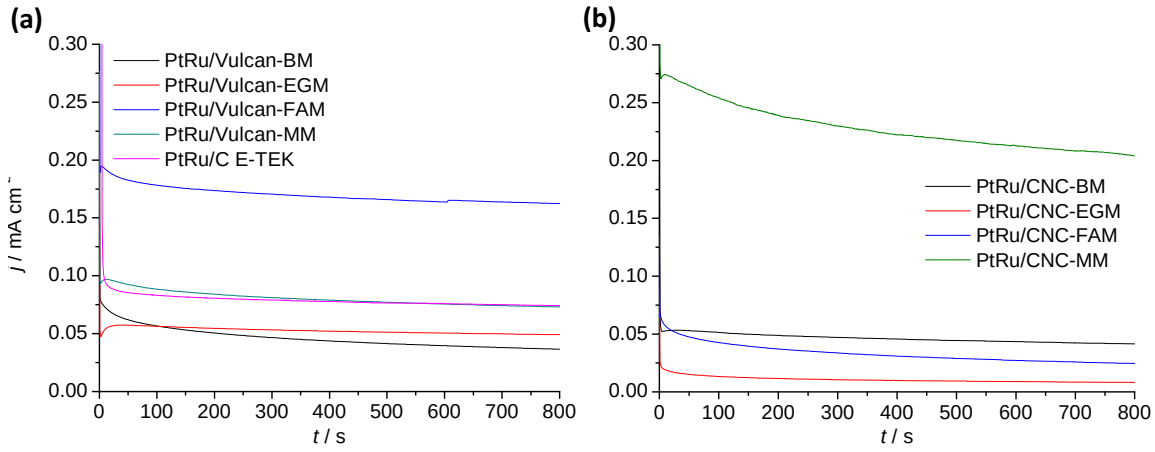

Figure 4.17. *Chronoamperometric curves for the PtRu/Vulcan (a) and PtRu/CNC (b) electrocatalysts, recorded in 2 M CH_3OH + 0.5 M H_2SO_4 solution, at E = 0.60 V and room temperature.*

Although the use of carbon nanocoils facilitates CO oxidation (see section 4.4.3.1), as a general rule, it can be seen that the performance of catalysts for the oxidation of methanol does not improve considerably. This could be explained, from the viewpoint of the reaction mechanism of the methanol oxidation (see Figure 1.5), stating that the limiting step in this reaction is not CO_{ads} oxidation to CO_2, but the oxidation of reaction intermediates formed.

To make a more precise study, we carried out a comparative analysis of the methanol oxidation reaction mechanism on the catalysts Pt/CNC-BM, Pt/Vulcan-FAM, Pt/C E-TEK, PtRu/CNC-MM, PtRu/Vulcan-FAM and PtRu/C E-TEK by differential electrochemical mass spectrometry (DEMS). DEMS allows the detection of volatile and gaseous products and intermediates generated in electrochemical reactions with good sensitivity. Thus, CO_2 conversion efficiencies were evaluated during the alcohol oxidation reaction.

Formic acid (m/z = 46) formation cannot be monitored directly by DEMS during methanol oxidation, due to the mass spectra overlap with that of CO_2^- (m/z = 45). However, formic acid reacts with methanol to form methylformate, and therefore,

formic acid formation in the MOR can be followed through methylformate, monitoring the ion current at m/z = 60.

Formaldehyde formation in the MOR cannot be monitored by DEMS, either directly or indirectly. The first is due to the overlap of the formaldehyde mass spectrum with that of methanol at m/z = 28-30. The latter results from the fact that the reaction between formaldehyde and methanol to form dimethoxymethane occurs only at elevated temperatures and/or high methanol concentrations and thus, cannot be used as indication for formaldehyde at room temperature and low methanol concentrations.

Figures 4.18 and 4.19 show the CVs (black line-upper pannel) and the MSCVs (Mass Spectrometric Cyclic Voltammetry) for the corresponding mass signals of CO_2 (m/z = 44) and formic acid (followed through methylformate formation, m/z = 60), during methanol electrooxidation. In the upper pannels, the faradic current expected for a 100% efficient conversion of methanol to CO_2 calculated from the m/z = 44 signal after calibration, was also included (red line). The difference in area between experimental (black curve) and theoretical (red curve) currents is the extra charge associated with the formation of products different to CO_2.

For these experiments, a low concentration of alcohol was used due to the fact that, with higher concentrations a continuous increase of the CO_2 signal (m/z = 44) was observed, which made the quantitative analysis difficult.

In the case of the supported platinum electrocatalysts, the m/z = 44 ion current (middle panels) generally traces the faradaic methanol oxidation reaction (MOR) current, taking into account the time constant of the DEMS cell. A closer comparison of faradaic (black line, upper panels) and m/z = 44 ion currents reveals that the ratio in MOR current depends on the potential scan direction, with relatively higher mass spectrometric currents in the negative-going scan. Also the MSCVs for methylformate formation (m/z = 60) largely follow the faradaic current for MOR. However, the separation between the positive- and negative-going potential scans is larger compared to the m/z = 44 mass signal, although the time constant should be essentially the same. This deviation could be explained by the relatively slow ester formation reaction between formic acid and methanol, compared to the instantaneous CO_2 formation [JUSYS 2003].

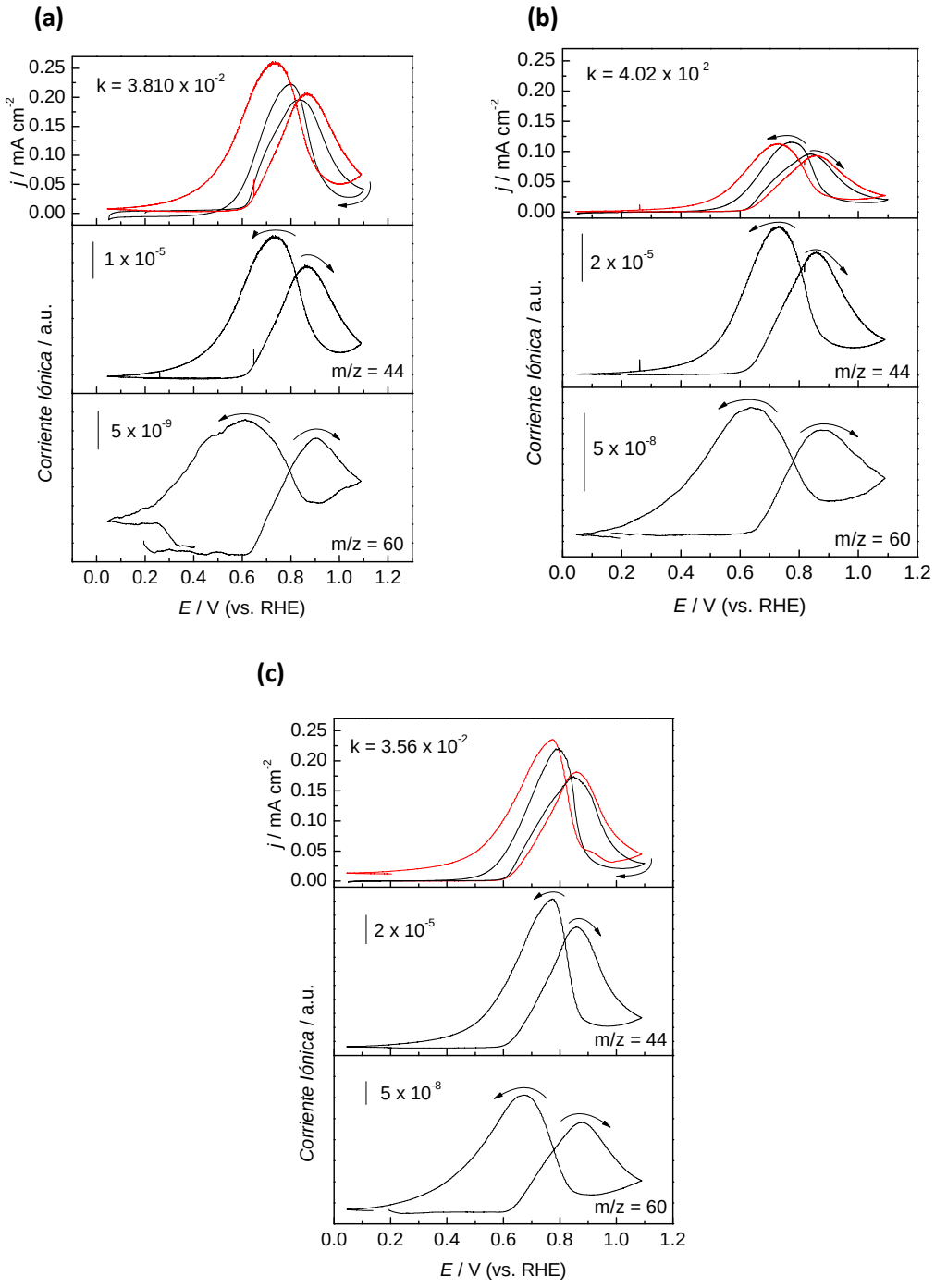

Figure 4.18. *CVs and MSCVs for 0.5 M methanol oxidation in 0.5 M H_2SO_4 at Pt/CNC-BM (a), Pt/Vulcan-FAM (b) and Pt/C E-TEK (c). υ = 0.001 V s^{-1}; T = 25 ºC.*

Regarding the PtRu-supported electrocatalysts, the formation of CO_2 starts at 0.4 V, *i.e.* about 200 mV more negative than on Pt. The formation of methylformate, on the other hand, starts at 0.5 V, which is the same as for Pt.

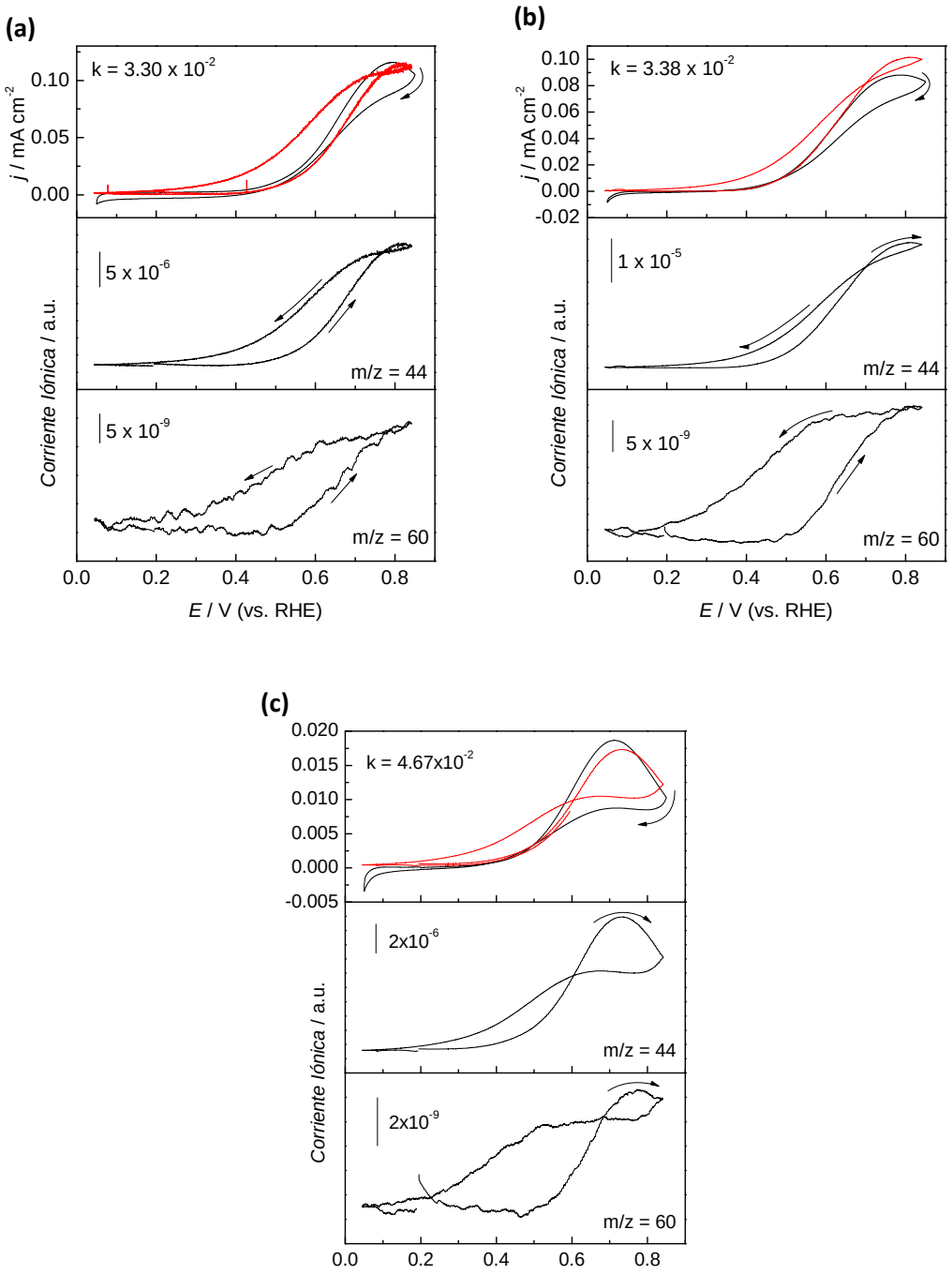

Figure 4.19. *CVs and MSCVs for 0.5 M methanol oxidation in 0.5 M H_2SO_4 at PtRu/CNC-MM (a), PtRu/Vulcan-FAM (b) and PtRu/C E-TEK (c). υ = 0.001 V s^{-1}; T = 25 ºC.*

A more accurate comparison between the electrodes is possible from the faradic and ion-charge integrations during the forward scans of the CV and MSCV for CO_2.

The average efficiency for each catalyst can be calculated on the basis of these integrated values and is presented in Table 4.11. It is observed that the electrodes presented similar CO_2 conversion efficiencies (~100 %). The high values of CO_2 conversion efficiencies are related to the re-adsorption and re-oxidation of by-products. Nevertheless, the electrodes synthesized using CNC as support showed the lowest CO_2 conversion efficiencies, which could be associated to a higher formation of by-products (*e.g.* formic acid and formaldehyde).

Therefore, it can deduced that the oxidation of methanol on the Pt/CNC catalyst is not a direct reaction and occurs *via* intermediates. Pt-CNC interactions promote the oxidation of CO_{ads}, while it is not helpful in the oxidation reaction intermediaries, so the obtained current densities are lower (Figure 4.16).

For the PtRu/CNC-MM catalyst, however, the current density reached after 800 s in the potentiostatic experiments (deduced from Figure 4.17) is higher. Thus, it can be deduced that the use of CNC, as support for Pt-Ru nanoparticles, facilitates the oxidation of reaction intermediates.

Table 4.9. *Calculated average efficiency of CO_2 conversion.*

Sample	CO_2 conversion efficiency (%)
Pt/CNC-BM	97
PtRu/CNC-MM	85
Pt/Vulcan-FAM	100
PtRu/Vulcan-FAM	100
Pt/C E-TEK	100
PtRu/C E-TEK	94

4.4.5. Ethanol oxidation

Nowadays, it is difficult to establish the appropriate catalyst to oxidize ethanol electrochemically. Besides platinum, other metals have been studied for the electrooxidation of ethanol, such as gold, rhodium or palladium, and they have shown some activity. However, only platinum-based materials show appropriate oxidation currents, especially in acid medium [TSIAKARAS 2007]; however, the efficiency of the DEFCs operating with these catalysts is still insufficient for practical applications. For these reasons, Pt catalysts supported on Vulcan and on CNC, synthesized by different

methods, were tested for the oxidation of ethanol. Figure 4.16 illustrates the CVs recorded in 2 M CH_3CH_2OH + 0.5 M H_2SO_4 at room temperature.

The curves for all catalysts displayed a rise in the current around 0.50 V during the positive-going potential scan, developing an anodic peak the position of which depends on the catalysts. On the backward scan, a new anodic contribution was observed, achieving a maximum also dependent on the catalyst. As can be observed, the onset for ethanol electrooxidation occurred between 0.50 and 0.64 V depending on the catalyst. For the same material, significant differences were found in the current densities achieved for the catalysts prepared using the different synthesis methods.

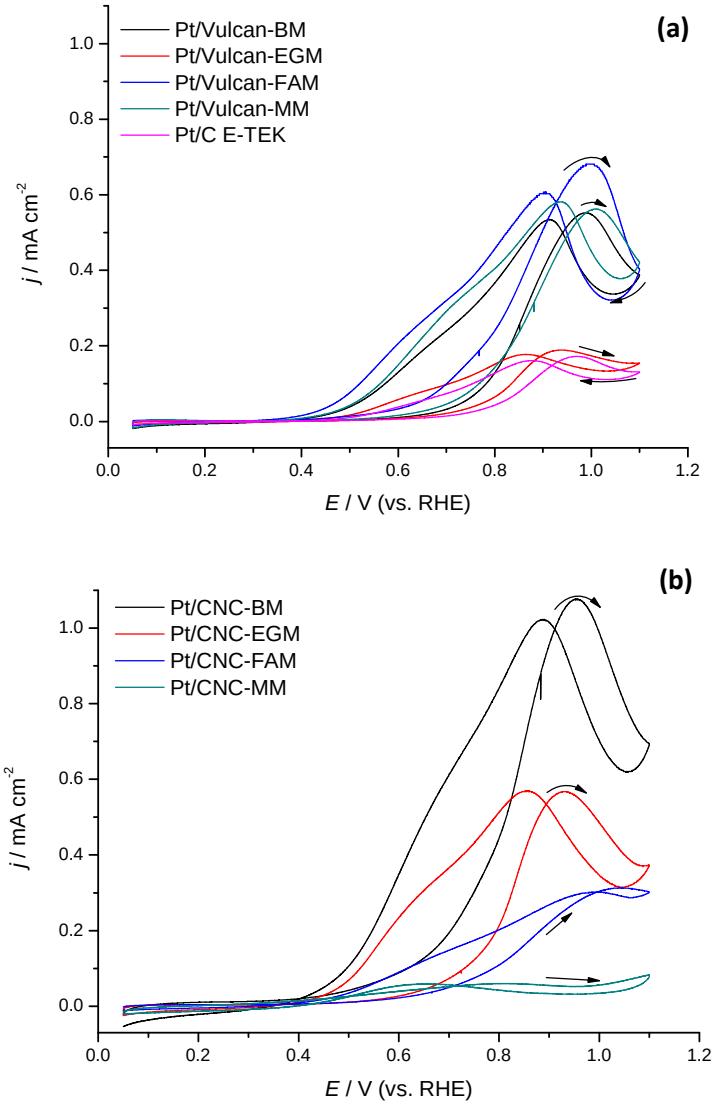

Figure 4.20. *Cyclic voltammograms for Pt/Vulcan (a) and Pt/CNC (b) electrocatalysts in 2M CH_3CH_2OH+ 0.5M H_2SO_4. υ = 0.02 V s^{-1}; T = 25 ºC.*

With the purpose of determining the performance of the catalysts towards ethanol electrooxidation under potentiostatic conditions, current-time curves were recorded at 0.60 V and 25 ºC during 850 s in the same solution (Figure 4.21). Pt catalysts based on CNCs prepared by BM and EGM presented higher quasi-stationary current densities, from chronoamperometric curves, than Pt catalysts based on Vulcan XC-72R. These values increased in the order Pt/CNC-MM < Pt/C E-TEK < Pt/Vulcan-EGM < Pt/Vulcan-BM < Pt/Vulcan-FAM= Pt/CNC-FAM < Pt/CNC-EGM < Pt/CNC-BM. However, in all cases, a stable performance was achieved in a short time. These results confirm that the Pt/CNC catalysts are notably more active in the electrooxidation of ethanol than catalysts supported on Vulcan XC-72R, commonly employed for DAFCs technical electrodes.

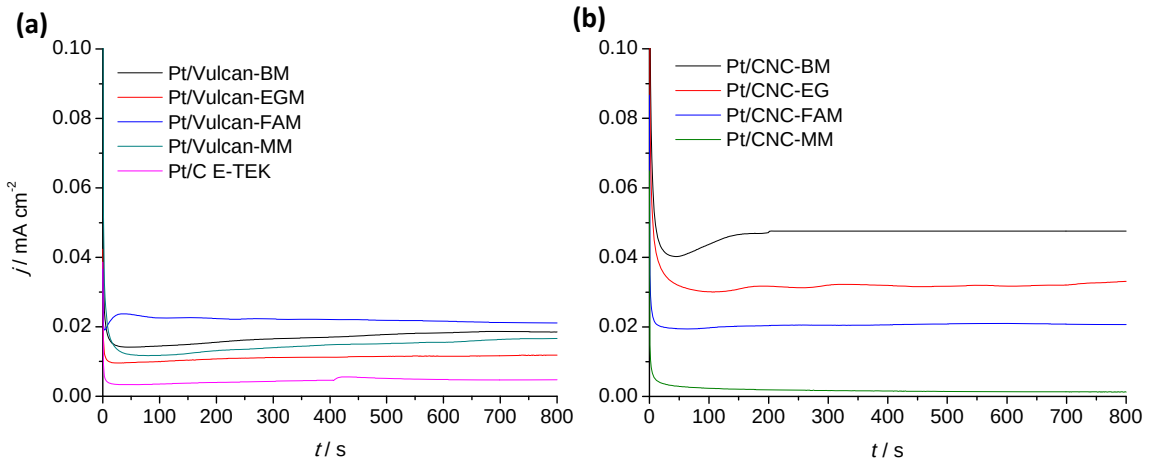

Figure 4.21. *Chronoamperometric curves for Pt/Vulcan (a) and Pt/CNC (b) electrocatalysts, recorded in 2 M CH_3CH_2OH + 0.5 M H_2SO_4 solution, at E = 0.60 V and room temperature.*

In general, the electrocatalysts that use CNC as support presented better performance for the ethanol oxidation. During ethanol oxidation, the limiting stage is the cleavage of the C-C bond and not the oxidation of the absorbed CO. So, the improvement in the current densities by using CNC could be attributed to metal-CNC interactions that aid this process.

Despite significant efforts and numerous studies, the mechanism of the ethanol electrooxidation reaction (EOR) still remains unclear or even contradictory. There is general agreement that ethanol electrooxidation proceeds *via* a complex multi-step mechanism, which involves a number of adsorbed intermediates and also leads to different by-products for incomplete ethanol oxidation [HITMI 1994]. Adsorbed CO, C1 and C2 hydrocarbon residues have been identified as major adsorbed intermediates by

means of in situ infrared spectroscopy and DEMS [IWASITA 1994, SCHMIEMANN 1994], while acetaldehyde and acetic acid have been detected as the main by-products using infrared spectroscopy, ion and liquid chromatography [HITMI 1994, LAMY 2001].

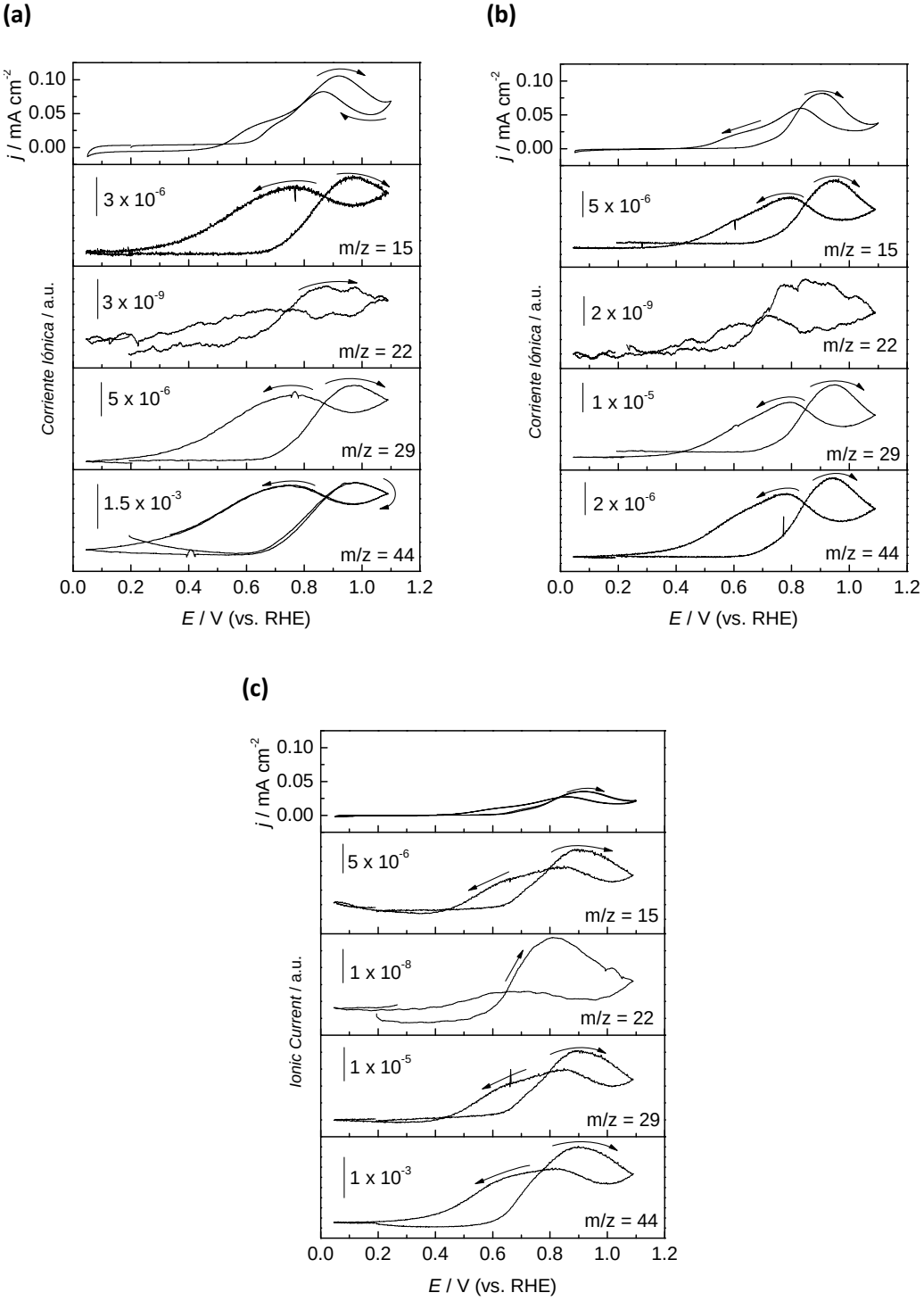

Figure 4.22. *CVs and MSCVs for 0.5 M ethanol oxidation in 0.5 M H_2SO_4, at Pt/CNC-BM (a), Pt/Vulcan-FAM (b) and Pt/C E-TEK (c). υ = 0.001 V s^{-1}; T = 25 ºC.*

In this case, DEMS studies have been used to provide information about the nature of intermediates and oxidation products. Due to the interferences between the ion currents of the major ethanol electrooxidation products CO_2^+ and CH_3CHO^+, which are both at m/z = 44, the formation of carbon dioxide and acetaldehyde were monitored individually at m/z = 22 (CO_2^{++}) and m/z = 29 (COH^+), respectively. However, the signal for CO_2 formation was very low, and a quantitative analysis was not possible. Additionally, the m/z = 15 signal, related to methane and/or to another ionic fragment of acetaldehyde formation (CH_3^+), was followed.

From Figure 4.29, it becomes clear that the electrochemical responses of m/z = 15, 29 and 44 signals are similar and can be related to acetaldehyde formation. All of them present the onset potential at ca. 0.40 V, simultaneously with the onset of the ethanol oxidation current. On the other hand, the signal for CO_2 formation (m/z = 22) is very low and occurs at potentials positive of ca. 0.5 V in the positive going scan. This fact could be explained according to the mechanism of ethanol electrooxidation on Pt [CAMARA 2004]: acetaldehyde readsorbs on Pt as acetyl species and dissociates into CH_x fragments and CO that can be completely oxidized to CO_2 at higher electrode potentials.

4.4.6. Formic acid oxidation

Formic acid has been investigated as an alternative fuel to hydrogen and methanol in PEMFCs. Formic acid is a strong liquid electrolyte, hence, it is expected to facilitate both electronic and proton transport within the anodic compartment of the fuel cell.

Nanostructured Pt catalysts for electrooxidation of formic acid are poisoned by adsorbed CO, an intermediate of the reaction. This suggests that the decomposition of HCOOH on platinum nanoparticles is likely to proceed *via* a dual path mechanism [CAPON 1973]. Nevertheless, it occurs primarily *via* a direct pathway on Pd, avoiding the formation of CO as intermediate. For this reason, only the palladium electrocatalysts were tested for the oxidation of formic acid.

Formic acid oxidation was studied using cyclic voltammetry and chronoamperometry. Cyclic voltammograms were recorded in 2 M HCOOH + 0.5 M

H_2SO_4, at a scan rate of 0.02 V s^{-1}. Potentiostatic current density - time (*j*-*t*) curves were recorded in the same solution, at 0.60 V, for 900 s.

Cyclic voltammograms showing the oxidation of formic acid at Pd/CNC, Pd/Vulcan and Pd/C E-TEK are contrasted in Figure 4.23. All three catalysts presented a broad peak on the forward scan and a drop in current as Pd oxide is formed, inhibiting further formic acid oxidation. On the backward scan, once the Pd surface is recuperated, formic acid is once again oxidized. Similar current densities were obtained on the forward and backward scans, indicating a high tolerance towards electrode poisoning [MIYAKE 2008]. Somewhat lower currents were obtained on Pd/Vulcan than on the other two electrocatalysts.

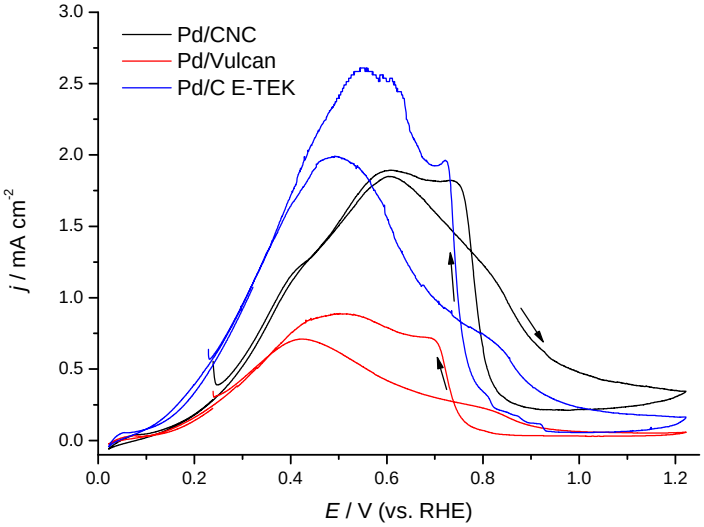

Figure 4.23. *Cyclic voltammograms for Pd/CNC, Pd/Vulcan and Pd/C from E-TEK electrocatalysts recorded in 2 M HCOOH + 0.5 M H_2SO_4. υ = 0.020 V s^{-1}; T = 25 ºC.*

Chronoamperometric transients at 0.6 V, in the presence of HCOOH, are compared in Figure 4.18. All the chronoamperograms are characterized by a decrease of the current with time, associated with the deactivation of the electrocatalysts. In general, the deactivation rate appears similar in all samples. However, Pd/C E-TEK needed more time to stabilize. At short times (< 600 s), the highest current density was obtained for the Pd/C E-ETEK but, after 700 s, the Pd/CNC sample was the most stable and gave the highest current density. It should be noticed that the relative changes in the current densities from the chronoamperograms are consistent with the cyclic voltammograms (Figure 4.18). From this analysis, it emerged that the most active catalyst is Pd/CNC.

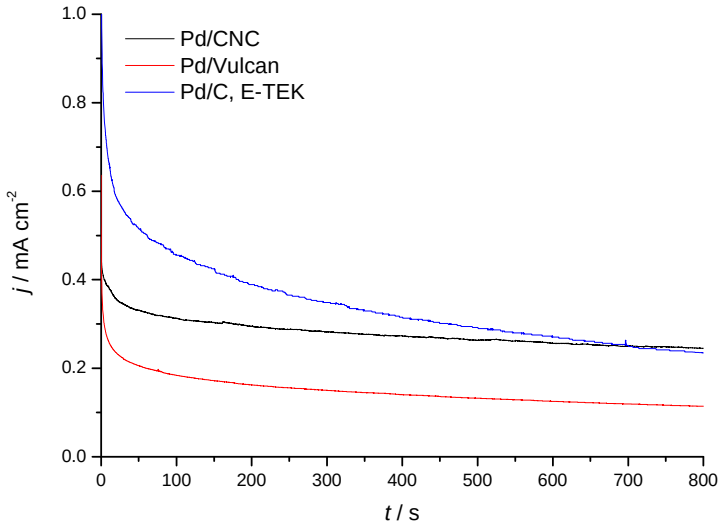

Figure 4.19. *Chronoamperometric curves for the Pd based electrocatalysts, recorded in 2 M HCOOH + 0.5 M H_2SO_4 solution, at E = 0.60 V and room temperature.*

4.5. CORE-SHELL STRUCTURED CATALYSTS

It is generally agreed that HCOOH oxidation at Pd occurs primarily *via* a direct pathway, avoiding the formation of CO as an intermediate. Nevertheless, Pd and Pd-based catalysts undergo substantial deactivation under operational conditions and a discussion has emerged in the literature regarding the long-term stability of Pd catalysts in direct formic acid fuel cells [YU 2009[a]].

The epitaxial growth of thin metallic films on a foreign substrate can lead to substantial changes in the structure of the *d*-band, which plays a crucial rol in the catalytic activity of the material [MONTES DE OCA 2011, EL-AZIZ 2002]. Therefore the role of the Pd lattice strain on the electrocatalytic activity of Pd shells grown on Au nanoparticles was examined.

On the other hand, investigations on the role of substrate on the reactivity of already formed nanostructures, *e.g. via* colloidal synthesis, are relatively scarce. Such an approach allows decoupling effects of the support on particle growth from specific chemical interactions linked to the reactivity of the metallic centers, *i.e.* any effect observed in the catalytic activity can be directly linked to the support on the electrochemical activity and not to particle size, distribution, etc. The effect of the support was studied, establishing comparisons between electrochemical behavior of the

same core-shell particles assembled at In-doped SnO_2 electrodes (ITO) and supported on Vulcan XC-72.

4.5.1. Synthesis

The preparation method of Au-core and Pd-shell nanoparticles (CS) was as reported in [MONTES DE OCA 2011]. The Au-Pd nanoparticles were synthesized by selective reduction of H_2PdCl_4 on 19 nm Au seeds in the presence of ascorbic acid. Different shell thicknesses were obtained by varying the amount of 0.1 M H_2PdCl_4 added to 50 mL solutions of the Au nanoparticles, placed in an ice bath and under vigorous stirring. This step was followed by adding an excess amount of L-ascorbic acid (0.1 M) dropwise, in order to avoid the formation of isolated Pd clusters.

The synthesis of Pd nanoparticles was performed by reduction of hexachloropalladate (IV) acid in the presence of trisodiumcitrate. The solution containing Na_2PdCl_4 was brought to its boiling point under vigorous agitation, and trisodium citrate was added. The mixture was kept under reflux and vigorous stirring for 4 h and the solution was then allowed to cool down at room temperature.

The electrostatic assembly of nanostructures was performed following previously established methods. Nanoparticles were adsorbed on poly-L-lysine hydrobromide modified ITO electrodes [MONTES DE OCA 2011, MONTES DE OCA 2012].

To prepare the supported samples, Vulcan (C) was used as support material. Controlled amounts of carbon, calculated to obtain a metal loading of 20 wt.%, were added to the colloidal solutions and stirred during 48 h. The as-prepared carbon-supported nanoparticle powders were filtered, washed with milli-Q water and dried at 60 ºC overnight.

4.5.2. Physicochemical characterization

Representative TEM images of Au-Pd CS nanoparticles are shown in Figure 4.25. As the core size is kept constant in the synthesis, the increase of shells manifests itself by an increase of overall particle size. The sequence of TEM images shows a clear

contrast between Au cores and Pd shells, confirming a systematic increase in Pd thickness. The average diameter of the various nanostructures corresponds to the following: 19.3±1.2 nm Au, 21.8±1.1 nm (CS1), 24.7±1.3 nm (CS3), 29.5±1.2 nm (CS5), 38.9±1.5 nm (CS10), and 10.2±1.5 nm Pd.

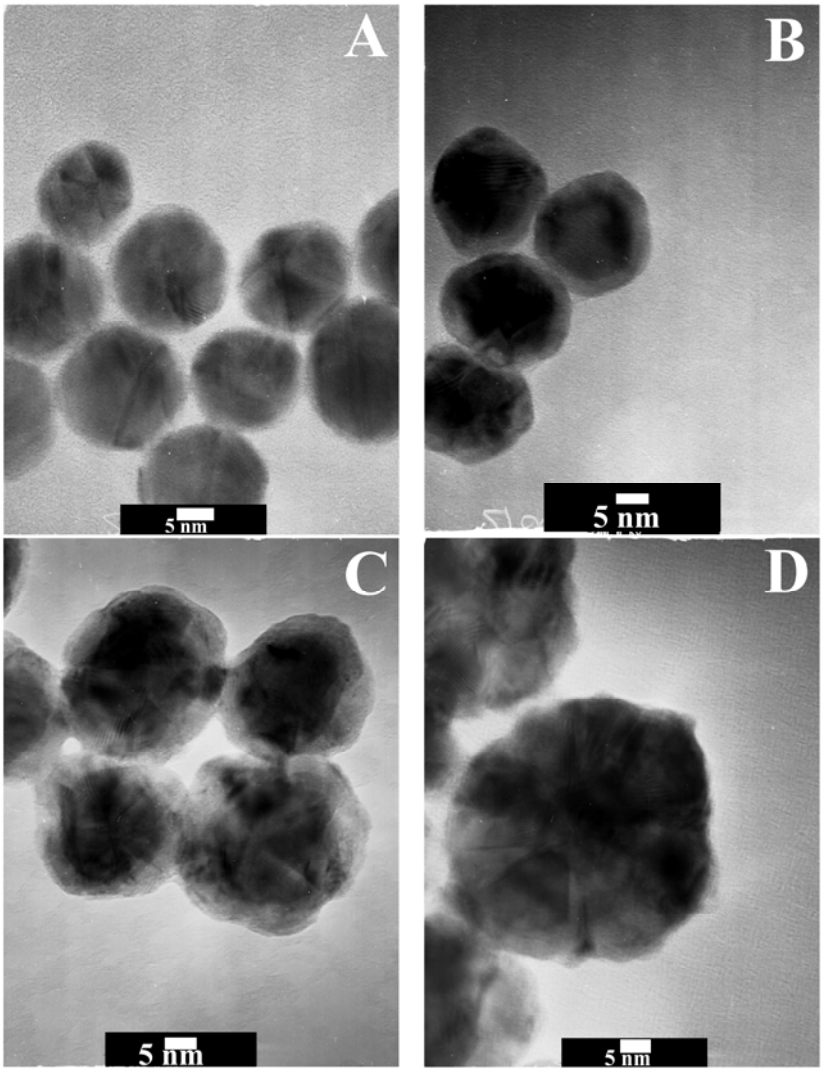

Figure 4.25. *HRTEM images of the core-shell nanoparticles featuring 19.3±1.2 nm Au cores, coated with Pd shells with thickness of 1.3±0.09 nm (A), 2.7±0.1 nm (B), 5.1±0.9 nm (C) and 9.9±1.0 nm (D) [MONTES DE OCA 2012].*

Average diameters of the core-shell structures, obtained from at least 200 particles per sample, and their elementary composition, estimated from EDX measurements, are summarised in Table 4.9. The mass ratio from the EDX data was highly consistent with the composition of the synthesis bath, demonstrating that Pd nucleation occurs exclusively at the Au surfaces.

Table 4.10. *Average diameter (D), Pd thickness (δ) and Au:Pd weight composition.*

Sample	D / nm	δ / nm	Au:Pd mass ratio (%)
Au	19.3 ± 1.2	---	100:0
CS1	21.8 ± 1.1	1.3 ± 0.9	80:20
CS3	24.7 ± 1.3	2.7 ± 1.0	60:40
CS5	29.5 ± 1.2	5.1 ± 0.9	40:60
CS10	38.9 ± 1.5	9.9 ± 1.1	20:80
Pd	10 ± 1.8	---	0:100

TEM images of the various CS nanostructures supported on Vulcan (Figure 4.26) showed that the nanoparticles were well dispersed in the carbon support, ensuring a high metal dispersion in the catalysts, with very low density of aggregates.

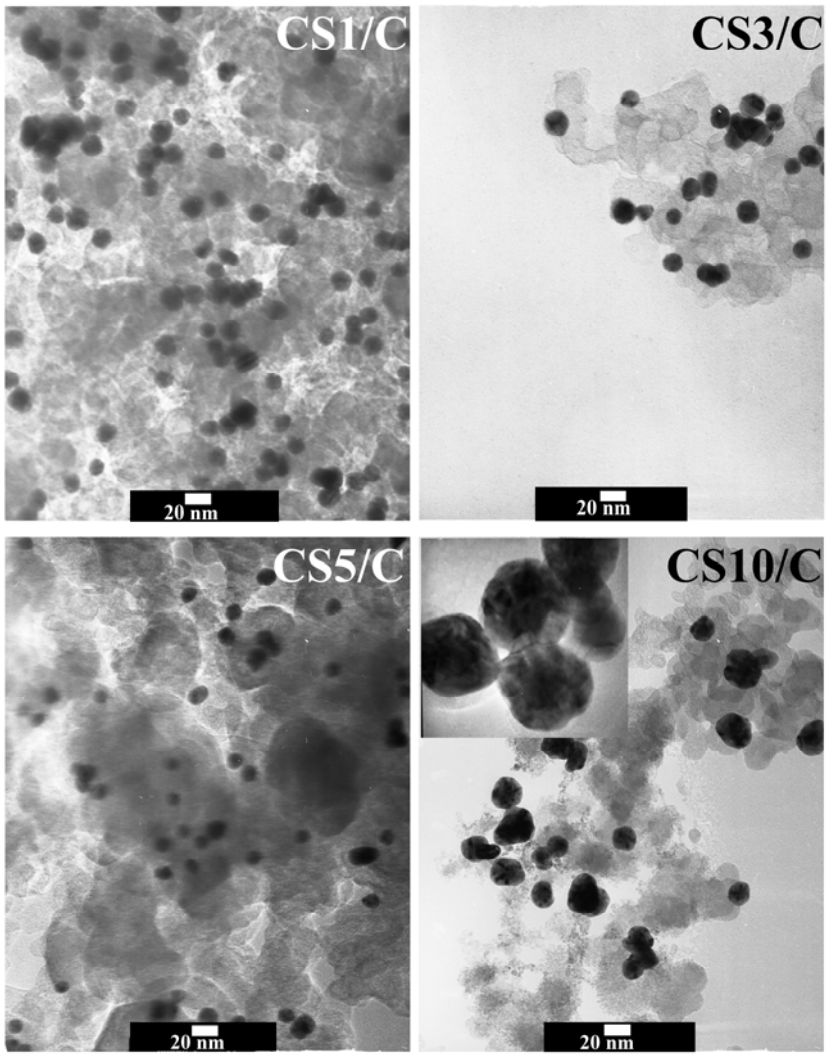

Figure 4.26. *TEM images of the various CS nanoparticles supported on Vulcan. The inset in CS10 is an image with higher magnification, showing the contrast between the Au core and the Pd shell [CELORRIO 2012].*

Table 4.11 summarizes the average metal loading of each catalyst as estimated from EDX. The total metal loading in the catalysts were in the range of 15 to 20%.

Table 4.11. *Average metal loading on the Vulcan support.*

Sample	Metal loading (wt.%)
Au/C	19.5 ± 1.2
CS1/C	15.0 ± 1.9
CS3/C	19.2 ± 2.1
CS5/C	18.5 ± 2.9
CS10/C	17.5 ± 1.4
Pd/C	18.4 ± 2.5

Figure 4.27 shows the powder X-ray diffractograms for the different catalysts. Au samples features sharp diffraction peaks due to the well-defined polycrystalline structure of Au. The signals at 38.3°, 43.9°, 64.8°, 77.7° and 81.5° are due to the (111), (200), (220), (311) and (222) planes of the face-centered cubic (fcc) gold phase, respectively. The highest diffraction peak can be seen at 38.3°, suggesting that Au nanoparticles have a strong (111) orientation. On the contrary, no clear diffraction peaks were observed for the Pd samples, suggesting a poor crystalline structure of the mono-metallic nanoparticles.

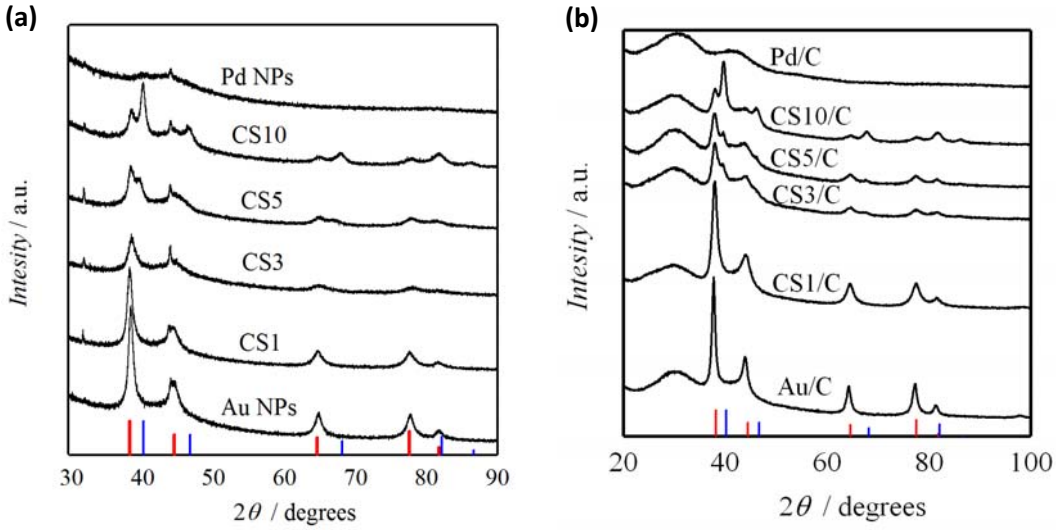

Figure 4.27. *Powder XRD diffractograms of the various metallic nanostructures assembled on ITO (a) or supported on Vulcan (b). The red lines at the bottom of the graph, at 38.1°, 44.4°, 64.6°, 77.5° and 81.7° indicate the standard Au diffraction pattern (PDF 040784), while the blue lines at 40.1°, 46.7°, 68.1°, 82.1° and 86.6° belong to Pd (PDF 461043) [MONTES DE OCA 2012, CELORRIO 2012].*

The presence of Au cores templates the growth of the Pd shells, allowing the progressive appearance of Pd diffraction peaks on the core-shell samples. The characteristic diffraction peak attributed to Pd (111) at 2θ = 40.2° appears in CS3, CS5 and CS10 samples, and its intensity increases with increasing Pd thickness. In addition to the peaks associated with the metallic nanostructures, samples supported on Vulcan (Figure 4.22.b) exhibit a broad peak at 2θ = 26º, characteristic of the plane (002) of graphite from the Vulcan support.

4.5.3. Carbon monoxide oxidation

Figure 4.28 shows a comparison of carbon monoxide oxidation on the different CS nanoparticles supported on ITO (a) and Vulcan (b). It is shown that CO oxidation is markedly dependent on Pd thickness. CO stripping on the CS1 and CS3 nanoparticles was observed at more positive potentials than those of pure Pd, CS5 and CS10 nanoparticles. It is also interesting to note that a similar shift in the potential position was observed in the Pd oxide formation. CO oxidation, which is enabled and accompanied by Pd oxide formation, is influenced by the adsorbed oxygen species on Pd surfaces [EL-AZIZ 2002]. A sharp CO stripping peak was observed for CS5 and CS10 nanostructures, with the onset at the same potential of Pd nanoparticles.

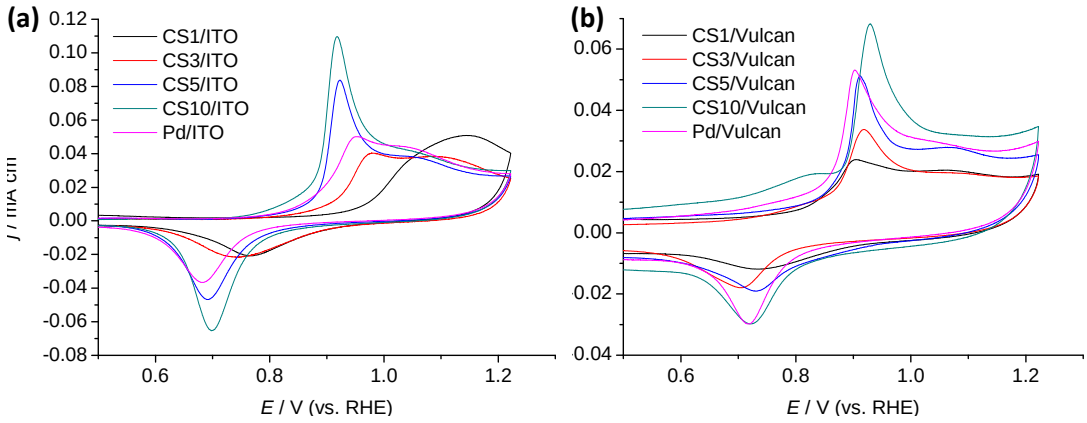

Figure 4.28. *First scan of the CO-stripping voltammetry on the nanoparticles assembled on ITO (a) or supported on Vulcan XC-72 (b).*

In the case of Vulcan-supported nanoparticles (Figure 4.28.b), a shift of the peak potential to slightly more positive potentials was observed as the palladium thickness increased, indicating a slower transfer kinetics of the CO oxidation process. On the

other hand, the oxidation peak was narrower as the Pd thickness increased, indicating that more of CO_{ads} was oxidized at lower potentials. Furthermore, it should be noted that the current densities also increased, as the palladium thickness increased.

Figure 4.29 shows that average charge density of CO stripping (Q_{CO}), which is indicative of CO coverage on the Pd surface, monotonically increases from 160 to 310 μC cm^{-2}, with increasing palladium thickness. CS10 nanoparticles present a value close to polycrystalline Pd, as expected from the small value of the Pd lattice strain [MONTES DE OCA 2011]. On the other hand, CS1 exhibits a comparable charge density to a pseudomorphic Pd overlayer on Au (111), which has been reported as 113 μC cm^{-2} [EL-AZIZ 2002]. The charge density of Pd nanoparticles is 257 μC cm^{-2}, which was lower than that on CS10. The diference of charge densities between Pd and CS10 nanoparticles can be related to poor crystalline structure of Pd nanoparticles. CO adsorption on CS nanoparticles is effectively dependent on crystalline structure and the strained Pd shell thickness.

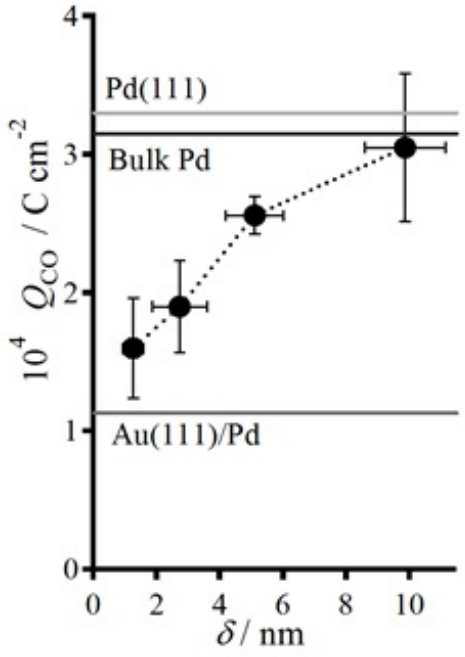

Figure 4.29. A*verage charge density of CO stripping (Q_{CO}) as a function of Pd thickness in Au-Pd core-shell nanostructures.*

5.4.4. Formic acid oxidation

The catalytic properties of carbon supported Pd and Au-Pd nanoparticles were also evaluated for formic acid oxidation. Figure 4.30 shows cyclic voltammograms, recorded at room temperature, for Pd and Au-Pd CS assembled on ITO (a) and supported on Vulcan (b) in 2 M HCOOH + 0.5 M H_2SO_4 solution.

Formic acid oxidation starts at 0.12 V and continues until it reaches a maximum in the positive scan at 0.42 V. A slight shift of the current peak towards more negative potentials is observed with increasing Pd content. The drop in the current densities at more positive potentials is associated with the Pd oxide formation. In the backward scan, the surface remains inactive until the Pd oxide reduction takes place. The current densities for the negative and positive scans were nearly identical, while consecutive scans were highly reproducible (results not shown), indicating a low tendency for poisoning of electrode surfaces via adsorbed intermediates.

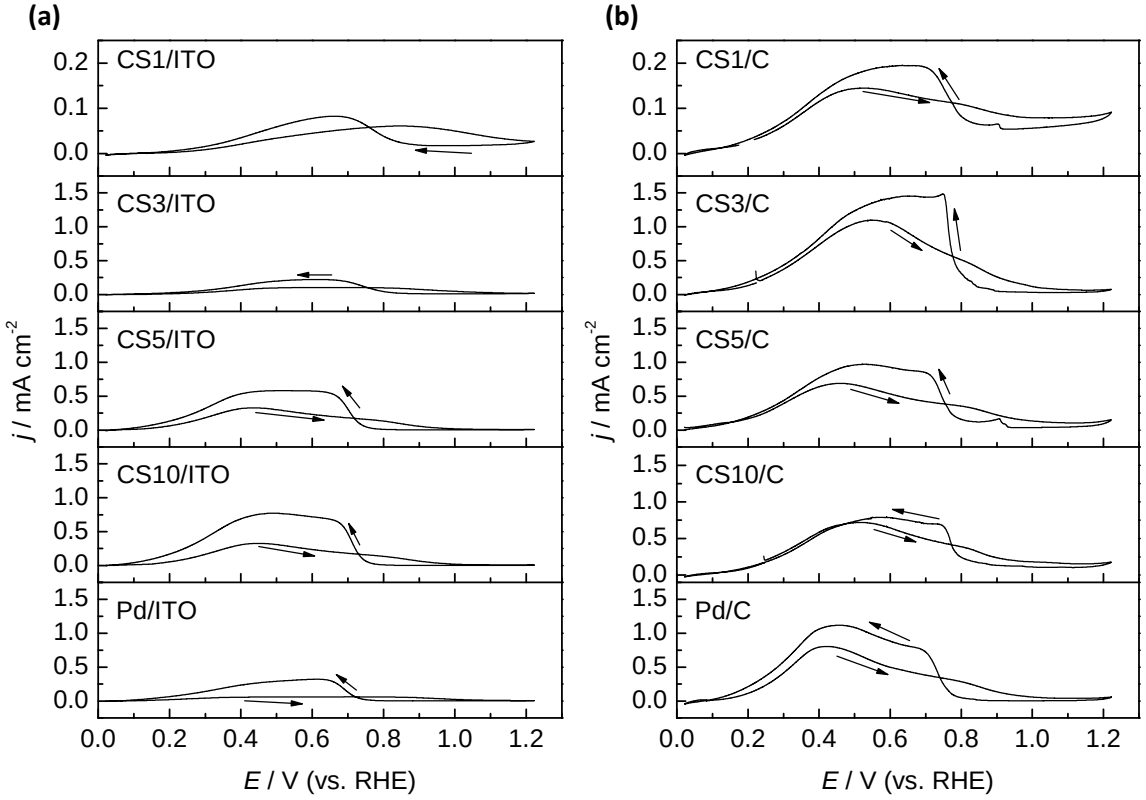

Figure 4.30. *Cyclic voltammograms of the core-shell and Pd nanoparticles assembled on ITO (a) and supported on Vulcan (b), at 0.02 V s^{-1}, in 2 M HCOOH + 0.5 M H_2SO_4.*

The currents were similar for CS with thick Pd shells and pure Pd NPs, while they are significantly lower for the thinnest Pd shell (CS1). A similar trend was observed on ITO assemblies and on Vulcan supported samples.

Figure 4.31 compares the average formic acid oxidation current density obtained after 750 seconds at 0.60 V (vs. RHE), for the various CS and Pd nanoparticles supported on Vulcan or assembled on modified ITO electrodes. The electrochemical active areas of the catalysts were determined from the charges obtained in CO-stripping voltammograms, using charge densities previously obtained as normalization parameters. The current densities associated with HCOOH oxidation strongly increase with increasing Pd thickness, probably due to the formation of highly reactive crystal facets on the thicker shells. Although CS/ITO and CS/C exhibit similar trends, the current densities obtained for the carbon-supported nanoparticles are significantly higher, particularly for the pure Pd NPs and those CS nanoparticles with thicker Pd layers. This behavior is connected to the slower deactivation rate of the catalytic active sites in the presence of the carbon support. Consequently, the overall activity of the catalysts strongly depends on the composition/structure of the metallic nanostructures, while the support plays an important role on the accumulation of intermediates at the active sites.

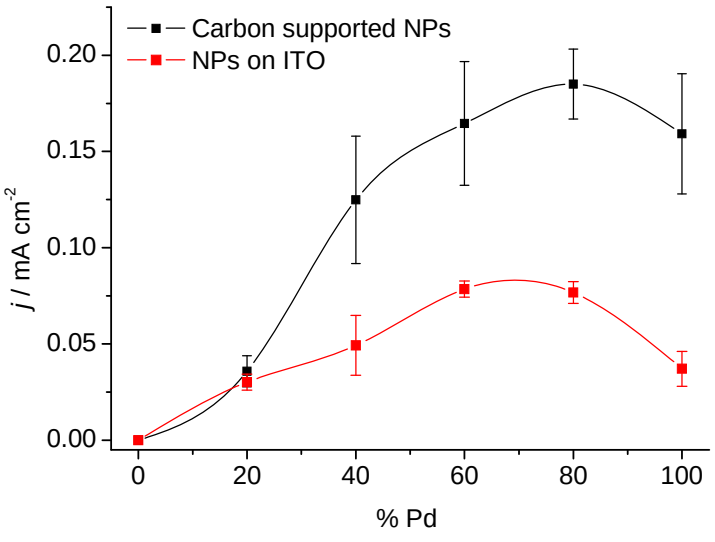

Figure 4.31. *Current density at 750 seconds associated with HCOOH oxidation at 0.60 V (vs. RHE), on the various metallic nanostructures assembled on ITO (red) and supported on Vulcan (black), in 0.5 M H_2SO_4 + 2 M HCOOH.*

The electrocatalysts supported on Vulcan, were studied by DEMS for the oxidation of formic acid, to better understand its reaction mechanism. It is known that formic acid oxidation occurs via a dual pathway mechanism. The most desirable reaction pathway for formic acid oxidation is *via* a dehydrogenation reaction, which does not form CO as a reaction intermediate. The direct formic acid oxidation pathway forms CO_2 directly. The second reaction pathway *via* dehydration, is somewhat similar to that of methanol oxidation, forming adsorbed CO as a reaction intermediate. Adsorbed OH groups are required to further oxidize the adsorbed CO intermediate to the gaseous CO_2 end product. Thus, the only reaction product to be monitored by DEMS is CO_2 (m/z = 44).

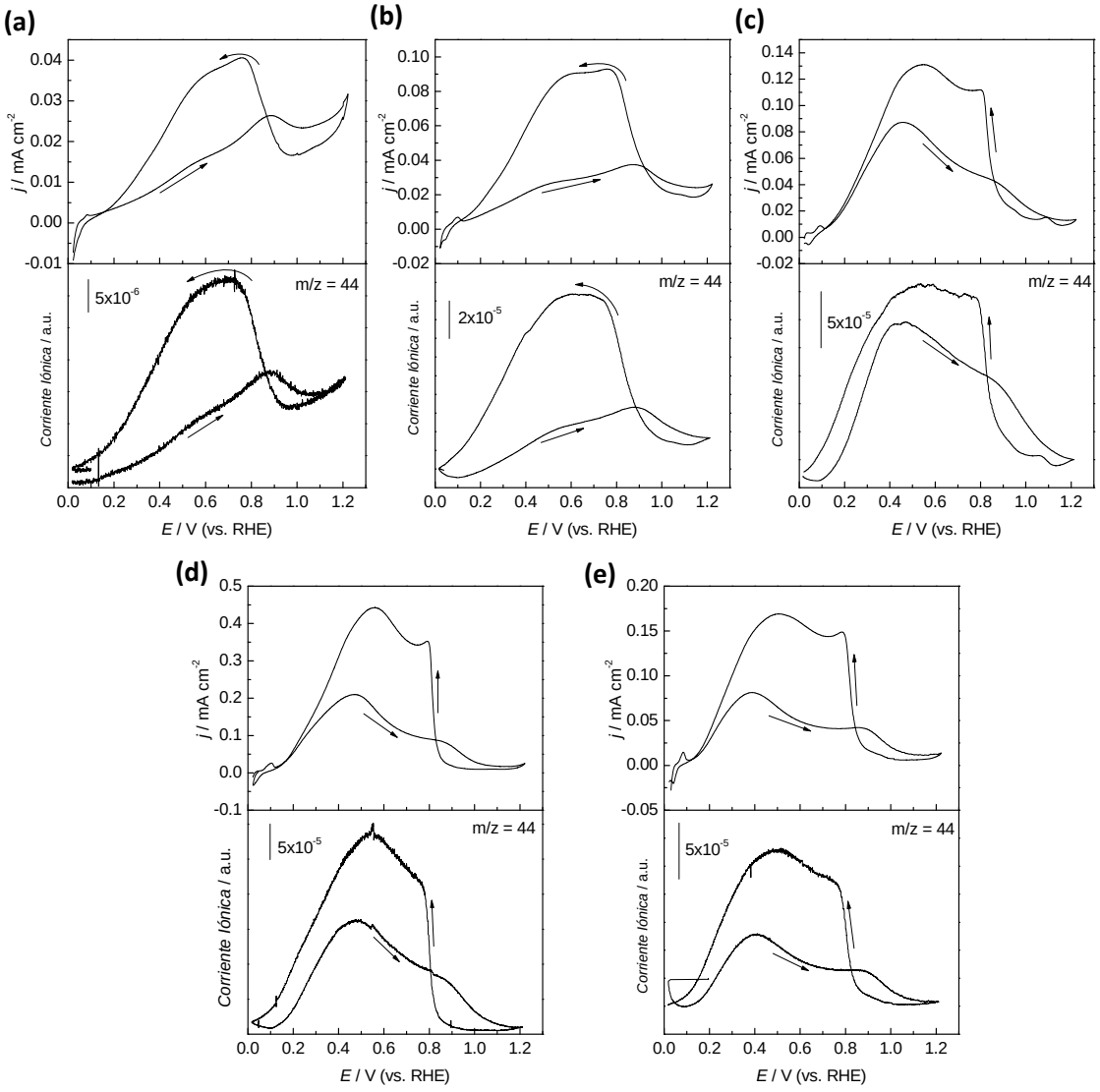

Figura 4.32. *DEMS experiments for the electrodes: CS1/C (a), CS3/C (b), CS5/C (c), CS10/C (d) and Pd/C (e); in 0.5 M HCOOH + 0.5 M* H^2SO_4. $\upsilon = 0.001\ V\ s^{-1}$; *T = 25 ºC.*

Figure 4.32 shows the CVs (upper pannels) and the simultaneously recorded MSCVs of m/z = 44 (lower pannels) of the different CS nanostructures supported on Vulcan in 0.5 M HCOOH + 0.5 M H_2SO_4. It can be seen that the CO_2 mass signals followed the corresponding voltametric profile for formic acid oxidation shown in the upper panels.

As expected, because CO_2 is the only product in formic acid oxidation, the current efficiencies for CO_2 formation were 100 %. The possible differences between the current in the CV and the Faradaic current calculated from the MSCV could be due to the contribution of the double-layer charging and OH adsorption-desorption processes to the current in the CV [CUESTA 2009].

It seems that Pd atoms provide a particular surface that allows formic acid to adsorb and dehydrogenate in an easy and very effective way. Consequently, adsorbed CO is not produced and the formic acid reaction is very fast.

4.6. CONCLUSIONS

In the present thesis, the synthesis of carbon nanocoils (CNC) was studied varying the molar ratios of the reactants used. The synthesis involved the heat treatment of composites formed by a carbon precursor (resorcinol-formaldehyde gel), silica, and a transition-metal salt (a mixture of cobalt and nickel salts). The characterization of these materials by means of different techniques allowed determing the textural and structural properties and the morphology of the synthetic carbon materials, confirming their high surface area, well-defined porosity, and good crystallinity. The material which presented the best characteristics to be used as support for noble metal catalysts for fuel cells was named CNC-3.

The surface of carbon nanocoils can be modified by replacing the HNO_3 treatment with other oxidation agents in liquid phase. CNC-3 was chosen, and carboxylic groups, lactones, phenols and quinones were created, increasing their number with the severity of the treatments. Carboxylic groups are stable only at low temperatures and increase the wettability of the carbon, facilitating the interaction of the metal precursor and the carbon during the impregnation stage. On the other hand,

phenols and quinones are stable at high temperatures and act as metal anchoring sites, which hinder the redistribution and agglomeration of metal during the reduction stage.

From the functionalization study, the material treated with concentrated nitric acid at room temperature for 2h (CNC-3 NcTa2) was selected to prepare supported platinum and platinum-ruthenium catalysts by different synthesis procedures. The same routes were used to prepare nanoparticles supported on Vulcan for comparison. In general terms, higher average particle sizes were obtained using CNC as support, due to the lower number of nucleation sites (in graphitized carbons, only the surface defects can function as nucleation sites). A strong influence of the synthesis method and the carbon support was found on the particle size.

CO oxidation on Pt and Pt-Ru electrocatalysts was favored by using CNC as support; CO_{ads} oxidation peaks were obtained at lower potentials than using Vulcan. However, in the case of Pt, this improvement did not aid methanol oxidation, obtaining higher current densities when Vulcan was used as support. This could be attributed to a higher formation of by-products on CNC samples (observed by DEMS analysis) that could poison the metal particles to a large extent. On the contrary, an improvement in the ethanol oxidation reaction was produced when CNC were used as support. As the key step in the EOR is the cleavage of the C-C bond, it can be deduced that Pt-CNC interactions favor this reaction.

Palladium electrocatalysts supported on CNC and Vulcan were also prepared, using sodium borohydride as reducing agent. CO oxidation peaks were obtained at slightly more negative potentials using CNC, however, these potentials were always more positive than in the case of Pt and Pt-Ru catalysts. Formic acid oxidation was studied, with the Pd nanoparticles supported on CNC being more active and stable than those supported on Vulcan and the commercial catalyst Pd/C from E-TEK. However, palladium catalysts were subjected to deactivation with time.

By growing metallic films on a foreign substrate, the structure of the *d*-band, which plays an important role in the catalytic activity of metal, can be modified. For this reason, Au-Pd core-shell structured nanoparticles were prepared. The influence of the Pd-shell thickness was studied, as well as the influence of the support. As the nanostructures were already formed, this approach allowed decoupling effects of the

support on particle growth from specific chemical interactions linked to the reactivity of the metallic centers; Vulcan and In-doped SnO_2 electrodes (ITO) were used.

It was demonstrated that the reactivity of Au-Pd core-shell nanostructures towards CO and HCOOH oxidation is not only determined by the composition and structure of Pd overlayer, but also by the interaction with the support. Analysis of the CO stripping voltammograms in acid solution concluded that the CO coverage is strongly linked with the average lattice strain of core-shell particles, while the carbon support affects the onset potential for CO oxidation. HCOOH oxidation also exhibits a strong dependence on the support. Particles supported on Vulcan exhibit a significantly slower deactivation rate in chronoamperometric measurements, in comparison to those assembled on ITO. Furthermore, core-shell nanoparticles with thicker Pd layers, presented higher current densities than pure Pd nanoparticles for HCOOH oxidation.

Referencias

AKSOYLU A.E., MADALENA M., FREITAS A., PEREIRA M.F.R., FIGUEIREDO J.L. *The effects of different activated carbon supports and support modifications on the properties of Pt/AC catalysts*. Carbon 39 (2001) 175-185

ALCAIDE F., ÁLVAREZ G., MIGUEL O., LÁZARO M.J., MOLINER R., LÓPEZ-CUDERO A., SOLLA-GULLÓN J., HERRERO E., ALDAZ A. *Pt supported on carbon nanofibers as electrocatalyst for low temperature polymer electrolyte membrane fuel cells*. Electrochemistry Communications 11 (2009) 1081-1084.

ÁLVAREZ G., ALCAIDE F., MIGUEL O., CALVILLO L., LÁZARO M.J., QUINTANA J.J., CALDERÓN J.C., PASTOR E., ESPARBÉ I. *Technical electrodes catalyzed with PtRu on mesoporous ordered carbons for liquid direct methanol fuel cells*. Journal of Solid State Electrochemistry 14 (2010) 1027-1034.

ANDREADIS G., TSIAKARAS P. *Ethanol crossover and direct ethanol PEM fuel cell performance modeling and experimental validation*. Chemical Engineering Science 61 (2006) 7497-7508.

ANTOLINI E., GIORGI L., CARDELLINI F., PASSALACQUA E. *Physical and morphological characteristics and electrochemical behaviour in PEM fuel cells of PtRu/C catalysts*. Journal of Solid State Electrochemistry 5 (2001) 131-140.

ANTOLINI E., SALGADO J.R.C., SANTOS L.G.R.A., GARCIA G., TICIANELLI E.A., PASTOR E., GONZALEZ E.R. *Carbon Supported Pt-Cr Alloys as Oxygen-Reduction catalysts for Direct Methanol fuel cells*. Journal of Applied Electrochemistry 36 (2006) 355-362.

ANTOLINI E. *Catalysts for direct ethanol fuel cells*. Journal of Power Sources 170 (2007) 1-12.

[a]ANTOLINI E. *Palladium in fuel cell catalysis*. Energy & Environmental Science 2 (2009) 915-931.

[b]ANTOLINI E. *Carbon supports for low-temperature fuel cell catalysts*. Applied Catalysis B: Environmental 88 (2009) 1-24.

ARICÓ A.S., SRINIVASAN S., ANTONUCCI V. *DMFCs: From Fundamental Aspects to Technology Development*. Fuel Cells 1 (2001) 133-161.

AUER E., FREUND A., PIETSCH J., TACKE T. *Carbons as supports for industrial precious metal catalysts*. Applied Catalysis A: General 173 (1998) 259-271.

AVGOUROPOULOS G., IOANNIDES T. *CO tolerance of Pt and Rh catalysts: effect of CO in the gas-phase oxidation of H_2 over Pt and Rh supported catalysts*. Applied Catalysis B: Environmental 56 (2005) 77-86.

BALDAUF M., KOLB D.M. *Formic Acid Oxidation on Ultrathin Pd Films on Au(hkl) and Pt(hkl) Electrodes*. Journal of Physical Chemistry 100 (1996) 11375-11381.

BARRET E.P., JOYNER L.G., HALENDA P.P. *The determination of pore volume and area distributions in porous substances. I. Computations from nitrogen isotherms*. Journal of the American Chemical Society 73 (1951) 373-380.

BESSEL C.A., LAUBERNDS K., RODRÍGUEZ N.M., BAKER R.T.K. *Graphite Nanofibers as an Electrode for Fuel Cell Applications*. Journal of Physical Chemistry B 105 (2001) 1115-1118.

BEZERRA C.W.B., ZHANG L., LIU H., LEE K., MARQUES A.L.B., MARQUES E.P., WANG H., ZHANG J. *A review of heat-treatment effects on activity and stability of PEM fuel cell catalysts for oxygen reduction reaction*. Journal of Power Sources 173 (2007) 891-908.

BROWN K.R., NATAN M.J. *Hydroxylamine Seeding of Colloidal Au Nanoparticles in Solution and on Surfaces*. Langmuir 14 (1998) 726-728.

CALVILLO L., LÁZARO M.J., BORDEJÉ E.G., MOLINER R., CABOT P.L., ESPARBÉ I., PASTOR E., QUINTANA J.J. *Platinum supported on functionalized ordered mesoporous carbon as electrocatalyst for direct methanol fuel cells*. Journal of Power Sources 169 (2007) 59-64.

CALVILLO L., LÁZARO M.J., SUELVES I., ECHEGOYEN Y., BORDEJÉ E.G., MOLINER R. *Study of the Surface Chemistry of Modified Carbon Nanofibers by Oxidation Treatments in Liquid Phase*. Journal of Nanoscience and Nanotechnology 9 (2009) 1-6.

CAMARA G.A., DE LIMA R.B., IWASITA, T. *Catalysis of ethanol electrooxidation by PtRu: The influence of catalyst composistion*. Electrochemical Communications 6 (2004) 812-815.

CARMO M., DOS SANTOS A.R., POCO J.G.R., LINARDI M. *Physical and electrochemical evaluation of commercial carbon black as electrocatalysts supports for DMFC applications.* Journal of Power Sources 173 (2007) 860-866.

CAPON A., PARSONS R. *The oxidation of formic acid at noble metal electrodes Part III. Intermediates and mechanism on platinum electrodes.* Journal of Electroanalytical Chemistry 45 (1973) 205-231.

CELORRIO V., CALVILLO L., MARTÍNEZ-HUERTA M.V., MOLINER R., LÁZARO M.J. *Study of the Synthesis Conditions of Carbon Nanocoils for Energetic Applications.* Energy&Fuels 24 (2010) 3361-3365.

CELORRIO V., CALVILLO L., PÉREZ-RODRÍGUEZ S., LÁZARO M.J., MOLINER R. *Modification of the properties of carbon nanocoils by different treatments in liquid phase*. Microporous and Mesoporous Materials 142 (2011) 55-61.

CELORRIO V., MONTES DE OCA M.G., PLANA D., MOLINER R., LÁZARO M.J., FERMÍN D.J. *The Effect of Carbon Supports on the Electrocatalytic Reactivity of Au-Pd Core-Shell Nanoparticles*. Journal of Physical Chemistry C (2012) aceptado.

CHAI G.S., YOON S.B., YU J.-S., CHOI J.-H., SUNG Y.-E. *Ordered porous carbons with tuneable pore sizes as catalyst supports in direct methanol fuel cell*. Journal of Physical Chemistry B 108 (2004) 7074-7079.

CHAN K.Y., DING J., REN J., CHENG S., YING K. *Supported mixed metal nanoparticles as electrocatalysts in low temperature fuel cells*. Journal of Materials Chemistry 14 (2004) 505-516.

CRABB E.M., RAVIKUMAR M.K., THOMPSETT D., HURFORD M., ROSE A., RUSSEL A.E. *Effect of Ru surface composition on the CO tolerance of Ru modified carbon supported Pt catalysts.* Physical Chemistry Chemical Physics 6 (2004) 1792-1798.

CUESTA A., DHAMELINCOURT P., LAUREYNS J., MARTÍNEZ-ALONSO A., TASCÓN, J.M.D. *Raman microprobe studies on carbon materials*. Carbon 32 (1994) 1523-1532.

CUESTA A., ESCUDERO M., LNOVA B., BALTRUSCHAT H. *Cyclic Voltammetry, FTIRS, and DEMS Study of the Electrooxidation of Carbon Monoxide, Formic Acid, and Methanol on Cyanide-Modified Pt(111) Electrodes*. Langmuir 25 (2009) 6500-6507.

DICKINSON A.J., CARRETE L.P.L, COLLINS J.A., FRIEDICH K.A., STIMMING U. *Preparation of Pt-Ru/C catalyst from carbonyl complexes for fuel cell applications*. Electrochimica Acta 47 (2002) 3733-3739.

DICKS A.L. *The role of carbon in fuel cells*. Journal of Power Sources. 156 (2006) 128-141

EL-AZIZ A.M., KIBLER L.A. *Influence of steps on the electrochemical oxidation of CO adlayers on Pd(111) and on Pd films electrodeposited onto Au(111)*. Journal of Electroanaytical Chemistry 534 (2002) 107-114.

FIGUEIREDO J.L., PEREIRA M.F.R., FREITAS M.M.A., ORFAO J.J.M. *Modification of the surface chemistry of activated carbons*. Carbon 37 (1999) 1379-1389.

GANGERI M., PERATHONER S., CENTI G. *Synthesis and performances of carbon-supported noble metal nanoclusters as electrodes for polymer electrolyte membrane fuel cells*. Inorganica Chimica Acta. 359 (2006) 4828-4832.

GARCÍA G., FLOREZ-MONTAÑO J., HERNANDEZ-CREUS A., PASTOR E., PLANES G.A. *Methanol electrooxidation at mesoporous Pt and Pt–Ru electrodes: A comparative study with carbon supported materials.* Journal of Power Sources 196 (2011) 2979-2986.

GASTEIGER H.A., MARKOVIC N., ROSS P.N., CAIRNS E.J. *Carbon monoxide electrooxidation on well-characterized platinum-ruthenium alloys.* Journal of Physical Chemistry 98 (1994) 617-625.

GROLLEAU C., COUTANCEAU C., PIERRE F., LÈGER J.-M. *Effect of potential cycling on structure and activity of Pt nanoparticles dispersed on different carbon supports*. Electrochimica Acta. 53 (2008) 7157-7165.

GUO T., NICOLAEV P., THESS A., COLBERT D.T., SMALLEY R.E. *Catalytic growth of single-walled nanotubes by laser vaporization*. Chemical Physics Letters 243 (1995) 49-54.

HA S., LARSEN R., MASEL R.I. *Performance characterization of Pd/C nanocatalyst for direct formic acid fuel cells*. Journal of Power Sources 144 (2005) 28-34.

HALL S.C., SUBRAMANIAN V., TEETER G., RAMBABU B. *Influence of metal-support interaction in Pt/C on CO and methanol oxidation reactions.* Solid State Ionics 175 (2004) 809-813.

HAN S., YUN Y., PARK K.-W., SUNG Y.-E., HYEON T. *Simple Solid-Phase Synthesis of Hollow Graphitic Nanoparticles and their Application to Direct Methanol Fuel Cell Electrodes.* Advanced Materials 15 (2003) 1922-1925.

HEINZEL A., BARRAGAN V.M. *A review of the state-of-the-art of the methanol crossover in direct methanol fuel cells*. Journal of Power Sources 84 (1999) 70-74.

HITMI H., BELGSIR E.M., LEGER J.M., LAMY C., LEZNA R.O. *A kinetic analysis of the electro-oxidation of ethanol at a platinum electrode in acid medium*. Electrochimica Acta 39 (1994) 407-415.

HOSHI N., KIDA K., MASASHI M., NAKADA M., OSADA K. *Structural Effects of Electrochemical Oxidation of Formic Acid on Single Crystal Electrodes of Palladium*. Journal of Physical Chemistry 110 (2006) 12480-12484.

HU J.W., ZHANG Y., LI J.-F., LIU Z., REN B., SUN S.-G., TIAN Z.-Q., LIAN T. *Synthesis of Au@Pd core-shell nanoparticles with controllable size and their application in surface-enhanced Raman spectroscopy*. Chemical Physics Letters 408 (2005) 354-359.

HU, J.W., LI, J.F., REN, B., WU, D.Y., SUN, S.G., TIAN, Z.Q. *Palladium-Coated Gold Nanoparticles with a Controlled Shell Thickness Used as Surface-Enhanced Raman Scattering Substrate*. Journal of Physical Chemistry C 111 (2007) 1105-1112.

HU C., BAI Z., YANG L., LV J., WANG K., GUO Y., CAO Y., ZHOU J. *Preparation of high performance Pd catalysts supported on untreated multi-walled carbon nanotubes for formic acid oxidation*. Electrochimica Acta 55 (2010) 6036-6041.

HUANG Y., ZHOU X., LIAO J., LIU C., LU T., XING W. *Preparation of Pd/C catalyst for formic acid oxidation using a novel colloid method*. Electrochemistry Communications 10 (2008) 621-624.

HUANG Y., LIAO J., LIU C., LU T., XING W. *The size-controlled synthesis of Pd/C catalysts by different solvents for formic acid electrooxidation*. Nanotechnology 20 (2009) 105604-105609.

HYEON T., HAN S., SUNG Y.E., PARK K.W., KIM Y.W. *High-Performance Direct Methanol Fuel Cell Electrodes using Solid-Phase-Synthesized Carbon Nanocoils*. Angewandte Chemie Internationl Edition 42 (2003) 4352-4356.

IIJIMA, S. *Helical microtubules of graphitic carbon*. Nature 354 (1991) 56-58.

IMRAN JAFRI R., RAJALAKSHMI N., RAMAPRABHU S. *Nitrogen-doped multi-walled carbon nanocoils as catalyst support for oxygen reduction reaction in proton exchange membrane fuel cell.* Journal of Power Sources 195 (2010) 8080-8083.

INOUE M., AKAMARU S., TAGUCHI A., ABE T. *Physical and electrochemical properties of Pt-Ru/C samples prepared on various carbon supports by using the barrel sputtering system*. Vacuum 83 (2009) 658-663.

ISMAGILOV Z.R., KERZHENTSEV M.A., SHIKINA N.V., LISITSYN A.S., OKHLOPKOVA L.B., BARNAKOV CH.N., SAKASHITA M., IIJIMA T., TADOKORO K. *Development of active catalysts for low Pt loading cathodes of PEMFC by surface tailoring of nanocarbon materials*. Catalysis Today 102-103 (2005) 58-66.

IWASITA T., PASTOR E. *A dems and FTir spectroscopic investigation of adsorbed ethanol on polycrystalline platinum*. Electrochimica Acta 39 (1994) 531-537.

JANA N.R., GEARHEART L., MURPHY C.J. *Evidence for Seed-Mediated Nucleation in the Chemical Reduction of Gold Salts to Gold Nanoparticles.* Chemistry of Materials 13 (2001) 2313-2322.

JEONG K.-J., MIESSE C.M., CHOI J.-H., LEE J., HANB J., YOON S.P., NAM S.W., LIM T.-H., LEE T.G. *Fuel crossover in direct formic acid fuel cells*. Journal of Power Sources 168 (2007) 119-125.

JIANG L., SUN G., ZHAO X., ZHOU Z., YAN S., TANG S., WANG G., ZHOU B., XIN Q. *Preparation of supported PtRu/C electrocatalyst for direct methanol fuel cells*. Electrochimica Acta 50 (2005) 2371-2376.

JOO J.B., KIM P., KIM W., KIM J., YI J. *Preparation of mesoporous carbon templated by silica particles for use as a catalyst support in polymer electrolyte membrane fuel cells*. Catalysis Today 111 (2006) 171-175.

JUNG W.S., HAN J., YOON S.P., NAM S.W., LIM T.-H., HONG S.-A. *Performance degradation of direct formic acid fuel cell incorporating a Pd anode catalyst*. Journal of Power Sources 196 (2011) 4573-4578.

JUSYS Z., KAISER J., BEHM R.J. *Methanol Electrooxidation over Pt/C Fuel Cell Catalysts: Dependence of Product Yield on Catalysts Loading*. Langmuir 19 (2003) 6759-6769.

KIBLER L.A., EL-AZIZ A.M., KOLB D.M. *Electrochemical behaviour of pseudomorphic overlayers: Pd on Au(111)*. Journal of Molecular Catalysis A: Chemical 199 (2003) 57-63.

KIM M., PARK J.-N., KIM H., SONG S., LEE W.-H. *The preparation of Pt/C catalysts using various carbon materials for the cathode of PEMFC*. Journal of Power Sources 163 (2006) 93-97.

KRUK M., JARONIEC M., GARDKAREE K.P. *Nitrogen adsorption studies of novel synthetic active carbons*. Journal of Colloid Interface Science 192 (1997) 250-256.

LAMY C., BELGSIR E.M., LEGER J.M. *Electrocatalytic oxidation of aliphatic alcohols: Application to the direct alcohol fuel cell (DAFC)*. Journal of Applied Electrochemistry 31 (2001) 799.

LAMY C., LIMA A., LERHUN V., DELIME F., COUTANCEAU C., LÉGER J.-M. *Recent advances in the development of direct alcohol fuel cells (DAFC)*. Journal of Power Sources 105 (2002) 283-296.

LARSEN R., HA S., ZAKZESKI J., MASEL R.I. *Unusually active palladium-based catalysts for the electrooxidation of formic acid*. Journal of Power Sources 157 (2006) 78-84.

[a]LÁZARO M.J., CELORRIO V., CALVILLO L., PASTOR E., MOLINER R. *Influence of the synthesis method on the properties of Pt catalysts supported on carbon nanocoils for ethanol oxidation*. Journal of Power Sources 196 (2011) 4236-4241.

[b]LÁZARO M.J., CALVILLO L., CELORRIO V., PARDO J.I., PERATHONER S., MOLINER R. *Study and application of Vulcan XC-72 in low temperature fuel cells* (Chapter of the Book Carbon Black: Production, Properties and Uses). F. Columbus (Eds.). ©2011 Nova Science Publishers, Inc. Chapter 2, pp 41-68.

LI J.-F., YANG Z.-L., REN B., LIU G.-K., FANG P.-P., JIANG Y.-X., WU D.-Y., TIAN Z.-Q. *Surface-Enhanced Raman Spectroscopy Using Gold-Core Platinum-Shell Nanoparticle Film Electrodes: Toward a Versatile Vibrational Strategy for Electrochemical Interfaces*. Langmuir 22 (2006) 10372-10379.

LITSTER S., MCLEAN G. *PEM fuel cell electrodes*. Journal of Power Sources 130 (2004) 61-76.

LIU H., SONG C., ZHANG L., ZHANG J., WANG H., WILKINSON D.P. *A review of anode catalysis in the direct methanol fuel cell*. Journal of Power Sources 155 (2006) 95-110.

LIU Y., WANG L., WANG G., DENG C., WU B., GAO Y. *High Active Carbon Supported PdAu Catalyst for Formic Acid Electrooxidation and Study of the Kinetics*. Journal of Physical Cheminstry C 114 (2010) 21417- 21422.

LU L., WANG H., SHIQUAN S., ZHANG H. *Improved size control of large palladium nanoparticles by a seeding growth method*. Journal of Materials Chemistry 12 (2002) 156-158.

MARIE J., BERTHON-FABRY S., ACHARD P., CHATENET M., PRADOURAT A., CHAINET E. *Highly dispersed platinum on carbon aerogels as supported catalysts for PEM fuel cell-electrodes: comparison of two different synthesis paths.* Journal of Non-Crystalite Solids 350 (2004) 88-96.

MARTÍN MARTÍNEZ J.M. *Adsorción física de gases y vapores por carbones*. Secretariado de Publicaciones Universidad de Alicante (1990).

MIYAKE H., OKADA T., SAMJESKE G., OSAWA M. *Formic acid electrooxidation on Pd in acidic solutions studied by surface-enhanced infrared absorption spectroscopy.* Physical Chemistry Chemical Physics 10 (2008) 3662-3669.

MOLINER R., SUELVES I., LÁZARO M.J., MORENO O. *Thermocatalytic decomposition of methane over activated carbons: Influence of textural properties and surface chemistry*. International Journal of Hydrogen Energy 30 (2005) 293-300.

MOLINER R., LÁZARO M.J., CALVILLO L., SEBASTIÁN D., ECHEGOYEN Y., GARCÍA-BORDEJÉ E., SALGADO J.R.C., PASTOR E., CABOT P.L., ESPARBÉ I. *Oxidised Carbon Nanofibers as Platinum Support for Proton Exchange Membrane (PEM) Fuel Cells*. Sensor Letters 6 (2008) 1-9.

MONTES DE OCA M.G., KUMARAKURU H., CHERNS D., FERMÍN D.J. *Hydrogen Adsorption at Strained Pd Nanoshells*. Journal of Physical Chemistry C 115 (2011) 10489-10496.

MONTES DE OCA M.G., PLANA D., CELORRIO V., LÁZARO M.J., FERMÍN D.J. *Electrocatalytic Properties of Strained Pd Nanoshells at Au Nanostructures: CO and HCOOH Oxidation.* Journal of Physical Chemistry C 116 (2012) 692-699.

MORENO-CASTILLA C., FERRO-GARCÍA M.A., JOLY J.P., BAUTISTA-TOLEDO I., CARRASCO-MARÍN F., RIVERA-UTRILLA J. *Activated Carbon Surface Modifications by Nitric Acid, Hydrogen Peroxide, and Ammonium Peroxydisulfate Treatments*. Langmuir 11 (1995) 4386-4392.

NOH J.S., SCHWARZ J.A. *Effect of HNO_3 treatment on the surface acidity of activated carbons*. Carbon 28 (1990) 675-682.

O'HAYRE R., BARNETT D.M., PRINZ F.B. *A mathematical model and experimental investigations for fuel cells.* Journal of the Electrochemical Society 152 (2005) A439-A444.

OYA A., OTANI S. *Catalytic graphitization of carbons by various metals*. Carbon 17 (1979) 131-137.

PARK K.W., SUNG Y.E., HAN S., YUN Y., HYEON T. *Origin of the Enhanced Catalytic Activity of Carbon Nanocoil-Supported PtRu Alloy Electrocatalysts*. Journal of Physical Chemistry B 108 (2004) 939-944.

PARK I.-S., LEE K.-S., YOO S.J., CHO Y.-H., SUNG Y.-E. *Electrocatalytic properties of Pd clusters on Au nanoparticles in formic acid electro-oxidation*. Electrochimica Acta 55 (2010) 4339-4345.

PAULUS U.A., ENDRUSCHAT U., FELDMEYER G.J., SCHMIDT T.J., BÖNNERMANN H., BEHM R.J. *New PtRu alloy colloids as precursors for fuel cell catalysts*. Journal of Catalysis 195 (2000) 383-393.

PLANES G.A., GARCÍA G., PASTOR E. *High performance mesoporous Pt electrode for methanol electrooxidation. A DEMS study*. Electrochemistry Communications 9 (2007) 839-844.

PRADO-BURGUETE C., LINARES-SOLANO A., RODRÍGUEZ-REINOSO F., SALINAS-MARTÍNEZ DE LECEA C. *The effect of oxygen surface groups of the support on platinum dispersion in Pt/carbon catalysts*. Journal of Catalysis 115 (1989) 98-106.

ROUZAUD J. N., OBERLIN A., BENY-BASSEZ C. *Carbon films: Structure and microtexture (optical and electron microscopy, Raman spectroscopy)*. Thin Solid Films 105 (1983) 75-96.

ROUSSEAU S., COUTANCEAU C., LAMY C., LEGER J.-M. *Direct ethanol fuel cell (DEFC): Electrical performances and reaction products distribution under operating conditions with different platinum-based anodes*. Journal of Power Sources 158 (2006) 18-24.

RUVINSKY P.S., PROKIN S.N., ZAIKOVSKII V.I., BERNHARDT P., SAVINOVA E.R. *On the enhanced electrocatalytic activity of Pd overlayers on carbon-supported gold particles in hydrogen electrooxidation*. Physical Chemistry Chemical Physics 10 (2008) 6665-6676.

SALGADO J.R.C., QUINTANA J.J., CALVILLO L., LÁZARO M.J., CABOT P.L., ESPARBÉ I., PASTOR E. *Carbon monoxide and methanol oxidation at platinum catalysts supported on ordered mesoporous carbon: the influence of functionalization of the support*. Physical Chemistry Chemical Physics 10 (2008) 6796-6806.

SALGADO J.R.C., ALCAIDE F., ÁLVAREZ G., CALVILLO L., LÁZARO M.J., PASTOR E. *Pt–Ru electrocatalysts supported on ordered mesoporous carbon for direct methanol fuel cell*. Journal of Power Sources 195 (2010) 4022-4029.

SAMANT P.V., GONÇALVES F., FREITAS M.M.A., PEREIRA M.F.R., FIGUEIREDO J.L. *Surface activation of a polymer based carbon*. Carbon 42 (2004) 1321-1325.

SASIKUMAR G., IHM J.W., RYU H. *Dependence of optimum Nafion content in catalyst layer on platinum loading*. Journal of Power Sources 132 (2004) 11-17.

SCHERER G.G. *Interfacial aspects in the development of polymer electrolyte fuel cells*. Solid State Ionics 94 (1997) 249-257.

SCHMIEMANN U., MUELLER U., BALTRUSCHAT H. *The influence of the surface structure on the adsorption of ethene, ethanol and cyclohexene as studied by DEMS*. Electrochimica Acta 40 (1994) 99-107.

SEBASTIÁN D., SUELVES I., MOLINER R., LÁZARO M.J. *The effect of the functionalization of carbon nanofibers on their electronic conductivity*. Carbon 48 (2010) 4421-4431.

SEVILLA M., LOTA G., FUERTES A.B. *Saccharide-based graphitic carbon nanocoils as supports for PtRu nanoparticles for methanol electrooxidation*. Journal of Power Sources 171 (2007) 546-551.

SEVILLA M., SANCHÍS C., VALDÉS-SOLÍS T., MORALLÓN E., FUERTES A.B. *Direct synthesis of graphitic carbon nanostructures from saccharides and their use as electrocatalytic supports*. Carbon 46 (2008) 931-939.

SEVILLA M., SANCHÍS C., VALDÉS-SOLÍS T., MORALLÓN E., FUERTES A.B. *Highly dispersed platinum nanoparticles on carbon nanocoils and their electrocatalytic performance for fuel cell reactions.* Electrochimica Acta 54 (2009) 2234-2238.

SHAO Y., YIN G., ZHANG J., GAO Y. *Comparative investigation of the resistance to electrochemical oxidation of carbon black and carbon nanotubes in aqueous sulphuric acid solution*. Electrochimica Acta 51 (2006) 5853-5857.

SING K.S.W., EVERETT D.H., HAUL R.A.W., MOSCOU L., PIEROTTI R.A., ROUQUÉROL J., SIEMIENIEWSKA T. *Reporting physisorption data for gas/solid systems with special reference to the determination of surface area porosity*. Pure and Applied Chemistry 57 (1985) 603-619.

SOLLA-GULLÓN J., VIDAL-IGLESIAS F.J., MONTIELV., ALDAZ A. *Electrochemical characterization of platinum-ruthenium manoparticles prepared by water-in-oil microemulsion*. Electrochimica Acta 49 (2004) 5079-5088.

[a]SONG S.Q., ZHOU W.J., ZHOU Z.H., JIANG L.H., SUN G.Q., XIN Q., LEONTIDIS V., KONTOU S., TSIAKARAS P. *Direct ethanol PEM fuel cells: The case of platinum based anodes*. International Journal of Hydrogen Energy 30 (2005) 995-1001.

[b]SONG S., ZHOU W., LIANG Z., CAI R., SUN G., XIN Q., STERGIOPOULOS V., TSIAKARAS P. *The effect of methanol and ethanol cross-over on the performance of PtRu/C-based anode DAFCs.* Applied Catalysis B: Environmental 55 (2005) 65-72.

SONG S., TSIAKARAS P. *Recent progress in direct ethanol proton exchange membrane fuel cells (DE-PEMFCs).* Applied Catalysis B: Environmental 63 (2006) 187-193.

SOPIAN K., WAN DAUD W.R. *Challenges and future developments in proton exchange membrane fuel cells*. Renewable Energy 31 (2006) 719-727.

SPINACE E.V., LINARDI M., OLIVEIRA NETO A. *Co-catalytic effect of nickel in the electro-oxidation of ethanol on binary Pt–Sn electrocatalysts*. Electrochemistry Communications 7 (2005) 365-369.

STRASSER P., KOH S., ANNIYEV T., GREELEY J., MORE K., YU C., LIU Z., KAYA S., NORDLUND D., OGASAWARA H., TONEY M.F., NILSSON A. *Lattice-strain control of the activity in dealloyed core–shell fuel cell catalysts*. Nature Chemistry 2 (2010) 454-460.

SURYANARAYANA C., GRANT NORTON M. *X-Ray diffraction: A practical Approach*. 1998 Plenum Press, New York.

SZYMANSKI G.S., KARPINSKI Z., BINIAK S., SWIATKOWSKI A. *The effect of the gradual thermal decomposition of surface oxygen species on the chemical and catalytic properties of oxidized activated carbon*. Carbon 40 (2002) 2627-2639.

TAKASU Y., KAWAGUCHI T., SUGIMOTO W., MURAKAMI Y. *Effects of the surface area of carbon support on the characteristics of highly-dispersed Pt-Ru particles as catalysts for methanol oxidation*. Electrochimica Acta 48 (2003) 3861-3868.

TANAKA S., UMEDA M., OJIMA H., USUI Y., KIMURA O., UCHIDA I. *Preparation and evaluation of a multi-component catalyst by using a co-sputtering system for anodic oxidation of ethanol*. Journal of Power Sources 152 (2005) 34-39.

TSIAKARAS P.E. *PtM/C (M = Sn, Ru, Pd, W) based anode direct ethanol–PEMFCs: Structural characteristics and cell performance*. Journal of Power Sources 171 (2007) 107-112.

UGARTE, D. *Onion-like graphitic particles*. Carbon 33 (1995) 989-993.

VIDANO R., FISCHBACH D.B. *New Lines in the Raman Spectra of Carbons and Graphite*. Journal of the American Ceramic Society 61 (1978) 13-17.

VIELSTICH W., LAMM A., GASTEIGER H.A. *Fuel Cells Technology and Applications*. Ed. Wiley, Chichester, 2003, vol. 3, part. 6.

[a]WANG, J. *Analytical Electrochemistry*. Wiley-VCH, 2000.

[b]WANG Y., REN J.W., DENG K., GUI L.L., TANG Y.Q. *Preparation of Tractable Platinum, Rhodium and Ruthenium Nanoclusters with Small Particle Size in Organic Media*. Chemistry of Materials 12 (2000) 1622-1627.

WANG X., HU J.M., HSING I.M. *Electrochemical investigation of formic acid electro-oxidation and its crossover through a Nafion® membrane.* Journal of Electroanalytical Chemistry 562 (2004) 73-80.

WANG R., LIAO S., JI S. *High performance Pd-based catalysts for oxidation of formic acid*. Journal of Power Sources 180 (2008) 205-208.

WATANABE M., SAEGUSA S. *High platinum electrocatalyst utilizations for direct methanol oxidation*. Journal of Electroannalytical Chemistry 271 (1989) 213-220.

WEE J-H., LEE K.Y., KIM S-H. *Fabrication methods for low-Pt-loading electrocatalysts in proton exchange membrane fuel cell systems*. Journal of Power Sources 165 (2007) 667-677.

WIKANDER K., EKSTRÖM H., PALMQVIST A.E.C., LUNDBLAD A., HOLMBERG K., LINDBERGH G. *Alternative catalysts and carbon support material for PEMFC*. Fuel Cells 6 (2006) 21-25.

WOLTER O., GIORDANO C., HEITBAUM J., VIELSTICH W. *Mass spectroccopic cyclic voltammetry for mechanistic studies in organic electrocatalysis.* Proceedings-The Electrochemical Society (1982) 235-253.

YANG S., CHEN X., KATSUNO T., MOTOJIMA S. *Controllable synthesis of carbon microcoils/nanocoils by catalysts supported on ceramics using catalyzed chemical vapor deposition process*. Materials Research Bulletin 42 (2007) 465-473.

YU X., YE S. *Recent advances in activity and durability enhancement of Pt/C catalytic cathode in PEMFC: Part I. Physico-chemical and electronic interaction between Pt and carbon support, and activity enhancement of Pt/C catalyst*. Journal of Power Sources 172 (2007) 133-144.

YU X., PICKUP P.G. *Recent advances in direct formic acid fuel cells (DFAFC)*. Journal of Power Sources 182 (2008) 124-132.

[a]YU X., PICKUP P.G. *Mechanistic study of the deactivation of carbon supported Pd during formic acid oxidation*. Electrochemistry Communications 11 (2009) 2012-2014.

[b]YU X., PICKUP P.G. *Deactivation/reactivation of a Pd/C catalyst in a direct formic acid fuel cell (DFAFC): Use of array membrane electrode assemblies*. Journal of Power Sources 187 (2009) 493-499.

ZHANG L., LU T., BAO J., TANG Y., LI C. *Preparation method of an ultrafine carbon supported Pd catalyst as an anodic catalyst in a direct formic acid fuel cell.* Electrochemistry Communications 8 (2006) 1625-1627.

ZHOU W.J., LI W.Z., SONG S.Q., ZHOU Z.H., JIANG L.H., SUN G.Q., XIN Q., POULIANITIS K., KONTOU S., TSIAKARAS P. *Bi- and tri-metallic Pt-based anode catalysts for direct ethanol fuel cells*. Jounal of Power Sources 131 (2004) 217-223.

ZHOU W., LEE J.Y. *Highly active core–shell Au@Pd catalyst for formic acid electrooxidation*. Electrochemistry Communications 9 (2007) 1725-1729.

ZHOU J.-H., HE J.-P., JI Y.-J., DANG W.-J., LIU X.-L., ZHAO G.-W., ZHANG C.-X., ZHAO J.-S., FU Q.-B., HU H.-P. *CTAB assisted microwave synthesis of ordered mesoporous carbon*

supported Pt nanoparticles for hydrogen electro-oxidation. Electrochimica Acta 52 (2008) 4691-4695.

ZHOU Y., LIU J., YE J., ZOU Z., YE J., GU J., YU T., YANG A. *Poisoning and regeneration of Pd catalyst in direct formic acid fuel cell*. Electrochimica Acta 55 (2010) 5024-5027.

Lista de símbolos y abreviaturas

BET	Ecuación de Brunauer-Emmett-Teller
BJH	Método de Barrett-Joyner-Halenda
BM	Método de reducción con borohidruro de sodio
CE	Contraelectrodo
CNC	Nanoespirales de carbono
CS	Estructura *core-shell*
CVD	Deposición química en fase vapor
E	Potencial (V)
E_{ad}	Potencial de adsorción de CO
E_r	Potencial teórico estándar o reversible de la celda (V)

EDX	Dispersión de energía de rayos X
EGM	Método de reducción con etilenglicol
E-TEK	Catalizador comercial
DAFC	Pila de combustible de alcohol directo
DEFC	Pila de combustible de etanol directo
DEMS	Espectrometría de masas diferencial electroquímica
DFAFC	Pila de combustible de ácido fórmico directo
DMFC	Pila de combustible de metanol directo
FAM	Método de reducción con ácido fórmico
GDE	Electrodo de difusión de gas
GDL	Capa de difusión de gas
HRTEM	Microcopía electrónica de transmisión de alta resolución
IUPAC	Unión internacional de química pura y aplicada
j	Densidad de corriente (A cm^{-2})
MEA	Conjunto membrana-electrodo
MM	Método de reducción con etilenglicol
NP	Nanopartícula
OCV	Potencial de la celda en circuito abierto
ORR	Reacción de reducción de oxígeno
PEFC	Pila de combustible de electrolito polimérico
PEMFC	Pila de combustible de membrana de intercambio de protones
PTFE	Politetrafluoroetileno
RE	Electrodo de referencia
SEM	Microscopia electrónica de barrido
STEM	Microscopía electrónica de transmisión de barrido

STEM-EDS	Microscopia electrónica de transmisión de barrido-Espectrometría de energía dispersiva de rayos X
STEM-HAADF	Microscopia electrónica de transmisión de barrido-Campo oscuro anular de gran ángulo
TEM	Microscopía electrónica de transmisión
TPB	Interfase de contacto triple
TPD	Desorción a temperatura programada
TPO	Oxidación a temperatura programada
VC	Voltamperograma cíclico
VCEM	Voltamperograma cíclico de intensidad de la señal de masa
Vulcan XC-72R	Negro de carbono suministrado por la empresa Cabot
WE	Electrodo de trabajo
XRD	Difracción de rayos X
υ	Velocidad de barrido

Compendio de publicaciones

1

Study of the Synthesis Conditions of Carbon Nanocoils for Energetic Applications

V. Celorrio, L. Calvillo, M.V. Martínez-Huerta, R. Moliner, M.J. Lázaro

Energy & Fuels 24 (2010) 3361-3365

Energy Fuels **2010,** *24,* 3361–3365 · DOI:10.1021/ef9015119
Published on Web 03/10/2010

energy&fuels
article

Study of the Synthesis Conditions of Carbon Nanocoils for Energetic Applications†

V. Celorrio,‡ L. Calvillo,‡ M. V. Martínez-Huerta,§ R. Moliner,‡ and M. J. Lázaro*,‡

‡*Instituto de Carboquímica, Consejo Superior de Investigaciones Científicas (CSIC), Miguel Luesma Castán 4, 50018 Zaragoza, Spain, and* §*Instituto de Catálisis y Petroleoquímica, Consejo Superior de Investigaciones Científicas (CSIC), Marie Curie 2, 28049 Madrid, Spain*

Received December 10, 2009. Revised Manuscript Received February 25, 2010

The synthesis of carbon nanocoils (CNCs) by the catalytic graphitization of composites has been studied. Resorcinol−formaldehyde gel was used as the carbon precursor; a mixture of cobalt and nickel salts was used as the graphitization catalysts in the synthesis; and silica sol was added to the reaction mixture to obtain carbon materials with high specific surface area and to achieve a good dispersion of the transition-metal nanoparticles. Different molar ratios of the reagents were used with the purpose of obtaining carbon materials with different structural and textural properties, seeking a compromise between the graphitization degree and surface area. X-ray diffraction (XRD), Raman spectrometry, transmission electron microscopy (TEM), temperature-programmed oxidation (TPO), N_2 physisorption, and temperature-programmed desorption (TPD) were used to characterize the morphology, textural properties, and surface chemistry of such materials. Results showed that obtained CNCs had good crystallinity and well-defined porosity, which depended upon the preparation conditions.

1. Introduction

Since the discovery of carbon nanotubes by Iijima,[1] much attention has been paid to the design of nanostructured graphitic carbon materials. Today graphite is the most important carbon in electrochemical applications because of its unique properties. Their high electrical conductivity, thermal stability, and chemical inertness make possible their use as catalytic supports,[2,3] nanocomposites,[4−6] and electrode materials.[7,8] The carbonaceous graphitic materials used as electrode materials in electrochemical devices must possess a high specific surface and porosity, high resistance to corrosion, high thermal stability, and relatively low cost, as well as high electrical conductivity.[9] On the other hand, these materials must have specific properties for the type of electrochemical device in which they work.

Many forms of graphitic nanostructured carbon materials, including carbon nanotubes, graphitic carbon nanofibers, and carbon nanocoils (CNCs), can be produced using various gas-phase reactions.[10,11] Among these materials, CNCs have recently received tremendous attention because of the combination of their good electrical conductivity, derived from their graphitic structure, and a wide porosity that allows for the diffusional resistances of reactants/products to be minimized. Nevertheless, the methods to synthesize them, such as arc discharge,[12] laser vaporization,[13] and thermal chemical vapor deposition,[14] have limitations in terms of large-scale and economical production because of the high temperatures that they need (arc discharge, 5000−20000 °C; laser vaporization, 4000−5000 °C). Therefore, taking these drawbacks into consideration, a solid-phase synthetic procedure has to be developed.[15,16]

Although several groups have reported the solid-phase synthesis of nanostructured graphitic carbon materials, the synthetic processes used cannot be applied for economical and large-scale applications because of the long reaction time and/or a complicated synthesis procedure. Synthetic graphites are all basically prepared by heating unstructured carbon at temperatures over 2500 °C. This heat treatment orients the disordered layers into the graphitic structure. Dependent upon the raw material used and the heat treatment process, the characteristics of the synthetic graphite differ.

† This paper has been designated for the special section Carbon for Energy Storage and Environment Protection.

*To whom correspondence should be addressed: Instituto de Carboquímica, Consejo Superior de Investigaciones Científicas (CSIC), Miguel Luesma Castán 4, 50018 Zaragoza, Spain. Telephone: +34-976733977. Fax: +34-976733318. E-mail: mlazaro@icb.csic.es.

(1) Iijima, S. *Nature* **1991**, *354*, 56–58.
(2) Moliner, R.; Lázaro, M. J.; Calvillo, L.; Sebastián, D.; Echegoyen, Y; García-Bordejé, E.; Salgado, J. R. C.; Pastor, E.; Cabot, P. L.; Esparbé, I. *Sens. Lett*. **2008**, *6*, 1–9.
(3) Sevilla, M.; Lota, G.; Fuertes, A. B. *J. Power Sources* **2007**, *171*, 546–551.
(4) Hammel, E.; Tang, X.; Trampert, M.; Schmitt, T.; Mauthner, K.; Eder, A.; Pötschke, P. *Carbon* **2004**, *42*, 1153–1158.
(5) Tibbetts, G. G.; Lake, M. L.; Strong, K. L.; Rice, B. P. *Compos. Sci. Technol*. **2007**, *67*, 1709–1718.
(6) Vera-Agullo, J.; Glória-Pereira, A.; Varela-Rizo, H.; Gonzalez, J. L.; Martin-Gullon, I. *Compos. Sci. Technol*. **2009**, *69*, 1521–1532.
(7) Hyeon, T.; Han, S.; Sung, Y. E.; Park, K. W.; Kim, Y. W. *Angew. Chem., Int. Ed*. **2003**, *42*, 4352–4356.
(8) Pico, F.; Ibañez, J.; Lillo-Rodenas, M. A.; Linares-Solano, A.; Rojas, R. M.; Amarilla, J. M.; Rojo, J. M. *J. Power Sources* **2008**, *176*, 417–425.
(9) Pandolfo, A. G.; Hollenkmp, A. F. *J. Power Sources* **2006**, *157*, 11–27.
(10) Zhao, D. L.; Shen, Z. M. *Mater. Lett*. **2008**, *62*, 3704–3706.
(11) Pinilla, J. L.; Moliner, R.; Suelves, I.; Lázaro, M. J.; Echegoyen, Y.; Palacios, J. M. *Int. J. Hydrogen Energy* **2007**, *32*, 4821–4829.
(12) Ugarte, D. *Carbon* **1995**, *33*, 989–993.
(13) Guo, T.; Nicolaev, P.; Thess, A.; Colbert, D. T.; Smalley, R. E. *Chem. Phys. Lett*. **1995**, *243*, 49–54.
(14) Yang, S.; Chen, X.; Katsuno, T.; Motojima, S. *Mater. Res. Bull*. **2007**, *42*, 465–473.
(15) Han, S.; Yun, Y.; Park, K. W.; Sung, Y. E.; Hyeon, T. *Adv. Mater*. **2003**, *15*, 1922–1925.
(16) Sevilla, M.; Fuertes, A. B. *Mater. Chem. Phys*. **2008**, *113*, 208–214.

In recent years, the phenomena of catalytic graphitization have been developed considerably. The use of transition metals or their inorganic compounds to promote graphitization at lower temperatures represents an attractive alternative. Several reviews of catalytic graphitization are available in the literature.[16,17] Among metals that act as catalysts are certain transition metals, such as nickel,[18,19] iron, cobalt, manganese,[19] aluminum,[20] etc.

Normally, catalytic graphitization lies in improving the crystalinity of a carbon material by the formation of graphitic material. This process involves a chemical reaction between the ungraphitized carbon and the metal or inorganic compound, which acts as the graphitization catalyst.[21−23] Its main advantage is that both graphitizing and non-graphitizing carbons can be transformed into crystalline materials at relatively low temperatures ($T < 1000$ °C), whereas uncatalysed graphitization requires the use of temperatures greater than 2000−2500 °C and carbon precursors that have graphitizable properties.

In this work, the catalytic graphitization is proposed as the synthesis procedure for CNCs; this way, carbon materials containing graphitic structures can be obtained at low temperature (< 1000 °C). In this paper, the synthesis of CNCs by the catalytic graphitization of resorcinol−formaldehyde gel using a mixture of nickel and cobalt salts as the graphitization catalysts has been studied. The aim of this work is to determine the more suitable conditions to obtain a graphitic material, making an arrangement between the graphitization degree and surface area, by varying the molar ratio of the reactants. Furthermore, the method reported here has the advantage of incorporating metal calalyst particles in the synthesis of the composite, avoiding a step of impregnation carbon materials with metal particles after their synthesis. Carbon materials obtained have been characterized by means of X-ray diffraction (XRD), Raman spectroscopy, transmission electron microscopy (TEM), temperature-programmed oxidation (TPO), N_2 physisorption, and temperature-programmed desorption (TPD) to study their physicochemical properties.

2. Experimental Section

2.1. Synthesis of CNCs. For the synthesis of CNCs, resorcinol−formaldehyde (Sigma−Aldrich) gel was used as the carbon precursor, and nickel(II) nitrate hexahydrate (Panreac) and cobalt(II) nitrate hexahydrate (Sigma−Aldrich) salts were used as the graphitization catalysts. In addition, silica sol (Supelco) was used to obtain carbon materials with a high specific surface area and to achieve a good dispersion of the transition-metal nanoparticles.

A typical synthesis involves the dissolution of formaldehyde and silica sol in 100 mL of deionized water and the subsequent addition of the nickel−cobalt salts mixture under stirring. Then, resorcinol is added, and the solution is maintained for 0.5 h under stirring conditions. This reaction mixture is subjected to heat treatment at 85 °C for 3 h in a closed system, then opened, and dried at 108 °C. Subsequently, it is carbonized in a nitrogen atmosphere at 900 °C for 3 h using a heating rate of 5 °C/min. The resulting material is washed with a 5 M NaOH (Panreac) solution for 12 h at 60 °C to remove silica particles, followed by a oxidative purification process with concentrated nitric acid (65 wt %, Fluka) for 2 h at room temperature to remove the metal salts. This process results in the formation of CNCs.

Different carbon materials were synthesized following this method by varying the molar ratio of the reactants. Table 1 shows the molar ratios and the nomenclature used for the different materials.

Table 1. Molar Ratios of Reactants Used in the Preparation of Carbon Materials

sample	H_2O/Co salt/Ni salt/resolcinol/formaldehyde/silica
CNC-1	100:0.2:0.2:1:2:0
CNC-2	100:0.4:0.4:1:2:0.6
CNC-3	100:0.2:0.2:1:2:0.6

2.2. Characterization. For the morphological characterization, XRD, Raman spectroscopy, and TEM were used. The textural properties were determined by N_2 physisorption. Thermal resistance of carbon materials was analyzed by TPO experiments, and surface chemistry was determined by TPD experiments.

XRD patterns were recorded using a Bruker AXS D8 Advance diffractometer with a $\theta-\theta$ configuration and using Cu Kα radiation. The error of this measure was estimated in ± 0.05 cm^{-1}.

The scanning electron microscopy apparatus was a Hitachi S3400-N. TEM studies were made using a JEM-2100F microscope, operated with an accelerating voltage of 200 kV.

Nitrogen adsorption−desorption isotherms were obtained at 77 K using a Micromeritics ASAP 2020. The total surface area was determined using the Brunauer−Emmett−Teller (BET) equation (with an error of ± 6 m^2/g), and the total pore volume was determined using the single-point method at $p/p_0 = 0.99$ (the error of this measure was ± 0.08 cm^3/g). The external surface area (S_{ext}) was estimated using the α_S-plot method, and a non-graphitized carbon black was used as a reference.[24] Pore size distribution (PSD) curves were calculated by the Barrett−Joyner−Halenda (BJH) method using the adsorption branch. The position of the maximum of the PSD was used as the average pore diameter.

TPO experiments were carried out in a SETARAM Setsys Evolution thermobalance, under an air atmosphere using a heating rate of 5 °C/min up to 700 °C.

Raman spectra were obtained using a Horiba Jobin Yvon HR800 UV, using the green line of an argon laser ($\lambda = 514.53$ nm) as the excitation source. An error of ± 0.1 cm^{-1} was assumed.

The determination of the amount of surface oxygen groups of the carbon materials was carried out by TPD experiments. The amounts of CO and CO_2 desorbed from the carbon samples were analyzed online by mass spectroscopy. The determination of deconvolutions was calculated using Origin software.

3. Results and Discussion

3.1. Morphology. Figure 1 shows the XRD patterns for the CNCs synthesized. A typical diffraction pattern of slightly graphitized carbon is represented by the data obtained for the CNC-1 sample. A characteristic broad (002) peak at ~24° and a less intense one at ~44°, which corresponds to a (100) reflection of a graphitic structure, were observed for this material. The increase in the amount of silica used decreased the width of the main (002) diffraction peak and made the other more visible. In addition, the main XRD peak for the graphitized samples CNC-2 and CNC-3

(17) Kasahara, N; Shiraishi, S; Oya, A. *Carbon* **2002**, *41*, 1645–1687.
(18) Ōya, A.; Ōtani, S. *Carbon* **1978**, *16*, 153–154.
(19) Ōya, A.; Ōtani, S. *Carbon* **1979**, *17*, 131–137.
(20) Ōya, A.; Ōtani, S. *Carbon* **1976**, *14*, 191–194.
(21) Maldonado-Hódar, F. J.; Moreno-Castilla, C.; Rivera-Utrilla, J.; Hanzawa, Y.; Yamada, Y. *Langmuir* **2000**, *16*, 4367–4373.
(22) Ōya, A.; Marsh, H. J. *Mater. Sci.* **1982**, *14*, 309–322.
(23) Sevilla, M.; Fuertes, B. *Carbon* **2006**, *44*, 468–474.
(24) Kruk, M.; Jaroniec, M.; Gardkaree, K. P. *J. Colloid Interface Sci.* **1997**, *192*, 250–256.

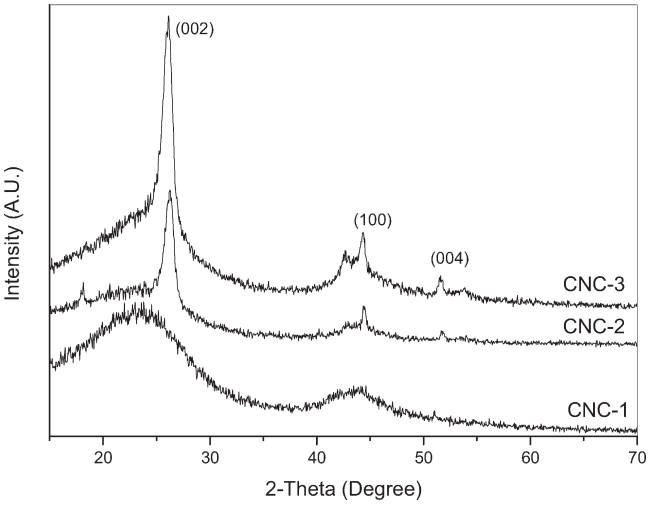

Figure 1. XRD patterns of CNCs.

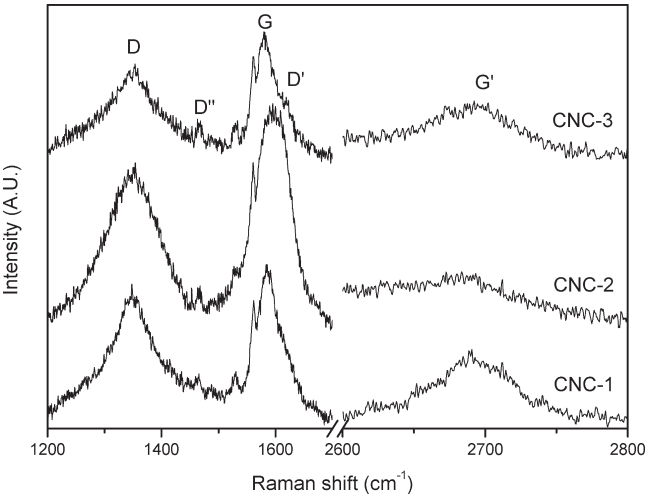

Figure 2. First- and second-order Raman spectra of CNCs.

Table 2. Structural Properties of the Synthesized CNCs Obtained from XRD and Raman Analysis

		Raman parameters	
sample	d_{002}[a] (nm)	I_D/I_G	$\Delta\upsilon_G$ (cm^{-1})
CNC-1	0.345	0.87	61
CNC-2	0.338	0.73	56
CNC-3	0.341	0.66	40

[a] Interplanar distance between (002) planes obtained from XRD data.

appeared to be a superposition of a broader peak and a narrow one centered at ~26°. This would suggest that major parts of the samples are well-graphitized, while minor parts of them are graphitic to a smaller extent.

The distance between hexagonal planes is known as (002) *d* spacing, which is 0.335 nm for an ideal graphite. The higher the crystallinity of a carbon material, the nearer the (002) *d* spacing of the carbon material to that of graphite. From the data obtained by XRD analysis and according to the Bragg's law, the interplanar distance between (002) planes of prepared samples can be calculated. Results are given in Table 2. As can be observed, these values were close to the value obtained for an ideal graphite; however, they were a bit higher than that. This suggests that the carbon materials had a light distortion in the crystalline structure.

The nature and graphitization degree of the carbon materials were further examined by Raman spectrometry. This technique is very useful to assess qualitatively or quantitatively the degree of structural ordering of carbon materials and also allows us to assess the degree of heterogenity of the material obtained by the catalytic graphitization process. The first-order (1200−1700 cm^{-1}) and second-order (2500−2900 cm^{-1}) Raman spectra of CNCs are shown in Figure 2. As can be seen, the first-order Raman spectrum shows two bands: the G band or graphite and the D band associated with the presence of different types of structural defects.[25] In addition to these two great bands, some authors postulate smaller ones, such as D′ and D″ bands.[26−28] The origin of these bands is open to discussion. Some authors associate them to the existence of surface oxygen groups,[29,30] while others prefer ascribing them to purely structural factors.[31] In the case of carbon materials studied in this work, they may be attributed to the presence of amorphous carbon associated with graphitic carbon, as well as the light functionalization suffered during the treatment with nitric acid. On the other hand, the second-order Raman spectrum shows the G′ band characteristic of ordered materials.

Table 2 shows the Raman parameters obtained for CNCs. In the literature, it is well-accepted that the D band represents the presence of defects in the material and the G band represents the graphitic order.[25,32] Consequently, a relationship between the intensities of both bands will be proportional to the degree of structural ordering;[25] a decrease in the ratio of these intensities indicates an increase in the structural ordering degree. As can be seen in Table 2, CNC-3 showed the lowest I_D/I_G value, indicating that it was the most ordered sample. This result confirmed that obtained by XRD analysis.

Another Raman parameter that is commonly used for structural characterization is the width of the G band in the middle of its height ($\Delta\upsilon_G$).[32] An increase in the structural ordering results in a narrowing of the G band, as can be seen in Table 2.

The morphology of prepared CNCs was studied by TEM. A single nanocoil exhibited well-aligned graphitic layers as can be observed in high-resolution transmission electron microscopy (HRTEM) images (panels A and B of Figure 3); this confirmed the XRD and Raman spectrometry results. TEM images (panels A and C of Figure 3) showed that the nanocoils have a diameter of around 30−40 nm and consist of a long curved ribbon of carbon. Particles of around 100−150 nm were formed containing several nanocoils, as can be seen in Figure 3D.

These carbon materials can be compared to others described in the literature. Han et al.[33] synthesized CNCs by the

(25) Cuesta, A.; Dhamelincourt, P.; Laureyns, J.; Martínez-Alonso, A.; Tascón, J. M. D. *Carbon* **1994**, *32*, 1523–1532.
(26) Vidano, R.; Fischbach, D. B. *J. Am. Ceram. Soc.* **1978**, *61*, 13–17.
(27) Beny-Bassez, C.; Rouzaud, J. N. *Scanning Electron Microsc.* **1985**, *1*, 119–132.
(28) Rouzaud, J. N.; Oberlin, A.; Beny-Bassez, C. *Thin Solid Films* **1983**, *105*, 75–96.
(29) Nakamizo, M.; Tamai, K. *Carbon* **1984**, *22*, 197–198.
(30) Nakamizo, M.; Honda, H.; Inagaki, M. *Carbon* **1978**, *16*, 281–283.
(31) Mernagh, T. P.; Cooney, R. P.; Johnson, R. A. *Carbon* **1984**, *22*, 39–42.
(32) Lespade, P.; Marchand, A.; Couzi, M.; Cruege, F. *Carbon* **1984**, *22*, 375–385.
(33) Han, S.; Yun, Y.; Park, K. W.; Sung, Y. E.; Hyeon, T. *Adv. Mater.* **2003**, *15*, 1922–1925.

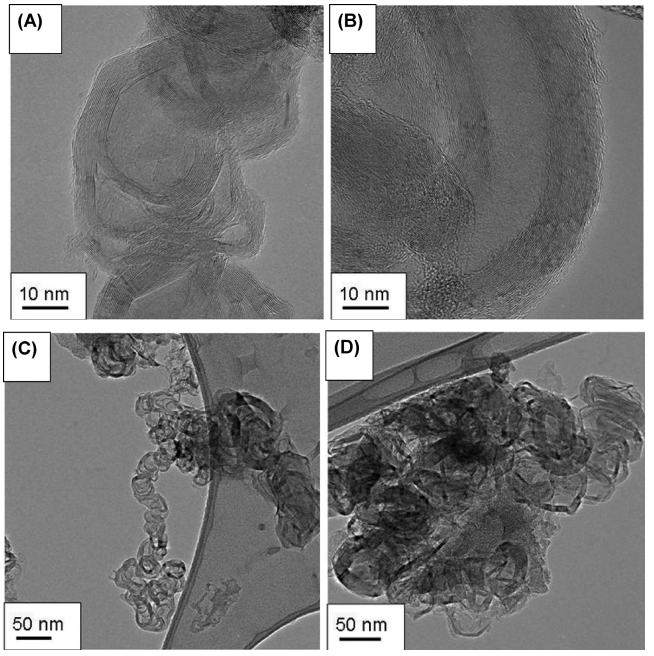

Figure 3. HRTEM (A and B) and TEM (C and D) images of CNCs.

same method using the same molar ratio of reactants as CNC-1. Although they treated the carbon material with $KMnO_4$ to oxidize amorphous carbon, they obtain less graphitic materials than those obtained in this work. However, Hyeon's group[7] synthesized CNCs with exactly the same methodology and molar ratio of sample CNC-2, obtaining a carbon material with a similar graphitization degree but more distorted crystalline structure, as indicated in their XRD parameters. Other authors synthesize CNCs by different methods. For example, Sevilla el al.[34] prepared CNCs using saccharides as the carbon precursor, and Huang's group[35] prepared CNCs by chemical vapor deposition. However, higher graphitization degrees are obtained in this work by the catalytic graphitization method using resorcinol−formaldehyde gel as the carbon precursor.

3.2. Thermal Stability. Thermal stability is an important characteristic of carbon materials for their application as electrode material in both supercapacitators and fuel cells. This property was studied by TPO experiments under an air atmosphere. Figure 4 shows the oxidation curves of CNCs. All samples exhibited a high resistance to the oxidation in air, with similar weight change patterns. The oxidation occurred around 600 °C, with the CNC-3 sample being the most resistant to the oxidation, although there were no significant differences with the rest of the material. This fact can be related to its more graphitic nature. It must be also noted that the oxidation of the carbon materials was complete; that is, there was not residue after the TPO experiments. This indicated that the removal of the silica and metal particles with NaOH and HNO_3 treatments, respectively, was complete.

3.3. Textural Properties. Textural properties of CNCs obtained by N_2 physisorption are summarized in Table 3. Carbon materials showed a specific surface area of 120−220 m^2/g and a pore volume of 0.10−0.19 cm^3/g. Both the

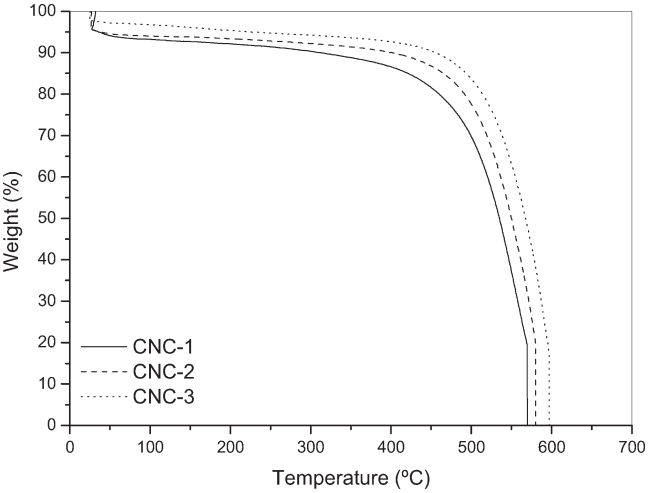

Figure 4. Thermogravimetric weight change curves under an air atmosphere for CNCs.

Table 3. Textural Properties of CNCs

			α_S method		
sample	A_{BET} ($m^2\ g^{-1}$)	V_{total} ($cm^3\ g^{-1}$)	S_{ext} ($m^2\ g^{-1}$)	V_{micro} ($cm^3\ g^{-1}$)	V_i ($cm^3\ g^{-1}$)
CNC-1	120	0.10	122	0.0	0.10
CNC-2	220	0.19	223	0.0	0.19
CNC-3	124	0.16	126	0.0	0.16

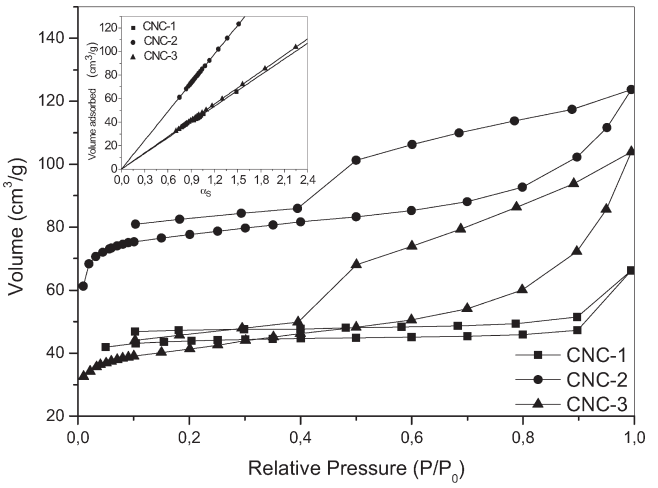

Figure 5. Nitrogen adsorption−desorption isotherms of CNCs. The inset represents the α_S-plot analysis applied to the adsorption branch of the N_2 adsorption isotherm.

specific surface area and the pore volume decreased as the graphitization degree of the sample increased. Thus, the CNC-3 sample showed the lowest surface area and pore volume, and the CNC-1 sample showed the highest ones. These results are comparable to those available in the literature for CNCs prepared by the same or different methods.[35−37]

Figure 5 shows the isotherms obtained for the different carbon materials. The shape of the isotherms was typical of nanoparticulate materials without structural pores. In this case, adsorption occurred on the external surface of the

(34) Sevilla, M.; Sanchís, C.; Valdés-Solís, T.; Morallón, E.; Fuertes, A. B. *Electrochim. Acta* **2009**, *54*, 2234–2238.
(35) Huang, Z. Y.; Chen, X.; Huang, J. R.; Li, M. Q.; Liu, J. H. *Mater. Lett.* **2006**, *60*, 2073–2075.
(36) Antolini, E. *Appl. Catal., B* **2009**, *88*, 1–24.
(37) Kruk, M.; Jaroniec, M.; Ryoo, R.; Joo, S. H. *J. Phys. Chem. B* **2000**, *104*, 7960–7968.

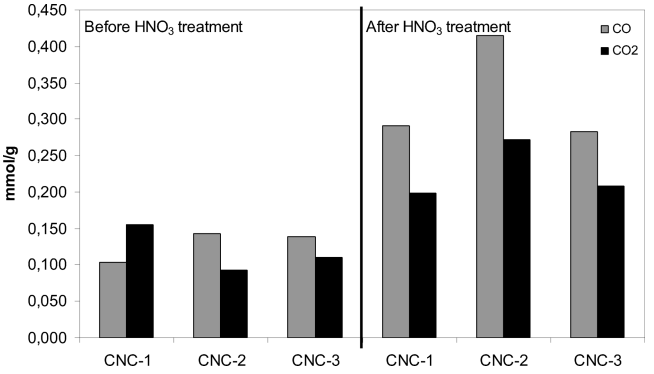

Figure 6. Total CO and CO_2 amount desorbed during the TPD experiments carried out before and after the HNO_3 treatment.

nanostructures. Therefore, the BET surface area (S_{BET}) corresponds to the external surface area (S_{ext}), as observed in Table 3. This was confirmed by the results derived from the α_S method (inset of Figure 5). These results showed that CNCs had not micropores, because the graphs passed through the origin, and therefore, the total pore volume corresponded to interparticular spaces (V_i). From this analysis, the pore size distribution of carbon materials was also determined. All of them showed a bimodal mesoporous structure with an average pore size of around 3 and 15 nm.

3.4. Surface Chemistry. CNCs were treated with concentrated nitric acid at room temperature for 2 h to remove the metal particles used as catalysts in the graphitization process. This treatment is commonly used to modify the surface chemistry of carbon materials, creating surface oxygen groups. Therefore, this effect was also studied in this work.

The surface chemistry of CNCs was studied by TPD experiments. Carbon materials were analized before and after the HNO_3 treatment, showing that, in all cases, surface oxygen groups were created during this treatment, as observed in Figure 6. Before the treatment with HNO_3, carbon materials possessed a small amount of surface oxygen groups and all samples had a similar content of these groups. This can be associated with their same nature (same carbon precursor and same synthesis process). After the HNO_3 treatment, the amount of oxygen groups increased and no significant differences for the three CNC samples were observed.

In the literature, it is well-established that acidic groups are decomposed into CO_2 at low temperatures and basic and neutral groups are decomposed into CO at high temperatures.[38] CO and CO_2 evolution curves can be deconvoluted, and the different types of functional groups can be estimated according to their desorption temperature. CO_2 peak areas

(38) Lázaro, M. J.; Calvillo, L.; Bordejé, E. G.; Moliner, R.; Juan, R.; Ruiz, C. R. *Microporous Mesoporous Mater.* **2007**, *103*, 158–165.

Table 4. Estimation of the Type and Number of the Oxygen Groups on the Surface of Carbon Materials from the Deconvolution of CO and CO_2 Curves Obtained in the TPD Experiments

	CO_2 peak areas (μmol g^{-1})		CO peak areas (μmol g^{-1})		
sample	carboxylic (100−400 °C)	anhydride and lactone (190−650 °C)	anhydride (350−627 °C)	phenol (600−700 °C)	quinone (700−980 °C)
CNC-1	10	130	20	190	10
CNC-2	140	70	160	130	10
CNC-3	90	80	110	90	10

are decomposed into two peaks: the first corresponding to carboxylic acid groups and the second corresponding to the decomposition of anhydrides and lactones. In the same way, CO peak areas are decomposed into three peaks, corresponding to anhydrides, phenols, and quinones, respectively. To analyze the type of oxygen surface groups, CO and CO_2 profiles were deconvoluted. The amounts of surface oxygen groups calculated by the areas of the deconvoluted peaks are given in Table 4. It can be observed that samples mainly contained carboxylic and phenol groups. It is expected that carboxylic groups will produce a decrease in the hydrophobicity of carbon materials and phenol groups will make the surface more accessible.

4. Conclusions

CNCs were prepared by catalytic graphitization using a mixture of resorcinol−formaldehyde gel as the carbon precursor and a mixture of nickel−cobalt salts as the graphitization catalysts.

The obtained materials had an ordered structure with a high or low graphitization degree depending upon the molar ratios of reagents used in their synthesis. It is expected that these materials show a high electrical conductivity because of their high graphitic nature and a suitable inertness. Specific surfaces areas of 120−220 m^2/g were achieved as well as pore volumes of 0.10−0.19 cm^3/g. A treatment with concentrated nitric acid was used to remove metal catalyst particles. Besides the elimination of metals, surface oxygen groups were created during this treatment. CNCs mainly contained carboxylic and phenol groups.

In short, CNCs had suitable surface areas and pore volumes, with textural and morphological properties that make them promising materials for application in several fields, such as catalysis, adsorption, or energy storage, and even for applications where their structure is not a relevant parameter.

Acknowledgment. The authors gratefully acknowledge financial support given by the MICINN through Project MAT2008-06631-C03-01. V. Celorrio and L. Calvillo also acknowledge CSIC and the Spanish National Research Council for their JAE and FPI Grants, respectively.

2

Modification of the properties of carbon nanocoils by different treatments in liquid phase

V. Celorrio, L. Calvillo, S. Pérez-Rodríguez, M.J. Lázaro, R. Moliner

Microporous and Mesoporous Materials 142 (2011) 55-61

Microporous and Mesoporous Materials 142 (2011) 55–61

Contents lists available at ScienceDirect

Microporous and Mesoporous Materials

journal homepage: www.elsevier.com/locate/micromeso

Modification of the properties of carbon nanocoils by different treatments in liquid phase

V. Celorrio, L. Calvillo, S. Pérez-Rodríguez, M.J. Lázaro *, R. Moliner

Instituto de Carboquímica (CSIC), Miguel Luesma Castán 4, 50018-Zaragoza, Spain

ARTICLE INFO

Article history:
Received 13 September 2010
Received in revised form 15 November 2010
Accepted 15 November 2010
Available online 20 November 2010

Keywords:
Carbon nanocoils
Mesoporous carbon
Oxidation treatments

ABSTRACT

Carbon nanocoils (CNCs) were synthesized using resorcinol–formaldehyde gel as carbon precursor and a mixture of cobalt and nickel salts as the graphitization catalysts. The last step of the synthesis process involves the elimination of the metals using an oxidative treatment, commonly HNO_3 treatment. However, during this treatment not only the metals are eliminated, but also the amorphous and graphitic carbon. On the other hand, this treatment can create surface oxygen groups, modifying the surface chemistry of CNCs. The aim of this work is to study the effect of different oxidative treatments on the final properties of carbon nanocoils in order to obtain materials with high graphitic character. The effect of liquid phase oxidation treatments on the texture, surface chemistry and structure of carbon nanocoils was studied by means of different analytical techniques as N_2-physisorption, X-ray diffraction (XRD), temperature programmed oxidation (TPO) and temperature programmed desorption (TPD). During these treatments, surface oxygen groups were created and their number was function of the concentration of the oxidizing agent used and the treatment time.

1. Introduction

Carbon materials are ideal for their use in electrochemical devices [1–4], due to their low cost and unique properties, such as the high corrosion resistance, high surface area, low density and especially good electrical conductivity.

Several types of commercial carbon materials have been studied for their use in electrochemical applications. Commonly, highly conductive carbon blacks are used for their high specific surface area, good conductivity and pore structure. Among them, oil-furnace blacks and acetylene blacks have been mainly used. Oil-furnace blacks are produced from aromatic residue oil from petroleum refineries and acetylene blacks are obtained by thermal decomposition of acetylene. Normally, furnace blacks have surface areas between 20 and 1500 $m^2 g^{-1}$, while acetylene blacks have surface areas below 100 $m^2 g^{-1}$ [5]. Vulcan XC-72(R) is the most frequently used. It is produced by controlled vapor-phase pyrolysis of hydrocarbons [6] and consists of primary carbon particles which are spherical and of colloidal size. Vulcan was found to have particle size between 30 and 50 nm and surface area around 250–300 $m^2 g^{-1}$ [7].

Recently, a new generation of carbon materials such as carbon nanofibers and nanotubes [8,9], carbon xerogels and aerogels [10,11], ordered mesoporous carbons [12,13] and carbon nanocoils [14,15], is actively being sought and tested with attempts to significantly improve their characteristics. The great majority of these carbonaceous materials are obtained from organic precursors under a heat treatment for carbonization in an inert atmosphere. Both carbon precursors and heat treatment conditions determine the physicochemical properties of the materials, especially the particle size and shape and the surface chemistry [16,17]. These factors also determine the electrical conductivity and the textural properties. Ordered mesoporous carbons have a high surface area, large pore volume and controllable pore size. Carbon nanofibers have a high electrical conductivity and a mesoporous structure, and carbon nanocoils have a high crystallinity and an open and accessible porosity. However, these materials only contain a small amount of surface oxygen groups, but the surface chemistry can be modified by oxidation treatments in order to create functional groups [18,19].

Carbon nanocoils (CNCs) constitute a new class of carbon nanomaterials with properties that differ significantly from other forms of carbon. There are several methods to synthesize CNCs, like arc discharge [20], laser vaporization [21], thermal chemical vapor deposition [22] or catalytic graphitization of carbon precursors [23,24]. The catalytic graphitization process reduces the costs of manufacturing in a significant way, because high temperatures are not needed. Different carbon precursors like resorcinol–formaldehyde gels [14,15] or saccharides [24] could be used as carbon precursors, and a mixture of transition metal salts as

* Corresponding author. Tel.: +34 976 733977; fax: +34 976 733318.
E-mail address: mlazaro@icb.csic.es (M.J. Lázaro).

1387-1811/$ - see front matter © 2010 Elsevier Inc. All rights reserved.
doi:10.1016/j.micromeso.2010.11.018

graphitization catalysts. After the heat treatment, most of works report the use of a HNO_3 treatment in order to remove the metal particles used during the synthesis, whereas others report the use an HCl treatment [25]. However, studies about the influence of different treatments on the properties of the carbon materials are not found in the literature.

In this work, we proposed some modifications to the carbon nanocoils synthesis procedure that we previously reported in [14] in order to obtain carbon materials with a high graphitic structure. With this aim, the HNO_3 treatment at room temperature for 2 h has been replaced by different treatments with HNO_3, HNO_3–H_2SO_4 mixtures, H_2SO_4–H_2O_2 mixtures and H_2O_2 Carbon materials have been characterized by X-ray diffraction (XRD), Raman spectroscopy, N_2-physisorption, temperature programmed desorption (TPD) and temperature programmed oxidation (TPO) to study the effect of these treatments on the final properties of CNCs.

2. Experimental

2.1. Synthesis of carbon materials

Carbon nanocoils were synthesized by simply heat-treating of composite materials using resorcinol–formaldehyde (Sigma–Aldrich) gel as carbon precursor. A mixture of cobalt(II) nitrate hexahydrate (Sigma–Aldrich) and nickel(II) nitrate hexahydrate (Panreac) salts was used as graphitization catalyst and silica sol (Supelco) was used to obtain a good dispersion of the transition-metal nanoparticles and to create a mesoporous structure, as described in [14]. This reaction mixture was thermally cured and, subsequently, carbonized. Finally, silica and metal particles were removed.

In a typical synthesis, a nickel–cobalt mixture salt was dissolved in an aqueous solution of formaldehyde (F) and silica. Afterwards, resorcinol (R) was added. The molar ratios used in the synthesis were selected from a previous work [14] and are H_2O/Co salt/Nisalt/R/F/silica = 100:0.2:0.2:1:2:0.6. This reaction mixture was subjected to heat treatment at 85 °C for 3 h in a closed system and, subsequently, was carbonized in a nitrogen atmosphere at 900 °C for 3 h. The resulting carbon material was washed with a 5 M NaOH (Panreac) solution to remove the residual silica particles, followed by an oxidative treatment to remove metal particles and amorphous carbon. During this oxidative treatment, a competitive oxidation takes place, since carbon nanocoils and amorphous carbon react simultaneously. In addition, this treatment can modify the morphological and textural properties of the carbon materials, as well as their surface chemistry. Therefore, different oxidative treatments were tested in order to study their effect on the properties of CNCs. Nitric acid (Nc), nitric–sulphuric mixtures (NS), hydrogen peroxide (Ox) and sulphuric acid-hydrogen peroxide mixtures (SOx) have been used as oxidizing agents. Table 1 shows the nomenclature of carbon materials and their oxidation conditions. These treatments were carried out at 25 (Ta) and 80 °C (Tb) for 0.5 and 2 h.

2.2. Characterization techniques

Morphological characterization was carried out by X-ray diffraction (XRD) and Raman Spectroscopy, N_2-physisorption was used to determine the textural properties, thermal resistance was analyzed by temperature programmed oxidation (TPO) experiments, and surface chemistry was studied by temperature programmed desorption (TPD) experiments.

XRD patterns were recorded using a Bruker AXS D8 Advance diffractometer with a θ–θ configuration and using Cu Kα radiation, whereas Raman spectra were obtained using a Horiba Jobin Yvon HR800 UV, using the green line of an argon laser (λ = 514.53 nm) as excitation source.

Nitrogen adsorption–desorption isotherms were obtained at −196 °C using a Micromeritics ASAP 2020. Total surface area was determined using the BET (Brunauer–Emmett–Teller) equation and total pore volume was determined using the single point method at P/P_0 = 0.99. The external surface area (S_{EXT}) was estimated using the α_S-plot method and a non-graphitized carbon black was used as reference [26]. Pore size distribution (PSD) curves were calculated by BJH (Barrett–Joyner–Halenda) method using the adsorption branch. The position of the maximum of the PSD was used as average pore diameter.

TPO experiments were carried out in a SETARAM Setsys Evolution thermobalance under air atmosphere, using a heating rate of 5 °C min^{-1} up to 800 °C.

TPD experiments were carried out in an inert atmosphere (He) using a heating rate of 10 °C min^{-1} up to 1050 °C. The amounts of CO and CO_2 desorbed from the carbon samples were analyzed online by mass spectroscopy. The deconvolution of the TPD curves was calculated using Origin software.

3. Results and discussion

3.1. Morphology: XRD and Raman analysis

Carbon materials were analyzed by X-ray diffraction to study their structure and degree of order. Fig. 1 shows the XRD patterns

Table 1
Nomenclature of carbon materials and oxidation conditions used in their synthesis.

Sample	Oxidizing agent	Temperature (°C)	Time (h)
CNC NcTa0.5	Concentrated HNO_3 (65%)	25	0.5
CNC NcTa2	Concentrated HNO_3 (65%)	25	2
CNC NcTb0.5	Concentrated HNO_3 (65%)	80	0.5
CNC NcTb2	Concentrated HNO_3 (65%)	80	2
CNC NSTa0.5	HNO_3 (65%)–H_2SO_4 (98%) (1:1, v/v)	25	0.5
CNC NSTa2	HNO_3 (65%)–H_2SO_4 (98%) (1:1, v/v)	25	2
CNC NSTb0.5	HNO_3 (65%)–H_2SO_4 (98%) (1:1, v/v)	80	0.5
CNC NSTb2	HNO_3 (65%)–H_2SO_4 (98%) (1:1, v/v)	80	2
CNC SOxTa0.5	H_2SO_4 (98%)–H_2O_2 (33%) (70:30, v/v)	25	0.5
CNC SOxTa2	H_2SO_4 (98%)–H_2O_2 (33%) (70:30, v/v)	25	2
CNC SOxTb0.5	H_2SO_4 (98%)–H_2O_2 (33%) (70:30, v/v)	80	0.5
CNC SOxTb2	H_2SO_4 (98%)–H_2O_2 (33%) (70:30, v/v)	80	2
CNC OxTa0.5	H_2O_2 (33%)	25	0.5
CNC OxTa2	H_2O_2 (33%)	25	2
CNC OxTb0.5	H_2O_2 (33%)	80	0.5
CNC OxTb2	H_2O_2 (33%)	80	2

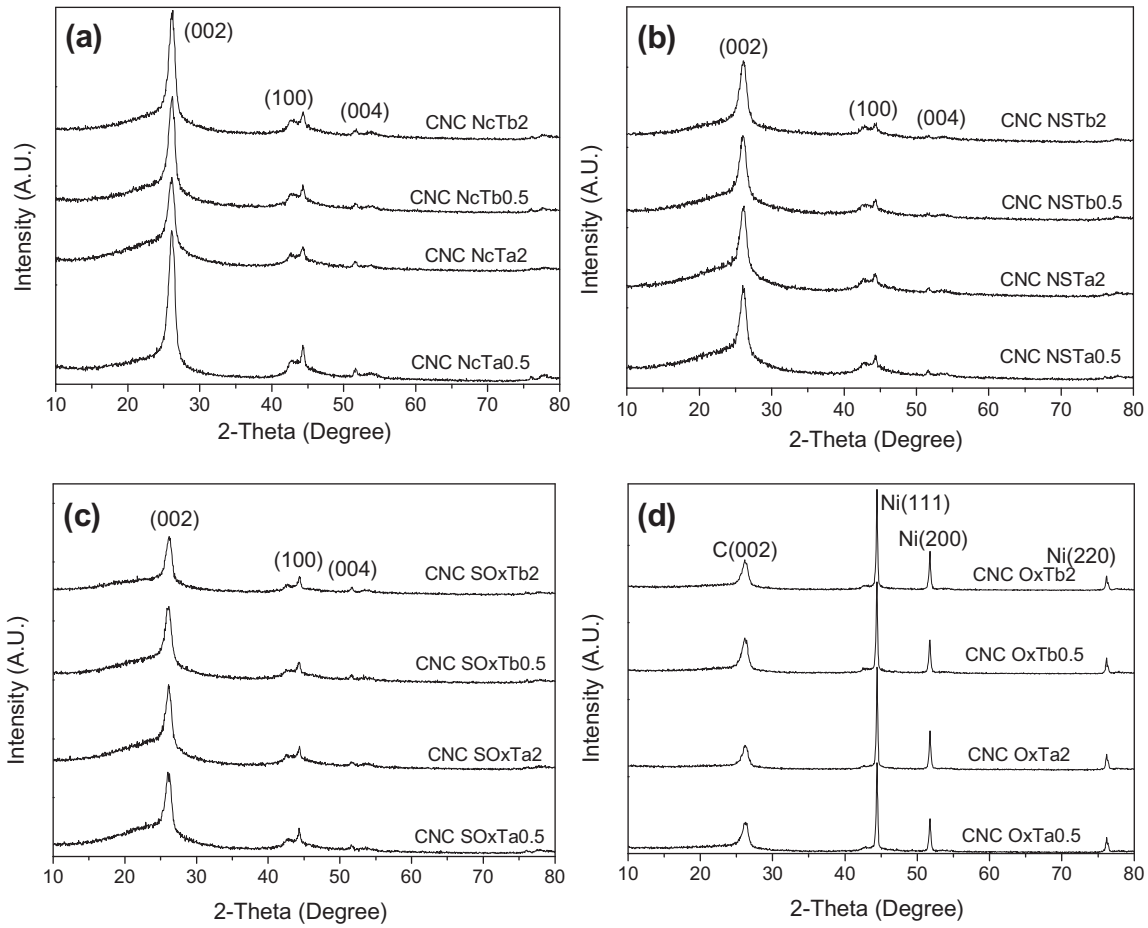

Fig. 1. XRD patterns obtained for: (a) Samples treated with HNO_3; (b) Samples treated with HNO_3–H_2SO_4; (c) Samples treated with H_2SO_4–H_2O_2; and (d) Samples treated with H_2O_2.

obtained for the different synthesized samples. It is noted that all the samples showed three peaks at $2\theta = 26.2°$, 44° and 51°, associated with the (0 0 2), (1 0 0) and (0 0 4) characteristics planes of graphite. However, the intensity of these peaks depended on the oxidative purification treatment used. These treatments affected on different way the carbon samples, since the competitive oxidation of amorphous and graphitic carbon does not occur to the same extent in all cases. In Fig. 1, it can be observed that the main XRD peak, (0 0 2), appeared to be a superposition of a broader peak centred at $2\theta = 22.6°$ and a narrow one centred at $2\theta = 26.2°$. This suggests that all samples contained a certain amount of amorphous carbon, which depended on the oxidizing treatment used in the synthesis. Taking the sample CNC NcTa2 as reference material, since is the treatment usually reported, it is observed that samples with graphite peaks better defined than the reference one were obtained using different treatments, such as CNC NcTa0.5 or CNC NSTb2. However, characteristic peaks of Ni and Co (they are coindents) were observed clearly for samples treated with H_2O_2 (CNC Ox), indicating that this oxidizing agent was not effective in the removal of metals.

Table 2
Structural parameters of CNCs deduced from an analysis of the XRD and Raman spectra.

Sample	d_{002} (Å)	Raman parameters	
		I_D/I_G	I_D/I_T
CNC NcTa0.5	3.410	0.59	0.40
CNC NcTa2	3.410	0.66	0.50
CNC NcTb0.5	3.397	0.83	0.59
CNC NcTb2	3.391	0.72	0.52
CNC NSTa0.5	3.423	0.88	0.60
CNC NSTa2	3.404	0.72	0.51
CNC NSTb0.5	3.442	0.88	0.61
CNC NSTb2	3.410	0.62	0.47
CNC SOxTa0.5	3.391	0.68	0.48
CNC SOxTa2	3.410	0.73	0.51
CNC SOxTb0.5	3.404	0.85	0.60
CNC SOxTb2	3.397	0.51	0.39
CNC OxTa0.5	3.385	0.86	0.62
CNC OxTa2	3.397	1.1	0.70
CNC OxTb0.5	3.404	0.73	0.53
CNC OxTb2	3.404	0.69	0.50

Interplanar distance (d_{002}) values calculated by the Bragg's law are shown in Table 2. This value allows to estimate the distance between graphitic planes and, thus, to establish a comparison between the carbon materials and the ideal graphite. It could be seen that there were not significant differences between them. All samples showed d_{002} values in the range 3.372–3.442 Å, close to that of the ideal graphite (3.354 Å). However, samples that present the value closer than graphite are CNC NcTa0.5 and CNC NcTa2.

The first-order (1200–1700 cm^{-1}) and second-order (2500–2900 cm^{-1}) Raman spectra of the carbon materials are shown in Fig. 2. The first-order Raman spectrum shows two bands associated with the presence of different types of structural defects [28]: the graphite band (G) at ~1565–1580 cm^{-1} and the D band at ~1342–1353 cm^{-1}. On the other hand, the second-order Raman spectrum

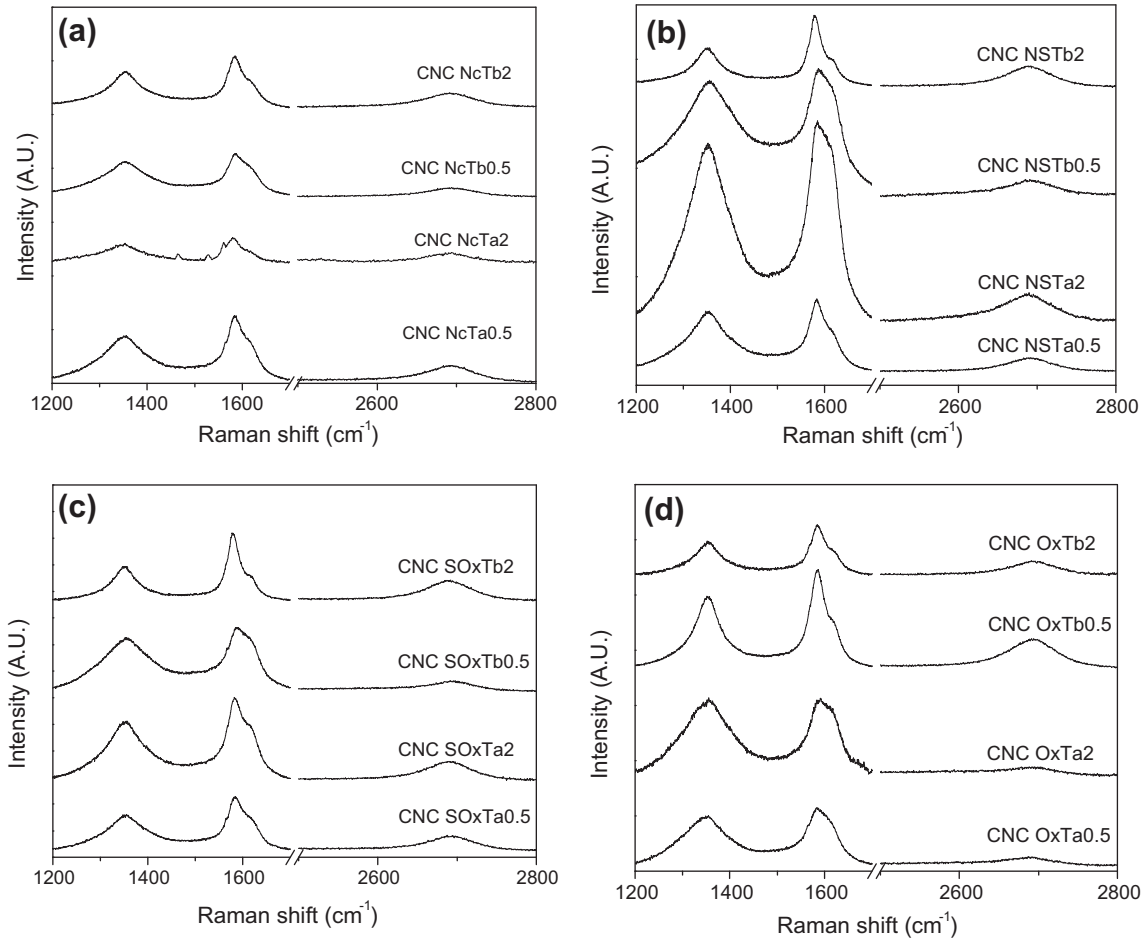

Fig. 2. Raman patterns obtained for: (a) Samples treated with HNO_3; (b) Samples treated with HNO_3–H_2SO_4; (c) Samples treated with H_2SO_4–H_2O_2; and (d) Samples treated with H_2O_2.

shows the G′ band which is characteristic of tridimensional ordered materials [28].

Table 2 shows the Raman parameters obtained. The degree of structural order with respect to graphite structure can be analyzed by the relationship between the intensities of D and G bands (I_D/I_G), since they are directly proportional, that is, a decrease in this ratio indicates an increase in the structural ordering degree [27]. On the other hand, the same property can be analyzed from the relative intensity of D band (I_D/I_T, where I_T is the total integrated intensity of the first-order spectrum), since it is less variable and statistically uncertain than the intensity ratio of the individual bands [29]. From both ratios (Table 2), it is deduced that, for each oxidizing agent except HNO_3, the most severe oxidation conditions (Tb2) resulted in the materials with major content of graphitic carbon and less content of amorphous carbon, since they had the lowest I_D/I_G and I_D/I_T values. This indicates that the amorphous carbon reacted preferentially in these conditions, respect to the graphitic carbon. However, as HNO_3 was used, the materials with major content of graphitic carbon and less content of amorphous carbon were obtained with the less severe conditions (Ta0.5). From these results it can be deduced that the material with less content of amorphous carbon sample was CNC SOxTb2. These results are in agreement with those obtained by XRD. In Fig. 1, it can be observed that samples that had the lowest I_D/I_G and I_D/I_T values also showed a better defined (0 0 2) peak, that is, the contribution of the broader peak centred at $2\theta = 22.6°$ was lower for these samples. This indicated the lower content of amorphous carbon in these samples.

3.2. Thermal stability

The resistance of carbon materials to oxidation in air was studied using temperature-programmed oxidation (TPO) experiments. Weight changes suffered by the samples during these experiments are shown in Fig. 3. It can be seen that the use of different oxidation treatments did not affect the resistance to oxidation in a significant way. In all cases the oxidation took place around 600 °C. This oxidation temperature is very high for a carbon material and is attributed to the graphitic character of this type of materials.

In addition, it can be observed that not all oxidation treatments were effective in the elimination of metals used as graphitization catalysts. After the treatments with H_2O_2 and H_2SO_4–H_2O_2 a residue was obtained, indicating that these treatments did not remove the metals completely. In the case of the treatments with H_2O_2 this residue was about 20 wt%, while in the case of treatments with H_2SO_4–H_2O_2 the residue was around 5–10 wt%. This result was confirmed by the peaks attributed to Ni and Co observed in the XRD patterns.

3.3. Textural properties

Textural properties of carbon materials after the different treatments in liquid phase were determined by N_2-physisorption. Table 3 shows the textural parameters obtained by this technique.

The liquid phase treatments used to remove the metal particles had a great influence in the textural properties of carbon materials. Thus, materials with specific surface areas (A_{BET}) in the range

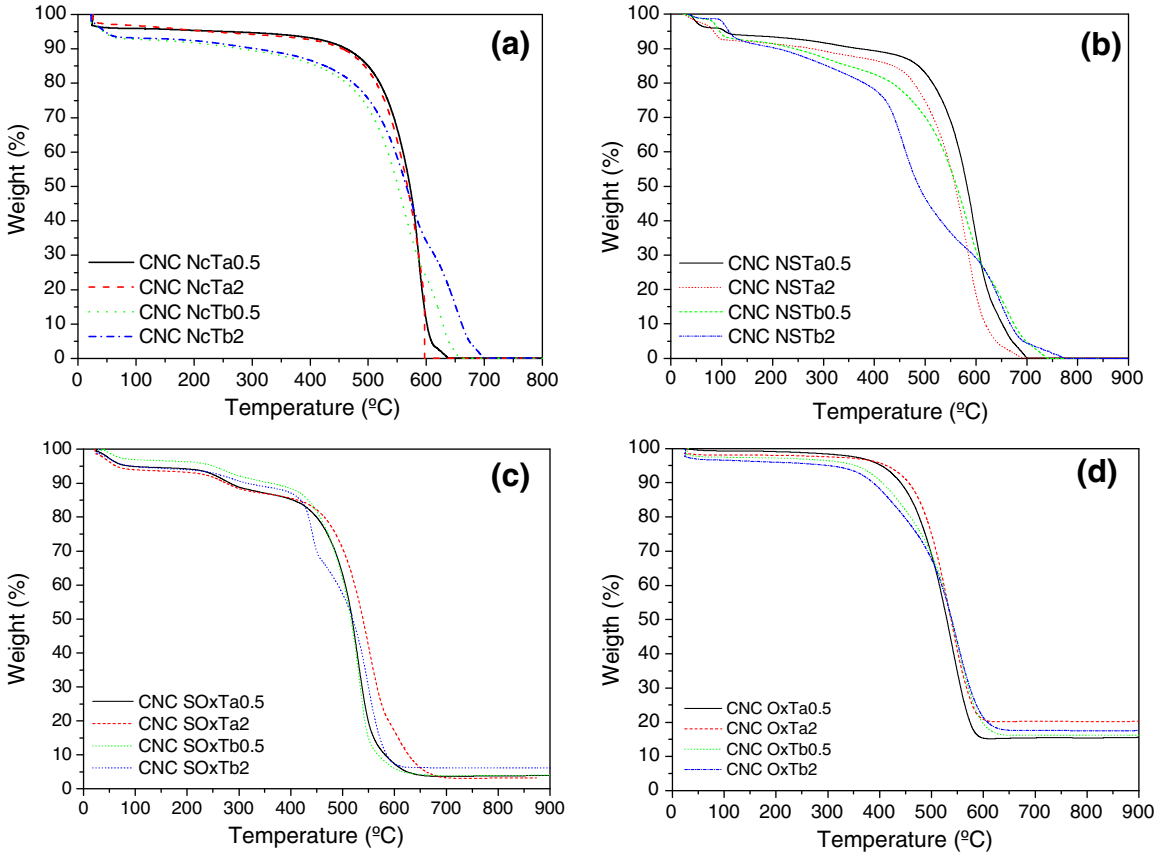

Fig. 3. Thermogravimetric weight change curves under air atmosphere for: (a) Samples treated with HNO_3; (b) Samples treated with HNO_3–H_2SO_4; (c) Samples treated with H_2SO_4–H_2O_2; and (d) Samples treated with H_2O_2.

30–250 $m^2\,g^{-1}$ and total pore volumes (V_{TOTAL}) of 0.08–0.30 $cm_3\,g^{-}1$ were obtained. As can be seen in Table 3, carbon materials treated with H_2SO_4–H_2O_2 mixtures (SOx) showed the lowest specific surfaces areas and total pore volumes. This result could be attributed to the destruction of the structure of the material during the oxidation treatments. For the other oxidizing agents, similar textural parameters were obtained for all the oxidation conditions (temperature and time), except for the most severe conditions (at boiling temperature for 2 h). In the last case, a decrease of specific surface area and pore volume was observed. This can be attributed to the partial destruction of the carbon material with the most severe oxidation conditions.

Table 3
Textural properties of carbon materials obtained.

Sample	A_{BET} ($m^2\,g^{-1}$)	V_{TOTAL} ($cm^3\,g^{-1}$)	α_s Method		
			S_{EXT} ($m^2\,g^{-1}$)	V_{MICRO} ($cm^3\,g^{-1}$)	V_i ($cm^3\,g^{-1}$)
CNC NcTa0.5	243	0.31	249	0.0	0.31
CNC NcTa2	124	0.16	126	0.0	0.16
CNC NcTb0.5	235	0.22	241	0.0	0.22
CNC NcTb2	246	0.24	252	0.0	0.24
CNC NSTa0.5	117	0.13	120	0.0	0.13
CNC NSTa2	213	0.19	218	0.0	0.19
CNC NSTb0.5	202	0.18	207	0.0	0.18
CNC NSTb2	120	0.13	123	0.0	0.13
CNC SOxTa0.5	84	0.12	86	0.0	0.12
CNC SOxTa2	75	0.10	77	0.0	0.10
CNC SOxTb0.5	74	0.11	76	0.0	0.11
CNC SOxTb2	46	0.09	47	0.0	0.09
CNC OxTa0.5	168	0.17	172	0.0	0.17
CNC OxTa2	183	0.19	187	0.0	0.19
CNC OxTb0.5	192	0.22	196	0.0	0.22
CNC OxTb2	187	0.20	196	0.0	0.20

The results derived from the α_S method showed that CNCs had not micropores, because the graphs volume adsorbed vs. α_S (not shown) passed through the origin and therefore, the total pore volume (V_{TOTAL}) corresponded to interparticular spaces (V_i).

The isotherms obtained for the different materials corresponded to the type IV, according to the classification established by the IUPAC, and showed a hysteresis, which is associated usually to capillary condensation in mesopores. Fig. 4 shows the isotherms obtained for different samples. The shape of the isotherms was typical of nanoparticulate materials without structural pores. In this case, adsorption occurred on the external surface of the nanostructures. Therefore, the BET surface area (A_{BET}) corresponds to the external surface area (S_{EXT}), as observed in Table 3. From this analysis, the pore size distribution of carbon materials was also determined. The carbon sample that has been established as reference in this work (CNC NcTa2) had a bimodal pore size distribution with average pore diameters of about 3 nm and 15 nm (not shown). It was observed that the different treatments studied in this work had no significant effect on the pore size distribution of the resultant carbon materials.

3.4. Surface chemistry

The surface chemistry of the carbon materials after the different oxidation treatments was studied by TPD experiments. TPD analysis are commonly used to analyze the surface chemistry of samples because, despite its limitations, has many advantages and it is an easy way to analyze the surface functional groups. It is also the

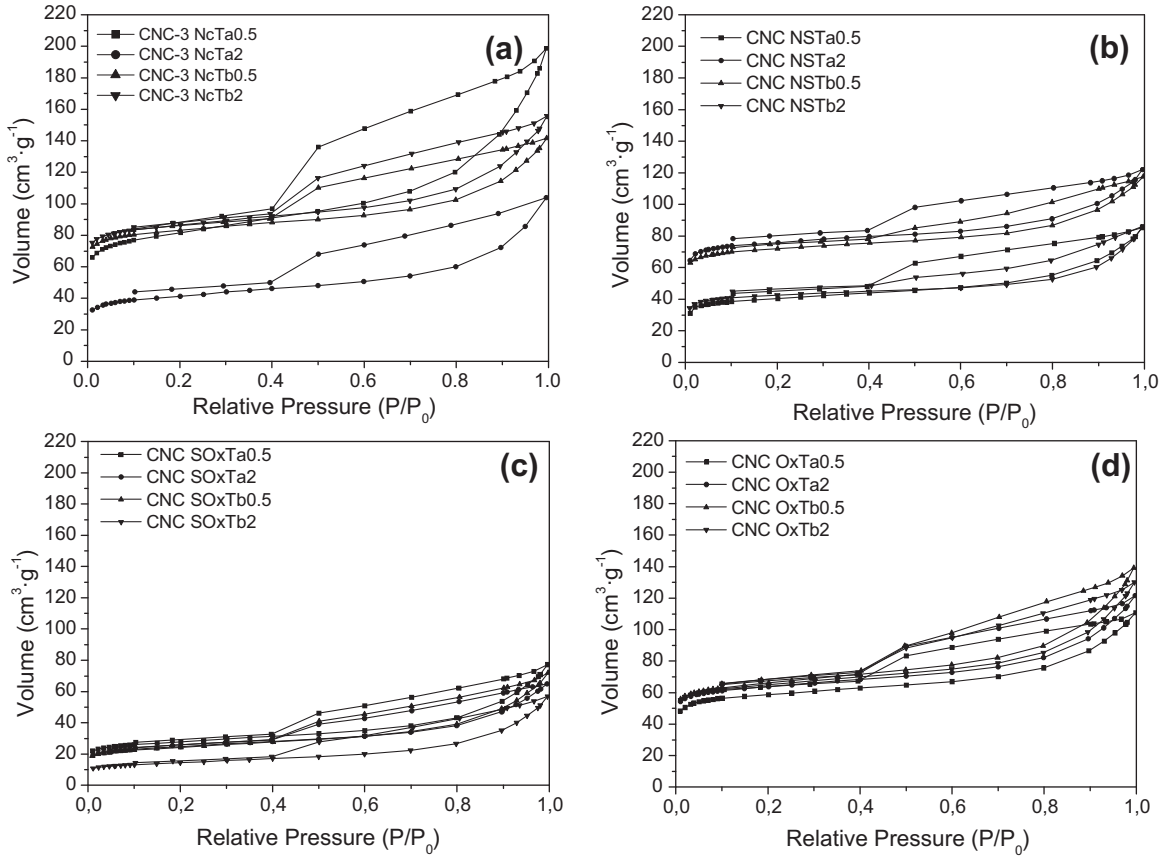

Fig. 4. Nitrogen adsorption–desorption isotherms of: (a) Samples treated with HNO_3; (b) Samples treated with HNO_3–H_2SO_4; (c) Samples treated with H_2SO_4–H_2O_2; and (d) Samples treated with H_2O_2.

Table 4
CO_2 and CO peak areas of the deconvolutioned TPD profiles.

Sample	CO_2 peak areas (μ mol g^{-1})		CO peak areas (μ mol g^{-1})			CO/CO_2
	Carboxylic (100–400 °C)	Anhydride Lactone (190–650 °C)	Anhydride (350–627 °C)	Phenol (600–700 °C)	Quinone (700–980 °C)	
CNC NcTa0.5	498	254	106	797	64	1.29
CNC NcTa2	440	410	450	1690	200	2.73
CNC NcTb0.5	595	1100	12	1862	173	1.21
CNC NcTb2	506	1077	36	1214	1131	1.50
CNC NSTa0.5	210	1060	890	960	240	1.6
CNC NSTa2	270	1420	1250	840	140	1.3
CNC NSTb0.5	570	2220	410	1460	210	0.7
CNC NSTb2	590	3220	0	3000	0	0.8
CNC SOxTa0.5	332	958	43	1111	448	1.24
CNC SOxTa2	237	1152	59	1341	111	1.09
CNC SOxTb0.5	287	953	24	1116	395	1.24
CNC SOxTb2	510	1165	43	862	32	0.56
CNC OxTa0.5	260	160	20	500	30	1.3
CNC OxTa2	240	110	20	420	90	1.5
CNC OxTb0.5	430	110	30	410	30	0.9
CNC OxTb2	280	340	0	310	200	0.8

most appropriate technique for studying the thermal stability of surface oxygen groups, which is important for applications at medium–high temperatures.

During TPD experiments surface oxygenated groups are desorbed as CO and CO_2. CO and CO_2 profiles can be deconvoluted in order to carry out a detailed study of the surface oxygenated groups created during these treatments. Table 4 summarizes the amounts of the different types of oxygenated groups calculated from the deconvoluted peak areas, and the relationship CO/CO_2, which was taken as a measure of acidity (low values) or basicity (high values) from the surface of the carbon materials [30].

For each oxidizing agent, an increase in the number of oxygenated groups was observed as the severity of the treatment increased, that is, as the temperature and time of the treatment increased. It was further noted that the ratio CO/CO_2 decreases as the severity of the oxidation treatments increased, indicating an

increase in the number of acid sites on the surface of the carbon materials.

As shown in Table 4, treatments with H_2O_2 were the least effective at creating functional groups due to H_2O_2 is the weakest oxidizing agent, among all the treatments used. From CO_2 profiles, it was observed that mainly carboxylic groups were produced with this oxidizing agent, whereas with the other ones mainly anhydride/lactone groups were created. From the deconvolution of the CO profiles, it was observed the creation of mainly phenol groups for all oxidizing agents. The most effective oxidation treatment in creating surface oxygenated groups, especially anhydride/lactone groups, was HNO_3–H2SO_4 treatment at boiling temperature for 2 h.

In the literature there are a large number of studies about the influence of the surface chemistry of the support on different applications, such as in the preparation of catalysts or the use of carbon materials as capacitors [1,31–34]. For example, surface oxygenated groups can influence the behavior of carbon materials used in capacitors increasing its capacitance by pseudocapacitance effects, which depends on the functional groups of the material [1]. On the other hand, there are a large number of studies on the influence of the support surface chemistry on the preparation of Pt/C catalysts. However, there are discrepancies about the effect of functionalization on the size and dispersion of metal particles [31–34]. These discrepancies are due to the fact that the size and dispersion of metal particles not only depends on the surface chemistry of the support, but also the synthesis method, the metal precursor and the nature of the support. From these studies is deduced that the surface chemistry of carbon materials can have an important effect on their applications and its study can help to improve their performance.

4. Conclusions

Different oxidation treatments were used in order to remove the metals used in the synthesis of carbon nanocoils (CNCs). The amorphous and graphitic carbons were also eliminated during these treatments. All samples had an ordered structure and their graphitization degree depended on the treatment used for the removal of metals. The treatments with H_2SO_4–H_2O_2 mixtures eliminate the amorphous carbon preferentially, thus obtaining low specific surface area materials, characteristics of graphitic materials. The use of different treatments had also an important effect on the textural properties of the carbon materials. CNCs showed specific surfaces areas in the range 30–250 $m^2\ g^{-1}$ and a total pore volume of 0.08–0.30 $cm^3\ g^{-1}$. On the other hand, surface oxygen groups were created during these treatments, modifying the surface chemistry of CNCs. Mainly, carboxylic and phenol groups were created and their number depended on the severity of the treatments. The treatment most effective in creating surface oxygen groups, especially groups carboxylic, was the treatment with HNO_3–H_2SO_4 at boiling temperature during 2 h.

Acknowledgments

The authors gratefully acknowledge financial support given by the MICINN through Project MAT2008-06631-C03-01. V. Celorrio and L. Calvillo and also acknowledge CSIC and the Spanish National Research Council for their JAE and FPI grants, respectively.

References

[1] A.L. Dicks, J. Power, Sources 156 (2006) 128–141.
[2] T. Shuihua, S. Gongquan, Q. Jing, S. Shiguo, G. Junsong, X. Qin, G.M. Haarberg, Chinese J. Catal. 31 (2010) 12–17.
[3] E. Frackowiak, F. Béguin, Carbon 39 (2001) 937–950.
[4] A.S. Aricò, P. Bruce, B. Scrosati, J.M. Tarascon, W. Van Schalkwijk, Nat. Mater. 4 (2005) 366–377.
[5] G. Hoogers, Fuel Cell Technology Handbook, first ed., CRC Press LLC, Germany, 2003.
[6] E. Auer, A. Freund, J. Pietsch, T. Tacke, Appl. Catal. A – Gen. 173 (1998) 259–271.
[7] L.R. Jordan, A.K. Shukla, J. Behrsing, N.R. Avery, B.C. Muddle, M. Forsyth, J. Appl. Electrochem. 30 (2000) 641–646.
[8] J.L. Pinilla, M.J. Lázaro, I. Suelves, R. Moliner, J.M. Palacios, Chem. Eng. J. 156 (2010) 170–176.
[9] D. Vairavapandian, P. Vichchulada, M.D. Lay, Anal. Chim. Acta 626 (2008) 119–129.
[10] C. Lin, J.A. Ritter, Carbon (1997) 1271–1278.
[11] N. Job, A. Théry, R. Pirard, J. Marien, L. Kocon, J.N. Rouzaud, F. Béguin, J.P. Pirard, Carbon 43 (2005) 2481–2494.
[12] L. Calvillo, V. Celorrio, R. Moliner, P.L. Cabot, I. Esparbé, M.J. Lázaro, Micropor. Mesopor. Mat. 116 (2008) 292–298.
[13] M.J. Lázaro, L. Calvillo, E.G. Bordejé, R. Moliner, R. Juan, C.R. Ruiz, Micropor. Mesopor. Mat. 103 (2007) 158–165.
[14] V. Celorrio, L. Calvillo, M.V. Martínez-Huerta, R. Moliner, M.J. Lázaro, Energ. Fuel 24 (2010) 3361–3365.
[15] T. Hyeon, S. Han, Y.E. Sung, K.W. Park, Y.W. Kim, Angew. Chem. Int. Ed. 42 (2003) 4352–4356.
[16] Q. Li, H. Yan, J. Zhang, Z. Liu, Carbon 42 (2004) 829–835.
[17] P. Serp, A. Madroñero, J.L. Figueiredo, Fuel 78 (1999) 837–844.
[18] L. Calvillo, M.J. Lázaro, I. Suelves, Y. Echegoyen, E.G. Bordejé, R. Moliner, J. Nanosci. Nanotechnol. 9 (2009) 1–6.
[19] A. Gil, G. de la Puente, P. Grange, Micropor. Mat. 12 (1997) 51–61.
[20] D. Ugarte, Carbon 33 (1995) 989–993.
[21] T. Guo, P. Nicolaev, A. Thess, D.T. Colbert, R.E. Smalley, Chem. Phys. Lett. 243 (1995) 49–54.
[22] S. Yang, X. Chen, T. Katsuno, S. Motojima, Mater. Res. Bull. 42 (2007) 465–473.
[23] S. Han, Y. Yun, K.W. Park, Y.E. Sung, T. Hyeon, Adv. Mater. 15 (2003) 1922–1925.
[24] M. Sevilla, A.B. Fuertes, Mater. Chem. Phys. 113 (2009) 208–214.
[25] M. Sevilla, G. Lota, A.B. Fuertes, J. Power Sources 171 (2007) 546–551.
[26] M. Kruk, M. Jaroniec, K.P.J. Gardkaree, J. Colloid Interface Sci. 192 (1997) 250–256.
[27] A. Cuesta, P. Dhamelincourt, J. Laureyns, A. Martínez-Alonso, J.M.D. Tascon, Carbon 32 (1994) 1523–1532.
[28] P. Lespade, A. Marchand, M. Couzi, F. Cruege, Carbon 22 (1984) 375–385.
[29] O. Beyssac, B. Goffé, J.P. Petitet, E. Froigneux, M. Moreau, J.N. Rouzaud, Spectrochim. Acta A 59 (2003) 2267–2276.
[30] J.L. Figueiredo, M.F.R. Pereira, M.M.A. Freitas, J.J.M. Orfao, Carbon 37 (1999) 1379–1389.
[31] A.E. Aksoylu, M. Madalena, A. Freitas, M.F.R. Pereira, J.L. Figueiredo, Carbon 39 (2001) 175–185.
[32] C. Prado-Burguete, A. Linares-Solano, F. Rodríguez-Reinoso, C. Salinas-Martínez de Lecea, J. Catal. 115 (1989) 98–106.
[33] M.A. Fraga, E. Jordao, M.J. Mendes, M.M.A. Freitas, J.L. Faria, J.L. Figueiredo, J. Catal. 209 (2002) 355–364.
[34] A. Guerrero-Ruiz, P. Badenes, I. Rodríguez-Ramos, Appl. Catal. A – Gen. 173 (1998) 313–321.

3

On the enhancement of activity of Pt and Pt-Ru catalysts in methanol electrooxidation by using carbon nanocoils as catalyst support

V. Celorrio, L. Calvillo, R. Moliner, E. Pastor, M.J. Lázaro

En preparación

On the enhancement of activity of Pt and Pt-Ru catalysts in methanol electrooxidation by using carbon nanocoils as catalyst support

V. Celorrio[1], L. Calvillo[1], R. Moliner[1], E. Pastor[2], M.J. Lázaro[1*]

[1]Instituto de Carboquímica (CSIC), Miguel Luesma Castán 4, 50018-Zaragoza, Spain

[2]Universidad de La Laguna, Dpto de Química-Física, Avda. Astrofísico Francisco Sánchez s/n, 38071-La Laguna (Tenerife), Spain

* Corresponding author: Tel. +34 976 733977; Fax: +34 976 733318; E-mail address: mlazaro@icb.csic.es

Abstract

Carbon nanocoils (CNCs) were used to prepare Pt and Pt-Ru catalysts by the sodium borohydride (BM), methanol (MM) and polyol (EGM) solution reduction methods. Their physicochemical properties were studied by means of energy dispersive X-ray analysis, X-ray diffraction and transmission electron microscopy, whereas the electrochemical activity towards carbon monoxide and methanol oxidations was studied using cyclic voltammetry and chronoamperometry. Furthermore, differential electrochemical mass spectrometry experiments were carried out to study the reaction mechanisms. Results were compared with those obtained for the commercial Pt/C and PtRu/C catalysts from E-TEK. Results showed that choosing an adequate synthesis procedure, better electrocatalytic behaviours towards CO and methanol oxidation can be obtained by using carbon nanocoils as support material.

Keywords: Carbon nanocoils, Pt and Pt-Ru electrocatalysts, methanol electrooxidation

1. Introduction

Direct methanol fuel cells (DMFCs) are promising power sources, especially for electric vehicles. Due to their low operating temperature (60-80 ºC), vehicle emissions are significantly lower than those of conventional vehicles using internal combustion engines. However, its low activity compared with H_2/O_2 systems, currently being achieved with polymeric electrolyte membrane fuel cells (PEMFCs), is still an important drawback to be solved [1-2]. The major limitation of DMFCs is the low activity at the anode side, therefore, more efficient catalysts for the electrooxidation of methanol are urgently needed. The state of the art of electrocatalysts for methanol electrooxidation is based on platinum nanoparticles supported on carbon black. Nowadays, only platinum-based catalysts reach the activity and stability required at the cathode and anode side. So far, not noble metal based catalysts have been found active enough for the oxidation of methanol. So currently, the main objective is to reduce the amount of Pt maintaining or improving its catalytic activity [3-5].

However, during the methanol electrooxidation process, various reaction intermediates are formed, some of them CO-like species that act poisoning monometallic platinum electrodes at a concentration up to 10 ppm. For this reason, in the last few years, many efforts have been devoted to obtain more CO-tolerant electrocatalysts. It has been shown that the alloying of Ru, Sn or Mo with Pt provides more CO-tolerant anodes with better performance [6-8]. By using bimetallic alloys, CO tolerance has increased to values up to 100-200 ppm [9-10]. Among them, Pt-Ru alloys have shown to be the most effective [11-17]. The presence of Ru facilitates the oxidation of CO species and, consequently, enhances the electrocatalytic activity for methanol oxidation. This effect is called bifunctional mechanism and/or “ligand effect” [4, 17].

In Pt-Ru systems, some aspects such as the preparation procedure, the Pt:Ru atomic ratio and the metal-support interactions, have been found to strongly influence their performance for methanol oxidation. Antolini et al. [18] studied the effect of the catalyst composition in Pt-Ru alloyed catalysts supported on carbon. They concluded that catalysts with nominal Pt:Ru compositions in the range of 1:1-1:3 present the best performance in presence of CO, which is in good agreement with other authors like Takasu and Zhang [15, 19]. The effects of the surface area of the carbon supports on the characteristics of Pt-Ru catalysts supported on different carbon blacks have been studied by Takasu et al. [15]. They showed that the extend of allowing, as well as the size of the $Pt_{50}Ru_{50}$ particles, decreased as the specific surface area of the carbon black increased, whereas the specific activity for methanol oxidation enhanced. Therefore, the selection of a carbon support with suitable properties is very important to obtain an active electrocatalysts, since carbon materials have a strong influence on both the physicochemical and electrochemical properties of supported noble metal catalysts [20].

On the other hand, the catalyst synthesis method has also a strong influence on their activity, since the Pt:Ru atomic ratio, the particle size distribution and the metal dispersion can be controlled by changing the synthesis conditions. Therefore, different synthesis methods can result in catalysts with different characteristics [21-22]. There are three important methods to prepare carbon-supported Pt-Ru catalysts: impregnation, colloidal and microemulsion methods; although the colloidal method is the most extensively explored [11, 23]. The high activity, the CO-tolerance reached and the possibility to control the particle size by using the colloidal method, make it an attractive alternative method to prepare electrocatalysts. However, it is still quite complicated and expensive compared to the impregnation-reduction one [14, 24].

Taking all the exposed above into account, in this work we propose the use of carbon nanocoils as catalysts support for platinum and platinum-ruthenium electrocatalysts and the study of the effect that different synthesis methods have on the catalyst properties. Pt and Pt-Ru electrocatalysts have been prepared by the sodium borohydride, methanol and polyol solution reduction methods. Their physicochemical properties have been studied by X-ray diffraction and transmission electron microscopy, whereas the electrochemical properties towards CO and methanol oxidation have been studied by cyclic voltammperometry and chronoamperometry. To complete the study, a comparison with commercial Pt/C and Pt-Ru/C catalysts from E-TEK is also reported. Furthermore, the electrocatalysts which presented the best behaviour were studied in a Differential Electrochemical Mass Espectrometer (DEMS) in order to study their different electrooxidation pathways.

2. Experimental

2.1. Synthesis of carbon nanocoils (CNCs)

CNCs were synthesized by a low temperature procedure as described elsewhere [25]. Briefly, nickel (Panreac) and cobalt (Sigma-Aldrich) salts were added to an aqueous solution of formaldehyde (Sigma-Aldrich) and silica sol (Supelco) under stirring conditions. Then, resorcinol (Sigma-Aldrich) was added and the stirring was maintained for 30 minutes, being the molar ratios H_2O/Co salt/Ni salt/R/F/silica = 100:0.2:0.2:1:2:0.6. Afterwards, this mixture was subjected to a heat treatment at 85 ºC during 3 h in a closed system, and then dried overnight at 108 ºC. Finally, it was carbonized in a nitrogen atmosphere at 900 ºC for 3 h. In order to remove the silica particles, the sample was treated with a 5 M NaOH (Panreac) solution and,

subsequently, with concentrated HNO_3 (65%, Fluka) at room temperature during 2 h to remove the metal salts.

2.2. Preparation of the electrocatalysts

Electrocatalysts were prepared by the solution-reduction method, using different reducing agents, such as methanol (MM), sodium borohydride (BM) and ethylene glycol (EGM). The three methods were used to prepare Pt and Pt-Ru catalysts supported on carbon nanocoils. These methods involve an impregnation step followed by a reduction step. In all cases, metal precursors (8 wt. % $H_2PtCl_6 \cdot 6\ H_2O$ solution, Sigma-Aldrich, and 45-55% $RuCl_3$ Sigma-Aldrich) were dissolved and mixed with the carbon support and, subsequently, the metal precursors were reduced in situ.

In the case of the BM method, an aqueous solution of the metal precursors was prepared and mixed with the carbon support. Subsequently, sodium borohydride was slowly added to the solution at room temperature, in order to reduce the metal precursors [26].

In MM and EGM methods, precursors were dissolved in a 1:3 (v/v) methanol-water mixture and ethylene glycol, respectively. In these cases, methanol and ethylene glycol acted as solvent and reducing agent. The syntheses were carried out at 90 and 195 ºC for 2 h, respectively [21, 27].

Appropriate concentrations of the precursors were used to obtain a theoretical metal loading of 20 wt.% and a Pt:Ru atomic ratio of 50:50.

2.3. Physicochemical characterization methods

The metal loading was determined by energy dispersive X-ray analyses (EDX) technique Röntec XFlash Si(Li), coupled to a scanning electron microscope Hitachi S-3400 N.

TEM studies were made using a JEOL-2000 FXII microscope, operated with an accelerating voltage of 200 kV.

X-ray diffraction (XRD) patterns were recorded using a Bruker AXS D8 Advance diffractometer with a θ–θ configuration and using Cu Kα radiation (λ = 0.154 nm). Values of 2θ between 0º and 100º were recorded and Scherrer's equation was applied to the (220) peak of the Pt in order to estimate the crystallite sizes from the diffractograms [28].

2.4. Electrochemical studies

A two compartment electrochemical cell was used to carry out the electrochemical experiments using a MicroAutolab potentiostat. A large area pyrolitic graphite bar was used as counter electrode and a reversible hydrogen electrode (RHE) as reference. The reference and working electrodes were placed in different compartments connected by a Luggin capillary. All potentials in this paper are referred to the RHE reference electrode. A thin-layer of the electrocatalysts was deposited on a pyrolitic graphite disk (7 mm diameter, 1.54 cm^2 geometric area) to prepare the working electrodes. A mixture of 2 mg of the catalyst and 10 μl of Nafion dispersion (5 wt.%, Aldrich) in 500 μl of ultrapure water (Millipore Milli-Q system) was used to prepare the catalyst inks. A 40 μl aliqout of the suspension was deposited onto the graphite disk and dried in air. A 0.5 M H_2SO_4 (Merck) was used as electrolyte solution and was deaerated using nitrogen gas. All the electrochemical experiments presented in this work were carried out at room temperature.

Electrochemical active areas of the catalysts were determined by CO_{ads} stripping voltammetry, assuming the adsorption of a CO monolayer and a charge of 420 μC cm^{-2} involved in the oxidation of CO_{ads}. These electroactive areas have been used to calculate the current densities given in the text.

Methanol oxidation was characterized by cyclic voltammetry and chronoamperometry in a 2 M CH_3OH + 0.5 M H_2SO_4 solution.

2.5. Differential Electrochemical Mass Spectrometry (DEMS)

Working electrodes were prepared using gass diffusion electrodes (GDEs) of 7 mm diameter. First, a layer of 0.8 mg/cm^2 of diffusion ink prepared by mixing Vulcan XC-72R, ultrapure water (Millipore Milli-Q system), isopropanol (Merck, p.a.) and a PTFE dispersion (60 wt. %, Dyneon) was deposited onto one side of a carbon cloth. Then, this carbon cloth was treated at 280 ºC during 0.5 hours and at 350 ºC during 0.5 hours.

Electrocatalyst inks were prepared by mixing the respective electrocatalysts with a Nafion dispersion (5 wt.%, Sigma-Aldrich) and ultrapure water (1:5:10 wt.) and deposited onto one side of the GDE. Final metal loading of the working electrodes was of 0.7 mg metal/cm^2.

DEMS measurements were carried out in the experimental set-up described in [29]. Briefly, the working electrode is fixed between a PTFE membrane (Scimat) and a carbon glassy rod, which is connected to a Au wire to keep the electrical contact. Being the counter electrode a high surface area carbon rod and the reference electrode a reversible hydrogen electrode (RHE) placed inside a Luggin capillary. The potenciostat-galvanostat used was an Autolab PGSTAT302 (Ecochemie). The cell was directly attached to the vacuum chamber of the mass spectrometer (Balzers QMG112) with a Faraday cup detector.

3. Results and discussion

3.1. Physicochemical characterization of the supports and electrocatalysts

The physicochemical characterization of the CNCs was stated in a previous work [25]. Carbon nanocoils presented a specific surface area of 124 m^2 g^{-1}, consisting on a long curved ribbon of carbon which exhibited well-aligned graphitic layers. On the other hand, commercial catalysts used for comparison are supported on Vulcan XC-72, which has a specific surface area around 250 m^2 g^{-1} and consist of an aggregation of 30-60 nm size-particles [30].

The metal content of the electrocatalysts was determined by EDX analysis. In all cases, the values obtained were closed to the nominal value of 20 wt.% (see Table 1). However, the Pt:Ru atomic ratio depended on the synthesis method. A good agreement between the theoretical and the experimental compositions was found with the EGM method. Nevertheless, for the BM and MM methods, the Pt:Ru ratios were 66:34 and 74:26, respectively, suggesting that the Ru precursor was not completely reduced under those synthesis conditions. It has already been demonstrated that many factors can affect the composition, morphology and dispersion of Pt-Ru/C catalysts when solution-reduction methods are used [17].

Figure 1 shows the X-ray diffraction patterns for the Pt and Pt-Ru catalysts. The diffraction peak at $2\theta = 26^{\circ}$ is attributed to the graphitic structure of the carbon materials used as support. In the case of Pt catalysts, the crystalline structure of the metal in the nanoparticles is evident and the XRD patterns clearly show the five characteristic peaks of the face-centred cubic (fcc) structure of Pt, namely (111), (200), (220), (311) and (222) planes. For the Pt-Ru catalysts, no peaks corresponding to metallic ruthenium with a hexagonal close packed (hcp) structure or ruthenium oxide phase were observed, indicating that Ru was incorporated in the Pt fcc structure.

Furthermore, it can be observed that the peaks for platinum catalysts were narrower than those for Pt-Ru catalysts, indicating larger metal particle sizes. This was confirmed by the calculation of the average metal crystallite sizes of the electrocatalysts using the Scherrer equation (Table 1). It is shown that platinum nanoparticles presented larger crystallite sizes than the bimetallic Pt-Ru ones, suggesting that the addition of Ru species could inhibit the agglomeration of Pt particles [18]. In addition, the crystallite size depended on the synthetic route. The largest crystallite size was obtained by using the EGM (5.6 nm for Pt/CNC and 3.8 nm for PtRu/CNC catalysts).

It can be also observed that higher particle sizes were obtained for catalysts supported on CNCs than for commercial ones (supported on Vulcan XC-72R). This could be attributed to that Vulcan XC-72R has a large number of nucleation sites, leading to the formation of smaller particles. In contrast, graphitized carbons, like CNCs, have a lower number of nucleation sites because only the surface defects can act as nucleation sites, and thus larger metal particles would be obtained.

The lattice parameter was also calculated from the XRD patterns and the results are summarized in Table 1. The lattice parameters for PtRu/C catalysts were smaller than those for the corresponding Pt/C catalysts. This result is in agreement with previous works and indicates the strong interaction between Pt and Ru [31].

In Figure 2, TEM images of the Pt and PtRu catalysts supported on CNCs and synthesized by different methods are shown. Metal particle sizes observed by TEM were in good agreement with those calculated before by the XRD data. A good distribution of the metal particles on the support was obtained using the BM and EGM methods (Figure 2.a., 2.b., 2.e., 2.f.). However, the agglomeration of the metal particles was observed for Pt and PtRu catalysts prepared by the MM method.

3.2. Electrochemical characterization

3.2.1. Carbon monoxide oxidation

In order to establish the CO tolerance of the catalysts, as well as the electroactive area, the adsorption and later electrochemical oxidation of a CO monolayer on the catalysts has been carried out. CO stripping voltammograms were obtained after bubbling CO through the electrolyte solution for 10 min applying a potential of 0.2 V (vs. RHE), followed by nitrogen purging for removing the CO from the solution. Figure 3 shows the CO-stripping voltammograms obtained at room temperature for Pt and Pt-Ru catalysts.

In the case of Pt supported catalysts, the peak potential for the CO_{ad} oxidation occurred at around 0.84 V for the commercial catalyst from E-TEK, whereas a shift to more negative potentials was observed when carbon nanocoils were used as support material. These results follow the tendency described in the literature which affirm that the CO oxidation peak shifts positively while increasing Pt particle size [maillard 2004]. However, between the different CNC-supported catalysts, the reverse behaviour was found. It could be attributed to an electronic effect [32] or to the remaining presence of oxygen groups on the support surface. In previous works, we have observed that the surface oxygen groups of the support can help to oxidize the adsorbed CO in a similar way that Ru does [33]. On the other hand, the CO oxidation peak potential strongly depended on the synthesis method. CO was easily oxidized on the Pt/CNC-BM catalyst, which could be attributed to the good metal dispersion or the lowest metal particle size obtained by the BM method.

With the addition of Ru, the hydride area of the voltammogram decreased and a shift of the oxide stripping peak to more negative potential was produced. The oxidation of CO on the commercial PtRu/C catalyst from E-TEK was found to begin at 0.52 V vs.

RHE and showed a current density peak at 0.58 V. For catalysts supported on carbon nanocoils, both the onset and the peak potentials were shifted towards more negative potentials, respect to the commercial catalyst. The comparison between the different PtRu catalysts is rather difficult, since different Pt:Ru ratios were obtained. In the literature, the shift of the oxidation peak potential to more negative potentials as the Ru content increases has been reported [9]. For the catalysts studied in this work, it was observed that CO_{ads} was more easily oxidized on the catalyst synthesised by the BM method (PtRu/CNC-BM), as happened for Pt catalysts, although it had a lower Ru content than expected (Pt:Ru ratio = 66:34). In this case, the onset potential occurred at 0.35 V and the CO oxidation peak was attained at 0.49 V.

Therefore, either for Pt and Pt-Ru catalysts, it was found that CO was more easily oxidized on catalysts prepared by the sodium borohydride method. This behaviour could be attributed to a slightly hydrogenation of the CNC surface during the reduction of the metal precursors, that could act promoting the oxidation of CO [34]. These results confirm the influence of the catalyst synthesis method and the use of carbon nanocoils as support on the CO oxidation reaction.

3.2.2. Methanol oxidation

Figure 4 illustrates cyclic voltammograms recorded at room temperature for the catalysts studied in this work in a 2 M CH_3OH + 0.5 M H_2SO_4 solution.

Pt based catalysts (Figure 4.a) presented the irreversible behaviour for the methanol electrooxidation, the onset potential occurred at around 0.60 V vs. RHE for all them. Watanabe et al. [35] examined the influence of platinum crystallite dispersion on the electrocatalytic oxidation of methanol, affirming no crystallite size effects (even for crystallites as small as 1.4 nm diameter). For this reason, our results are entirely

compalable. The highest current density was achieved by the Pt/CNC-BM catalyst during the positive scan at potentials around 0.98 V, corresponding to the methanol oxidation. This result could be associated to the higher CO tolerance of this catalyst, as shown above. Another peak at around 0.85 V was observed during the backward scan, which is attributed to the oxidation of the intermediates formed during the methanol oxidation. Pt/CNC-BM also exhibited the highest current density at 0.60 V vs. RHE (potential near to the working potential in a DMFC). These specific activities are summarized in Table 3. The current density for the methanol oxidation on the Pt/C E-TEK reached a value of 10 μA cm^{-2}, whereas the Pt catalysts supported on carbon nanocoils presented current densities two (Pt/CNC-EGM and Pt/CNC-MM) or three (Pt/CNC-BM) times higher. Pt/CNC catalysts showed higher activity towards methanol electrooxidation than the commercial Pt/C catalyst. This behaviour could be attributed to the carbon-platinum interaction, which could also be favoured by the presence of more oxygen groups on the surface of carbon nanocoils than on Vulcan [25]. These oxygen groups could help to oxidize the CO adsorbed on the Pt particles, thus increasing the efficiency of the catalysts in the methanol oxidation. From these result, it could be stated that the CO oxidation would be the limiting stage, since the improvement of this stage results in an improvement of the global process.

Methanol electrooxidation was also evaluated by chronoamperometry. Figure 5 shows the potentiostatic current densities, normalized by the electroactive surface area, as a function of time at 0.60 V vs. RHE. The response increased in the order: Pt/CNC-MM < Pt/C E-TEK ~ Pt/CNC-EGM < Pt/CNC-BM (Table 3). These values followed the same trend than that observed before by cyclic voltammperometry.

For Pt-Ru catalysts, the onset potential varied between 0.3 to 0.5 V (Figure 4.b), taking place a shift to more negative potentials respect to the corresponding Pt catalysts.

In this case, the PtRu/CNC-MM catalyst showed the highest activity towards the methanol oxidation. For this catalyst, the current density grew faster than for the commercial PtRu/C from E-TEK. It was found that PtRu/CNC-MM catalyst displayed about 5-fold higher specific current density than the commercial PtRu/C catalyst at 0.60 V vs. RHE (see Table 3). This result is in agreement with that published by Jusys et al. [36] confirming that at positive potentials (0.6-0.65 V) the Pt-rich catalysts are more active in the MOR. The chronoamperometric current density values increased in the following order: PtRu/CNC-EGM < PtRu/CNC-BM < PtRu/C E-TEK < PtRu/CNC-MM. For all of them, the values reached were higher than those for the corresponding Pt catalysts.

3.3. DEMS measurements

According to the electrochemical results previously described, DEMS experiments were performed in order to clarify the different behaviors. Pt/CNC-BM and PtRu/CNC-MM samples were chosen to test in the DEMS setup in order to explain their better behaviour compared with the commercial catalysts.

Figure 6 shows the CVs (solid line) for the Pt//CNC-BM (a), Pt/C E-TEK (b), PtRu/CNC-MM (c) and PtRu/C E-TEK (d) respectively and the corresponding mass signals for CO_2 (m/z = 44) and formic acid (followed through methylformate formation, m/z = 60) during methanol electrooxidation. In the upper pannel, the faradic current expected for a 100% efficient conversion of methanol to CO_2 calculated from the m/z = 44 signal after calibration, was also included (dashed line). The difference in area between experimental (solid curve) and theoretical (dashed curve) currents is the extra charge associated with the formation of products different from CO_2 (formic acid can be indirectly detected by DEMS, but not formaldehyde).

In the case of the platinum-supported electrocatalysts, the m/z = 44 ion current (middle panels) generally traces the faradaic methanol oxidation reaction (MOR) current, taking into account the time constant of the DEMS cell. A closer comparison of Faradaic (black line, upper panels) and m/z = 44 ion currents reveals, that the ratio in MOR current depends on the potential scan direction, with relatively higher mass spectrometric currents in the negative-going scan. Also the MSCVs for methylformate formation (m/z = 60) largely follow the Faradaic current for MOR. However, the separation between the positive- and negative-going potential scans is larger compared to the m/z = 44 mass signal, although the time constant should be essentially the same. This deviation could be explained by the relative slow ester formation reaction between formic acid and methanol compared to the instantaneous CO_2 formation [36].

Regarding to the PtRu-supported electrocatalysts, the formation of CO_2 starts at 0.4 V, i.e. about 200 mV more negative than that of Pt. Whereas the formation of methylformate starts at 0.5 V, which is the same as in the case of Pt.

A more accurate comparison between the electrodes is possible from the faradic and ion-charge integrations during the forward scans of the CV and MSCV for CO_2. The average efficiency for each catalyst can be calculated on the bases of these integrated values and is present in Table 4. As can be seen, CO_2 efficiencies for the electrocatalysts supported on carbon nanocoils are lower that that for the commertial catalysts. However, the current densities achieved after 800 s in the oxidation of 2 M CH_3OH + 0.5 M H_2SO_4 (see Table 3) were higher. So it can be suggested that the use of CNC as electrocatalysts support facilitates the oxidation of methanol reaction intermediates.

4. Conclusions

Carbon nanocoils have been proposed as alternative material that could replace carbon blacks as electrocatalyst support for low temperature fuel cells. Pt and PtRu catalysts were supported on this carbon material by the solution-reduction method using different reducing agents (BM, MM and EGM), and their behaviour was compared with that of commercial Pt/C and PtRu/C catalysts from E-TEK. The results showed that an increase of the electrocatalytic activity can be obtained by using carbon nanocoils as electrocatalyst support and that the use of different synthesis conditions can affect the physicochemical and electrochemical properties of the catalysts.

For Pt catalysts, larger particle sizes were obtained using CNCs as support, compared with the commercial catalyst, getting the biggest particle size by the EGM method. On the contrary, for PtRu catalysts, similar or smaller particle sizes were obtained using CNCs as support, compared with the commercial catalyst from E-TEK. In this case, the smallest particle size was obtained by the MM method. Therefore, it can not be conclude that one method is better than the other ones, since the effect of the synthesis method depends also on the metals deposited.

The electrocatalysts performance also depended on the synthesis method. The catalysts synthesised by the BM method (Pt/CNC-BM and PtRu/CNC-BM) oxidized the CO_{ads} at more negative potentials than the rest of catalysts. This could be attributed to the slight hydrogenation of the carbon surface during the metal reduction step with sodium borohydride which promote the oxidation of carbon monoxide.

For the methanol oxidation, higher current densities were obtained on Pt/CNC electrocatalysts than on Pt/C from E-TEK. Taking into account that the commercial catalysts had smaller metal particle size, this result is attributed to the surface oxygen groups of carbon nanocoils, created during the HNO_3 treatment, which help to oxidize the CO adsorbed on Pt particles. The addition of Ru to Pt markedly increased the

electrocatalytic activity towards methanol oxidation through the adsorption of oxygenated species on Ru-sites. The highest current densities were recorded for the PtRu/CNC-MM catalyst. However, a proper comparison between all PtRu catalysts could not be carried out due to their different Pt:Ru atomic ratio.

DEMS measurements suggest that the use of carbon nanocoils as catalysts support faticitate the oxidation of intermedietes like formic acid compared with the commertial catalysts.

ACKNOWLEDGMENTS.

The authors gratefully acknowledge financial support given by the MICINN through Project MAT2008-06631-C03-01. V. Celorrio also acknowledges CSIC for her JAE grant.

REFERENCES

[1] J.M. Andújar, F. Segura, Renew. Sust. Energ. Rev. 13 (2009) 2309-2322.

[2] S.K. Kamarudin, F. Achmad, W.R.W. Daud, Int. J. Hydrogen Energ. 34 (2009) 6902-6916.

[3] A.M. Zainoodin, S.K. Kamarudin, W.R.W. Daud, Int. J. Hydrogen Energ. 35 (2010) 4606-4621.

[4] A.S. Aricò, S. Srinivasan, V. Antonucci, Fuel C*-ells 1 (2001) 133-161.

[5] T. Iwasita, Electrochim. Acta 47 (2002) 3663-3674.

[6] N. Tsiouvaras, M.V. Martínez-Huerta, O. Paschos, U. Stimming, J.L.G. Fierro, M.A. Peña, Int. J. Hydrogen Energ. 35 (2010) 11478-11488.

[7] J.H. Kim, S.M. Choi, S.H. Nam, M.H. Seo, S.H. Choi, W.B. Kim, Appl. Catal. B: Environ. 82 (2008) 89-102.

[8] L.C. Ordóñez, P. Roquero, P.J. Sebastian, J. Ramírez, Int. J. Hydrogen Energ. 32 (2007) 3147-3153.

[9] E.M. Crabb, M.K. Ravikumar, D. Thompsett, M. Hurford, A. Rose, A.E. Russel, Phys. Chem. Chem. Phys. 6 (2004) 1792-1798.

[10] S.J. Lee, S. Mukerjee, E.A. Ticianelli, J. McBreen, Acta 44 (1999) 3283-3293.

[11] U.A. Paulus, U. Endruschat, G.J. Feldmeyer, T.J. Schmidt, H. Bönnermann, R.J. Behm, J. Catal. 195 (2000) 383-393.

[12] J. Solla-Gullón, F.J. Vidal-Iglesias, V. Montiel, A. Aldaz, Electrochim. Acta 49 (2004) 5079-5088.

[13] W. Chen, J.Y. Lee, Z. Liu, Mater. Lett. 58 (2004) 3166-3169.

[14] A.J. Dickinson, L.P.L. Carrete, J.A. Collins, K.A. Friedich, U. Stimming, Electrochim. Acta 47 (2002) 3733-3739.

[15] Y.J. Zhang, A. Maroto-Valiente, I. Rodríguez-Ramos, Q. Xin, A. Guerrero-Ruiz, Catal. Today 93 -95 (2004) 619-626.

[16] Z. Qi, A. Kaufman, J. Power Sources 113 (2003) 115-123.

[17] H. Liu, C. Song, L. Zhang, J. Zhang, H. Wang, D.P. Wilkinson, J. Power Sources 155 (2006) 95-110.

[18] E. Antolini, L. Giorgi, F. Cardellini, E. Passalacqua, J. Solid State Electr. 5 (2001) 131-140, 2001.

[19] Y. Takasu, T. Kawaguchi, W. Sugimoto, Y. Murakami, Electrochim. Acta 48 (2003) 3861-3868.

[20] L. Calvillo, V. Celorrio, R. Moliner, M.J. Lázaro, Mater. Chem. Phys. 127 (2011) 335-341.

[21] M.J. Lázaro, V. Celorrio, L. Calvillo, E. Pastor, R. Moliner, J. Power Sources 196 (2011) 4236-4241.

[22] D. Sebastián, J.C. Calderón, J.A. González-Expósito, E. Pastor, M.V. Martínez-Huerta, I. Suelves, R. Moliner, M.J. Lázaro, Int. J. Hydrogen Energ. 35 (2010) 9934-9942.

[23] M. Götz, H. Wendt, Electrochim. Acta 43 (1998) 3637-3644.

[24] N. Fujiwara, K. Yasuda, T. Ioroi, Z. Siroma, Y. Miyazaki, Electrochim. Acta 47 (2002) 4079-4084.

[25] V. Celorrio, L. Calvillo, M.V. Martínez-Huerta, R. Moliner, M.J. Lázaro, Energ. Fuels 24 (2010) 3361-3365.

[26] L. Calvillo, M.J. Lázaro, E. García-Bordejé, R. Moliner, P.L. Cabot, I. Esparbé, E. Pastor, J.J. Quintana, J. Power Sources 169, 59-64, 2007.

[27] X. Wang, I.-M. Hsing, Electrochim. Acta 47 (2002) 2981-2987.

[28] B.E. Warren, Addison-Wesley, Reading, 1969.

[29] S. Pérez-Rodríguez, M. Corengia, G. García, F.C. Zinola, M.J. Lázaro, E. Pastor, Int. J. Hydrogen Energ. (2012), doi:10.1016/j.ijhydene.2011.11.090

[30] M.J. Lázaro, L. Calvillo, V. Celorrio, J.I. Pardo, S. Perathoner, R. Moliner, Carbon Black: Production, Properties and Uses. F. Columbus (Eds.). ©2011 Nova Science Publishers, Inc.

[31] L. Jiang, G. Sun, X. Zhao, Z. Zhou, S. Yan, S. Tang, G. Wang, B. Zhou, Q. Xin, Electrochim. Acta 50 (2005) 2371-2376.

[32] J.-H. Wee, K.-Y. Lee, J. Power Sources 157 (2006) 128-135.

[33] J.R.C. Salgado, F. Alcaide, G. Álvarez, L. Calvillo, M.J. Lázaro, E. Pastor, J. Power Sources 195 (2010) 4022-4029.

[34] A. Moore, V. Celorrio, M. Montes de Oca, D. Plana, W. Hongthani, M.J. Lázaro, D. Fermín, Chem. Commun. 47 (2011) 7656–7658.

[35]

[36] Z. Jusys, J. Kaiser, J. Behm. Langmuir 19 (2003) 6759-6769.

FIGURE CAPTIONS

Figure 1. XRD diffractograms for the Pt/CNC and PtRu/CNC catalysts synthesised by different methods and for the commercial Pt/C and PtRu/C catalysts from E-TEK.

Figure 2. TEM images of the Pt/CNC and PtRu/CNC catalysts synthesised by different methods: (a) Pt/CNC-BM; (b) PtRu/CNC-BM; (c) Pt/CNC-MM; (d) PtRu/CNC-MM; (e) Pt/CNC-EGM; and (f), PtRu/CNC-EGM.

Figure 3. CO_{ads} stripping voltammograms for the platinum based (a) and platinum-ruthenium based (b) electrocatalysts. E_{ad} = 0.20 V; υ = 20 mV s^{-1}; T = 25 ºC.

Figure 4. CVs for platinum based (a) and platinum-ruthenium based (b) electrocatalysts in 2 M MeOH + 0.5 M H_2SO_4. υ = 20 mV s^{-1}; T = 25 ºC.

Figure 5. *j/t* response recorded at 0.60 V vs. RHE in 2 M MeOH + 0.5 M H_2SO_4 for platinum based (a) and platinum-ruthenium based (b) electrocatalysts. T = 25 ºC.

Figure 6. CVs and MSCVs for 0.5 M CH_3OH oxidation in 0.5 M H_2SO_4 at Pt/CNC-BM (a), PtRu/CNC-MM (b), Pt/C E-TEK (c) and PtRu/C E-TEK (d) electrocatalysts. υ = 0.001 V s^{-1}; T = 25 ºC.

Table 1. Total metal content and Pt:Ru ratio obtained from EDX analysis.

Electrocatalyst	wt.% Total metal content	Pt:Ru
Pt/CNC-BM	20.0	---
PtRu/CNC-BM	17.3	66:34
Pt/CNC-EGM	16.2	---
PtRu/CNC-EGM	20.0	50:50
Pt/CNC-MM	20.1	---
PtRu/CNC-MM	20.0	74:26
Pt/C E-TEK	16.3	---
PtRu/C E-TEK	20.0	50:50

Table 2. Physical characteristics of the catalysts obtained from XRD analysis.

Electrocatalyst	(220) diffraction peak position, 2θ (º)	Latticce parameter (Å)	d (nm)	Metal surface area (m^2 g^{-1})
Pt/CNC-BM	67.67	3.9198	4.7	60
PtRu/CNC-BM	67.94	3.9062	3.9	91
Pt/CNC-EGM	67.75	3.9158	5.6	50
PtRu/CNC-EGM	68.10	3.8981	3.8	94
Pt/CNC-MM	67.70	3.9184	4.8	58
PtRu/CNC-MM	68.40	3.8830	2.7	117
Pt/C E-TEK	67.53	3.9231	3.0	93
PtRu/C E-TEK	68.00	3.9031	3.4	82

Table 3. Current densities obtained from cyclic voltammetry (CV) and chronoamperometric curves (CR) for Pt/C and PtRu/C catalysts in 2 M CH_3OH + 0.5 M H_2SO_4 solution at 0.60 V vs. RHE.

Electrocatalyst	$CV_{0.60}$ ($\mu A\ cm^{-2}$)	$CR_{0.60}$ ($\mu A\ cm^{-2}$)
Pt/CNC-BM	32	29
PtRu/CNC-BM	76	42
Pt/CNC-EGM	22	14
PtRu/CNC-EGM	54	8
Pt/CNC-MM	20	0.3
PtRu/CNC-MM	353	204
Pt/C E-TEK	10	14
PtRu/C E-TEK	66	74

Table 4. Calculated average efficiency to CO_2.

Electrocatalyst	CO_2 conversion efficiency (%)
Pt/CNC-BM	97
PtRu/CNC-MM	85
Pt/C E-TEK	100
PtRu/C E-TEK	94

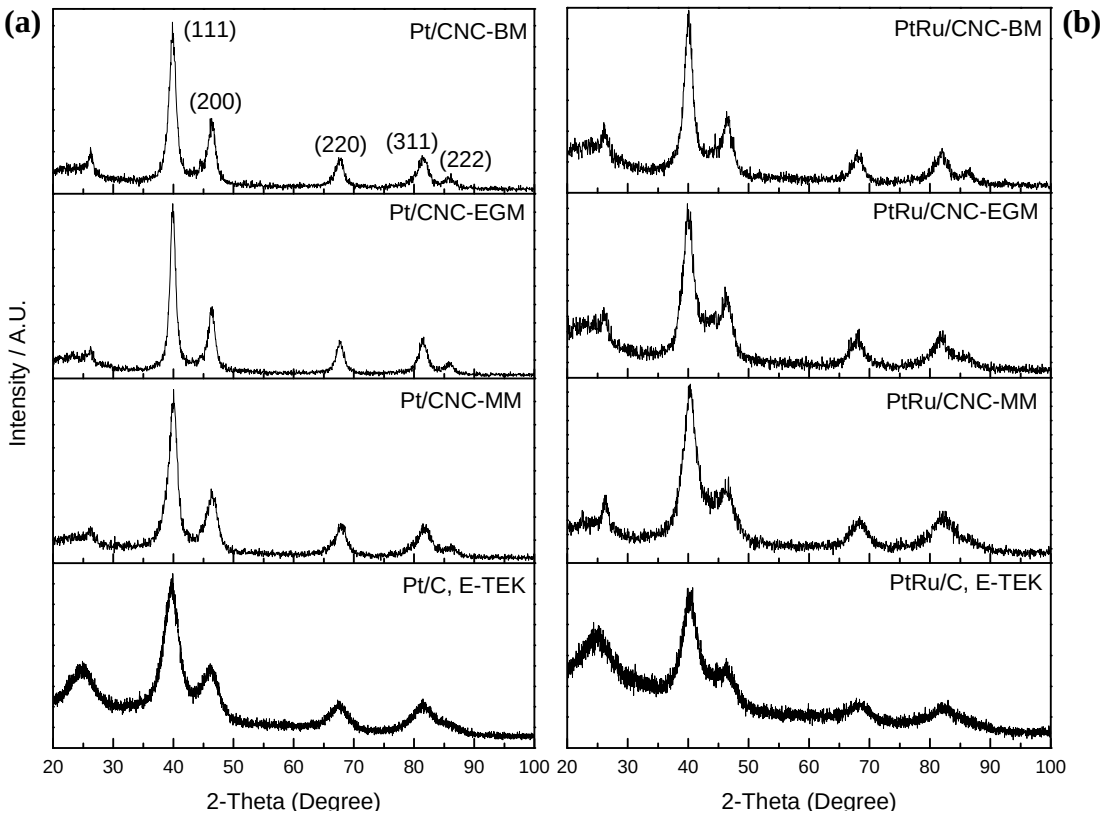
(a)
(b)
(111)
(200)
(220)
(311)
(222)
Pt/CNC-BM
Pt/CNC-EGM
Pt/CNC-MM
Pt/C, E-TEK
PtRu/CNC-BM
PtRu/CNC-EGM
PtRu/CNC-MM
PtRu/C, E-TEK
Intensity / A.U.
20 30 40 50 60 70 80 90 100
2-Theta (Degree)
20 30 40 50 60 70 80 90 100
2-Theta (Degree)

Figure 1.

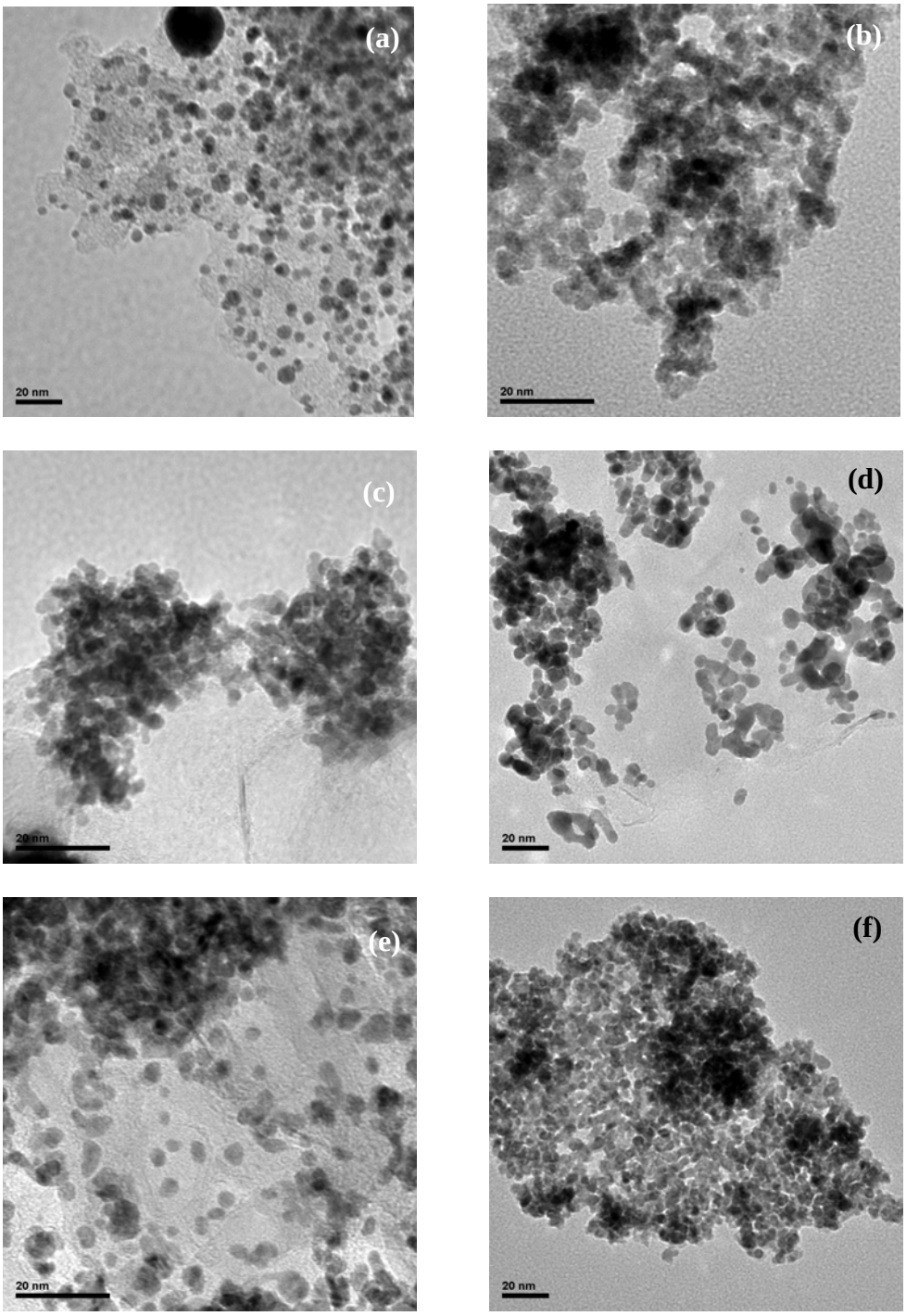

Figure 2.

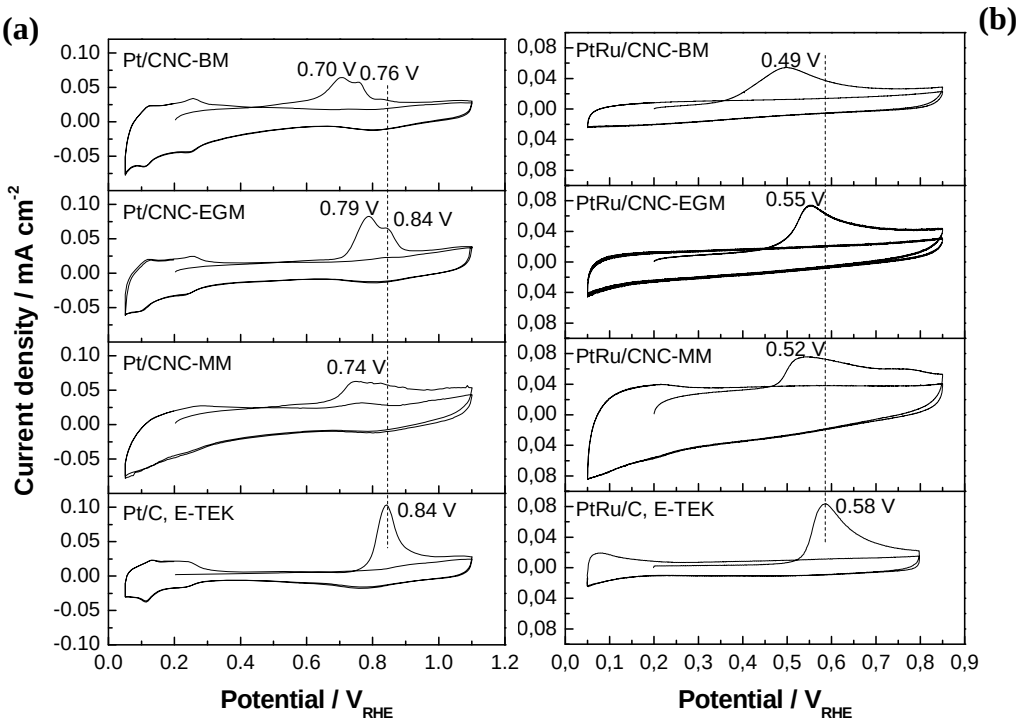
(a)
(b)
Pt/CNC-BM
0.70 V
0.76 V
Pt/CNC-EGM
0.79 V
0.84 V
Pt/CNC-MM
0.74 V
Pt/C, E-TEK
0.84 V
PtRu/CNC-BM
0.49 V
PtRu/CNC-EGM
0.55 V
PtRu/CNC-MM
0.52 V
PtRu/C, E-TEK
0.58 V
Current density / mA cm-2
Potential / VRHE
Potential / VRHE

Figure 3.

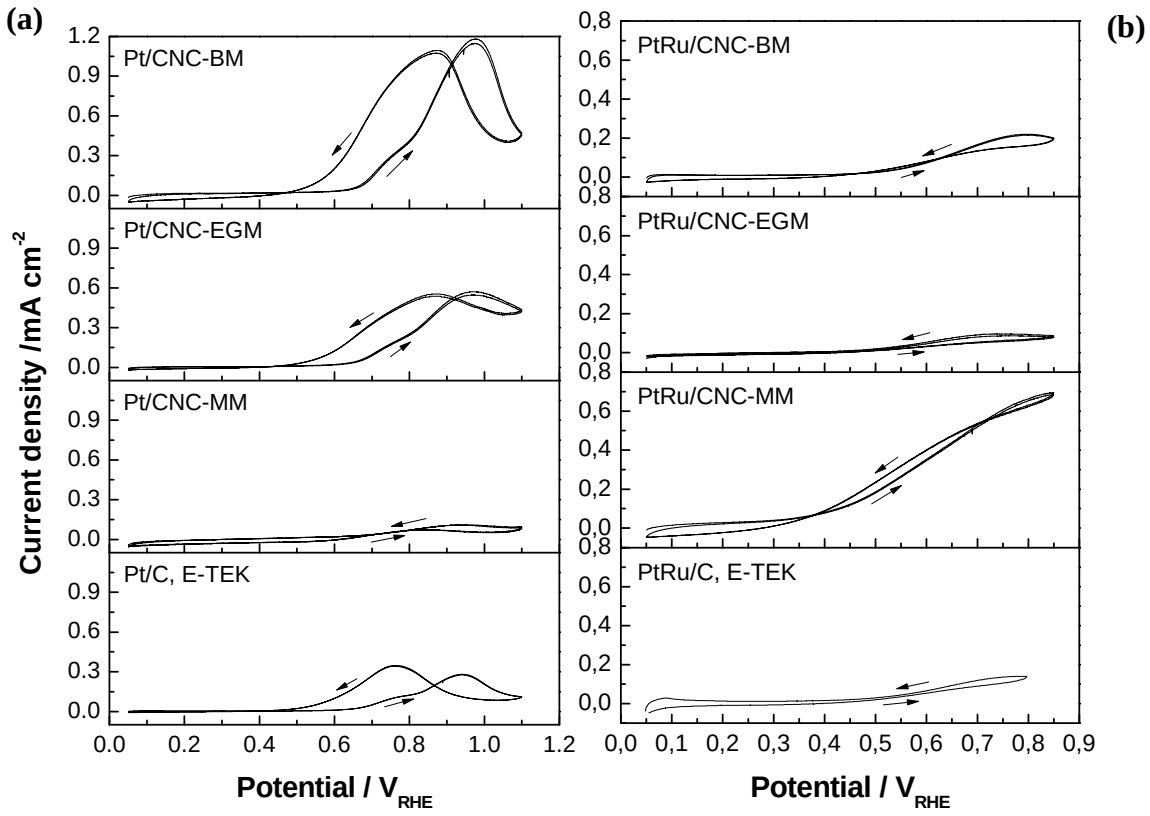
(a)
(b)
Pt/CNC-BM
Pt/CNC-EGM
Pt/CNC-MM
Pt/C, E-TEK
PtRu/CNC-BM
PtRu/CNC-EGM
PtRu/CNC-MM
PtRu/C, E-TEK
Current density /mA cm-2
Potential / VRHE
Potential / VRHE

Figure 4.

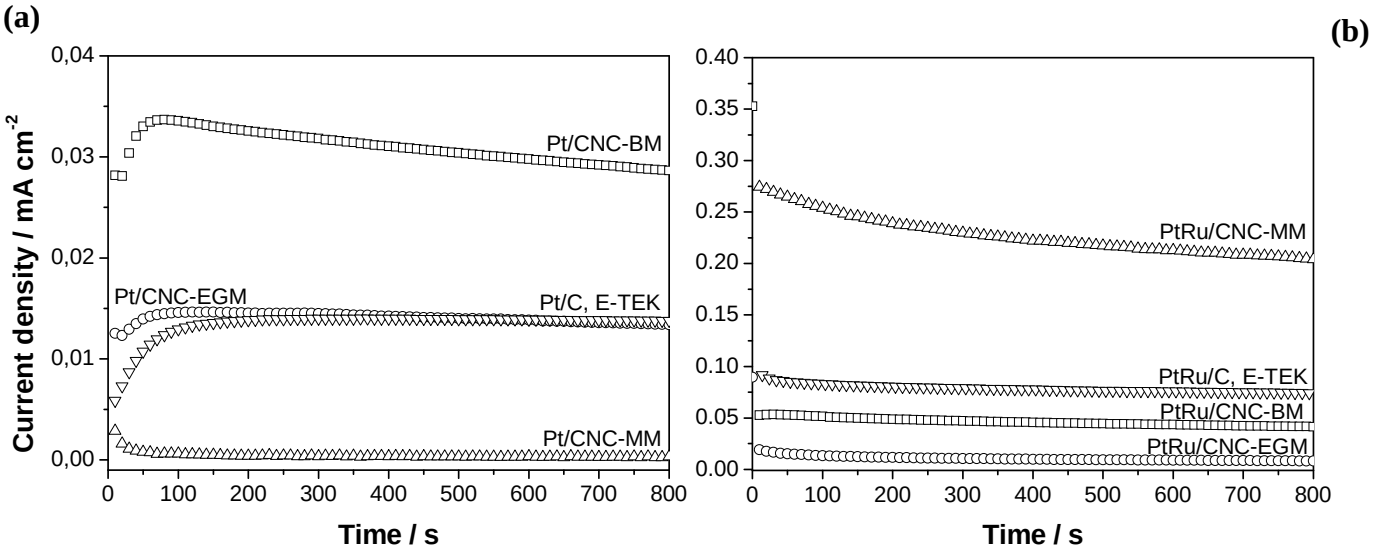
(a)
(b)
Current density / mA cm-2
Time / s
Time / s
Pt/CNC-BM
Pt/CNC-EGM
Pt/C, E-TEK
Pt/CNC-MM
PtRu/CNC-MM
PtRu/C, E-TEK
PtRu/CNC-BM
PtRu/CNC-EGM

Figure 5.

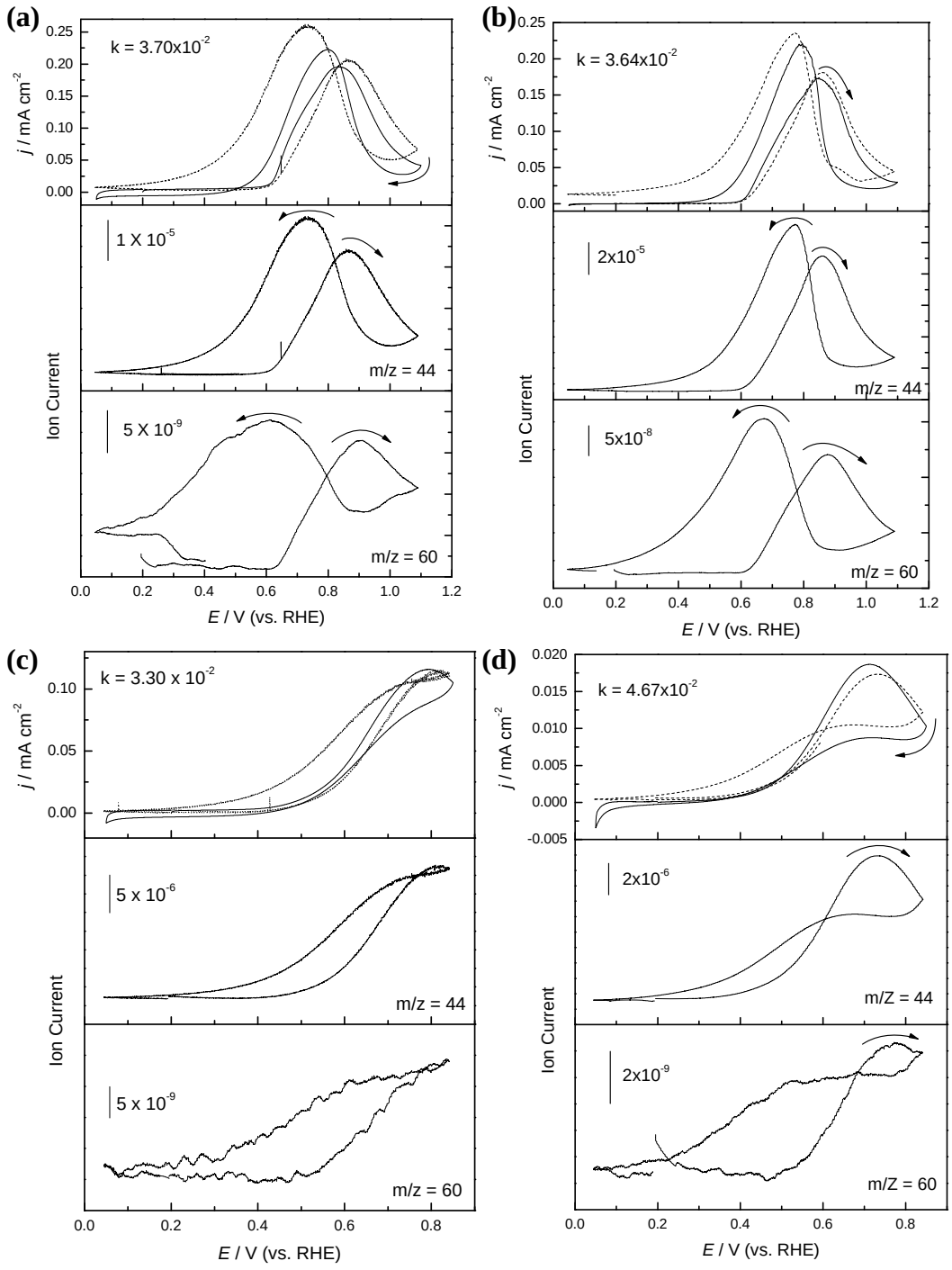
(a)
k = 3.70x10-2
j / mA cm-2
1 X 10-5
m/z = 44
5 X 10-9
m/z = 60
Ion Current
E / V (vs. RHE)
(b)
k = 3.64x10-2
2x10-5
m/z = 44
5x10-8
m/z = 60
(c)
k = 3.30 x 10-2
5 x 10-6
m/z = 44
5 x 10-9
m/z = 60
(d)
k = 4.67x10-2
2x10-6
m/Z = 44
2x10-9
m/Z = 60

Figure 6.

4

Influence of the synthesis method on the properties of Pt catalysts supported on carbon nanocoils for ethanol oxidation

M.J. Lázaro, V. Celorrio, L. Calvillo, E. Pastor, R. Moliner

Journal of Power Sources 196 (2011) 4236-4241

Journal of Power Sources 196 (2011) 4236–4241

Contents lists available at ScienceDirect

Journal of Power Sources

journal homepage: www.elsevier.com/locate/jpowsour

Influence of the synthesis method on the properties of Pt catalysts supported on carbon nanocoils for ethanol oxidation

M.J. Lázaro[a,*], V. Celorrio[a], L. Calvillo[a], E. Pastor[b], R. Moliner[a]

[a] Instituto de Carboquímica (CSIC), Miguel Luesma Castán 4, 50018 Zaragoza, Spain
[b] Departamento de Química Física, Universidad de La Laguna, Avda. Astrofísico Francisco Sánchez s/n, 38071 La Laguna, Tenerife, Spain

ARTICLE INFO

Article history:
Received 7 October 2010
Accepted 11 October 2010
Available online 23 October 2010

Keywords:
Pt electrocatalysts
Carbon nanocoils
Ethanol electrooxidation
DAFC

ABSTRACT

Pt electrocatalysts supported on carbon nanocoils (CNCs) were prepared by the sodium borohydride (BM), formic acid (FAM) and ethylene glycol (EGM) reduction methods in order to determine the influence of the synthesis method on the physicochemical and electrochemical properties of Pt/CNC catalysts. For this purpose, physicochemical properties of these materials were studied by means of energy dispersive X-ray analyses, X-ray diffraction and N_2-physisorption, whereas their electrochemical activity towards ethanol and carbon monoxide oxidation was studied using cyclic voltammetry and chronoamperometry. Furthermore, in order to complete this study, the results obtained for Pt/CNC catalysts were compared with those obtained for Pt catalysts supported on Vulcan XC-72R (commercial support) prepared by the same methods and for the commercial Pt/C catalysts from E-TEK. Results showed that, for all studied methods, CO oxidation occurred at more negative potentials on Pt/CNC catalysts than on Pt/Vulcan and Pt/C E-TEK ones. On the other hand, higher current densities for the ethanol electrooxidation were obtained when CNCs were used as support for BM and EGM. It is concluded that optimizing the synthesis method on CNC, materials with enhanced electrooxidation properties could be developed.

1. Introduction

Low-temperature fuel cells, operated by hydrogen (polymer electrolyte fuel cell, PEMFC), methanol (direct methanol fuel cell, DMFC) or ethanol (direct ethanol fuel cell, DEFC) as fuels, represent an environmentally friendly technology and are attracting much interest as a means of producing electricity by direct electrochemical conversion [1–5]. Direct alcohol fuel cells (DMFCs and DEFCs) have the advantage of running with pure different alcohols mixed with water steam and supplied directly to the anode, eliminating the problems of hydrogen transport and supply. Due to their characteristics, they are promising candidates for portable power source, electric vehicle and transport applications.

The direct oxidation of methanol in fuel cells has been widely investigated. However, the high toxicity of methanol is still an important drawback for their use. In this context, the use of ethanol as fuel seems to be a possible solution to this problem, due to it is not toxic and can be produced in large quantities from agricultural products (bioethanol) [1,6,7]. Furthermore, ethanol provides a volumetric energy density (21 MJ l^{-1}) that approaches that of gasoline (31 MJ l^{-1}).

In the case of methanol, many efforts have been done during the past decades to establish not only the oxidation reaction mechanism, but also the type of electrocatalyst to be used as anode material. However, in the case of ethanol, nowadays, it is difficult to establish the appropriate catalyst to oxidize it electrochemically. Besides platinum, other metals have been studied for the electrooxidation of ethanol, such as gold, rhodium or palladium, and they have shown some activity. However, only platinum-based materials show appropriate oxidation currents, especially in acid medium [8], but the efficiency of the DAFCs operating with these catalysts is still insufficient for practical applications. Therefore, further optimization of the anode material for DAFCs is necessary for their development and commercialisation.

The utilization of nanostructured carbonaceous materials as catalyst supports has been proposed as a promising solution to improve the efficiency and durability of electrocatalysts, due to carbon supports have been found to strongly influence the properties of metal supported nanoparticles, such as metal particle size, morphology, size distribution, stability and dispersion [9]. The ideal support material for fuel cell electrocatalysts should have at least the following characteristics: (i) high electrical conductivity to facilitate electron transport during the electrochemical reactions; (ii) high specific surface area in order to achieve large metal dispersions (which usually results in a high catalytic activity); (iii) suitable mesoporous structure for a good diffusion of reactant and by-products to and from the catalyst; and (iv) presence of surface oxygen groups for a good interaction between the catalysts nanoparticles and the carbon support [10].

* Corresponding author. Tel.: +34 976 733977; fax: +34 976 733318.
E-mail address: mlazaro@icb.csic.es (M.J. Lázaro).

0378-7753/$ – see front matter © 2010 Elsevier B.V. All rights reserved.
doi:10.1016/j.jpowsour.2010.10.055

Vulcan XC-72(R) is the most commonly used electrocatalyst support due to its high electrical conductivity and appropriate textural properties [11,12]. However, it has a considerable content of micropores (~30% of total area) which difficult the access of the fuel. For this reason, a portion of metal nanoparticles could be sunk into the micropores and may have less or no electrochemical activity due to the difficulty in reactant accessibility. Thus, nowadays, novel non-conventional carbon supports with mesoporous structure, such as carbon nanotubes and nanofibers [13,14], carbon xerogels and aerogels [15,16], ordered mesoporous carbons [5] and carbon nanocoils [17] are being studied.

Carbon nanocoils (CNCs) have recently received great attention as catalytic support in fuel cell electrodes due to the combination of their good electrical conductivity, derived from their graphitic structure, and a wide porosity that allows the diffusional resistances of reactants/products to be minimized. Only few works have been performed on catalysts supported on carbon nanocoils for their use both at the anode and cathode side of a direct methanol fuel cell [17–23]. Hyeon et al. synthesized Pt/Ru (1:1) alloy catalyst (60% wt.), prepared by sodium borohydride reduction method, supported on CNCs. They studied its behaviour towards the methanol oxidation, showing its good electrocatalytic activity [17]. Sevilla et al. also demonstrated the high catalytic activity of PtRu/CNC electrocatalyst for the methanol oxidation [18]. In addition, they compared its activity to that of a Pt/Vulcan catalyst prepared by the same method, demonstrating that catalysts supported on CNCs exhibited a higher utilization of metals [19,20]. Park et al. employed carbon nanocoils with variable surface areas and crystallinity as Pt/Ru catalyst supports [21,22]. They found that catalysts supported on carbon nanocoils exhibited better electrocatalytic performance towards the methanol electrooxidation than the catalyst supported on Vulcan XC-72. On the other hand, Imran Jafri et al. studied the activity of Pt nanoparticles dispersed on multi-walled carbon nanocoils for the oxygen reduction reaction in proton-exchange membrane fuel cells [23], the results obtained support the use of this new type of catalyst support material for PEMFC.

The most extended methods for preparing carbon-supported catalysts are the impregnation, the colloidal and the microemulsion methods [4,24]. The most widely used is the impregnation method due to its simplicity and good results. It consists of an impregnation step followed by a chemical reduction step (in liquid or gas phase). It has been found that the catalyst synthesis method can affect the composition, morphology and dispersion of the catalysts, as well as their electrocatalytic performance [25]. However, scarce works about the comparison of catalysts synthesized by different methods can be found in the literature [26], none about carbon nanocoils.

In this paper, Pt catalysts supported on carbon nanocoils produced by the catalytic graphitization of resorcinol-formaldehyde gel [27] have been synthesized. The metal nanoparticles were deposited on the carbon support following formic acid [26,27], sodium borohydride [5] or etilenglicol [28] reduction methods. The aim of this study is to compare different synthesis procedures in order to determine their influence on the properties of catalysts and to obtain an effective catalyst. These results were also compared to the same catalysts supported on Vulcan XC-72, demonstrating that the use of this non-conventional carbon material (CNCs) can improve the performance of the DEFC.

2. Experimental methods

2.1. Synthesis of carbon supports

Carbon nanocoils were synthesized by the catalytic graphitization of resorcinol-formaldehyde gel as described in [27]. In a typical synthesis, formaldehyde (Sigma–Aldrich) and silica sol (Supelco) were disolved in 100 mL of deionized water, then a mixture of nickel (Panreac) and cobalt (Sigma–Aldrich) salts was added under stirring conditions. Subsequently, resorcinol (Sigma–Aldrich) was added, and the stirring conditions maintained for 0.5 h. After a heat treatment at 85 °C for 3 h in a closed system of this reaction mixture, the system was then opened, and the mixture dried at 108 °C. Finally it was carbonized in a nitrogen atmosphere at 900 °C for 3 h. A 5 M NaOH (Panreac) solution was used to remove silica particles, followed by a treatment with concentrated HNO_3 (65%, Fluka) at room temperature during 2 h to remove the metal salts.

2.2. Preparation of the carbon-supported Pt electrocatalysts

The carbon supported Pt electrocatalysts were prepared by formic acid (FAM), sodium borohydride (BM) and ethylene glycol (EGM) reduction methods. Appropiate concentrations of the metal precursor were used to obtain a theoretical platinum loading of 20 wt.% on the different carbon materials. Chloroplatinic acid (8 wt.% $H_2PtCl_6{\cdot}6H_2O$ solution, Sigma–Aldrich) was used as metal precursor.

FAM method involved the suspension of the carbon material in a 2 M formic acid solution (98%, Panreac) and the slowly addition of the chloroplatinic acid solution under stirring conditions at 80 °C [26,27].

In the BM reduction method, catalysts were prepared by impregnating the carbon supports with an 8 wt.% chloroplatinic acid solution. Subsequently, the metal was reduced with a 26.4 mM sodium borohydride solution (99%, Sigma–Aldrich), which was slowly added to the precursor solution under sonication [5].

In the EGM reduction method, ethylene glycol was used as solvent and reducing agent. In a typical procedure, the metal precursor was dissolved in ethylene glycol (1 mL EG/1 mg Pt) and the pH was adjusted to 11 using a 1 M NaOH solution in EG. Then, the carbon support was added. The resulting mixture was treated at 195 °C for 2 h and then cooled in a cold water bath. The pH was measured and adjusted to 1 using HCl (37%, Sigma–Aldrich) [28].

The catalysts were named Pt/CNC or Pt/Vulcan if they are supported on carbon nanocoils or Vulcan XC-72R respectively, followed by the abbreviation of the method used for synthesized them (-FAM, -BM, or -EGM).

2.3. Physicochemical characterization of Pt/C electrocatalysts

The real content of Pt in the electrocatalysts was determined by energy dispersive X-ray analyses (EDX) technique Röntec XFlash Si(Li), coupled to a scanning electron microscopy Hitachi S-3400 N.

X-ray diffraction (XRD) patterns were recorded using a Bruker AXS D8 Advance diffractometer with a θ–θ configuration and using Cu Kα radiation (λ = 0.154 nm). Scans were done for 2θ values between 0° and 100°. Scherrer's equation was applied to the (2 2 0) peak of the Pt fcc structure, around 2θ = 70°, in order to estimate the Pt crystallite size from the diffractograms [29]. This region was chosen to avoid the influence of a broad band of the carbon substrate (2θ = 25°) on the (1 1 1) and (2 0 0) peaks of Pt structure [30,31].

2.4. Electrochemical characterization of Pt/C electrocatalysts

Electrochemical experiments were carried out in a three-electrode cell using a MicroAutolab potentiostat. The counter electrode was a large area pyrolitic graphite bar and a reversible hydrogen electrode (RHE) placed inside a Luggin capillary was used as reference one. All potentials in this work are referred to this electrode. Working electrodes were prepared depositing a thin-layer of the electrocatalysts over a pyrolitic graphite disk (7 mm diameter, 1.54 cm^2 geometric area). A catalyst ink was prepared by

mixing 2 mg of the catalyst and 10 μl of Nafion dispersion (5 wt.%, Aldrich) in 500 μl of ultrapure water (Millipore Milli-Q system). A 40 μl aliqout of the suspension was deposited onto the graphite disk and dried. After that, the working electrode was immersed into H_2SO_4 0.5 M electrolyte solution, prepared from high purity reagents (Merck) and deaerated with nitrogen gas. All the electrochemical experiments presented in this work were carried out at room temperature.

Electrochemical active areas of catalysts were measured from CO-stripping voltammograms by the integration of the CO_{ad} oxidation region, assuming a charge of 420 μC cm^{-2} involved in the oxidation of a monolayer of linearly adsorbed CO. This electroactive area has been used to calculate the current densities given in the text. CO (99.99%, Air Liquide) adsorbs onto the metal surface by bubbling this gas at 1 atm though the electrolyte during 10 min to achieve full monolayer coverage of CO on Pt. The CO adsorption process was carried out at 0.20 V. Then an inert gas such as nitrogen is used to purge out for a few minutes the CO from the solution, leaving only the CO adsorbed on the surface of Pt. A potential scanning between 0.05 and 1.10 V at 0.02 V s^{-1} was then carried out to induce the oxidation of CO for two complete oxidation/reduction scans.

Ethanol oxidation was characterized by cyclic voltammetry and chronoamperometry. Cyclic voltammograms (CVs) were recorded in 2 M CH_3CH_2OH + 0.5 M H_2SO_4 between 0.05 and 1.10 V at a scan rate of 0.02 V s^{-1}. Potentiostatic current density–time (j–t) curves were recorded in the same solutions at 0.60 V for 900 s.

3. Results and discussion

3.1. Physicochemical characterization of the supports and electrocatalysts

Catalysts are usually supported on a carbonaceous material to reduce the amount of metal used and improve its performance. It has been shown that carbonaceous support has great influence on the properties of the catalyst [32]. The physicochemical characterization of the CNC was stated in a previous work [27]. Carbon nanocoils consist of a long curved ribbon of carbon which exhibited well-aligned graphitic layers. Nevertheless, Vulcan XC-72 consisted of an aggregation of spherical carbon nanoparticles.

Table 1 shows the nomenclature and the metal content obtained by EDX for the catalysts prepared and the commercial catalysts Pt/C from E-TEK. The values obtained are similar to the nominal value of 20%.

The textural properties of the supports and the catalysts were studied by N_2-physisorption to determine the effect of the deposition of metal particles on the pore structure of the support (Table 2). CNC had a specific surface area and pore volume of 124 m^2 g^{-1} and 0.16 m^3 g^{-1}, respectively, and a mesoporous structure, whereas Vulcan XC-72R had a specific surface area of around 218 m^2 g^{-1} and a total pore volume of 0.41 m^3 g^{-1}, being the 30% of its area belonging to the micropores. Metal particles deposited in the micropores of this material may have a lower electrocatalytic activity, or even not to operate, because of the worst diffusion of reagents through this structure to the active sites.

Table 1
Pt content from EDX and physical characteristics from XRD analysis of the catalysts.

Electrocatalyst	% Pt	d (nm)	Latticce parameter (Å)	Metal surface area (m^2 g^{-1})
Pt/CNC-BM	20.0	4.7	3.9198	60
Pt/CNC-EGM	16.2	5.6	3.9158	50
Pt/CNC-FAM	19.4	3.8	3.9233	74
Pt/Vulcan-BM	17.3	3.7	3.9029	76
Pt/Vulcan-EGM	20.0	5.4	3.9174	52
Pt/Vulcan-FAM	19.2	3.2	3.9158	88
Pt/C E-TEK	16.3	3.0	3.9231	93

Table 2
Textural parameters of carbon supports and catalysts.

Sample	S_{BET} (m^2 g^{-1})	V_{Total} (cm^3 g^{-1})	$S_{Mesopore}$ (m^2 g^{-1})	$S_{Micropore}$ (m^2 g^{-1})
CNC	124	0.16	124	0.0
Vulcan	218	0.41	153	65

The morphological and crystallographic properties of the catalysts were studied by X-ray diffraction (XRD). X-ray diffractograms for Pt/C electrocatalysts are shown in Fig. 1. All of them showed the typical form of the face-centered cubic (fcc) Pt structure, indicating the effective reduction of the metal precursor producing crystalline nanoparticles. Peaks at $2\theta = 40^\circ$, 47°, 67°, 81° and 85°, associated with the Pt crystal planes (1 1 1), Pt (2 0 0), Pt (2 2 0), Pt (3 1 1) and Pt (2 2 2), respectively, were observed. Furthermore, the XRD patterns displayed a peak at $2\theta = 26.2^\circ$, characteristic of the plane (0 0 2) of graphite, which is attributed to the CNCs used as support. In the case of Pt/Vulcan and commercial catalysts, the peak attributed to the support was less intense due to the lower crystalline grade of Vulcan XC-72R. Both metal crystallite size and specific activity are influenced by the interaction of the active phase with the support as will be seen below.

Average metal crystallite sizes, calculated from the Scherrer' equation, are given in Table 2. Differences in the Pt average crystallite sizes were observed for the different carbon supports and synthesis methods. Higher Pt average sizes were obtained as CNCs were used as support, compared with those obtained using Vulcan XC-72R. However, these differences were not significant. This could be attributed to that Vulcan XC-72R has a large number of nucleation sites, leading to the formation of smaller Pt particles. In contrast, graphitized carbons, like CNCs, have a lower number of nucleation sites because only the surface defects can function as nucleation sites, and thus larger Pt particles would be obtained. However, for both carbon materials, the smallest particle size was obtained by FAM and the highest ones by EGM.

The surface area (SA) can be calculated (Table 2), assuming that Pt particles are spherical, by the ratio SA (m^2 g^{-1}) = $6 \times 10^3/\rho d$, where d is the mean metal crystallite size in nm, and ρ is the density of Pt (21.4 g cm^{-3}). Different values were obtained using CNCs as support modifying the metal precursor reducing agent. Of those methods, the catalysts synthesized by FAM presented a smaller

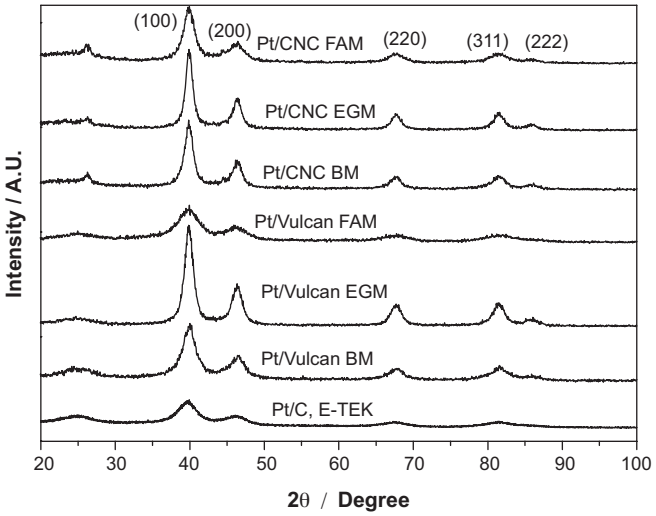

Fig. 1. XRD diffractograms for the Pt electrocatalysts supported on CNCs and Vulcan XC-72R, including the Pt/C E-TEK catalyst.

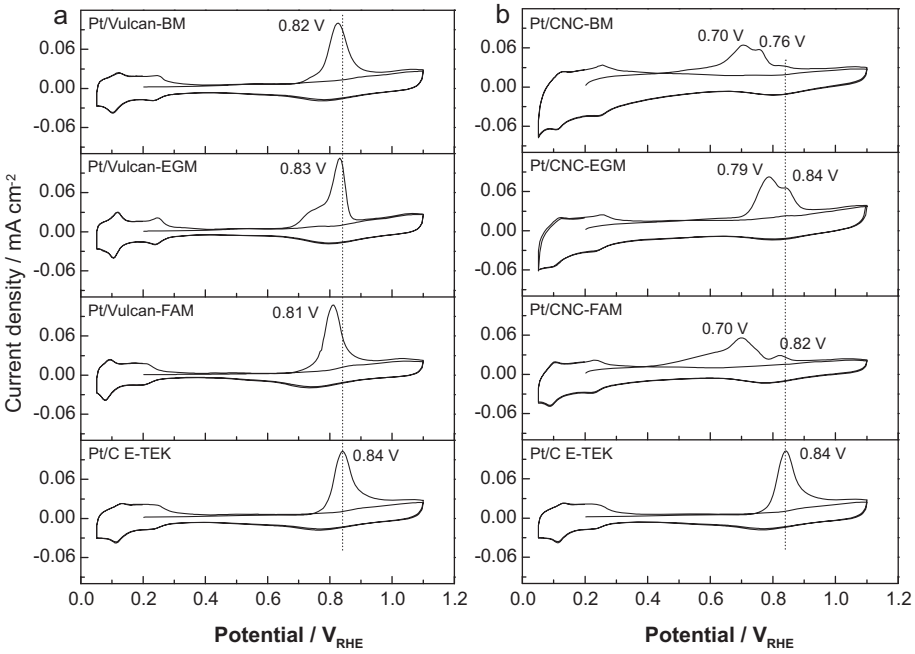

Fig. 2. CO-stripping voltammetries for Pt/Vulcan (a) and Pt/CNC (b) electrocatalysts in 0.5 M H_2SO_4. E_{ad} = 0.20 V; υ = 20 mV s^{-1}; T = 25 °C.

crystal size and, therefore, a greater metal surface area, opposite to EGM.

The lattice parameter was also calculated from XRD patterns and the results are summarized in Table 1. The value of the lattice parameter of the Pt/C electrocatalysts decreases with increasing the crystallite size. These values were close to 3.92 Å, which is the value correspondent to pure platinum.

3.2. Electrochemical studies

3.2.1. Carbon monoxide oxidation

CO-stripping voltammetry can be used to obtain some in situ information about the electroactive composition and surfaces areas of catalysts, as well as, to establish their tolerance towards CO poisoning. CO-stripping voltammograms obtained at room temperature are shown in Fig. 2, where the first and second cycles are represented. As observed, in the first cycle, when the Pt surface is blocked by the CO adsorbed, hydrogen adsorption is blocked. Therefore, the cyclic voltammogram in the hydrogen adsorption–desorption potential region becomes featureless. Once the CO monolayer is removed through oxidation at higher potentials, the Pt surface becomes available again for hydrogen adsorption and desorption, and the corresponding peaks appear (corresponding to the voltammograms in the base electrolyte for the clean surfaces) in the second cycle.

Similar results were obtained for Pt/Vulcan and commercial Pt/C E-TEK catalysts. As can be seen in Fig. 2a, the peak potential for the CO_{ad} oxidation occurred approx. at the same potential for Pt/C E-TEK and Pt/Vulcan catalysts, in the 0.81–0.84 potential range. However, the onset for CO oxidation was placed of CO started at more negative potentials for Pt/Vulcan catalysts (around 0.7 V) than for Pt/C E-TEK one (0.76 V). No significant differences were observed for the Pt/Vulcan catalysts synthesized by different methods, only for the Pt/Vulcan-EGM a shoulder centred at 0,72 V is apparent which implies that for this catalyst part of CO oxidation occurs at more negative potentials.

In the case of Pt/CNC catalysts, the oxidation of CO_{ad} is shifted negatively compared with Pt/Vulcan and Pt/C E-TEK catalysts (Fig. 2b). For these catalysts, two CO oxidation peaks were observed in the CVs. One peak around 0.84 V was observed, which corresponds to that observed for catalysts supported on Vulcan XC-72R. In addition, a second CO oxidation peak was obtained at around 0.70 V for Pt/CNC-BM and Pt/CNC-FAM and at 0.79 V for Pt/CNC-EG. This implies that CO can be easily oxidized on these materials. The presence of this additional peak at lower potentials could be attributed to the nature and surface chemistry of the carbon support, specifically to the surface oxygen groups of the CNCs [1,33], which could alter the electronic structure of the metal, helping to the CO oxidation process and making catalysts more tolerant to CO than Vulcan-supported catalysts.

It is noticeable the presence of an important CO oxidation current at E < 0.60 V for catalysts prepared on CNC by BM and FAM, especially for the latter, which implies that CO can be oxidized at potentials as low as 0.40 V at Pt on CNC.

However, as can be observed in Fig. 2b, the ratio between the two peak areas varied with the synthesis method. This demonstrates that the deposition method of the metal particles plays an important role in the final performance of the electrocatalysts.

3.2.2. Ethanol oxidation

Fig. 3 illustrates the CVs recorded in 2 M CH_3CH_2OH + 0.5 M H_2SO_4 at room temperature for Pt/CNC, Pt/Vulcan and commercial Pt/C E-TEK catalysts. The curves for all catalysts displayed a rise in the current around 0.50 V during the positive-going potential scan, developing an anodic peak which position depends on the catalysts. At the backward scan, a new anodic contribution was observed, achieving a maximum also dependent on the catalyst.

As can be observed in Fig. 3, the onset for ethanol electrooxidation occurred between 0.50 and 0.64 V depending on the catalysts. For the same material, significant differences were found in the current densities achieved for the catalysts prepared following the different synthesis methods. In the case of Pt/CNC catalysts, the highest current densities were observed for the Pt/CNC-BM (1.1 mA cm^{-2}), whereas in the case of Pt/Vulcan ones, Pt/Vulcan-FAM (0.7 mA cm^{-2}) showed the highest current densities during the positive potential scan. In all cases, higher current densities than those for Pt/C E-TEK (0.2 mA cm^{-2}) were obtained.

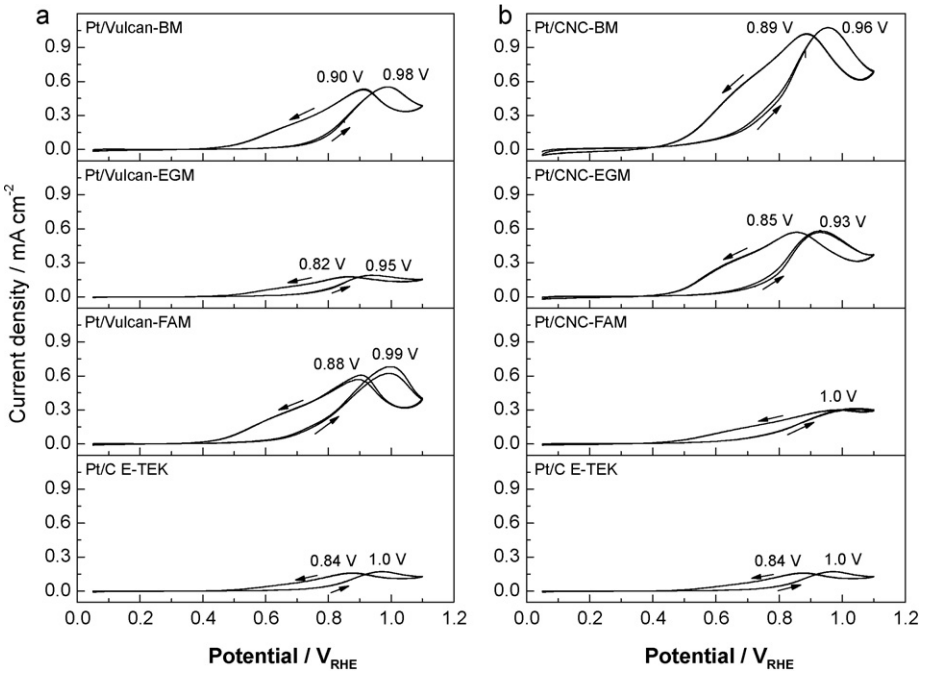

Fig. 3. Cyclic voltammograms for Pt/Vulcan (a) and Pt/CNC (b) electrocatalysts in 2 M CH_3CH_2OH + 0.5 M H_2SO_4. υ = 20 mV s^{-1}; T = 25 °C.

Table 3
Current densities obtained from cyclic voltammetry (CV) and chronoamperometric (CR) curves for Pt/C catalysts in 2 M CH_3CH_2OH + 0.5 M H_2SO_4 solution at 0.60 V.

Electrocatalyst	$CV_{0.60}$ ($\mu A\,cm^{-2}$)	$CR_{0.60}$ ($\mu A\,cm^{-2}$)
Pt/CNC-BM	110	47
Pt/CNC-EGM	33	33
Pt/CNC-FAM	22	21
Pt/Vulcan-BM	13	18
Pt/Vulcan-EGM	8	12
Pt/Vulcan-FAM	27	21
Pt/C E-TEK	6	5

The current densities obtained for the different catalysts at 0.60 V (a potential near to the working potential in a DEFC) are listed in Table 3.

From Fig. 3, it is demonstrated that the utilization of CNCs as catalysts support results in an increase of the current densities registered at the maximum in the CVs for BM and EGM. The onset potential for the oxidation of ethanol during the positive-going potential scan on Pt/CNC-BM appears at the most negative potential whereas the most positive corresponds to Pt/CNC-FAM. Accordingly, the maximum current density at the first peak of the ethanol electrooxidation is achieved for Pt/CNC-BM, followed by Pt/CNC-EGM, Pt/CNC-FAM and Pt/C E-TEK. It is clear that Pt/CNC-BM presents a higher positive peak current density, and consequently, higher activity to ethanol electro-oxidation which indicates that it is a promising catalyst for ethanol electrooxidation.

Interestingly, Pt/Vulcan catalysts showed higher oxidation activity than the commercial Pt/C E-TEK. This improvement could be attributed to the catalysts preparation method.

With the purpose to determine the performance of the catalysts towards ethanol electrooxidation under potentiostatic conditions, current–time curves were recorded at 0.60 V and 25 °C during 850 s in a 2 M CH_3CH_2OH + 0.5 M H_2SO_4 solution. Fig. 4 shows such curves for the Pt-supported catalysts. Pt catalysts based on CNCs prepared by BM and EGM presented higher quasi-stationary current densities from chronoamperometric curves than Pt catalysts based on Vulcan XC-72R. These values increased in the order Pt/C E-TEK < Pt/Vulcan-EGM < Pt/Vulcan-BM < Pt/Vulcan-FAM = Pt/CNC-FAM < Pt/CNC-EGM < Pt/CNC-BM as can be seen in Table 3. However, in all cases, a stable performance was achieved in a short time.

These results confirm that the Pt/CNC catalysts are notably more active for electrooxidizing ethanol than catalysts supported on Vulcan XC-72R, commonly employed for DAFCs technical electrodes.

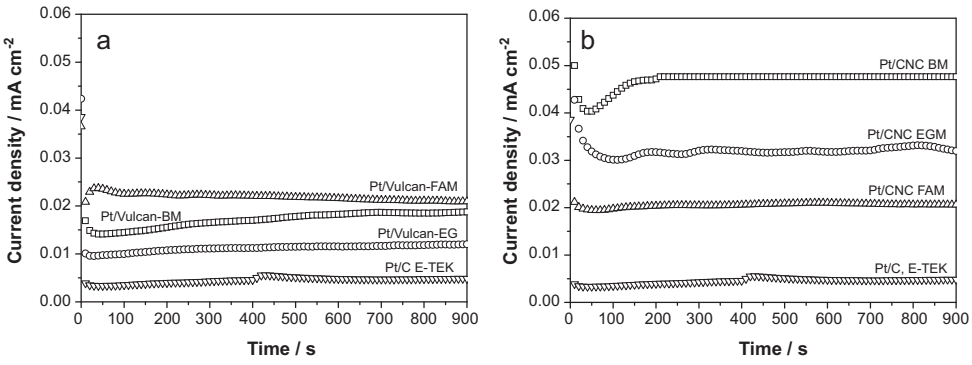

Fig. 4. Chronoamperometric curves for Pt/Vulcan (a) and Pt/CNC (b) electrocatalysts recorded in 2 M CH_3CH_2OH + 0.5 M H_2SO_4 solution at E = 0.60 V.

4. Conclusions

The main conclusions derived from this work can be summarized as follows:

- The size of the platinum crystallites depends on the synthesis method used to prepare the catalysts. For both carbon materials used as support, the FAM ~~r~~esulted in the smallest metal crystallite sizes, whereas the EGM resulted in the highest ones. For each the synthesis methods, higher platinum crystallite size was obtained as CNCs were used as support, respect to that obtained using Vulcan, although differences were no significant. This effect could be attributed to the less content of nucleation sites in CNCs due to their graphitic nature.
- Pt electrocatalysts supported on carbon nanocoils showed more negative CO oxidation potentials compared with catalysts supported on Vulcan and the commercial Pt/C E-TEK one. This can be attributed to the carbon nanocoils used as catalyst support, which could alter the electronic structure of the metal, helping to the CO oxidation process and making catalysts more tolerant to CO than Vulcan-supported ones. On the other hand, differences in the CO oxidation were observed for the catalysts synthesized by different methods, demonstrating that the deposition method of the metal particles plays an important role in the final performance of the electrocatalysts.
- Catalysts based on carbon nanocoils were also notably more active for electrooxidizing ethanol than catalysts supported on Vulcan XC-72R, commonly employed as anodes in DEFCs, which can be also attributed to the positive effect of carbon nanocoils as support. The highest current densities were achieved by the Pt/CNC-BM catalyst.

These results prove that the Pt/CNC catalysts are promising candidates as alternative to replace Pt/Vulcan in order to improve the performance of the direct ethanol fuel cells.

Acknowledgment

The authors gratefully acknowledge financial support given by the MICINN and Gobierno Autónomo de Canarias through Projects MAT2008-06631-C03-01 and MAT2008-06631-C03-02, and PI2007/023, respectively. V. Celorrio and L. Calvillo and also acknowledge CSIC and the Spanish National Research Council for their JAE and FPI grants, respectively.

References

[1] E. Antolini, Appl. Catal. B: Environ. 88 (2009) 1–24.
[2] S. Song, P. Tsiakaras, Appl. Catal. B: Environ. 63 (2006) 187–193.
[3] E. Antolini, J. Power Sources 170 (2007) 1–12.
[4] H. Liu, C. Song, L. Zhang, J. Zhang, H. Wang, D.P. Wilkinson, J. Power Sources 155 (2006) 95–110.
[5] L. Calvillo, M.J. Lázaro, E. García-Bordejé, R. Moliner, P.L. Cabot, I. Esparbé, E. Pastor, J.J. Quintana, J. Power Sources 169 (2007) 59–64.
[6] G. Andreadis, P. Tsiakaras, Chem. Eng. Sci. 61 (2006) 7497–7508.
[7] S.Q. Song, W.J. Zhou, Z.H. Zhou, L.H. Jiang, G.Q. Sun, Q. Xin, V. Leontidis, S. Kontou, P. Tsiakaras, Int. J. Hydrogen Energy 30 (2005) 995–1001.
[8] P.E. Tsiakaras, J. Power Sources 171 (2007) 107–112.
[9] L. Calvillo, M. Gangeri, S. Perathoner, G. Centi, R. Moliner, M.J. Lázaro, J. Power Sources 192 (2009) 144–150.
[10] A.L. Dicks, J. Power Sources 156 (2006) 128–141.
[11] K. Wikander, H. Ekström, A.E.C. Palmqvist, A. Lundblad, K. Holmberg, G. Lindbergh, Fuel Cells 6 (2006) 21–25.
[12] Y. Shao, G. Yin, J. Zhang, Y. Gao, Electrochim. Acta 51 (2006) 5853–5857.
[13] C. Paoletti, A. Cemmi, L. Giorgi, R. Giorgi, L. Pilloni, E. Serra, M. Pasquali, J. Power Sources 183 (2008) 84–91.
[14] H. Tang, J. Chen, L. Nie, D. Liu, W. Deng, Y. Kuang, S. Yao, J. Colloid Interface Sci. 269 (2004) 26–31.
[15] N. Job, J. Marie, S. Lambert, S. Berthon-Fabry, P. Achard, Energy Convers. Manage. 29 (2008) 2461–2470.
[16] J. Marie, S. Berthon-Fabry, P. Achard, M. Chatenet, A. Pradourat, E. Chainet, J. Non-Cryst. Solids 350 (2004) 88–96.
[17] T. Hyeon, S. Han, Y.E. Sung, K.W Park, Y.W. Kim, Angew. Chem. Int. Ed. 42 (2003) 4352–4356.
[18] M. Sevilla, G. Lota, A.B. Fuertes, J. Power Sources 171 (2007) 546–551.
[19] M. Sevilla, C. Sanchís, T. Valdés-Solís, E. Morallón, A.B. Fuertes, Electrochim. Acta 54 (2009) 2234–2238.
[20] M. Sevilla, C. Sanchís, T. Valdés-Solís, E. Morallón, A.B. Fuertes, Carbon 46 (2008) 931–939.
[21] K.W. Park, Y.E. Sung, S. Han, Y. Yun, T. Hyeon, J. Phys. Chem. B 108 (2004) 939–944.
[22] S. Han, Y. Yun, K.-W. Park, Y.-E. Sung, T. Hyeon, Adv. Mater. 15 (2003) 1922–1925.
[23] R. Imran Jafri, N. Rajalakshmi, S. Ramaprabhu, J. Power Sources 195 (2010) 8080–8083.
[24] Z. Liu, X.Y. Ling, X. Su, J.Y. Lee, L.M. Gan, J. Power Sources 149 (2005) 1–7.
[25] J.R.C. Salgado, F. Alcaide, G. Álvarez, L. Calvillo, M.J. Lázaro, E. Pastor, J. Power Sources 195 (2010) 4022–4029.
[26] J.R.C. Salgado, J.J. Quintana, L. Calvillo, M.J. Lázaro, P.L. Cabot, I. Esparbé, E. Pastor, Phys. Chem. Chem. Phys. 10 (2008) 6796–6806.
[27] V. Celorrio, L. Calvillo, M.V. Martínez-Huerta, R. Moliner, M.J. Lázaro, Energy Fuels 24 (2010) 3361–3365.
[28] X. Wang, I.M. Hsing, Electrochim. Acta 47 (2002) 2981–2987.
[29] B.E. Warren, X-ray Diffraction, Addison-Wesley, Reading, 1969.
[30] S. Kim, S.-J. Park, Electrochim. Acta 52 (2007) 3013–3021.
[31] W. Li, W. Zhou, H. Li, Z. Zhou, G. Sun, Q. Xin, Electrochim. Acta 49 (2004) 1045–1055.
[32] T.S. Ahmadi, Z.L. Wang, T.C. Green, A. Henglein, M.A. El-Sayed, Science 272 (1996) 1924–1925.
[33] X. Yu, S. Ye, J. Power Sources 172 (2007) 133.

5

Electrocatalytic properties of strained Pd nanoshells at Au nanostructures: CO and HCOOH oxidation

M.G. Montes de Oca, D. Plana, V. Celorrio, M.J. Lázaro, D.J. Fermín

Journal of Physical Chemistry C 116 (2012) 692-699

THE JOURNAL OF PHYSICAL CHEMISTRY C

ARTICLE

pubs.acs.org/JPCC

Electrocatalytic Properties of Strained Pd Nanoshells at Au Nanostructures: CO and HCOOH Oxidation

María G. Montes de Oca,[†] Daniela Plana,[†] Verónica Celorrio,[‡] María J. Lazaro,[‡] and David J. Fermín*[,†]

[†]School of Chemistry, University of Bristol, Cantocks Close, Bristol, BS8 1TS, United Kingdom

[‡]Instituto de Carboquímica (CSIC), Miguel Luesma Castán 4, 50018 Zaragoza, Spain

ABSTRACT: The oxidations of carbon monoxide and formic acid at ultrathin Pd layers grown on Au nanoparticles were studied as a function of Pd thickness. Pd shells with thickness between 1 and 10 nm were grown on 19 nm Au nanoparticles by chemical reduction of H_2PdCl_4 with ascorbic acid. High-resolution transmission electron microscopy and X-ray diffraction confirm the core−shell configuration of the nanostructures. While the synthesis of pure Pd nanostructures led to a rather amorphous material, Pd nanoshells exhibited a polycrystalline structure confirming that Au nanostructures act as templates for Pd growth. Three-dimensional assemblies of nanoparticles were generated by alternate electrostatic layer-by-layer adsorption steps, involving poly-L-lysine and colloidal dispersions. Electrochemical studies in H_2SO_4 containing electrolyte solution demonstrate that CO coverage and anodic stripping potential are affected by the thickness of Pd nanoshells. In addition, the faradaic current density associated with HCOOH oxidation significantly increases with increasing Pd thickness. The thickness-dependent reactivity of Pd nanoshells is discussed in terms of lattice strain relaxation.

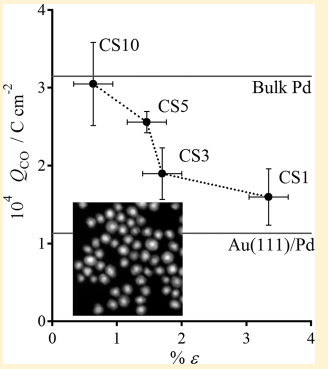

1. INTRODUCTION

Binary metallic catalysts can exhibit rather different reactivity to the corresponding individual metallic constituents as a result of the so-called electronic, geometric, and ensemble effects.[1,2] All these interactions can significantly affect the position of the *d*-band center which is a key parameter in the electrocatalytic activity of metals. Hydrogen and CO binding energies at pseudomorphic Pd monolayers on Au(111) surfaces, for instance, are higher than on Pd(111) due to a 0.35 eV shift of the *d*-band center with respect to bulk Pd.[1] Roudgar and Gross concluded from DFT calculations that the CO binding energy as a function of the number of Pd monolayers goes through a maximum for the second Pd monolayer on Au(111) and Au(100).[3] The use of binding energies as the main reactivity descriptor of electrode surfaces should be considered very cautiously, as key parameters such as solvation effects, coadsorption of ionic species, and bond breaking/making steps (as in the case of hydrogen oxidation/evolution) can play a significant role in the experimental behavior. Furthermore, the experimental verification of these theoretical trends is rather challenging due to the convolution of electronic and geometric (strain) effects on the binding energies. A limited number of studies, however, have demonstrated, by combining theoretical and experimental approaches, that, for example, compressive stress on dealloyed core−shell nanoparticles controls their catalytic activity toward oxygen reduction[4] or that, while electronic effects are only present on up to three monolayers of Pt on Ru(0001), lattice strain remains up to at least an additional layer.[5]

The anodic stripping of CO on Pd layers grown on Au single crystal electrodes is strongly dependent on the substrate structure as was elegantly demonstrated by El-Aziz and Kibler.[6] The current responses become sharper as the number of Pd monolayers deposited on Au(111) surfaces increases due to the concomitant increase in atomic step density. These authors also demonstrated that CO coverage on pseudomorphic Pd monolayers is smaller than on massive Pd(111) crystals and increases with increasing step density on Au substrates.[6] Wandlowski and co-workers have also shown that CO coverage on single-crystal Pd electrodes is dependent on the surface orientation, following the trend (100) < (110) < (111).[7] These and other studies[8,9] establish a link between the formation of oxygenated species at Pd surfaces and CO anodic stripping.

Pd-based electrocatalysts have generated considerable attention in the context of direct formic acid (HCOOH) fuel cells. HCOOH is an attractive fuel due to its safety and very high concentration threshold for crossover through Nafion membranes.[10] It is generally considered that HCOOH oxidation at Pt surfaces occurs through a two-step process in which CO is formed in the intermediate step.[11−14] By contrast, Pd-based catalysts are thought to activate the direct oxidation of HCOOH to CO_2, without forming CO as an intermediate step.[11−14] Miyake et al. have demonstrated that formate is preferentially formed as a short-lived and highly reactive intermediate of HCOOH oxidation on Pd, while CO production through dehydration of formic acid is slow and has little effect on the oxidation process.[15] Recent studies by Yu and Pickup suggest, however, that long-term deactivation of Pd catalysts is associated with CO poisoning.[16] Although Kibler et al. have shown that the

Received: August 1, 2011
Revised: December 2, 2011
Published: December 08, 2011

potential at which HCOOH oxidation occurs on pseudomorphic monolayers of Pd is heavily influenced by the underlying metal,[17] Baldauf and Kolb demonstrated that the current density of HCOOH oxidation on Pd/Au(111) is little dependent on the thickness of Pd overlayers, while the activity of Pd/Au(100) appears significantly higher than on bulk Pd and Pd/Au(111).[18] Recent works on nanostructures and alloys have provided evidence that Pd−Au exhibit high reactivity toward HCOOH oxidation.[19,20] Zhang et al. have recently suggested that the catalytic activity is dependent on the alloying degree of Pd−Au nanoparticles.[21] Fang and co-workers have also shown that the activity of Au−Pd−Pt core−shell−cluster trimetallic nanostructures is rather high, particularly in the case of two Pd atomic layers and a half-monolayer of Pt.[22]

In this article, we shall examine the role of the Pd lattice strain on the electrocatalytic activity of Pd shells grown on Au nanoparticles obtained by colloidal seeding growth methods in aqueous solution.[23,24] Our recent studies, based on selected area electron diffraction patterns, have shown that the growth of Pd shells on 19 nm Au particles between approximately 1 and 10 nm leads to a decrease in the lattice strain from 3.5 to 1%.[24] The relaxation of the average lattice strain can be described to a large extent by considering the formation of pure edge dislocations equivalent to those assessed at epitaxial Pd layer on Au(111) surfaces.[25] Electrostatic assemblies of these metallic nanoparticles, employing polycationic layers such as poly-L-lysine (PLL), lead to stable mono- and multilayers in which the particle number density can be controlled while the particle surface remains largely exposed to the electrolyte solution.[24,26] We provide conclusive evidence that CO coverage and stripping potential are strongly affected by the strain of the Pd lattice. Furthermore, we observe a strong increase in the average catalytic activity of core−shell nanoparticles toward HCOOH oxidation with increasing Pd thickness. Finally, marked differences between the reactivity of Pd and CS nanoparticles of similar dimensions are discussed in terms of their crystalline structure.

2. EXPERIMENTAL SECTION

2.1. Synthesis and Assembly of Nanostructures to the Electrode Surface. The synthesis of the various nanostructures was performed employing high-purity reagents: gold(III) chloride trihydrate ($HAuCl_4 \cdot 3H_2O$, 99.9%), sodium tetrachloropalladate tetrahydrate ($Na_2PdCl_4 \cdot 4H_2O$, 98%), palladium dichloride ($PdCl_2$, 99.9999%), trisodium citrate ($C_2H_5Na_3O_7 \cdot 2H_2O$, 99.5%), and L-ascorbic acid ($C_6H_8O_6$, 99.7%). All solutions were prepared with ultrapure Milli-Q water (18.2 MΩ cm).

The first step in the preparation of Au−Pd core−shell (CS) nanoparticles involves the growth of 19 nm Au seeds employing trisodium citrate as a reducing reagent.[23,27,28] In a different container, an aqueous solution of H_2PdCl_4 was prepared by mixing $PdCl_2$, HCl, and Milli-Q water. Different shell thicknesses were obtained by varying the amount of 0.1 mol dm^{-3} H_2PdCl_4 added to 50 mL solutions of the as-grown Au nanoparticles, placed in an ice bath under vigorous stirring.[23,24] This step is followed by adding an excess amount of L-ascorbic acid (0.1 mol dm^{-3}, 6 mL) dropwise, during 1 h, in order to avoid the formation of isolated Pd clusters. The reaction is allowed to continue for an additional 30 min. The H_2PdCl_4 solution volume was adjusted in order to control the Pd thicknesses from 1 to 10 nm.

The synthesis of Pd nanoparticles was also performed by reduction of hexachloropalladate(IV) acid in the presence of trisodium citrate.[29,30] The solution containing 3.0×10^{-4} mol dm^{-3} Na_2PdCl_4 was brought to its boiling point under vigorous agitation, and 18 mL of a 0.1% solution of trisodium citrate was added. The mixture was kept under reflux and vigorous stirring for at least 4 h; the solution was then allowed to cool down at room temperature. The average particle size obtained by this method is 10.2 ± 1.5 nm, as estimated from TEM and AFM methods.[30]

The electrostatic assembly of nanostructures was performed following previously established methods.[26,29,31] Nanoparticles were adsorbed on poly-L-lysine hydrobromide (M_w 30.000−70.000) modified indium-doped tin oxide (ITO) electrodes. ITO electrodes were cleaned by sequential sonication in acetone, ethanol, and ultrapure Milli-Q-water, for 15 min in each solvent, and dried in a stream of pure argon. The clean surfaces were modified by dipping in a solution of PLL (1 mg cm^{-3}) for 10 min, followed by copious rinsing with Milli-Q water and drying under a high-purity argon flow. Electrostatic adsorption of nanoparticles was achieved by dipping the freshly prepared PLL-ITO electrodes into colloidal solutions for 1 h. The surface was again rinsed with Milli-Q water and dried in a stream of pure argon. Electrochemical studies previously reported, using the same Au nanoparticles, provide evidence of a high electrical connectivity in the nanoparticle assembly.[26]

2.2. Characterization of the Nanostructures and Electrochemical Studies. Average nanoparticle sizes were estimated from high-resolution transmission electron microscopy (TEM), using a JEOL JEM 1200 EX MKI and the image analysis software Soft Imaging Systems GmbH analySIS 3.0. Samples for TEM images were produced by placing 10 μL drops on a carbon-coated copper grid of 3 mm diameter. Excess solution was absorbed with filter paper, and the sample was dried in air at room temperature. Topographic images of the nanoparticle assemblies were obtained by AFM measurements in acoustic mode (Veeco Multimode with Nanoscope V controller with Picoforce Extender). AFM tips used in these experiments typically exhibited a radius of curvature below 20 nm, 40 N m^{-1} force constant, and 300 kHz resonance frequency. The AFM images were processed with Gwyddion software. X-ray diffraction (XRD) patterns were measured on a Bruker AXS Advance D8 diffractometer, with a $\theta-\theta$ and using Cu Kα radiation (40 kV, 40 mA), at room temperature. The diffractograms were recorded with a linear position-sensitive detector in a 2θ range of 0−100° with a resolution of 0.01°.

A two-compartment electrochemical cell was used, incorporating a Pt wire and a KCl-saturated silver/silver chloride (KCl-saturated Ag/AgCl) as counter and reference electrodes, respectively. The reference and working electrodes were placed in different compartments, connected by a Luggin capillary. All potentials in this work are quoted with respect to the Ag/AgCl reference electrode. The electrochemical cell was placed in a Faraday cage to isolate it from environmental electronic noise. Measurements were carried out in a solution containing 0.5 mol dm^{-3} sulfuric acid (H_2SO_4, 98%). Solutions were purged with highly purified argon, for at least 20 min, prior to a series of experiments. Cyclic voltammograms were recorded with the Autolab PGSTAT30. All the electrochemical experiments were carried out at room temperature.

CO oxidation studies were carried out by bubbling CO (99.97%, CK Gas) in the electrolyte solution for 15 min, while keeping the electrode potential at −0.166 V. Prior to cycling the electrode potential, the solution was purged with high-purity

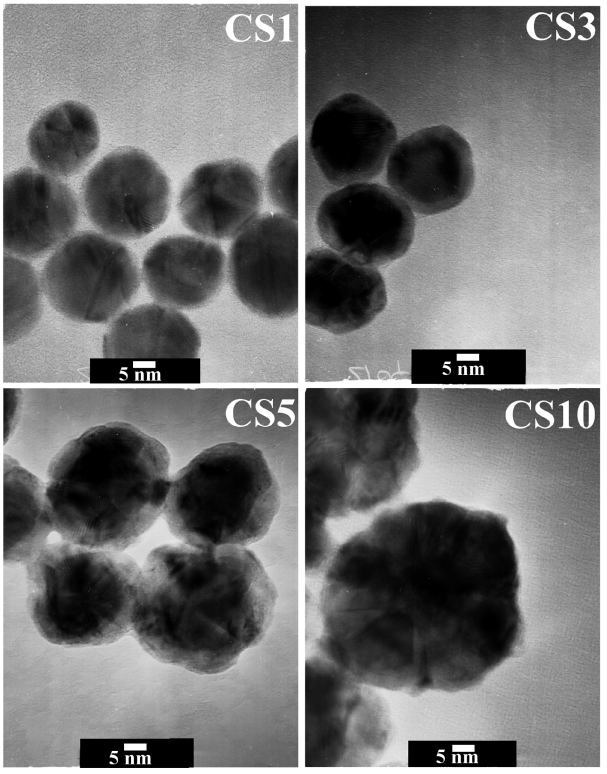

Figure 1. TEM images of Au−Pd nanoparticles featuring a 19.3 ± 1.2 nm Au seed coated with Pd shells with thicknesses of 1.3 ± 0.1 nm (CS1), 2.7 ± 1.0 nm (CS3), 5.1 ± 0.9 nm (CS5), and 9.9 ± 1.0 nm (CS10).

Ar for 30 min, in order to displace the dissolved CO. The electrode potential was scanned from −0.20 to 1.0 V, at 20 mV s^{-1}. Consecutive cycles of the assembly in this potential range did not produce any decrease in the characteristic H and oxide signals, confirming the stability of Pd nanoshells. Formic acid oxidation was studied by cyclic voltammetry in 2 mol dm^{-3} HCOOH (99.99%, Sigma-Aldich) solutions, in the same potential range. Deactivation of the nanostructured assemblies was investigated by chronoamperometric transients at 0.4 V in the same electrolyte solution.

3. RESULTS AND DISCUSSION

3.1. Three-Dimensional Assemblies of CS Nanostructures.

Illustrative TEM images of the various CS nanostructures with different shell thicknesses are displayed in Figure 1. The average shell thickness can be controlled by varying Pd content in the synthesis. The micrographs are characterized by a clear contrast between Au cores and Pd shells, confirming a systematic increase in the Pd shell thickness between 1.3 ± 0.1 and 9.9 ± 1.0 nm.[24] As discussed in previous work, analysis of a large ensemble of samples revealed the formation of a continuous layer of Pd over Au cores, with the core−shell composition (as examined from EDX analysis) matching the composition of the synthesis bath.[24] Colloidal solutions of the various particles, kept under clean conditions, were stable for several months. The average diameter of the various nanostructures corresponds to the following: 19.3 ± 1.2 nm Au, 21.8 ± 1.1 nm (CS1), 24.7 ± 1.3 nm (CS3), 29.5 ± 1.2 nm (CS5), 38.9 ± 1.5 nm (CS10), and 10.2 ± 1.5 nm Pd.[24,29,31]

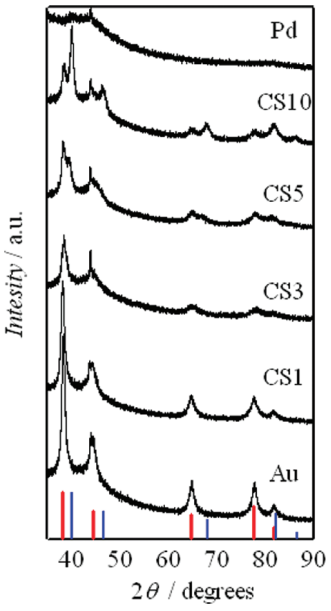

Figure 2. Powder XRD diffractograms of Au, Pd, CS1, CS3, CS5, and CS10 nanoparticles. The red lines at 38.1°, 44.4°, 64.6°, 77.5°, and 81.7° indicate the standard Au diffraction pattern, while the blue lines at 40.1° (111), 46.7° (200), 68.1° (220), 82.1° (311), and 86.6° belong to Pd.

Powder X-ray diffractograms of Au, Pd, and Au−Pd core−shell nanoparticles are contrasted in Figure 2. The XRD pattern of Au nanoparticles exhibits peaks at 2θ = 38.1°, 44.4°, 64.6°, 77.5°, and 81.7°, which are associated with the (111), (200), (220), (311), and (222) planes of the face-centered cubic (fcc) crystalline structure, respectively. The strongest diffraction peak is observed at 38.1°, suggesting a strong (111) orientation of the nanocrystalline planes. On the other hand, Pd nanoparticles generated by citrate reduction exhibited poor crystallinity. Rather weak diffraction signals are observed at 2θ = 40.2° and 46.7°, which correspond to the (111) and (200) planes. We shall demonstrate that the poor crystallinity of Pd nanoparticles plays an important role in their electrocatalytic properties.

CS nanoparticles exhibit the characteristic Au and Pd diffraction peaks, with different ratios depending on Pd thickness. Au cores template the growth of Pd shells, allowing the progressive appearance of Pd diffraction peaks at 2θ = 40.1° (111), 46.7° (200), 68.1° (220), 82.1° (311), and 86.6° (222). In the sequence from CS1 to CS10, the intensity of the diffraction peaks associated with Au decreases, while those of Pd increase without significant shifts in 2θ. A small shift in the position of the Au(111) and Pd(111) peaks can be observed, which is likely due to the convolution of both peaks, as they appear close together and peaks at higher angles do not shift. A peak associated with the Pd(200) phase was observed in the CS10 nanoparticles around 48°. A corresponding small broad peak can be seen for the CS5 nanoparticles, while it is completely absent for the other CS nanostructures.

The observed behavior of the XRD patterns is consistent with a core−shell configuration, rather than Au−Pd alloys. The tendency of Pd and Au to segregate rather than alloy, with Pd tending toward the surface and Au to the core, has been previously noted.[32,33] Similar seeding growth methods to form Au−Pd core−shell structure have been amply studied, and a range of characterization techniques, such as UV−vis spectroscopy, XRD,

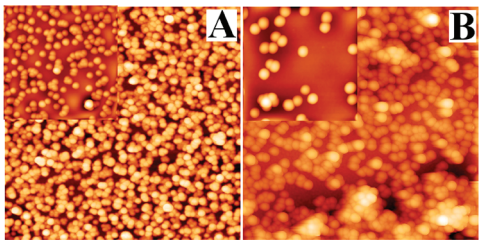

Figure 3. Acoustic AFM images of Si(111) surfaces after five immersion steps into solutions of core−shells and PLL. (A) 1 μm × 1 μm × 34.7 nm of 5×(CS1:PLL) and (B) 1 μm × 1 μm × 62.2 nm of 5×(CS10:PLL). The insets correspond to 1 μm × 1 μm × 131.6 nm (A) and 1 μm × 1 μm × 182.8 nm (B) images of the corresponding 1×(CS:PLL).

TEM (high-resolution and dark-field), EDX and elemental mapping, XANES, and EXAFS, have all confirmed the core−shell nature of the nanostructures.[23,27,34−38] Our previous studies using selected area electron diffraction patterns (SADPs) provide a quantitative relationship between the average Pd shell thickness and the corresponding lattice strain induced by the Au core.[24] XRD patterns identical to Au have been reported for very thin Pd shells,[19,36] while shoulder peaks are seen for increasingly thicker shells;[37] alloyed particles, on the other hand, present peaks that shift from the position of the gold pattern to that of Pd, without shoulders or individual peaks being observed for each metal.[39,40] It has been established that in order for significant alloying to occur, the temperature needs to be increased considerably above room temperature (a range between 200 and 300 °C has been reported).[23,34]

Topographic AFM images of 3D assemblies of CS1 and CS10 at Si(111) wafers are illustrated in Figure 3. An ultrathin PLL film is initially adsorbed on the native oxide layer of Si wafer, followed by adsorption of CS nanostructures. It has been previously demonstrated that the particle number density and overall distribution of particles electrostatically adsorbed at PLL-modified surfaces are little dependent on the structure and topography of the substrate.[26] Consequently, the particle assembly structure can be clearly illustrated on a flat Si(111) wafer, rather than on the significantly rougher ITO surface. The first layer of CS nanoparticles (shown in the insets of parts A and B of Figure 3) exhibits submonolayer coverage, with an apparent random particle distribution across the PLL-modified surface. Similar structures were also observed for layers of CS nanoparticles with different Pd thicknesses. Previous studies have shown that the particle number density can be varied by adjusting the adsorption time and solution concentration.[26,29,31,41,42] Alternate adsorption steps of PLL and CS nanoparticles lead to the formation of corrugated assemblies. The layer-by-layer assembly leads to an increase in the particle number density, although some sections of the surface remain uncovered. The PLL layer generates an ultrathin film with surface roughness below 1 nm;[31] consequently, no topographic features associated with the polyelectrolyte can be identified in AFM images. This corrugated films with controlled particle number density are also characterized by a good electrical conductivity between the whole ensemble of nanoparticles and the electrode surface.[26]

3.2. Electrochemical Study of CO Adsorption and Stripping. Figure 4 shows the characteristic cyclic voltammograms of 5×(CS:PLL) and 5×(Pd:PLL) assemblies in 0.5 mol dm^{-3} H_2SO_4, at 100 mV s^{-1}. The assemblies were electrochemically

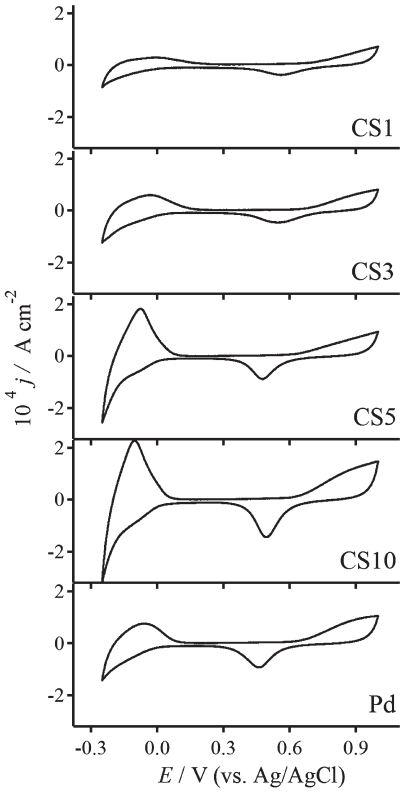

Figure 4. Cyclic voltammograms at 100 mV s^{-1} of 5×(CS:PLL) assemblies featuring CS1, CS3, CS5, and CS10. These responses are compared with the voltammogram of a 5×(Pd:PLL) assembly (Pd). The electrolyte solution was 0.5 mol dm^{-3} H_2SO_4.

pretreated in a controlled potential range in order to desorb the citrate layer from the particle surface.[24] Careful preparation of CS assemblies and electrochemical pretreatment ensure a high reproducibility in the electrochemical responses. Following the approach developed by Montes de Oca et al., the average charge per particle associated with the reduction of Pd oxide (cathodic responses in the range of 0.2−0.7 V) in 2D assemblies was used for estimating the particle number density and real surface area of 3D assemblies.[24,26] Consequently, the current density in Figure 4, as well as in subsequent voltammograms, is calculated employing the real surface area of the assembly. It should be mentioned that the real surface area is not only determined by the number of particles adsorbed in each immersion step but also by the particle roughness.[24] In the case of Pd nanoparticles, the real surface area of the Pd assembly was calculated considering the charge associated with the reduction of an oxide monolayer at polycrystalline Pd (424 μC cm^{-2}).[43]

The electrochemical pretreatment of the CS and Pd assemblies resulted in clear responses associated with hydrogen adsorption/absorption in the range of −0.15 to −0.3 V as shown in Figure 4. Scanning toward more negative potentials leads to hydrogen evolution in all of the assemblies. Estimation of H loading as a function of Pd content in the assemblies leads to a H/Pd ratio close to the characteristic stoichiometry of the β-phase in bulk Pd hydride.[24] Furthermore, these results also confirm that the PLL layers in the assembly do not play any role in the electrochemical responses of nanoparticles.

The Pd oxide formation is linked to the current responses upon scanning the potential from 0.6 to 1.0 V, while the corresponding

dx.doi.org/10.1021/jp208998j |J. Phys. Chem. C 2012, 116, 692–699

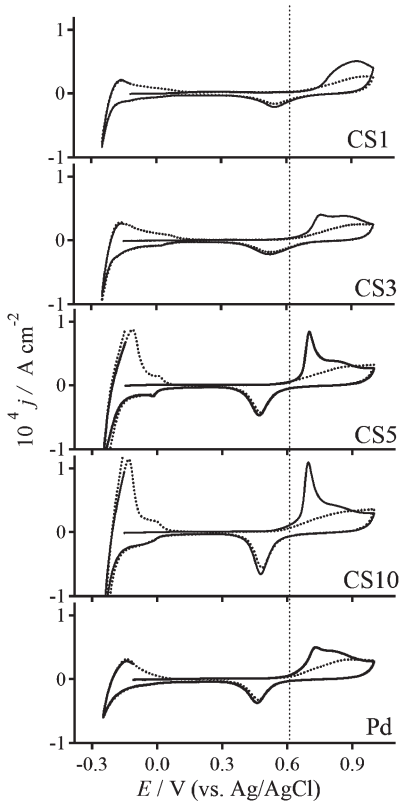

Figure 5. CO stripping voltammograms at 20 mV s^{-1} of the various core−shell and Pd nanoparticle assemblies. Potential scans were initiated at open circuit potential. The dotted voltammograms show the second scan after CO desorption. The vertical dotted line corresponds to the onset of CO oxidation at Pd nanoparticles. The composition of the assembly and electrolyte solution are indicated in the caption of Figure 4.

reduction manifests by a cathodic peak close to 0.5 V in the reverse scan. *An important observation in Figure 4 is the shift of the onset potential for oxide formation and oxide stripping peak toward more positive values as Pd thickness (δ) decreases*. Recent works have reported similar observations for core−shell and alloys of Au−Pd nanoparticles,[19,20,44] as well as for thin layers of Pd on Au single-crystal surfaces.[45] The origin of the thickness-dependent oxide formation in Pd nanoshells is yet to be fully understood, although changes to the Fermi level of the Pd layers induced by their interactions with the underlying Au, as well as changes in the surface atomic structure of Pd on Au, have been proposed as possible explanations of this behavior.[45] Considering that the tensile strain of the nanoshell changes between 1 and 3.5% in this set of particles,[24] it could be envisaged that electronic and geometric effects can affect the Pd−O interactions. On the other hand, results to be published elsewhere suggest that these interactions are also determined by the nature of the surface acting as particle support. In any case, the Pd−O interactions do play a crucial role in the electrocatalytic activity of particles as demonstrated further below.

Figure 5 displays CO stripping voltammograms for CS and Pd electrodes, recorded at 20 mV s^{-1}. Hydrogen adsorption and desorption are completely blocked in the initial forward scan by the adsorbed CO. The main response in the positive scan is the CO stripping occurring in the potential range of the Pd oxide formation. In the second scan (dotted line in Figure 5), the

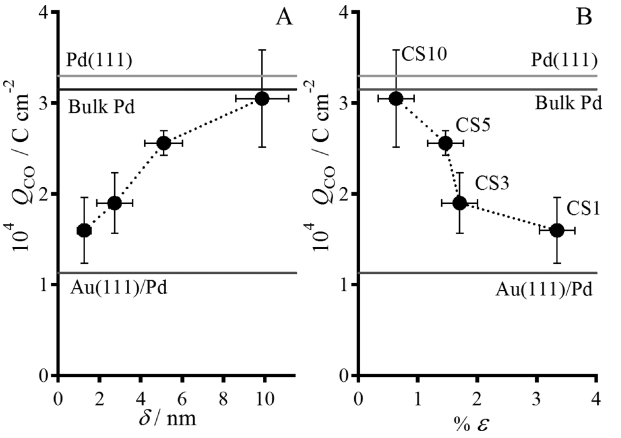

Figure 6. Average charge density of CO oxidation (Q_{CO}) as a function of Pd thickness, δ, (A) and lattice strain, ε, (B) in Au−Pd core−shell nanostructures. The characteristic charges for bulk Pd(111),[7] polycrystalline,[48] and pseudomorphic monolayer on Au(111) surfaces[6] are indicated.

hydrogen responses are fully recovered, indicating a complete removal of the adsorbed CO in the first scan. The most striking behavior in Figure 5 is the decrease in the CO stripping current density and shift toward more positive potentials with decreasing Pd thickness. More positive peak potentials with decreasing Pd coverage have been previously reported by Ruvinsky et al. for Au nanoparticles with submonolayers of Pd.[46] The shift in the onset potential of CO stripping is consistent with the behavior of Pd oxide formation discussed above. It is well established that CO oxidation is enabled by the adsorption of oxygenated species at Pd surfaces.[6] A sharp CO stripping peak is observed for CS5 and CS10 nanostructures, with the onset at the same potential as that of Pd nanoparticles. On the other hand, CO stripping on the "amorphous" Pd nanoparticles shows a significantly broader peak in comparison to CS10.

Parts A and B of Figure 6 show the average charge density of CO stripping (Q_{CO}) as a function of Pd thickness (δ) and Pd strain (ε); ε was estimated from previously reported TEM and selected area electron diffraction studies on the same set of particles.[24] The values of Q_{CO} represent the average of at least four different nanoparticle assemblies, obtained after integration of CO oxidation peak in the first scan and subtraction of the Pd oxide signal in the second scan (dotted lines in Figure 5). Figure 6A shows that Q_{CO} monotonically increases from 160 to 310 μC cm^{-2} as Pd thickness increases from 1.3 ± 0.1 (CS1) to 9.9 ± 1.0 nm (CS10). In order to compare the experimental trends, the reported values for Q_{CO} at bulk Pd (111),[7] polycrystalline Pd,[47] and pseudomorphic Pd monolayers on Au(111) surfaces[6] are included in Figure 6 as horizontal lines. The trends observed for the CS clearly show a progressive variation between the limiting cases reported for extended surfaces. On the other hand, the values obtained for Pd particles were 20% lower than the value reported for polycrystalline Pd surfaces. The apparent difference between polycrystalline and "amorphous" surfaces provides an indication of the role of defect sites on CO coverage.

To a first approximation, the behavior of Q_{CO} can be linked to the evolution of the lattice strain as illustrated in Figure 6B. In the case of CS10, the strain decreases to about 1% and Q_{CO} approaches the value for bulk polycrystalline Pd. The systematic decrease in CO coverage with increasing strain provides a very

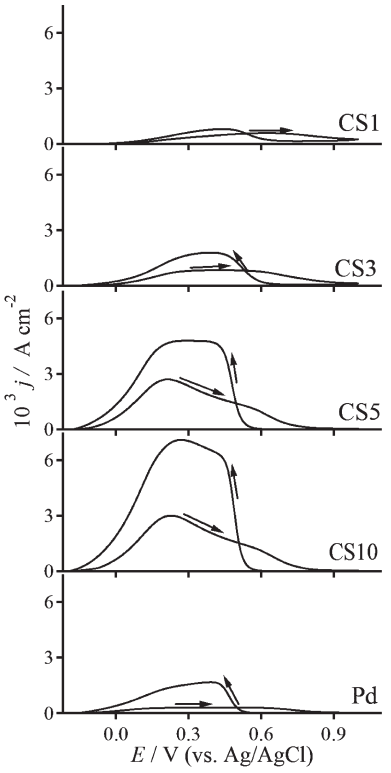

Figure 7. Cyclic voltammograms of the core−shell and Pd nanoassemblies, at 20 mV s^{-1} in 2 mol dm^{-3} HCOOH and 0.5 mol dm^{-3} H_2SO_4.

important correlation toward understanding the role of electronic and strain effects in the electrocatalytic properties of ultrathin metallic layers. According to DFT calculations by Roudgar and Gross, the binding energy of CO on fcc hollow sites of Pd overlayers on Au(111) decrease with increasing number of Pd monolayers above two bilayers.[3] This behavior was rationalized in terms of electronic effects, while strain effects have a more limited contribution. Our experimental results do not directly probe CO binding energy but rather the coverage on the Pd surface. However, assuming that coverage is somewhat correlated with binding energies, it appears that our experimental trends are qualitatively opposite to the DFT calculations. We are currently revisiting these theoretical studies on the basis of the structural information obtained experimentally, in order to gain further understanding of these issues.

3.3. HCOOH Oxidation. Cyclic voltammograms associated with the CS and Pd nanoparticle assemblies in 2 mol dm^{-3} HCOOH + 0.5 mol dm^{-3} H_2SO_4 solutions are contrasted in Figure 7. As in the case of CO, no electrochemical responses are observed in the presence of HCOOH at Au nanoparticle assemblies, under the conditions studied (results not shown). The onset of HCOOH oxidation occurs at −0.1 V for all of the assemblies, although the current density shows a strong dependence on Pd thickness. In the forward scan, the current density shows a maximum at around 0.29 V in the case of CS5 and CS10. On the other hand, CS1, CS3, and Pd nanoparticles exhibit a significantly weaker increase in the current density. A strong decrease in the current density is observed as the potential is scanned above the onset of Pd oxide formation. The inhibition of HCOOH oxidation, at oxygen-covered Pd surfaces, is a rather well-documented behavior in the literature.[15,18,47] However, a rather fascinating trend is observed in the evolution of the current

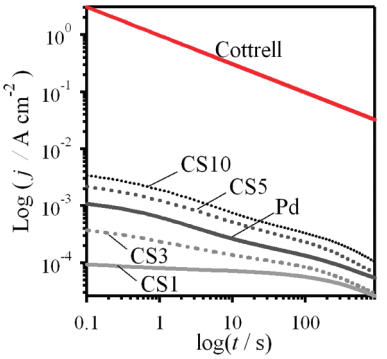

Figure 8. Log−log representation of chronoamperometric transients for HCOOH oxidation on Pd and CS nanoparticle assemblies, at 0.4 V in 0.5 mol dm^{-3} H_2SO_4 and 2 mol dm^{-3} HCOOH. In all cases, it can be seen that the current responses are orders of magnitude lower than the Cottrell (diffusional) limit.

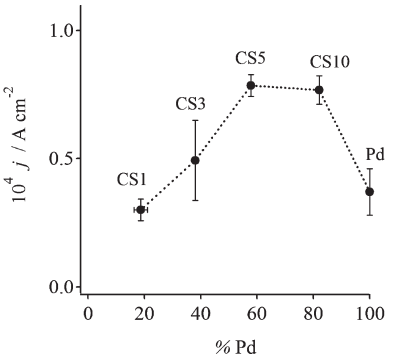

Figure 9. Current densities of HCOOH oxidation after 750 s at 0.4 V at the nanoparticle assemblies expressed in terms of the Pd mass ratio.

responses in the reverse cycle. CS1 and CS3 exhibit a lesser degree of hysteresis in comparison to the case of CS5, CS10, and Pd. This result suggests that the contrast in reactivity between the equilibrium surface energy of the metal phase (forward scan) and the dynamic state generated after stripping of the Pd oxide species (backward scan) is very small for the strained Pd nanoshells.

Although the HCOOH oxidation current exhibits a clear increase with increasing Pd thickness, a correlation with lattice strain should be considered cautiously. First, it should be clarified that the maximum current responses in all cases are at least 2 orders of magnitude smaller than the limiting diffusional current. Baldauf and Kolb did not observe a clear dependence in the HCOOH oxidation current density with the number of Pd layers epitaxially grown on Au single-crystal surfaces, although (100) orientation showed significantly higher currents than (111) surfaces.[18] A rather interesting observation is that a significant increase in the current responses is observed for CS which exhibit clear (200) diffraction signals in the XRD analysis (Figure 2). This appears consistent with the fact that "amorphous" Pd nanoparticles show significantly smaller currents than CS10 nanoparticles.

Figure 8 compares temporal changes in the current for HCOOH oxidation at 0.4 V on the various nanoassemblies. In all cases the current density is more than 2 orders of magnitude smaller than the Cottrell limit. The deactivation appears to follow a similar trend in all of the assemblies, suggesting that

dx.doi.org/10.1021/jp208998j |J. Phys. Chem. C 2012, 116, 692–699

the generated poison is formed independently of the strain and structural properties of the CS assembly.

The average current density recorded after 750 s, at 0.4 V, for several CS and Pd assemblies is contrasted in Figure 9. As observed from the potentiodynamic experiments, the current density increases with the Pd mass ratio in CS nanostructures and decreases in the case of "amorphous" Pd nanoparticles. Although the difference in reactivity between the CS and pure Pd nanoparticles could be linked to size effects, we believe it is not the main contributor. Size effects are mainly observed for particles smaller than 10 nm, and the reactivity toward HCOOH oxidation has been shown to increase with decreasing particle size,[49] contrary to the trend observed here. Additionally, size effects have recently been linked to the formation of different crystal phases in the Pd particles.[19] The behavior observed here further suggests that the reactivity toward HCOOH oxidation is primarily determined by the generation of crystal facets with the appropriate orientation (e.g., 100) rather than by strain or electronic effects. Recent reports have indeed shown that alloyed and core−shell nanoparticles exhibit higher reactivity than Pd nanostructures.[19−21] However, the results described here suggest that the origin of this enhanced reactivity is not only linked to electronic and strain effects.

4. CONCLUSIONS

The present work describes a systematic study of CO and HCOOH electrooxidation at Pd−Au core−shell nanostructure assemblies. Pd thickness is varied between ca. 1 and 10 nm, which corresponds to a decrease in the average lattice strain from 3.5 and 1%.[24] The onset potential for CO stripping exhibited a systematic shift toward more positive potential as Pd thickness decreases. This behavior correlates well with the shift of Pd oxide formation at CS nanostructures. Furthermore, the average CO coverage increases with increasing Pd thickness. Comparison with values reported for bulk Pd and extended epitaxial layers at Au(111) surfaces suggest that a key parameter determining CO coverage is the Pd lattice strain. Although electronic effects may also play a role in this reactivity trend, theoretical predictions suggest that such effects are negligible for the thickness of the Pd shells investigated in this report.[3,5]

The reactivity of the nanostructures toward HCOOH oxidation revealed a more complex behavior. The current density increases with Pd thickness, although the trend does not appear to correlate with the changes in lattice strain. Furthermore, pure Pd nanoparticles, featuring a rather amorphous structure as probed by XRD, exhibit significantly smaller current densities than the relaxed Pd nanoshells. We believe that the changes in the reactivity are linked to the formation of crystal facets with higher reactivity templated by Au cores, rather than electronic or strain effects. Our experimental approach, which strongly relies on the controlled adsorption of metal nanostructures, provides a valuable tool for uncovering structure−reactivity relationships in these complex systems. We are currently investigating the effect of the nanoparticle support on their catalytic activity, in order to have a more complete picture toward a rational design of novel fuel cell electrocatalysts.

AUTHOR INFORMATION

Corresponding Author

*Tel. +44 117 9288981; fax +44 117 9250612; www.bristol.ac.uk/pt/electrochemistry; e-mail David.Fermin@bristol.ac.uk.

ACKNOWLEDGMENT

The authors are grateful to the valuable support from Prof. David Cherns, Dr. Mairi Haddow, Haridas Kumarakuru, and Jonathan A. Jones (University of Bristol), as well as Dr. Paramaconi Rodriguez (Paul Scherrer Institute). M.G.M.O and V.C. acknowledge the financial support from the Mexican National Council for Science and Technology (CONACyT) and CSIC (Spain), respectively. D.P. and D.J.F. acknowledge the financial support from the U.K. Engineering and Physical Science Research Council (project EP/H046305/1) and the University of Bristol. V.C. and M.J.L. are also grateful for the financial assistance from the MICINN (Spain) through Project MAT2008-06631-C03-01.

REFERENCES

(1) Ruban, A.; Hammer, B.; Stoltze, P.; Skriver, H. L.; Norskov, J. K. *J. Mol. Catal. A: Chem.* **1997**, *115*, 421–429.
(2) Liu, P.; Norskov, J. K. *Phys. Chem. Chem. Phys.* **2001**, *3*, 3814–3818.
(3) Roudgar, A.; Gross, A. *Phys. Rev. B* **2003**, *67*, 0334091–0334094.
(4) Strasser, P.; Koh, S.; Anniyev, T.; Greeley, J.; More, K.; Yu, C. F.; Liu, Z. C.; Kaya, S.; Nordlund, D.; Ogasawara, H.; Toney, M. F.; Nilsson, A. *Nat. Chem.* **2010**, *2*, 454–460.
(5) Schlapka, A.; Lischka, M.; Gross, A.; Kasberger, U.; Jakob, P. *Phys. Rev. Lett.* **2003**, 91.
(6) El-Aziz, A. M.; Kibler, L. A. *J. Electroanal. Chem.* **2002**, *534*, 107–114.
(7) Hara, M.; Linke, U.; Wandlowski, T. *Electrochim. Acta* **2007**, *52*, 5733–5748.
(8) Llorca, M. J.; Feliu, J. M.; Aldaz, A.; Clavilier, J. *J. Electroanal. Chem.* **1994**, *376*, 151–160.
(9) Schmidt, T. J.; Jusys, Z.; Gasteiger, H. A.; Behm, R. J.; Endruschat, U.; Boennemann, H. *J. Electroanal. Chem.* **2001**, *501*, 132–140.
(10) Rice, C.; Ha, S.; Masel, R. I.; Wieckowski, A. *J. Power Sources* **2003**, *115*, 229–235.
(11) Capon, A.; Parsons, R. *J. Electroanal. Chem.* **1975**, *65*, 285–305.
(12) Capon, A.; Parsons, R. *J. Electroanal. Chem.* **1973**, *44*, 239–254.
(13) Capon, A.; Parsons, R. *J. Electroanal. Chem.* **1973**, *45*, 205–231.
(14) Capon, A.; Parsons, R. *J. Electroanal. Chem.* **1973**, *44*, 1–7.
(15) Miyake, H.; Okada, T.; Samjeske, G.; Osawa, M. *Phys. Chem. Chem. Phys.* **2008**, *10*, 3662–3669.
(16) Yu, X.; Pickup, P. G. *Electrochem. Commun.* **2009**, *11*, 2012–2014.
(17) Kibler, L. A.; El-Aziz, A. M.; Hoyer, R.; Kolb, D. M. *Angew. Chem., Int. Ed.* **2005**, *44*, 2080–2084.
(18) Baldauf, M.; Kolb, D. M. *J. Phys. Chem.* **1996**, *100*, 11375–11381.
(19) Zhou, W. J.; Lee, J. Y. *Electrochem. Commun.* **2007**, *9*, 1725–1729.
(20) Suo, Y. G.; Hsing, I. M. *Electrochim. Acta* **2011**, *56*, 2174–2183.
(21) Zhang, G. J.; Wang, Y. E.; Wang, X.; Chen, Y.; Zhou, Y. M.; Tang, Y. W.; Lu, L. D.; Bao, J. C.; Lu, T. H. *Appl. Catal. B* **2011**, *102*, 614–619.
(22) Fang, P. P.; Duan, S.; Lin, X. D.; Anema, J. R.; Li, J. F.; Buriez, O.; Ding, Y.; Fan, F. R.; Wu, D. Y.; Ren, B.; Wang, Z. L.; Amatore, C.; Tian, Z. Q. *Chem. Sci.* **2011**, *2*, 531–539.
(23) Hu, J. W.; Li, J. F.; Ren, B.; Wu, D. Y.; Sun, S. G.; Tian, Z. Q. *J. Phys. Chem. C* **2007**, *111*, 1105–1112.
(24) Montes de Oca, M. G; Kurnarakuru, H.; Cherns, D.; Fermin, D. J. *J. Phys. Chem. C* **2011**, *115*, 10489–10496.
(25) Cherns, D.; Stowell, M. J. *Thin Solid Films* **1975**, *29*, 127–143.
(26) Montes de Oca, M. G.; Fermin, D. J. *Electrochim. Acta* **2010**, *55*, 8986–8991.
(27) Hu, J. W.; Zhang, Y.; Li, J. F.; Liu, Z.; Ren, B.; Sun, S. G.; Tian, Z. Q.; Lian, T. *Chem. Phys. Lett.* **2005**, *408*, 354–359.
(28) Schmid, G.; Lehnert, A.; Malm, J. O.; Bovin, J. O. *Angew. Chem., Int. Ed.* **1991**, *30*, 874–876.
(29) Li, F.; Ciani, I.; Bertoncello, P.; Unwin, P. R.; Zhao, J. J.; Bradbury, C. R.; Fermin, D. J. *J. Phys. Chem. C* **2008**, *112*, 9686–9694.
(30) Turkevich, J.; Miner, R. S.; Babenkova, L. *J. Phys. Chem.* **1986**, *90*, 4765–4767.

(31) Zhao, J. J.; Bradbury, C. R.; Huclova, S.; Potapova, I.; Carrara, M.; Fermin, D. J. *J. Phys. Chem. B* **2005**, *109*, 22985–22994.
(32) Kobayashi, H.; Yamauchi, M.; Ikeda, R.; Kitagawa, H. *Chem. Commun.* **2009**, 4806–4808.
(33) Teng, X.; Wang, Q.; Liu, P.; Han, W.; Frenkel, A.; Wen, W.; Marinkovic, N.; Hanson, J. C.; Rodriguez, J. A. *J. Am. Chem. Soc.* **2008**, *130*, 1093–1101.
(34) Lee, A. F.; Baddeley, C. J.; Hardacre, C.; Ormerod, R. M.; Lambert, R. M.; Schmid, G.; West, H. *J. Phys. Chem.* **1995**, *99*, 6096–6102.
(35) Zhu, L. D.; Zhao, T. S.; Xu, J. B.; Liang, Z. X. *J. Power Sources* **2009**, *187*, 80–84.
(36) Nitani, H.; Yuya, M.; Ono, T.; Nakagawa, T.; Seino, S.; Okitsu, K.; Mizukoshi, Y.; Emura, S.; Yamamoto, T. A. *J. Nanopart. Res.* **2006**, *8*, 951–958.
(37) Liang, H.-P.; Lawrence, N. S.; Jones, T. G. J.; Banks, C. E.; Ducati, C. *J. Am. Chem. Soc.* **2007**, *129*, 6068–6069.
(38) Lu, L. H.; Wang, H. S.; Xi, S. Q.; Zhang, H. J. *J. Mater. Chem.* **2002**, *12*, 156–158.
(39) Nie, M.; Shen, P. K.; Wei, Z. *J. Power Sources* **2007**, *167*, 69–73.
(40) Lee, Y. W.; Kim, N. H.; Lee, K. Y.; Kwon, K.; Kim, M.; Han, S. W. *J. Phys. Chem. C* **2008**, *112*, 6717–6722.
(41) Zhao, J.; Wasem, M.; Bradbury, C. R.; Fermin, D. J. *J. Phys. Chem. C* **2008**, *112*, 7284–7289.
(42) Zhao, J. J.; Bradbury, C. R.; Fermin, D. J. *J. Phys. Chem. C* **2008**, *112*, 6832–6841.
(43) Grden, M.; Lukaszewski, M.; Jerkiewicz, G.; Czerwinski, A. *Electrochim. Acta* **2008**, *53*, 7583–7598.
(44) Park, I. S.; Lee, K. S.; Yoo, S. J.; Cho, Y. H.; Sung, Y. E. *Electrochim. Acta* **2010**, *55*, 4339–4345.
(45) Naohara, H.; Ye, S.; Uosaki, K. *J. Electroanal. Chem.* **2001**, *500*, 435–445.
(46) Ruvinsky, P. S.; Pronkin, S. N.; Zaikovskii, V. I.; Bernhardt, P.; Savinova, E. R. *Phys. Chem. Chem. Phys.* **2008**, *10*, 6665–6676.
(47) Manzanares, M. I.; Pavese, A. G.; Solis, V. M. *J. Electroanal. Chem.* **1991**, *310*, 159–167.
(48) Losiewicz, B.; Birry, L.; Lasia, A. *J. Electroanal. Chem.* **2007**, *611*, 26–34.
(49) Zhang, X. G.; Arikawa, T.; Murakami, Y.; Yahikozawa, K.; Takasu, Y. *Electrochim. Acta* **1995**, *40*, 1889–1897.

6

The Effect of Carbon Supports on the Electrocatalytic Reactivity of Au-Pd Core-Shell Nanoparticles

V. Celorrio, M.G. Montes de Oca, D. Plana, R. Moliner, M.J. Lázaro, D.J. Fermín

Journal of Physical Chemistry C 116 (2012) 6275-6282

THE JOURNAL OF PHYSICAL CHEMISTRY C

Article

pubs.acs.org/JPCC

Effect of Carbon Supports on Electrocatalytic Reactivity of Au–Pd Core–Shell Nanoparticles

V. Celorrio,[†] M. G. Montes de Oca,[‡] D. Plana,[‡] R. Moliner,[†] M. J. Lázaro,[†] and D. J. Fermín*[,‡]

[†]Instituto de Carboquímica (CSIC), Miguel Luesma Castán 4, 50018 Zaragoza, Spain

[‡]School of Chemistry, University of Bristol, Cantocks Close, Bristol BS8 1TS, U.K.

ABSTRACT: The role of particle-substrate interactions on the reactivity of bimetallic nanostructures is investigated in the case of Au–Pd core–shell nanoparticles supported on Vulcan XC-72R (Vulcan). Core–shell nanostructures (CS) featuring 19 nm Au cores and Pd shells with thicknesses between ca. 1 and 10 nm were synthesized by controlled colloidal methods and subsequently incorporated in the carbon support. X-ray diffraction, energy dispersive X-ray analysis, and high resolution transmission electron microscopy confirmed the CS nature of the nanostructures, which remain unaffected upon incorporation onto the carbon matrix. Their electrochemical properties toward CO and HCOOH electro-oxidation were studied, using cyclic voltammetry and chronoamperometry. The results show that the CO stripping potential becomes independent of the average Pd lattice strain in the case of Vulcan supported CS. This behavior is significantly different to the trend observed in CS assemblies at In-doped SnO_2 electrodes. Formic acid oxidation is also strongly affected not only by the thickness of the Pd nanoshell but also by the support. These reactivity trends are discussed in terms of strain (geometric) effects, CS crystalline structure, and substrate effects on the onset potential for the formation of oxygenated species at the catalyst surface.

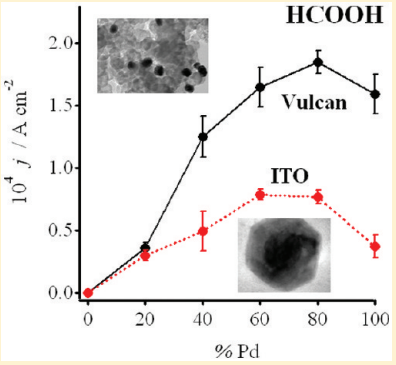

1. INTRODUCTION

Highly porous carbon supports play a key role on the performance of fuel cell electrocatalysts. Some of the key requirements for electrocatalysts supports include (i) large specific surface area for achieving high metal dispersions, (ii) good electrical conductivity, (iii) suitable pore size for optimum diffusion of reactants and byproduct to and from the catalyst, (iv) good corrosion resistance, and (v) low cost.[1,2] Carbon black is the most commonly used material for these applications, in particular Vulcan XC-72R, which combines good electrical conductivity and high surface area.[3] Conventional methods for preparing metallic nanostructures supported on porous carbon matrices involve the impregnation of the metal precursor followed by chemical reduction. In this type of approach, the structure and surface composition of carbon supports can exert a strong influence on the growth of metallic centers, affecting key parameters such as size, morphology, size distribution, stability, and dispersion, which in turn can affect catalytic activity.[4−7] However, investigations on the role of substrate on the reactivity of already formed nanostructures, e.g., via colloidal synthesis, are relatively scarce.[8] Such an approach would allow decoupling effects of the support on particle growth from specific chemical interactions linked to the reactivity of the metallic centers, i.e., any effect observed in the catalytic activity could be directly linked to the support on the electrochemical activity and not to particle size, distribution, etc.

The direct formic acid fuel cell (DFAFC) is emerging as a rather attractive alternative to more established systems such as hydrogen (HFC) and direct methanol fuel cells (DMFC). The latter two technologies still face important drawbacks such as hydrogen generation, storage and distribution, or the high toxicity of methanol.[9−11] Although formic acid exhibits a lower volumetric energy density than methanol (2086 Wh L^{-1} vs 4690 Wh L^{-1}), the smaller crossover through the membrane allows the use of high fuel concentrations.[12−14]

The electro-oxidation of formic acid has been investigated at catalytically active surfaces[12,15−21] on which a dual pathway mechanism has been proposed.[22] It is generally agreed that HCOOH oxidation at Pt surfaces undergoes the formation of adsorbed CO intermediates, requiring the presence of surface oxygenated species to proceed to the formation of CO_2. However, on Pd it occurs primarily via a direct pathway, avoiding the formation of CO as an intermediate. Nevertheless, Pd and Pd-based catalysts undergo substantial deactivation under operational conditions, and a discussion has emerged in the literature regarding the long-term stability of Pd catalysts in direct formic acid fuel cells.[23−26] Yu and Pickup have recently concluded that deactivation is due to CO poisoning, occurring at longer time-scales than on Pt centers.[14]

We have recently proposed that the interaction between CO and Pd can be significantly affected by the average lattice strain, as determined by selected area electron diffraction patterns (SADPs).[27] Pd nanoshells grown on Au nanoparticles exhibit a

Received: December 6, 2011
Revised: February 5, 2012
Published: February 9, 2012

thickness dependence lattice strain in the range of 1 to 10 nm, which can be described in terms of the Matthew's model.[28] Other studies, employing a slightly different synthesis method, have shown that Pd monolayers on Au cores exhibit Shockley partial dislocations, while further layers mainly present stacking faults.[29] Changes in the average lattice strain affect the position of the d-band center, which plays a crucial role on the interaction with organic adsorbates.[30,31] Pioneering works in this area were based on the pseudomorphic growth of Pd layers on Au single crystal surfaces.[32−34] Recent studies on Au−Pd core−shell[35] and alloyed nanoparticles[16,36] supported on various carbon matrices have also suggested enhanced catalytic activity with respect to pure Pd catalysts.

In the present work, we attempt to elucidate the effect of a particular carbon support, Vulcan XC-72R (Vulcan), on the electrocatalytic activity of Au−Pd core−shell nanostructures (CS) toward CO and HCOOH oxidation. We systematically vary the thickness of the Pd shell in order to evaluate whether the so-called support effects counteract or enhance changes in reactivity induced by lattice strain. Electron microscopy and XRD analysis confirm that the adsorption of CS nanoparticles on Vulcan (CS/C) resulted in a homogeneous distribution of particles, without affecting their structure. Valuable insights into the effect of the support are established from comparisons with electrochemical behavior of the same CS nanoparticles assembled at In-doped SnO_2 electrodes. Voltammetric studies in sulfuric acid containing electrolytes indicate that, while CO coverage is affected by the average Pd thickness,[27] the stripping potential changes significantly only in the case of highly strained nanoshells supported on Vulcan. Furthermore, the deactivation rate during HCOOH oxidation at constant potential is slower on the carbon supported nanoparticles. The fact that we decouple the synthesis of the nanostructures from the preparation of the assemblies allows the identification of support effects on the reactivity of the system rather than on the structure or morphology of the metallic centers.

2. EXPERIMENTAL METHODS

2.1. Synthesis of the Core−Shell Nanoparticles Supported on Vulcan. Pd nanoparticles (NPs) were prepared with a reaction mixture of $Na_2PdCl_6{\cdot}4H_2O$ and trisodium citrate under reflux and strong stirring for 4 h.[37,38] The synthesis of Au−Pd CS nanostructures involved a two step process initiated by the preparation of Au nanoparticles, employing trisodium citrate as a reducing and stabilizing agent. The second step was the Pd growth onto the as-grown Au cores by reduction of H_2PdCl_4, in the presence of ascorbic acid.[28,39] Pd thickness can be controlled by the amount of Pd precursor added in the second step.

The metallic nanostructures were supported on Vulcan XC-72R (Cabot), which consists of spherical particle aggregates, with sizes ranging from 30 to 60 nm. It has a relatively large specific surface area of 218 $m^2\ g^{-1}$ and a total pore volume of 0.41 $cm^3\ g^{-1}$, presenting a mesoporous structure; however, it also contains a large number of micropores (30% of total surface area).[3] A set amount of the as received Vulcan powder was suspended and stirred during 48 h in controlled amounts of nanoparticle dispersions, calculated to obtain a total metal loading of 20 wt %. The as-prepared carbon-supported nanoparticle powders were filtered, washed with Milli-Q water, and dried at 60 °C overnight.

2.2. Characterization of Electrocatalysts. The metal loading on the carbon support was controlled by monitoring the weight ratio of the nanoparticles versus that of Vulcan. The real loading was determined by energy dispersive X-ray (EDX) analysis using an Oxford Instruments ISIS 300, coupled to a JEOL JSM 5600LV scanning electron microscope. TEM images, for determination of the size and morphology, were obtained using a JEOL JEM 1200 EX MKI and the image analysis software Soft Imaging Systems GmbH analySIS 3.0. Samples for TEM were produced by placing 10 μL drops of the carbon supported catalysts dissolved in ethanol on a 3 mm diameter carbon-coated copper grid. Excess solution was absorbed with filter paper, and the sample was dried in air at room temperature. Average diameters and shell thicknesses of the core−shell structures were obtained from HR-TEM images of at least 200 nanoparticles per sample and their elementary composition was estimated from EDX measurements.[28]

High-angle annular dark-field scanning transmission electron microscopy (STEM-HAADF) images and EDX analysis were performed in a FEI Tecnai F30, equipped with a field emission gun working at 300 kV. EDX spectra were obtained with an energy dispersion of 0.5 eV per channel. Spatially resolved EDX analysis was used to analyze the chemical composition of each Au−Pd CS sample. Since each element has a characteristic energy edge, chemical profiles of each element can be plotted. This technique is known as spectrum-line or line-scan acquisition. The supported catalysts were also examined by powder X-ray diffraction (XRD) using a Bruker AXS D8 Advance diffractometer with a $\theta-\theta$ configuration and Cu$K\alpha$ radiation. Scans were done for 2θ values between 20 and 100°. XRD patterns were compared to the Au and Pd reference patterns from the powder diffraction file (PDF), International Centre for Diffraction Data; the powder diffraction files used as reference were PDF 040784 and 461043, for Au and Pd, respectively.

2.3. Electrochemical Studies. A two-compartment electrochemical cell was used, incorporating a Pt wire and KCl-saturated silver/silver chloride (KCl-saturated Ag/AgCl) as counter and reference electrodes, respectively. The reference and working electrodes were placed in different compartments connected by a Luggin capillary. All potentials were measured and are quoted with respect to the Ag/AgCl reference electrode. The electrochemical cell was placed in a Faraday cage to isolate it from environmental electronic noise. All measurements were carried out at room temperature, in aqueous solutions (Milli-Q, 18.2 MΩ cm resistivity) containing high purity 0.5 mol dm^{-3} sulfuric acid (H_2SO_4, 98%, Fisher). Solutions were purged with high purity argon, for at least 20 min prior to a series of experiments. Cyclic voltammograms were recorded with an Autolab PGSTAT30.

Catalyst inks were prepared by mixing 2 mg of the catalyst powder, 15 μL of Nafion dispersion (5 wt.%, Aldrich) and 500 μL of ultrapure water (Millipore Milli-Q system). A 40 μL aliquot of the ink was drop-cast onto a glassy carbon electrode (7 mm diameter) and dried. The working electrode was introduced into the electrochemical cell in a meniscus configuration. The electrochemical active areas of the catalysts were determined from the charges obtained in CO-stripping voltammograms, using charge densities obtained in previous work as normalization parameters.[27] These experiments were carried out by bubbling CO (99.97%, CK gas) through the electrolyte during 15 min, while the electrode was immersed in solution and held at −0.166 V. Argon was used to purge CO out from solution before running the stripping voltammetry, leaving only the CO adsorbed on Pd surface. The potential was

dx.doi.org/10.1021/jp211747a | J. Phys. Chem. C 2012, 116, 6275−6282

scanned between −0.20 and 1.0 V, at 0.02 V s^{-1}. HCOOH oxidation was studied by cyclic voltammetry and chronoamperometry. Cyclic voltammograms were recorded in 2 mol dm^{-3} HCOOH (98%, Fluka) and 0.5 mol dm^{-3} H_2SO_4 aqueous solutions between −0.2 and 1.0 V at 0.02 V s^{-1}. Chronoamperometric measurements were recorded in the same solution at 0.4 V for 900 s.

3. RESULTS AND DISCUSSION

3.1. CS Nanostructures Supported on Vulcan. Figure 1 shows characteristic TEM images of the various CS nanostructures supported on Vulcan. The images show a systematic increase in the particle size as the Pd atomic ratio with respect to Au content increases from 20 to 80%. CS nanoparticles are well dispersed in the carbon support, ensuring a high metal dispersion in the catalysts with very low density of aggregates. The average particle diameter (D) and shell thickness (δ) are consistent with those obtained from analysis of a large number of as-prepared (unsupported) nanoparticles.[28] Table 1 summarizes the average dimensions of particles as a function of Pd content, as well as the average metal loading of each catalyst as estimated from EDX. No metallic nanostructures with sizes significantly smaller than 20 nm are observed in any of the samples investigated, strongly suggesting that Pd nucleation occurs exclusively at the Au cores. The average atomic metal weight ratio obtained from EDX measurements corresponds very accurately to the composition of the synthesis bath, further confirming that the Pd precursor is entirely reduced at the Au nanoparticles. The total metal loading in the catalysts are in the range of 15 to 20%.

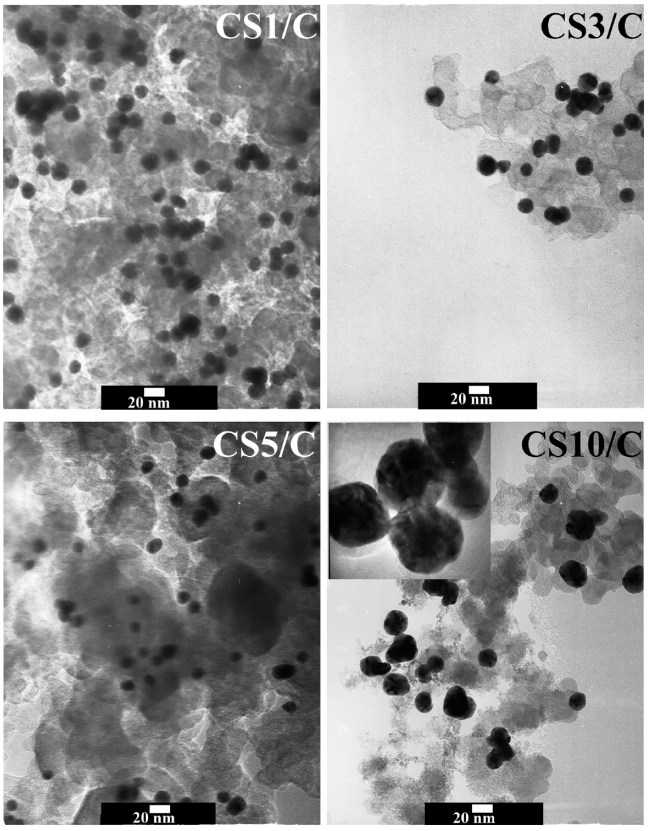

Figure 1. TEM images of the various CS nanoparticles supported on Vulcan. The inset in CS10 is an image with higher magnification, showing the contrast between the Au core and the Pd shell.

Table 1. Average Diameter (D), Pd Thickness (δ), Au:Pd Weight Composition, and Metal Loading on the Vulcan Support

	D (nm)[a]	δ (nm)[a]	Au:Pd weight ratio	metal loading (wt %)
Au/C	19.3 ± 1.2		100:0	19.5 ± 1.2
CS1/C	21.8 ± 1.1	1.3 ± 0.1	81.3:18.7 ± 2.4	15.0 ± 1.9
CS3/C	24.7 ± 1.3	2.7 ± 1.0	61.9:38.1 ± 1.1	19.2 ± 2.1
CS5/C	29.5 ± 1.2	5.1 ± 0.9	42.2:57.8 ± 0.9	18.5 ± 2.9
CS10/C	38.9 ± 1.5	9.9 ± 1.1	17.9: 82.1 ± 0.7	17.5 ± 1.4
Pd/C	10.0 ± 1.8		0:100	18.4 ± 2.5

[a]Values obtained after analysis of more than 200 as-prepared nanoparticles.[28]

The core−shell configuration of the nanostructures is demonstrated by the STEM-HAADF images of CS1 and CS5 shown in Figure 2, where a strong contrast is observed between the bright Au core and the more opaque Pd shell (Figure 2A,C). The intensity profiles produced by the line-scan analysis of Au−Mα and Pd−Lα X-rays along the line on the STEM-HAADF images are plotted in Figure 2B,D, for CS1 and CS5 nanoparticles, respectively. The EDX line-scan analysis confirmed that nanoparticles are composed of Au and Pd. The initial point of the scan is located at the particle edge, showing that the CS surface mainly contains Pd. The crossing over point in Figure 2B,D between the Au and Pd intensity lines, as Au content increases, agrees well with the Pd layer thickness determined from the difference in average diameter

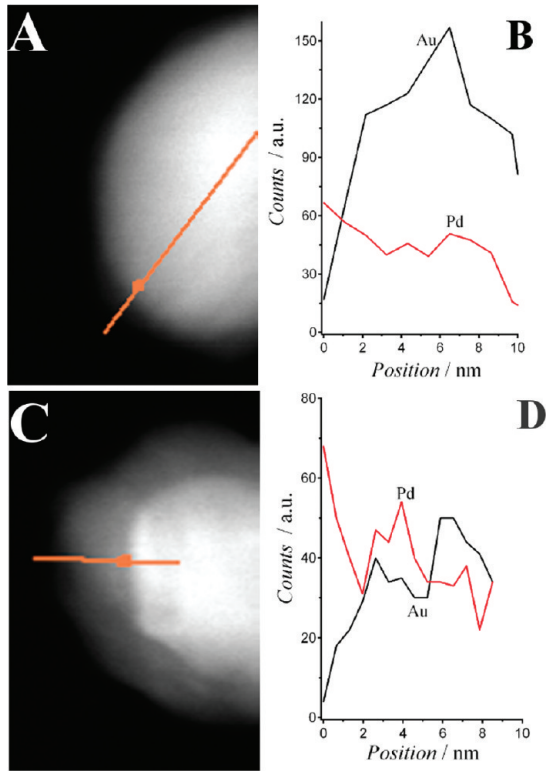

Figure 2. STEM-HAADF images and EDX intensity profile of CS1 (A,B) and CS5 (C,D) nanoparticles. The EDX intensity profile is obtained along the red line indicated in the corresponding STEM image.

dx.doi.org/10.1021/jp211747a | J. Phys. Chem. C 2012, 116, 6275−6282

between CS nanoparticles and the initial Au core. Although this analysis does not entirely exclude the possibility of a degree of metallic intermixing at the Au−Pd boundary layer (the spatial resolution of the technique is approximately 1 nm), it can be concluded that the surface of the CS nanoparticle is overwhelmingly composed of Pd. These results agree with previous reports, which conclude that, although there might be a degree of mixing in the first layer of Pd, high temperatures are required to observe a significant amount of alloying between Pd shells and Au cores.[29,40−42]

Figure 3 shows the powder X-ray diffractograms for the different catalysts. The Au/C sample features sharp diffraction

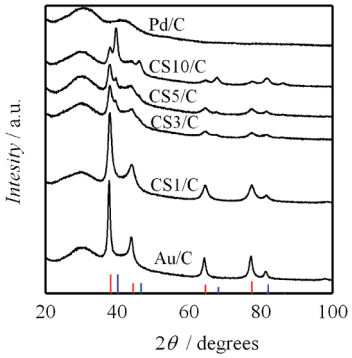

Figure 3. Powder XRD diffractograms of the various metallic nanostructures on the Vulcan support. Composition and dimension of the various samples are indicated in Table 1. The red lines at the bottom of the graph, at 38.1°, 44.4°, 64.6°, 77.5°, and 81.7°, indicate the standard Au diffraction pattern (PDF 040784), while the blue lines at 40.1°, 46.7°, 68.1°, 82.1° and 86.6° belong to Pd (PDF 461043).

peaks due to the well-defined polycrystalline structure of Au. The signals at 38.3°, 43.9°, 64.8°, 77.7°, and 81.5° are due to the (111), (200), (220), (311), and (222) planes of the face-centered cubic (fcc) gold phase, respectively. The highest diffraction peak can be seen at 38.3°, suggesting that Au nanoparticles have a strong (111) orientation. No clear diffraction peaks are observed for Pd/C sample, suggesting a poor crystalline structure of the monometallic nanoparticles. The presence of Au cores templates the growth of the Pd shells, allowing the progressive appearance of Pd diffraction peaks on the core−shell samples. The characteristic diffraction peak attributed to Pd(111) at 2θ = 40.2° appears in CS3/C, CS5/C, and CS10/C samples, and its intensity increases with increasing Pd thickness. In addition to the peaks associated with the metallic nanostructures, all samples exhibit a broad peak at 2θ = 26° that is characteristic of the plane (002) of graphite from Vulcan support.

The behavior of the XRD patterns in Figure 3 is consistent with a core−shell configuration of the metal nanoparticles, rather than with Au−Pd alloy formation. Alloyed particles have been shown to present peaks that shift from the position of the gold pattern to that of palladium as the Pd content increases, without shoulders or individual peaks being observed for each metal.[41,43] However, XRD patterns identical to Au are reported for very thin Pd shells on Au substrates,[44,45] with shoulder peaks appearing for increasingly thicker shells.[46] The tendency of Pd and Au to segregate, with Pd rich surfaces and Au cores, rather than forming alloys, has been reported.[47,48] Similar seeding growth methods as the one used here have been widely studied, with a variety of characterization techniques, such as UV−vis spectroscopy, XRD, TEM (high resolution and dark field), EDX, elemental mapping, XANES, and EXAFS, have all confirmed the core−shell nature of Pd−Au nanostructures.[39,40,42,44,46,49,50] Our own previous work with selected area electron diffraction patterns (SADPs) provided a quantitative relationship between the average Pd shell thickness and its corresponding lattice strain induced by the Au core.[28] It has been established that in order for significant alloying to occur, the temperature needs to be increased considerably above room temperature (a range between 200 and 300 °C has been reported).[40,42] An important aspect of these results is that XRD patterns are almost identical to those reported for the same set of nanoparticles in the absence of Vulcan support.[27] This observation further confirms that the structure of the nanoparticles does not undergo any significant change, such as extensive aggregation or sintering, upon loading in the carbon matrix.

3.2. CO-Stripping from Vulcan Supported Nanostructures. Figure 4 contrasts the CO-stripping voltammetry of Pd/

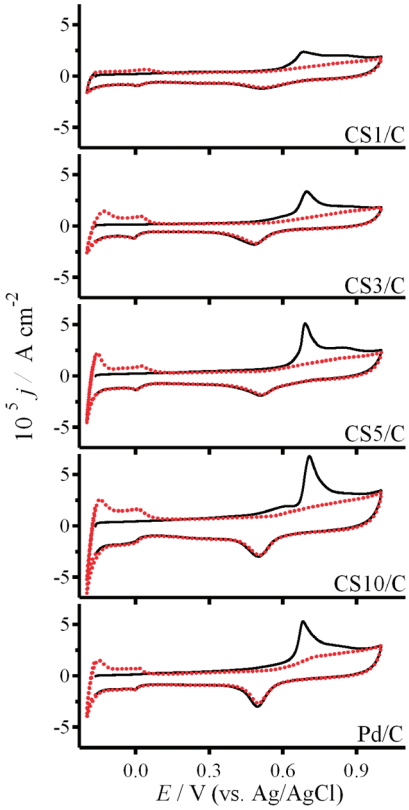

Figure 4. CO stripping voltammograms of the various nanostructures supported on Vulcan, in 0.5 mol dm^{-3} H_2SO_4 solution, at 0.02 V s^{-1}. The black full line corresponds to the first cycle, while the second cycle is displayed as a red dotted line.

C and the various CS/C materials as a function of the thickness of Pd shell. Hydrogen adsorption signals in the initial forward scan (solid line) appear completely suppressed due to the adsorbed CO blocking of the Pd active sites. The key feature of the forward scan is the CO stripping peak. The second cycle (dotted line) following CO stripping corresponds to the voltammogram of ultrathin Pd films in acidic media. Pd oxide formation and reduction are present at 0.6 V in the positive scan and 0.5 V in the negative scan, respectively. The peaks due to hydrogen adsorption and absorption are clearly developed in

dx.doi.org/10.1021/jp211747a | J. Phys. Chem. C 2012, 116, 6275−6282

the second cycle, suggesting a complete removal of CO in the initial forward scan. As expected, the hydrogen absorption signal at the negative end of the potential window exhibits a progressive increase with increasing Pd thickness. No detectable CO-stripping peak was found on the Au/C sample in the potential range studied (results not shown), which is consistent with the fact that CO does not adsorb on Au in acid solutions.[51]

The electroactive surface areas used for estimating the current density of the various catalysts in Figure 4 were calculated from the charge associated with the CO-stripping signal. In our previous studies, the average CO coverage as a function of Pd thickness was quantitatively determined employing electrostatic assemblies of CS nanostructures with controlled particle number density on ITO electrodes.[27] Employing the charge obtained from experiments in the absence of Vulcan support allows a more accurate determination of the active surface area. Obviously, this analysis is based on the assumption that the Vulcan support has little influence on the CO coverage at CS nanostructures. Other commonly used methods of determining the electroactive area of Pd involve oxide reduction or hydrogen signals. Taking the charge associated with the Pd oxide reduction, the effective surface area appears consistent to the values estimated from the CO-stripping charge, particularly in the case of larger Pd thickness. However, the use of hydrogen adsorption and PdO signals for estimating effective current densities is affected by the relatively large capacitive currents of the carbon-supported catalysts. All current densities presented in this work are normalized by the electrochemical active area of Pd obtained for each individual electrode as described above. On average, the electroactive areas are found to be between 6.2 and 8.5 cm^2, for the CS10/C and the CS1/C samples, respectively. It should also be mentioned that the average active surface area increases not only with increasing Pd thickness (geometric factor) but also due to an increase in the average roughness factor.[28]

One of the most important observations from Figure 4 is related to the position of the CO stripping peak as a function of the nanoparticle composition. Pd/C catalyst shows a CO-stripping peak potential at 0.69 V, following the common behavior described in the literature for these catalysts.[45,52] The potential at which CO stripping occurs is similar on all CS/C catalysts, although a small pre-peak is observed on the CS10/C sample. This feature is probably due to oxidation of CO at defect sites associated with the high surface roughness of this catalyst;[28] the effect of step edges at Pd (111) surfaces on the kinetics of CO oxidation has been previously noted in the literature.[33] The weak dependence of the CO stripping potential on Pd thickness on the CS/C samples is rather different to the behavior observed at electrostatically adsorbed CS nanoparticles on ITO electrodes (CS/ITO). A substantial shift of the CO-stripping peak toward more positive potential was observed upon decreasing Pd thickness on CS/ITO assemblies.[27] *This observation points toward a clear change in the particle reactivity induced by Vulcan support.* The origin of this change in reactivity is most likely related to the effect of the support on the generation of oxygen-containing groups at Pd surfaces, which is the initial step in both the formation of Pd oxides and CO stripping. It should also be noted that the onset potential of Pd oxide formation also exhibits a significantly weaker dependence on Pd thickness on CS/C with respect to CS/ITO. As an interesting comparison, Hayden et al. reported a strong increase of the potentials for CO stripping and oxide formation with decreasing Pt center sizes supported on TiO_2, while this shift appears attenuated when supported on carbon.[53] We propose that the carbon support affects the structure of the water layer at the catalyst surface, which manifests itself by a common onset potential for the formation of oxygenated species at all CS nanoparticle surfaces supported on Vulcan. Although the mechanisms of water (and other oxygenated species such as hydroxides) adsorption on carbon surfaces is still under debate, it is clear that surface chemistry plays an important role.[54] The formation of water clusters of between 4 and 12 molecules, for example, has been reported to enhance adsorption in graphitic nanopores, changing the chemical affinity of the surface, as well as limiting the freedom of motion of the water molecules at the surface.[55] The role of water orientation on the properties of liquid/solid interfaces, and the influence of potential on the adopted configuration of water molecules at the surface has been reported; in the case of RuO_2, for example, water can be adsorbed through hydrogen bonds at reductive potentials, mainly as hydroxide linked through the oxygen atoms at intermediate potentials and forms a double water layer with closely packed oxygen at potentials just below oxygen evolution.[56] The effect of water orientation on electrochemical reactions has also attracted attention, with nitrobenzene reactions on Au electrodes being very dependent on whether water is adsorbed through the hydrogen or the oxygen atom at the electrode surface, for example.[57]

The average stripping charge density (CO coverage) exhibits a systematic decrease with decreasing Pd thickness in the CS containing catalysts. The fact that this parameter is used in the normalization of the current density prevents us from establishing quantitative relationships. However, this trend is qualitatively consistent with our previous studies on CS/ITO assemblies, revealing strain-induced effects on the interaction between Pd and CO.[27,28] *Consequently, it can be concluded that the CO coverage on Vulcan supported CS nanoparticles is determined by the lattice strain of Pd layer, while carbon support has a clear effect on the surface oxidation potential.*

3.3. Oxidation of Formic Acid. Figure 5 shows cyclic voltammograms recorded at room temperature for Pd and Au–Pd CS supported on Vulcan in 2 mol dm^{-3} HCOOH and 0.5 mol dm^{-3} H_2SO_4. Formic acid oxidation starts at −0.1 V and continues until it reaches a maximum in the positive scan at 0.3 V. A slight shift of the current peak toward more negative potentials is observed with increasing Pd content, reaching a value of 0.2 V for Pd/C. The drop in the current densities at more positive potentials is associated with the Pd oxide formation. In the backward scan, the surface remains inactive until the Pd oxide reduction takes place. The current densities for the negative and positive scans were nearly identical, while consecutive scans were highly reproducible (results not shown), indicating a low tendency for poisoning of electrode surfaces via adsorbed intermediates.[32]

The currents are similar for CS with thick Pd shells and pure Pd NPs, while they are significantly lower for the thinnest Pd shell (CS1/C). A similar trend was reported in the case of CS/ITO assemblies.[27] The rationale behind these observations is yet to be fully clarified. In the seminal work by Baldauf and Kolb on epitaxial Pd layers at Au single crystal electrodes, a very weak dependence of the HCOOH oxidation current was observed with Pd thickness.[32] However, the reactivity of Pd/Au(100) appears significantly higher than on Pd/Au(110) and Pd/Au(111). We can tentatively correlate the high currents observed on the thicker Pd layers with the appearance of the

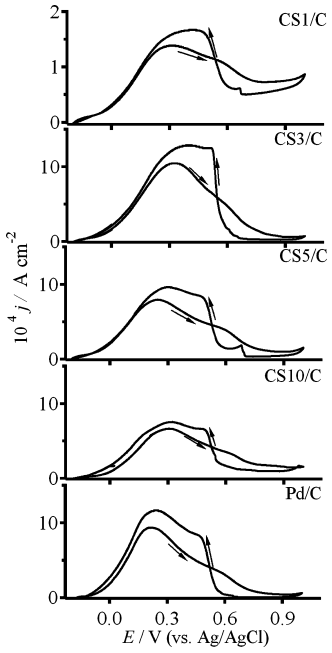

Figure 5. Cyclic voltammograms of the various nanostructures supported on Vulcan in the presence of 2 mol dm^{-3} HCOOH and 0.5 mol dm^{-3} H_2SO_4, at 0.02 V s^{-1}.

more reactive crystal planes in XRD patterns (see Figure 3). However, it is important to highlight the fact that our observations are qualitatively different to other reports in the literature.[45,58,59]

Although particle size effects can be significant in HCOOH oxidation, the results obtained here present the opposite trend to that established in previous works. Catalytic activity toward HCOOH oxidation is heavily affected by size when using particles below 10 nm and increases with decreasing size.[20,60] All particles used in this work are 10 nm or larger, and the catalytic activity increases with increasing particle size. Additionally, size effects have been recently linked to the appearance of crystal phases in the Pd nanoparticles, which agrees with our tentative explanations above.[20,27]

Figure 6 compares chronoamperometric transients at 0.40 V in the HCOOH containing electrolyte solution. As Au/C exhibited negligible activity for formic acid electro-oxidation under these experimental conditions, it was not included in the graph. All of the transients are characterized by a decay of the

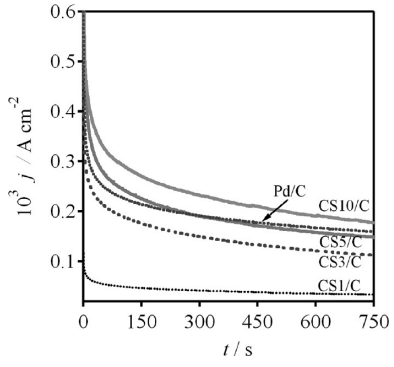

Figure 6. Chronoamperometric transients of Pd and CS catalysts supported on Vulcan at 0.40 V, in 2 mol dm^{-3} HCOOH and 0.5 mol dm^{-3} H_2SO_4.

current with time. This current decay is significantly stronger than expected for diffusion controlled process, suggesting that the origin of this process is the deactivation of the catalyst active sites. The apparent deactivation rate is rather similar for all of the samples, suggesting that the deactivation mechanism is not affected by the catalyst structure. However, the results show a clear increase of the reactivity toward formic acid oxidation with increasing Pd thickness.

The effect of support on the reactivity toward HCOOH oxidation is exemplified in Figure 7. The current density of

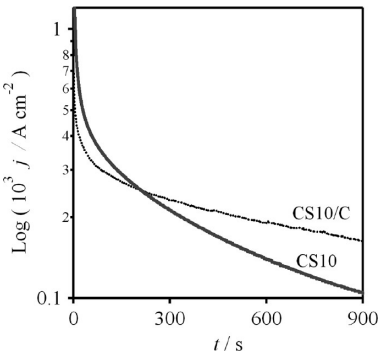

Figure 7. Comparison of transients associated with HCOOH oxidation on CS10 nanoparticles assembled at ITO (CS10/ITO) and supported on Vulcan (CS10/C), at 0.40 V. The composition of the electrolyte solution can be found in the caption of Figure 6.

CS10/ITO is slightly higher than at CS10/C at short times. However, *the deactivation rate of the carbon supported nanoparticles is significantly slower than on CS10/ITO assemblies.* The same behavior was observed for all CS and Pd nanostructures, suggesting that Vulcan support increases the catalyst tolerance toward poisoning intermediates. This effect could be related to the promotion of oxygenated species at Pd shells induced by Vulcan support, although further investigation is required in order to elucidate this trend. As mentioned above, it has been already demonstrated that a CO-like intermediate can be only oxidatively removed from the active sites by oxygen-containing species on a neighboring surface site.[18] Larsen et al. also concluded that the chronoamperometric activity of carbon supported Pd nanoparticles is higher than that of unsupported catalysts.[16] However, unlike the previously mentioned work, our studies are not affected by differences in particle size and dispersion.

Figure 8 compares the average formic acid oxidation current density obtained after 750 s at 0.40 V, for the various CS and Pd nanoparticles supported on Vulcan or assembled on modified ITO electrodes.[27] As mentioned previously, the current density associated with HCOOH strongly increases with increasing Pd thickness, probably due to the formation of highly reactive crystal facets on the thicker shells, as seen through XRD patterns in Figure 3. Although CS/ITO and CS/C exhibit similar trends, the current densities obtained for the carbon-supported nanoparticles are significantly higher, particularly for the pure Pd NPs and those CS nanoparticles with thicker Pd layers. As mentioned above, this behavior is connected to the slower deactivation rate of the catalytic active sites in the presence of carbon support. Consequently, the overall activity of the catalysts strongly depends on the composition/structure of the metallic nanostructures, while

dx.doi.org/10.1021/jp211747a | J. Phys. Chem. C 2012, 116, 6275−6282

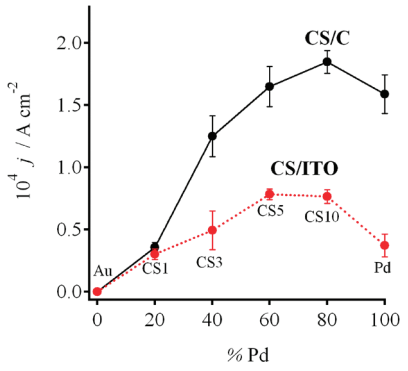

Figure 8. Current density at 750 s associated with HCOOH oxidation at 0.40 V on the various metallic nanostructures assembled on ITO (red) and supported on Vulcan (black). See caption of Figure 6 for the composition of the electrolyte solution.

the support plays an important role on the accumulation of intermediates at the active sites.

4. CONCLUSIONS

The reactivity of Au−Pd CS nanostructures toward CO and HCOOH electro-oxidation is not only determined by the composition and structure of Pd overlayer but also by interaction with the support. The approach described in this report is based on the synthesis of CS nanoparticles by colloidal methods with accurate control over the size and Pd thickness. The latter parameter strongly affect the average lattice strain of the Pd overlayer.[28] These nanoparticles are subsequently incorporated in Vulcan with a controlled total metal loading and without compromising the nanoparticle structure. Detailed analysis of the responses associated with CO striping in acid solution, employing independent CO coverage measurements at assemblies with control particle number density,[27] allows estimating the electrochemical active area of the nanoparticles supported on Vulcan.

Analysis of the CO stripping voltammograms in acid solution concluded that the CO coverage is strongly linked with the average lattice strain of CS nanoparticles, while the carbon support affects the onset potential for CO oxidation. In particular, the CO stripping peak potential on CS1/ITO[27] is shifted by approximately 100 mV toward more negative potentials on CS1/C. We propose that this shift in the oxidation potential is related to the structure of the water layer around CS/C structures, which decreases the onset for the formation of oxygenated species at the Pd surface.

HCOOH oxidation also exhibits a strong dependence on the support. Our results confirm that the current density is dependent on the thickness of Pd shells, although the physical rational for this behavior is yet to be clarified.[27] However, nanoparticles supported on Vulcan exhibit a significantly slower deactivation rate in chronoamperometric measurements, in comparison to CS/ITO assemblies. Although further studies are required to fully uncover the role of the substrate in the catalytic activity of metal centers, we believe the approach highlighted here elucidates some important trends. More importantly, these trends are not related to the effect of the substrate in the structure of the metallic center; a limitation in studies featuring conventional impregnation methods followed by nucleation of the nanoparticles in the carbon matrix. We are extending this methodology in order to evaluate a series of carbon supports with different structures and functionalities.

AUTHOR INFORMATION

Corresponding Author

*Tel: +44 117 9288981. Fax: +44 117 9250612. E-mail: David.Fermin@bristol.ac.uk. Weblink: www.bristol.ac.uk/pt/electrochemistry.

Notes

The authors declare no competing financial interest.

ACKNOWLEDGMENTS

We are indebted to Dr. Paramaconi Rodriguez (Paul Scherrer Institut) for the enlightening discussions. We also acknowledge J.A. Jones, Dr. Mairi Haddow (University of Bristol) and R. Fernandez-Pacheco (Instituto Universitario de Nanociencias de Aragón) for their support with the characterization of nanostructures by electron microscopy and X-ray diffraction. M.G.M.O and V.C. acknowledge the financial support from the Mexican National Council for Science and Technology (CONACyT) and CSIC (Spain) for her JAE grant, respectively. V.C. and M.J.L. gratefully acknowledge the financial support by the MICINN through Project MAT2008-06631-C03-01. D.P. and D.J.F. are grateful for the financial support from the U.K. Engineering and Physical Sciences Research Council (project EP/H046305/1) and the University of Bristol.

REFERENCES

(1) Dicks, A. L. *J. Power Sources* **2006**, *156*, 128.
(2) Tang, S.; Sun, G.; Qi, J.; Sun, S.; Guo, J.; Xin, Q.; Haarberg, G. M. *Chin. J. Catal.* **2010**, *31*, 12.
(3) Lázaro, M. J.; Calvillo, L.; Celorrio, V.; Pardo, J. I.; Perathoner, S.; Moliner, R. In *Carbon Black: Production, Properties and Uses*; Sanders, I. J., Peeten, T. L., Eds.; Nova Science Publishers, Inc.: Hauppauge, NY, 2011; p 41.
(4) Kim, M.; Park, J.-N.; Kim, H.; Song, S.; Lee, W.-H. *J. Power Sources* **2006**, *163*, 93.
(5) Yu, X.; Ye, S. *J. Power Sources* **2007**, *172*, 133.
(6) Calvillo, L.; Celorrio, V.; Moliner, R.; Lázaro, M. J. *Mater. Chem. Phys.* **2011**, *127*, 335.
(7) Liu, H.; Song, C.; Zhang, L.; Zhang, J.; Wang, H.; Wilkinson, D. P. *J. Power Sources* **2006**, *155*, 95.
(8) Celorrio, V.; Montes de Oca, M. G.; Plana, D.; Moliner, R.; Lázaro, M. J.; Fermín, D. J. *Int. J. Hydrogen Energy*, **2011**. DOI:10.1016/j.ijhydene.2011.12.014.
(9) Lamy, C.; Lima, A.; LeRhun, V.; Delime, F.; Coutanceau, C.; Léger, J.-M. *J. Power Sources* **2002**, *105*, 283.
(10) Edwards, P. P.; Kuznetsov, V. L.; David, W. I. F.; Brandon, N. P. *Energy Policy* **2008**, *36*, 4356.
(11) McNicol, B. D.; Rand, D. A. J.; Williams, K. R. *J. Power Sources* **1999**, *83*, 15.
(12) Huang, Y.; Zhou, X.; Liao, J.; Liu, C.; Lu, T.; Xing, W. *Electrochem. Commun.* **2008**, *10*, 621.
(13) Jeong, K.-J.; Miesse, C. M.; Choi, J.-H.; Lee, J.; Han, J.; Yoon, S. P.; Nam, S. W.; Lim, T.-H.; Lee, T. G. *J. Power Sources* **2007**, *168*, 119.
(14) Yu, X.; Pickup, P. G. *J. Power Sources* **2008**, *182*, 124.
(15) Ha, S.; Larsen, R.; Masel, R. I. *J. Power Sources* **2005**, *144*, 28.
(16) Larsen, R.; Ha, S.; Zakzeski, J.; Masel, R. I. *J. Power Sources* **2006**, *157*, 78.
(17) Huang, Y.; Liao, J.; Liu, C.; Lu, T.; Xing, W. *Nanotechnology* **2009**, *20*, 105604.
(18) Hu, C.; Bai, Z.; Yang, L.; Lv, J.; Wang, K.; Guo, Y.; Cao, Y.; Zhou, J. *Electrochim. Acta* **2010**, *55*, 6036.
(19) Wang, R.; Liao, S.; Ji, S. *J. Power Sources* **2008**, *180*, 205.
(20) Zhou, W.; Lee, J. Y. *J. Phys. Chem. C* **2008**, *112*, 3789.
(21) Zhang, L.; Lu, T.; Bao, J.; Tang, Y.; Li, C. *Electrochem. Commun.* **2006**, *8*, 1625.
(22) Capon, A.; Parsons, R. *J. Electroanal. Chem.* **1973**, *45*, 205.

(23) Jung, W. S.; Han, J.; Yoon, S. P.; Nam, S. W.; Lim, T.-H.; Hong, S.-A. *J. Power Sources* **2011**, *196*, 4573.
(24) Yu, X.; Pickup, P. G. *Electrochem. Commun.* **2009**, *11*, 2012.
(25) Yu, X.; Pickup, P. G. *J. Power Sources* **2009**, *187*, 493.
(26) Zhou, Y.; Liu, J.; Ye, J.; Zou, Z.; Ye, J.; Gu, J.; Yu, T.; Yang, A. *Electrochim. Acta* **2010**, *55*, 5024.
(27) Montes de Oca, M. G.; Plana, D.; Celorrio, V.; Lázaro, M. J.; Fermín, D. J. *J. Phys. Chem. C* **2012**, *116*, 692.
(28) Montes de Oca, M. G.; Kumarakuru, H.; Cherns, D.; Fermín, D. J. *J. Phys. Chem. C* **2011**, *115*, 10489.
(29) Ding, Y.; Fan, F.; Tian, Z.; Wang, Z. L. *J. Am. Chem. Soc.* **2010**, *132*, 12480.
(30) Alcaide, F.; Álvarez, G.; Cabot, P. L.; Grande, H.-J.; Miguel, O.; Querejeta, A. *Int. J. Hydrogen Energy* **2011**, *36*, 4432.
(31) Xu, J. B.; Zhao, T. S.; Shen, S. Y.; Li, Y. S. *Int. J. Hydrogen Energy* **2010**, *35*, 6490.
(32) Baldauf, M.; Kolb, D. M. *J. Phys. Chem.* **1996**, *100*, 11375.
(33) El-Aziz, A. M.; Kibler, L. A. *J. Electroanal. Chem.* **2002**, *534*, 107.
(34) Kibler, L. A.; El-Aziz, A. M.; Kolb, D. M. *J. Mol. Catal. A: Chem.* **2003**, *199*, 57.
(35) Ruvinsky, P. S.; Prokin, S. N.; Zaikovskii, V. I.; Bernhardt, P.; Savinova, E. R. *Phys. Chem. Chem. Phys.* **2008**, *10*, 6665.
(36) Liu, Y.; Wang, L.; Wang, G.; Deng, C.; Wu, B.; Gao, Y. *J. Phys. Chem. C* **2010**, *114*, 21417.
(37) Turkevich, J.; Miner, R. S.; Babenkova, L. *J. Phys. Chem.* **1986**, *90*, 4765.
(38) Li, F.; Ciani, I.; Bertoncello, P.; Unwin, P. R.; Zhao, J. J.; Bradbury, C. R.; Fermin, D. J. *J. Phys. Chem. C* **2008**, *112*, 9686.
(39) Lu, L.; Wang, H.; Shiquan, S.; Zhang, H. *J. Mater. Chem.* **2002**, *12*, 156.
(40) Lee, A. F.; Baddeley, C. J.; Hardacre, C.; Ormerod, R. M.; Lambert, R. M.; Schmid, G.; West, H. *J. Phys. Chem.* **1995**, *99*, 6096.
(41) Nie, M.; Shen, P. K.; Wei, Z. *J. Power Sources* **2007**, *167*, 69.
(42) Hu, J.-W.; Li, J.-F.; Ren, B.; Wu, D.-Y.; Sun, S.-G.; Tian, Z.-Q. *J. Phys. Chem. C* **2007**, *111*, 1105.
(43) Lee, Y. W.; Kim, N. H.; Lee, K. Y.; Kwon, K.; Kim, M.; Han, S. W. *J. Phys. Chem. C* **2008**, *112*, 6717.
(44) Nitani, H.; Yuya, M.; Ono, T.; Nakagawa, T.; Seino, S.; Okitsu, K.; Mizukoshi, Y.; Emura, S.; Yamamoto, T. A. *J. Nanopart. Res.* **2006**, *8*, 951.
(45) Zhou, W.; Lee, J. Y. *Electrochem. Commun.* **2007**, *9*, 1725.
(46) Liang, H.-P.; Lawrence, N. S.; Jones, T. G. J.; Banks, C. E.; Ducati, C. *J. Am. Chem. Soc.* **2007**, *129*, 6068.
(47) Kobayashi, H.; Yamauchi, M.; Ikeda, R.; Kitagawa, H. *Chem. Commun.* **2009**, 4806.
(48) Teng, X.; Wang, Q.; Liu, P.; Han, W.; Frenkel, A.; Wen, W.; Marinkovic, N.; Hanson, J. C.; Rodriguez, J. A. *J. Am. Chem. Soc.* **2008**, *130*, 1093.
(49) Zhu, L. D.; Zhao, T. S.; Xu, J. B.; Liang, Z. X. *J. Power Sources* **2009**, *187*, 80.
(50) Hu, J. W.; Zhang, Y.; Li, J. F.; Liu, Z.; Ren, B.; Sun, S. G.; Tian, Z. Q.; Lian, T. *Chem. Phys. Lett.* **2005**, *408*, 354.
(51) Rodriguez, P.; Garcia-Araez, N.; Koper, M. T. M. *Phys. Chem. Chem. Phys.* **2010**, *12*, 9373.
(52) Moore, A.; Celorrio, V.; Montes de Oca, M. G.; Plana, D.; Hongthani, W.; Lázaro, M. J.; Fermín, D. J. *Chem. Commun.* **2011**, *47*, 7656.
(53) Hayden, B. E.; Pletcher, D.; Suchsland, J.-P.; Williams, L. J. *Phys. Chem. Chem. Phys.* **2009**, *11*, 9141.
(54) Phillips, J.; Kelly, D.; Radovic, L.; Xie, F. *J. Phys. Chem. B* **2000**, *104*, 8170.
(55) Ohba, T.; Kanoh, H.; Kaneko, K. *J. Am. Chem. Soc.* **2004**, *126*, 1560.
(56) Chu, Y. S.; Lister, T. E.; Cullen, W. G.; You, H.; Nagy, Z. *Phys. Rev. Lett.* **2001**, *86*, 3364.
(57) Fan, L. J.; Wang, C.; Chang, S. C.; Yang, Y. W. *J. Electroanal. Chem.* **1999**, *477*, 111.
(58) Zhang, G.; Wang, Y.; Wang, X.; Chen, Y.; Zhou, Y.; Tang, Y.; Lu, L.; Bao, J.; Lu, T. *Appl. Catal., B* **2011**, *102*, 614.
(59) Suo, Y.; Hsing, I. M. *Electrochim. Acta* **2011**, *56*, 2174.
(60) Zhang, X. G.; Arikawa, T.; Murakami, Y.; Yahikozawa, K.; Takasu, Y. *Electrochim. Acta* **1995**, *40*, 1889.

Apéndice 1

Datos revistas

1. ENERGY & FUELS

Energy & Fuels publica artículos de investigación en todos los ámbitos de la química de las fuentes de energía no nucleares, incluyendo la relacionada con la formación de, exploración de, y producción de combustibles fósiles; las propiedades y la estructura o la composición molecular de los combustibles crudos y productos refinados; la química relacionada con el procesado y la utilización de combustibles; pilas de combustible y sus aplicaciones; y las técnicas analíticas e instrumentales utilizados en las investigaciones de las áreas anteriores.

Investigaciones sobre sustancias distintas a los combustibles cuyo objetivo sea aclarar algún aspecto de la química de los combustibles son bienvenidas, así como documentos sobre fotoquímica de combustibles y producción de energía. No serán publicados los artículos que traten sobre energía nuclear o exclusivamente de aspectos

económicos del proceso. Tanto la investigación básica, como la aplicada son bienvenidas.

Esta revista se encuentra indexada en: CAS, SCOPUS, EBSCOHost, Thomson-Gale, British Library, Web of Science.

Factor de impacto 2010: 2.444

Área temática (ISI Web of Knowledge): Energía & Combustibles, Ingeniería, Química

Mi contribución como autora en el artículo publicado en esta revista titulado "*Study of the Synthesis Conditions of Carbon Nanocoils for Energetic Applications*" fue la de responsable de la parte experimental, del análisis de los resultados y de la redacción del artículo.

2. MICROPOROUS AND MESOPOROUS MATERIALS

Microporous and Mesoporous Materials es una revista internacional que cubre aspectos novedosos e importantes de los sólidos porosos clasificados como microporos (tamaños de poro hasta 2 nm) o mesoporosos (tamaños de poro entre 2 y 50 nm). Ejemplos típicos son las zeolitas, tamices moleculares de carbon, materiales híbridos porosos orgánicos/inorgánicos u óxidos metálicos porosos. Tanto los materiales sintéticos como naturales entran dentro del alcance de la revista. Los temas de particular interés incluyen: todos los aspectos de sólidos microporosos y mesoporosos que ocurren en la naturaleza; la síntesis de materiales cristalinos o amorfos con poros en el rango adecuado; las propiedades físico-químicas, especialmente la caracterización espectroscópica y microscópica de estos materiales; su modificación, por ejemplo mediante intercambio iónico o reacciones en estado sólido; todos los temas relacionados con la difusión de especies móviles en los poros de estos materiales; adsorción (y otras técnicas de separación) mediante adsorbentes microporosos o mesoporosos; catálisis por esos materiales; todos los temas relacionados con su aplicación o de posible aplicación en catálisis industrial, tecnología de separación, protección del medio ambiente, electroquímica, membranas, sensores, dispositivos ópticos, etc.

Esta revista se encuentra indexada en: Chemical Abstracts, Current Contents/Physics, Chemical, & Earth Sciences, Inorganic Crystal Structure Database, Scopus.

Factor de impacto 2009: 3.220

Área temática (ISI Web of Knowledge): Química Aplicada, Físico-Química, Nanociencia & Nanotecnología, Ciencia de Materiales

Mi contribución como autora en el artículo publicado en esta revista titulado "*Modification of the properties of carbon nanocoils by different treatments in liquid phase*" fue la de responsable de la parte experimental, del análisis de los resultados y de la redacción del artículo.

4. JOURNAL OF POWER SOURCES

El *Journal of Power Sources* constituye un foro interdisciplinar sobre todos los aspectos de la ciencia, tecnología y comercialización de baterías primarias/secundarias y pilas de combustible, supercondensadores, celdas fotoelectroquímicas; incluyendo sus aplicaciones en vehículos eléctricos, electrónica portátil, vehículos eléctricos híbridos, sistemas de UPS, sistemas de energía estacionaria, sistemas remotos de energía basados en eólica y/o solar, satélites y sondas espaciales.

Esta revista se encuentra indexada en: Cadscan, Chemical Abstracts, Compendex Plus, Congressional Information Service Inc, Current Contents, EIC/Intelligence (Energy Information Abstracts), Fuel and Energy Abstracts, INSPEC, Leadscan, Metals Abstracts, PASCAL/CNRS, Science Citation Index, Scopus, Zincscan.

Factor de impacto 2010: 4.283

Área temática (ISI Web of Knowledge): Electroquímica, Energía & Combustibles

Mi contribución como autora en el artículo publicado en esta revista titulado "*Influence of the synthesis method on the properties of Pt catalysts supported on carbon nanocoils for etanol oxidation*" fue la de responsable de la parte experimental, del análisis de los resultados y de la redacción del artículo.

5. THE JOURNAL OF PHYSICAL CHEMISTRY C

El *Journal of Physical Chemistry C* (Nanomateriales, Interfaces, y Física de Materia Condensada) publica trabajos originales de investigación experimental y básica dirigidos a científicos en química-física de nanopartículas y nanoestructuras,

superficies, interfaces, catálisis, transporte de electrones, dispositivos ópticos y electrónicos, sólidos cristalinos, y conversión y almacenamiento de energía.

Esta revista se encuentra indexada en: CAS, SCOPUS, British Library.

Factor de impacto 2010: 4.520

Área temática (ISI Web of Knowledge): Química, Física, Nanociencia & Nanotecnología, Ciencia de Materiales, Multidisciplinar

Mi contribución como autora en el artículo publicado en esta revista titulado "*Electrocatalytic properties of strained Pd nanoshells at Au nanostructures: CO and HCOOH oxidation*" fue la de responsable de la parte experimental y participación en el análisis de los resultados.

Mi contribución como autora en el artículo publicado en esta revista titulado "*The Effect of Carbon Supports on the Electrocatalytic Reactivity of Au-Pd Core-Shell Nanoparticles*" fue la de responsable de la parte experimental, del análisis de los resultados y de la redacción del artículo.